Modélisation du régime thermique des glaciers : applications à l'étude du risque glaciaire et à la quantification des changements climatiques à haute altitude

Adrien Gilbert

UNIVERSITÉ DE GRENOBLE

THÈSE

Pour obtenir le grade de

DOCTEUR DE L'UNIVERSITÉ DE GRENOBLE

Spécialité : **Science de la Terre et de l'Environnement**

Arrêté ministériel : 7 août 2006

Présentée par

Adrien GILBERT

Thèse dirigée par **Christian VINCENT et Patrick WAGNON**

préparée au sein du
Laboratoire de Glaciologie et Géophysique de l'Environnement
et de l'École Doctorale
Terre, Univers, Environnement

Modélisation du régime thermique des glaciers : applications à l'étude du risque glaciaire et à la quantification des changements climatiques à haute altitude.

Soutenue le **19 Décembre 2013**,
devant le jury composé de :

M. Olivier GAGLIARDINI
Professeur à l'UJF, Grenoble, Président
M. Martin FUNK
Professeur à l'ETH, Zürich, Rapporteur
M. Frank PATTYN
Professeur à l'UBL, Bruxelles, Rapporteur
M. Pierre RIBSTEIN
Professeur à l'UPMC, Paris, Examinateur
M. Christian VINCENT
Ingénieur de recherche au CNRS, LGGE, Grenoble, Directeur de thèse
M. Patrick WAGNON
Chargé de recherche à l'IRD, ICIMOD, Katmandou, Népal, Co-Directeur de thèse
M. Emannuel THIBERT
Ingénieur de Recherche à l'IRSTEA, Grenoble, Invité

Résumé

La température au sein des glaciers varie en fonction des variations climatiques. Dans un contexte de réchauffement climatique, ces variations peuvent être importantes et avoir des conséquences sur l'apparition de nouveaux aléas glaciaires.

Les travaux présentés dans cette thèse se focalisent sur la modélisation numérique de la réponse thermique des glaciers froids aux variations climatiques. La prise en compte du forçage climatique par la modification des conditions de surface des glaciers est l'un des points clefs de cette étude. On montre l'importance des processus de fusion/regel en zone d'accumulation froide ainsi que de l'épaisseur de la couverture de neige et névé autour de la ligne d'équilibre. Les modèles développés dans cette thèse s'appliquent à des cas concrets sur trois glaciers du massif du Mont Blanc (Alpes françaises). Ces études permettent d'analyser des situations à risque et de reconstituer le climat passé à haute altitude. Le jeu de données très complet acquis sur le site du Col du Dôme (4250 m) comprend des mesures profondes de températures et de densités ainsi que des mesures d'accumulation et de vitesses de surface. Il a permis de valider et développer un modèle à trois dimensions de régime thermique couplé à un modèle d'écoulement et forcé par des données climatiques. Ce modèle permet d'étudier en détail la réponse thermique des zones d'accumulation froides aux changements climatiques. Il peut aussi être utilisé pour la prédiction du réchauffement futur des glaciers suspendus présentant un risque comme le glacier de Taconnaz dont une analyse préliminaire est effectuée ici. Le réchauffement basal jusqu'au point de fusion pourrait conduire à la déstabilisation de ce type de glacier.

Le site du glacier de Tête Rousse (environ 3200 m) a permis d'établir clairement l'influence de la couverture de neige et de névé sur le régime thermique des glaciers autour de la ligne d'équilibre. Les résultats obtenus à partir du couplage d'un modèle de neige (CROCUS) avec un modèle de régime thermique sont en excellent accord avec les observations de températures réalisées dans le glacier. On explique ainsi les causes de la structure thermique particulière du glacier de Tête Rousse responsable de la formation d'une poche présentant un risque pour la commune à l'aval. Dans le futur, les simulations indiquent que le glacier va continuer de se refroidir, limitant ainsi le risque de formation de poche d'eau.

Dans le dernier chapitre, nous avons développé une nouvelle méthode inverse pour reconstituer les températures du passé à partir de profils de températures observées dans la glace. Elle est basée sur l'inversion simultanée de plusieurs profils de températures provenant de différents sites de forage ayant subi le même forçage climatique. La méthode permet de s'affranchir de l'impact des processus de fonte/regel en surface pour reconstruire les variations passées des températures de l'air. Les résultats obtenus sur le Col du Dôme montrent que le réchauffement climatique sur le site à 4250 m est similaire à celui observé à basse altitude. Ces résultats tendent à montrer que le réchauffement climatique n'est pas amplifié avec l'altitude.

Mots clés : Régime thermique, glaciers, climat, Alpes, aléas glaciaires, modèle inverse

Abstract

This thesis focuses on the numerical modeling of the thermal response of glaciers to climate changes. The change in surface conditions related to climate forcing is one of the key point of this study. We point out the crucial role of the meltwater refreezing in cold accumulation zone and the thickness of the snow and firn cover around the equilibrium line. The models are developed from the study of specific cases of three glaciers in Mont Blanc range (French Alps). These studies allow us to analyze the risk related to hanging glaciers and to reconstruct the past temperaures at high altitude from observed englacial temperatures. The very extensive dataset obtained at the site of the Col du Dôme (4250 m) includes measurements of deep temperatures and density profiles as well as measurements of snow accumulation and surface velocities. These observations allow us to develop and validate a three-dimensional thermal regime model coupled with a flow model and forced by meteorological data. This model is used to perform a thorough study of the thermal response of cold accumulation zone to climate change. It can also be used for the prediction of future glacial hazard related to hanging glaciers warming. A preliminary analysis has been carried out on the hanging glacier of Taconnaz. The warming could have a major impact on the stability of this kind of glaciers frozen to their beds if the melting point is reached.

The study performed on Tête Rousse glacier (about 3200 m) shows clearly the influence of the snowpack and firn cover on the thermal regime of glaciers around the equilibrium line. The results obtained from coupling of a snow model (CROCUS) with a model of thermal regime reveal a very good agreement with the observed ice temperatures. This study provides insights into the thermal processes responsible for water storage inside a small almost static glacier, which can lead to catastrophic outburst floods. In the future, according to atmospheric temperature increase scenarios for the coming century, most of the glacier will become cold which will reduce the risk of water filled cavity formation.

Finally, a new inverse method has been developed to reconstruct temperatures in the past from observed englacial temperatures. The method is based on the simultaneous inversion of several temperature profiles coming from different drilling sites with the same climate forcing. The method overcomes the impact of refreezing meltwater to reconstruct past air temperatures variations. This is similar to the observed regional low altitude trend. The results obtained on the Col du Dome shows that climate warming on the site at 4250 m is similar to the observed regional low altitude trend in the northwestern Alps, suggesting that air temperature trends are not altitude dependent.

Keywords : Thermal regime, glaciers, climate, Alpes, glacier hazards, borehole temperature inversion

Remerciements

L'ensemble des travaux réalisés dans cette thèse ont été possibles grâce au nombre important de données recueillies sur les glaciers Alpins depuis une vingtaine d'années sous l'impulsion de mon directeur de thèse Christian et avec l'aide d'un grand nombre de personnes. Je remercie donc Christian de m'avoir fait confiance pour exploiter cet exceptionnel jeu de données dont j'ai pu tirer de nombreuses valorisations et de m'avoir toujours intégré activement au sein de son équipe de recherche. Je salue aussi ses qualités humaines qui ont fait de cette thèse un vrai plaisir. Je remercie Patrick qui m'a introduit dans le milieu de la recherche en 2007, qui m'a toujours soutenu, m'a toujours encouragé et qui m'a été d'une aide précieuse depuis cette date. C'est en grande partie grâce (à cause ?) de lui si je fais de la Glaciologie aujourd'hui et que j'aime ça... merci.

Je remercie Gag avec qui j'ai beaucoup de plaisir à travailler pour m'avoir ouvert de nouvelles perspectives dans la simulation numérique et pour son accueil à Vancouver. Merci à Manu Thibert pour son soutien et de son aide tout au long de ma thèse. Merci à Patrick G. pour les aventures Boliviennes de pré-thèse qui ont contribué à ma motivation pour commencer une thèse en Glaciologie et pour les petites collaborations qui ont continué par-ci, par-là... Je remercie les membres du jury Pierre Ribstein, Martin Funk et Frank Pattyn pour avoir rapporté et examiné mon travail et pour l'intérêt qu'ils y ont porté.

Je pense aussi bien sûr à toutes les personnes avec qui j'ai passé de bons moments sur le terrain (qui représentent tout de même au moins six mois de ma thèse...) dans les Alpes, au Népal et à Kerguelen. Merci à toutes les personnes du laboratoire de Glaciologie qui ont contribué à une atmosphère de travail très plaisante. Une spéciale dédicace à la team CSU entre midi et deux...

Merci aux amis et compagnons de montagne pour les nombreuses sorties qui ont rythmé ces trois années de thèse.

Merci aux plus proches durant ces trois années, Sophie, Flo, An So, Gasp, Gui, Pierre, Martin, Sim, Bat, Xav, la famille Malvoisin, Max, Cam, Alex, Marion, Pierre B., Thomas pour tous les moments partagés.

Merci à mes parents, mes grands parents, Tatie, Mathilde et Alexis qui je sais sont fiers de moi !

Table des matières

Notes au lecteur

Ce manuscript de thèse s'organise autour de quatres articles en anglais (2 publiés, 1 soumis et 1 en préparation). Ces articles sont destinés à être publiés dans des revues scientifiques internationnales. Chaque article est introduit et conclut par une section en français qui le résume. Le manuscript a été écrit de telle sorte que le texte français suffise au lecteur pour connaitre les principaux résultats et conclusions de la thèse. Il existe donc des répétitions entre articles en anglais et sections françaises mais qui permettent la diffusion des résultats à un plus large public.

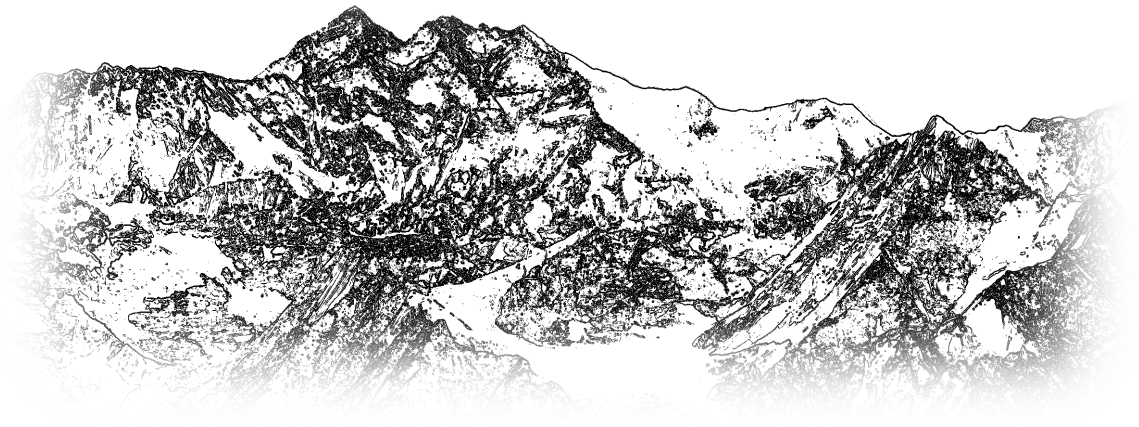

Chapitre 1

Glaciers, régime thermique et climat

Les changements climatiques influencent les variations de masse des glaciers et la variation de leur énergie interne. Les variations de masse se traduisent par des changements géométriques comme la taille et le volume très facilement observables. Les variations d'énergie se traduisent par des changements de la température interne du glacier et de son contenu en eau liquide. Ces changements, moins spectaculaires que les variations de volume du glacier, ont pourtant leur importance car ils influencent très largement la dynamique et l'hydrologie interne du glacier. Les conséquences sur les glaciers de montagne sont très importantes en termes de risques naturels d'origine glaciaire (chutes de séracs, ruptures de poches d'eau ou de lacs). L'objectif de cette thèse est d'identifier et de modéliser les principaux processus d'échange énergétique entre le glacier et son environnement extérieur ainsi que le transport de cette énergie au sein du glacier. Cette étude se base sur plusieurs cas concrets dans le Massif du Mt Blanc (France) . Elle a pour but de modéliser l'évolution thermique d'un glacier dans un climat donné passé, présent ou futur. Elle contribue à l'analyse et à la compréhension des risques naturels d'origine glaciaire futurs associés aux changements climatiques. Elle permet également de quantifier les variations climatiques passées par la mesure des variations de la température interne du glacier.

1.1 Les composantes du régime thermique d'un glacier

Le régime thermique des glaciers résulte d'un ensemble de processus qui interagissent entre eux que l'on va énumérer dans cette section pour situer la complexité du problème. On distinguera les processus d'échange avec l'environnement extérieur (contrôle climatique), des processus de transport et de production d'énergie au sein du glacier (contrôle physique). On appellera glacier ici l'ensemble de la matière située sur le substrat rocheux fixe c'est à dire la glace, le névé et la neige (saisonnière).

1.1.1 Définition de l'énergie

On définit l'énergie interne du glacier par l'enthalpie H (J kg^{-1}) qui s'exprime par :

$$\Delta H(T,\omega) = \begin{cases} \int_{T_0}^{T} C_p(T)dT & \text{si} \quad \Delta H < \Delta H_f(p) \\ \\ \int_{T_0}^{T_m(p)} C_p(T)dT + \omega L & \text{si} \quad \Delta H \geq \Delta H_f(p) \end{cases} \tag{1.1}$$

avec C_p la capacité thermique (J K^{-1} kg^{-1}), T_0 une température de référence (K), L la chaleur latente de fusion (= 3.34 103 J kg^{-1}), T la température (K), ω la teneur en eau liquide, T_m la température de fusion (K) à la pression p (Pa) et ΔH_f l'enthalpie de fusion (J kg^{-1}). L'énergie

interne totale (J) du glacier est donc définie par :

$$E_{tot} = \int_{\Omega} \rho \Delta H d\Omega \tag{1.2}$$

avec ρ la densité (kg m^{-3}) et Ω le volume du glacier (m^3). Dorénavant le terme d'énergie pour le glacier fera référence à l'énergie interne défini précédemment. Ce terme ne prend pas en compte les énergies cinétiques et potentielles du glacier car elles ne sont pas directement fonction du champ de température ou du contenu en eau. L'énergie cinétique du glacier peut en revanche être vu comme une source d'énergie interne lors de phénomène de dissipation thermique par frottement ou déformation.

1.1.2 Échanges avec l'environnement extérieur : contrôle climatique

Les échanges énergétiques du glacier avec l'extérieur se font par l'intermédiaire de deux interfaces qui sont la surface libre en contact avec l'atmosphère et le lit rocheux du glacier. Le forçage climatique passe essentiellement par les échanges avec l'atmosphère via le bilan d'énergie de surface (SEB). Par définition, le SEB contrôle l'énergie entrante et sortante à la surface du glacier. Il est le bilan des flux radiatifs, turbulents et de l'énergie apportée par les précipitations à la surface et s'exprime ainsi :

$$SW_{in} + SW_{out} + LW_{in} + LW_{out} + LE + H_e + Q = Q_m + P \tag{1.3}$$

où Q est le flux d'énergie absorbée par le glacier (W m^{-2}), SW_{in}, SW_{out}, LW_{in}, and LW_{out} sont respectivement les rayonnements courtes et longues longueurs d'onde incidents et réémis (W m^{-2}). LE et He sont respectivement les flux turbulents latent et sensible. Q_m est l'énergie disponible pour la fonte et P le flux d'énergie associé aux précipitations liquides ou solides. Q est un flux essentiellement diffusif et peut s'exprimer par la loi de Fourier :

$$Q = -k \overrightarrow{\nabla T} \ (z = 0) \tag{1.4}$$

avec k la conductivité thermique de surface (J K^{-1} m^{-1} s^{-1}) et T la température interne (K).

Tant que la température de surface est en dessous du point de fusion de la glace les variations du SEB se traduisent par des variations de température et $Q_m = 0$. Dans le cas où la température de surface atteint le point de fusion, la majeure partie de l'énergie absorbée par le glacier est convertie en fonte et de l'eau liquide est produite en surface ($Q_m > 0$). Le flux diffusif Q devient très limité car le gradient de température sur les premiers centimètres devient faible voir nul ($\overrightarrow{\nabla T}$ tend vers 0). Dans ce cas, l'état de surface du glacier est extrêmement important. En effet, soit l'eau liquide est évacuée par ruissellement et l'énergie absorbée pour fondre est perdue (Qm est perdue), soit cette eau reste dans le glacier (retenue par le névé ou percole dans des moulins et crevasses) et l'énergie est restituée au glacier sous forme de chaleur latente auquel cas l'énergie absorbée par la fonte de surface est conservée (énergie absorbée par le glacier = $Q + Q_m$). Les conséquences sont :

- Un glacier avec une surface étanche à 0°C n'absorbe qu'une très faible partie de l'énergie absorbée par cette surface (= Q)

- Un glacier avec un surface perméable à 0°C peut absorber de l'énergie supplémentaire (= Q+Qm) dans la mesure où l'eau liquide est conservée dans le glacier (stockée sous forme liquide ou regelée)

L'étude de l'impact d'une variation climatique sur le bilan d'énergie total du glacier doit ainsi prendre en compte à la fois des variations de l'état de surface et du SEB. Le SEB dépend majoritairement de l'altitude et de l'exposition et l'état de surface de la présence ou non de névé ou de neige.

A la base du glacier, les échanges entre le glacier et la roche sont diffusifs et dépendent ainsi du gradient de température dans la roche. Le glacier reçoit un flux fb que l'on peut exprimer par :

$$f_b = -k_{rock}\ \overrightarrow{\nabla T_{rock}} \cdot \overrightarrow{n} \tag{1.5}$$

avec k_{rock} la conductivité thermique de la roche, T_{rock} la température dans la roche et $\overrightarrow{n}$ le vecteur normal à l'interface glace/roche. Ce flux est généralement positif à cause du flux géothermique venant de la terre. De la même manière qu'en surface si la glace atteint son point de fusion l'énergie entrante est convertie en fonte. Si l'eau produite est évacuée, l'énergie est perdue.

1.1.3 Processus interne : contrôle physique

L'équation de conservation de l'énergie dans le glacier s'écrit :

$$\rho\left(\frac{\partial H}{\partial t} + \overrightarrow{v} \cdot \overrightarrow{\nabla H}\right) = -\nabla(\overrightarrow{q}) + Q \tag{1.6}$$

avec ρ la densité (kg m^{-3}), $\overrightarrow{v}$ le vecteur vitesse (m s^{-1}), $\overrightarrow{q}$ les flux d'énergie (W m^{-2}) et Q la production interne d'énergie par chaleur de déformation (W m^{-3}). La résolution de cette équation permet de décrire l'évolution du champ d'enthalpie dans le glacier. Les différents termes de cette équation sont détaillés ci-dessous.

1.1.3.1 Production interne d'énergie

Le principal terme de production interne est la dissipation thermique produite par la déformation interne de la glace ou par le frottement basal de la glace sur le rocher en cas de glissement. La production d'énergie associée à la déformation interne s'exprime comme la somme du produit de tous les termes des tenseurs de contrainte (σ) et de taux de déformation ($\dot{\epsilon}$) :

$$Q = \sigma_{ij}\dot{\epsilon}_{ij} \tag{1.7}$$

1.1.3.2 Transport interne de l'énergie

Le transport de l'énergie au sein du glacier est relativement complexe car il est couplé avec l'écoulement et l'hydrologie. On peut ainsi distinguer trois types de transport :

- le transport diffusif contrôlé par les lois de Fick (pour la teneur en eau) et de Fourier (pour la température)

- le transport advectif dû à l'écoulement du glacier
- le transport associé aux flux gravitaires de l'eau liquide

Le couplage thermomécanique : flux advectif Le flux advectif ($q_a = \rho H \overrightarrow{v}$) est l'énergie transportée par le mouvement du glacier selon son champ de vitesse. C'est un terme de transport très efficace dès que la vitesse d'écoulement du glacier est suffisamment importante. Le champ de vitesse du glacier joue ainsi un rôle important sur le régime thermique du glacier qui lui même contrôle la viscosité de la glace et donc la vitesse. C'est la raison pour laquelle on parle de couplage thermomécanique.

Flux diffusif Le flux diffusif obéit à la loi de Fourier et est inversement proportionnel au gradient de température. Le facteur de proportionnalité k, appelé conductivité thermique (W m^{-1} K^{-1}), dépend de la température elle-même et de la densité (pour le névé et la neige) :

$$\overrightarrow{q_T} = -k(T)\ \overrightarrow{\nabla T} \tag{1.8}$$

Le contenu en eau de la glace tempérée sous forme diffuse dans la glace peut aussi être transporté par diffusion suivant la loi de Fick, le flux de chaleur latente s'exprime alors par :

$$\overrightarrow{q_\omega} = -k_0\ L\ \overrightarrow{\nabla(\omega\rho_w)} \tag{1.9}$$

où k_0 est le coefficient de diffusion de l'eau dans la glace tempérée (m^2 s^{-1}) et ρ_w la masse volumique de l'eau (kg m^{-3}).

Flux gravitaire de l'eau liquide et écoulement de Darcy Étant donné que l'on considère que l'eau liquide dans le glacier est de l'énergie sous forme de chaleur latente, tout mouvement de l'eau est considéré comme un transport d'énergie. Ces mouvements sont relativement complexes et difficiles à modéliser. La percolation de la fonte de surface dans la neige et le névé peut être décrite comme un flux gravitaire en milieu poreux. Dans la glace, l'écoulement de l'eau se localise dans des chenaux intra-glaciaires de tailles importantes ou dans des petites veines. Il peut aussi obéir à la loi de Darcy lorsque le milieu est poreux (dans le sédiment à la base du glacier). Ce transport peut très largement influencer le régime thermique d'un glacier quand l'eau transportée regèle dans une zone froide. En revanche une grande partie de cette eau est évacuée et l'énergie est donc perdue par le glacier. Là aussi le système est couplé dans la mesure où le régime thermique influence la formation des chenaux et veines qui se forment en général seulement dans la glace tempérée.

1.2 Les différents types de régimes thermiques

De ces différents processus d'échanges et de transports découlent plusieurs structures thermiques caractéristiques allant du glacier entièrement tempéré (au point de fusion) au glacier totalement froid (sous le point de fusion). Mais en réalité la plupart des glaciers sont polythermes. Dans un

glacier polythermal, la glace froide coexiste avec de la glace tempérée. On peut ainsi rencontrer plusieurs cas de figures comme l'illustre la figure 1.1.

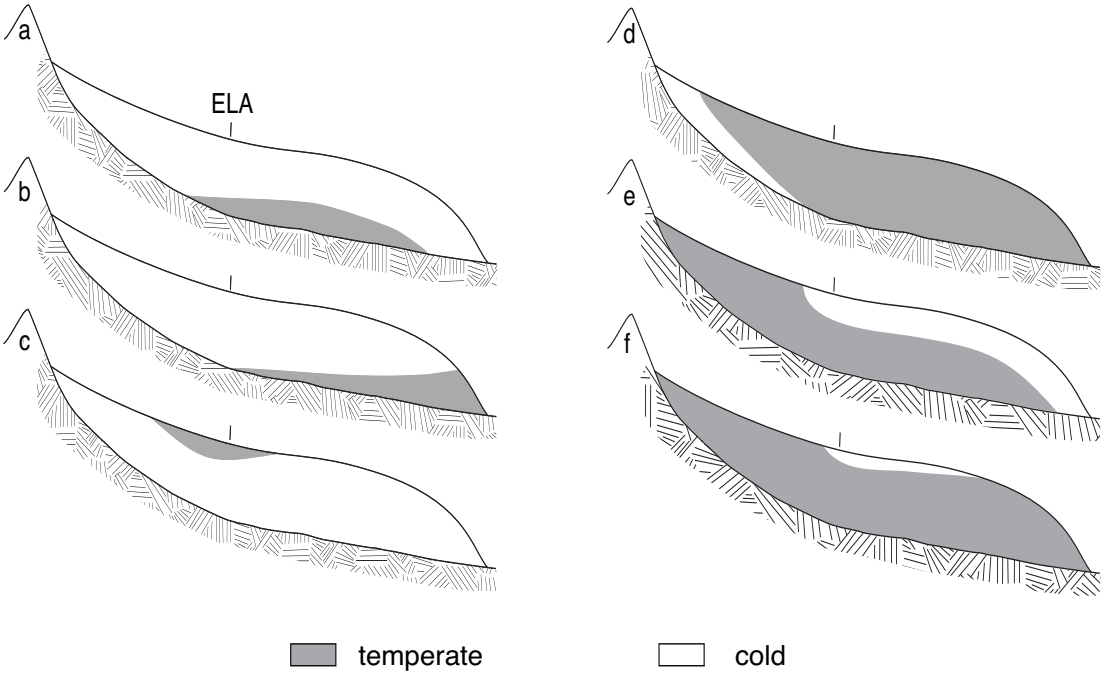

FIGURE 1.1 – Schémas de différentes structures thermiques rencontrées sur les glaciers. Source : *Aschwanden* (2008).

Dans les cas (a) à (c) le glacier est majoritairement froid et possède une petite zone de glace tempérée. Les causes possibles sont :

(a) Les échanges au niveau de la surface libre mènent à un glacier froid autant en zone d'accumulation qu'en zone d'ablation mais celui-ci se tempère en profondeur, là où il est le plus épais, à cause du flux géothermique, de l'abaissement du point de fusion avec l'augmentation de la pression et de l'énergie dissipée par la déformation et le glissement basal.

(b) Les échanges avec la surface libre conduisent à un glacier froid mais le glacier se tempère localement à cause de l'énergie dissipée par la déformation et le glissement basal.

(c) Il existe une petite partie de la zone d'accumulation qui est tempérée grâce au regel de l'eau de fonte de surface qui est en revanche évacuée dans la zone d'ablation.

Dans les cas (d) à (f) le glacier est majoritairement tempéré et possède une petite zone de glace froide. Les causes possibles sont :

(d) Seule la partie haute de la zone d'accumulation rencontre des conditions favorables pour former de la glace froide. Les échanges énergétiques en zone d'ablation ne permettent pas de former une zone froide malgré l'évacuation de l'eau de fonte (par exemple, la température de l'air est trop élevée en moyenne annuelle).

(e) Seule la zone d'ablation rencontre les conditions pour avoir un glacier froid grâce à l'évacuation de l'eau de fonte et des températures de l'air suffisamment froides. La glace tempérée formée

en zone d'accumulation est advectée et se refroidit progressivement par la surface en zone d'ablation.

(f) Même situation qu'en (e) mais avec des températures de l'air moins froides.

Ces exemples illustrent la grande variété de régimes thermiques que l'on peut rencontrer suite aux différentes configurations et caractéristiques du SEB, de l'état de surface, du flux basal ainsi qu'à l'intensité de la production interne d'énergie. Ces facteurs dépendent du climat, de la topographie locale et de la taille du glacier. L'étude du régime thermique d'un glacier et de son évolution doit donc prendre en compte tous ces facteurs et être adaptée selon le glacier étudié.

1.3 Applications associées à l'étude du régime thermique

1.3.1 Reconstitution du climat passé

Le glacier possède une mémoire des événements climatiques passés, notamment dans ses zones froides. Une variation climatique, selon sa durée et son intensité, va créer une anomalie de température dans le glacier. La quantification de ces anomalies par mesure directe de la température interne du glacier peut alors permettre d'obtenir des informations sur les variations climatiques qui les ont produites. La modélisation du régime thermique peut ainsi permettre la reconstitution du climat passé par résolution du problème inverse (*Dahl-Jensen et al.*, 1998). Les sites de mesures doivent être froids et choisis pour rendre la modélisation la plus simple possible afin de limiter la complexité du problème inverse à résoudre et de diminuer les incertitudes sur le résultat final. En outre, il est préférable de choisir un col, un dôme ou un plateau afin que tous les flux horizontaux puissent être négligés et de pouvoir travailler avec l'hypothèse unidimensionnelle.

1.3.2 Influence sur la dynamique

La température contrôle le glissement basal de la glace sur la roche. Aucun glissement n'est possible lorsque la glace est froide alors qu'il l'est pour de la glace tempérée (*Paterson*, 1994). Pour des glaciers froids mais proches du point de fusion, un changement de régime thermique peut conduire à un changement des conditions basales de glissement qui peut avoir de lourdes conséquences comme la déstabilisation du glacier (*Faillettaz et al.*, 2011).

La déformation de la glace est aussi fortement dépendante de la température. La partie déviatorique des tenseurs de contraintes (τ_{ij}) et les taux de déformations ($\dot{\epsilon}_{ij}$) sont classiquement reliés par la loi de Glen :

$$\dot{\epsilon}_{ij} = A(T)\ \tau^{n-1}\ \tau_{ij} \tag{1.10}$$

avec τ le second invariant de la partie déviatorique du tenseur des contraintes, n l'exposant de Glen et $A(T)$ un facteur dépendant de la température ($\mathrm{Pa}^{-3}\ \mathrm{s}^{-1}$). Ce facteur peut varier de trois ordres de grandeur entre -50°C et 0°C suivant la loi d'Arrhenius (Fig. 1.2) :

$$A(T) = A(T_0)\ e^{-\frac{Q_0}{R}\left(\frac{1}{T}-\frac{1}{T_0}\right)} \tag{1.11}$$

avec Q_0 l'énergie d'activation (J mol^{-1}), T_0 la température de transition (K) et R la constante des gaz parfaits (J mol^{-1} K^{-1}).

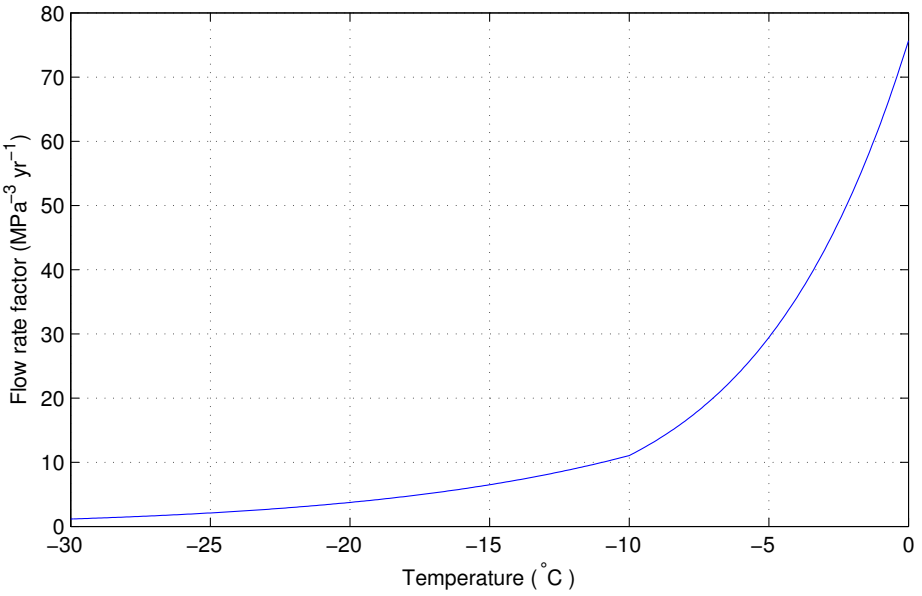

FIGURE 1.2 – Dépendance en température du facteur A de la loi de Glen. Adapté de *Paterson* (1994).

Les variations de régime thermique peuvent dont significativement influencer la vitesse de déformation de la glace et donc la vitesse du glacier.

1.3.3 Influence sur l'hydrologie glaciaire

La glace froide est pratiquement imperméable sauf en présence de chenaux et fractures qui peuvent permettre localement le passage d'eau liquide (*Boon and Sharp*, 2003). Les chenaux se forment en revanche plus difficilement dans la glace froide que dans la glace tempérée. Cette dernière, est bien plus perméable et autorise plus facilement le développement de chenaux à la base du glacier (*Fountain and Walder*, 1998). Ceux-ci évacuent efficacement l'eau de fonte qui pénètre le glacier par des veines, des fractures et des moulins qui sont entretenus par l'écoulement de l'eau elle-même (*Fountain and Walder*, 1998). Une modification du régime thermique peut donc conduire à la formation de bouchons de glace froide en zone d'ablation qui peuvent localement produire des surpressions d'eau (*Vincent et al.*, 2012; *Copland et al.*, 2003) (Fig. 1.3) ou encore à la formation de lacs supra-glaciaires sur une zone de glace froide (*Irvine-Fynn et al.*, 2011).

1.3.4 Conséquence pour l'étude du risque d'origine glaciaire

Les deux sous-sections précédentes concernaient l'influence du champ de température sur la dynamique, le glissement et l'hydrologie du glacier. La modification du régime thermique du glacier conduit ainsi à des changements de ces caractéristiques qui peuvent conduire, par la suite, à la formation de lacs supra ou intra-glaciaires, ou encore, à la déstabilisation d'une partie du glacier selon la configuration de la topographie du socle rocheux. Ainsi l'étude du régime thermique intervient

FIGURE 1.3 – Fontaine de type artésienne à la surface d'un glacier due à une surpression d'eau créée par la présence de glace froide sur la langue du glacier. Source : *Copland et al.* (2003).

en amont d'une étude complète sur le risque. Elle est essentielle à la prédiction de l'apparition de nouveaux aléas dans le futur, en réponse aux variations climatiques, mais ne suffit pas à estimer l'aléa. Par exemple, elle peut permettre de déterminer les zones d'un glacier qui vont se mettre à glisser mais une étude de mécanique de la rupture est indispensable pour déterminer si ce changement pourrait impliquer une déstabilisation. De la même manière, l'étude du régime thermique peut permettre d'identifier une configuration potentiellement dangereuse conduisant à la formation de réservoir d'eau mais ne peut déterminer la possibilité de rupture du réservoir.

Les notions de risques, d'aléas et de vulnérabilité sont différentes. La risque est en faite défini par :

$$\text{(Risque)} = \text{(aléa) x (vulnérabilité)}$$

Le risque est donc la confrontation d'un aléa (phénomène naturel dangereux) et d'une zone géographique où existent des enjeux qui peuvent être humains, économiques ou environnementaux. Dans cette thèse le terme de risque fait généralement référence à l'aléa dans la mesure où l'étude ne concerne pas la vulnérabilité.

1.4 Contexte de l'étude

De nombreuses études sont consacrées au bilan d'énergie de surface des glaciers pour des applications qui sont généralement destinées au calcul du bilan de masse des glaciers et calottes (*Sicart et al.*, 2008; *Wagnon et al.*, 1999; *Van de Wal*, 1996; *Oerlemans*, 1991; *Oerlemans and Fortuin*, 1992; *Ohmura et al.*, 1996). L'influence des variations climatiques sur le bilan de masse est donc largement étudiée et de nombreux modèles de complexité plus ou moins importante allant du modèle purement empirique (degré jour) au modèle sophistiqué de bilan d'énergie existent (*Pellicciotti*

et al., 2005; *Hock and Holmgren*, 2005; *Klok and Oerlemans*, 2002; *Braithwaite and Zhang*, 2000). Ils permettent de simuler de manière satisfaisante le bilan de masse de surface à partir de données climatiques.

La modélisation du régime thermique des glaciers concerne en revanche un nombre d'étude plus restreint. Néanmoins ces travaux offrent des modèles mathématiques qui permettent une bonne simulation de la plupart des structures thermiques observées. Cette thèse essaie de faire le lien entre ces deux types d'étude en forçant des modèles de régime thermique basés sur les formulations mathématiques de travaux existants par des conditions aux limites dictées par le bilan d'énergie de surface. Une attention toute particulière sera accordée au traitement de la fonte de surface d'un point de vue thermique. Cette étude permet des simulations en régime transitoire du régime thermique à partir de données météorologiques.

1.4.1 Base de la modélisation du régime thermique des glaciers

Les bases de la formulation mathématique du problème du transport de l'énergie dans les glaciers ont été posées par *Fowler and Larson* (1978) puis par *Hutter* (1982). Dans son approche, la glace froide est considérée comme un fluide visqueux, conducteur de la chaleur et incompressible. La présence de poussières, débris, sédiments ou de l'air est négligée. La glace tempérée est vue comme un mélange binaire d'eau et de glace dont la température est fixée à la température du point de fusion de la glace. Glace froide et tempérée sont explicitement séparées par la surface de transition froide/tempérée (Cold-temperate Transition Surface, CTS). Cette surface constitue une condition aux limites pour les deux domaines distincts que sont la glace froide et la glace tempérée dans lesquelles sont résolues deux équations distinctes décrivant respectivement la température et le contenu en eau (≪moisture content≫) (*Hutter et al.*, 1988). Les conditions aux limites au niveau de la CTS se basent sur la continuité du champ de température et la conservation du flux d'énergie. C'est le respect de ces conditions aux limites qui permet de déterminer la position de la CTS.

Cette méthode fut utilisée par (*Blatter and Hutter*, 1991) et (*Funk et al.*, 1994) pour la modélisation de glaciers polythermes de type (a) et (b) (voir Figure 1.1). Ces approches négligeaient le transport diffusif du contenu en eau de la glace tempérée puisque elle était uniquement produite par la chaleur de déformation de la glace. La prise en compte de la diffusion du contenu en eau dans la glace tempérée par une loi de Fick nécessite d'imposer des conditions aux limites pour le contenu en eau à la base du glacier et au niveau de la CTS. *Greve* (1997) a aussi repris cette formulation pour, cette fois, des simulations trois dimensions de la calotte Groenlandaise.

Au vu de la complexité de la résolution numérique liée à cette condition aux limites non fixée (libre) qu'est la CTS, de nombreux modèles font généralement l'approximation dite de la ≪glace froide≫ (≪cold-ice≫ models) (*Payne et al.*, 2000; *Pattyn et al.*, 2005; *Bueler et al.*, 2007; *Zwinger and Moore*, 2009). Dans ce cas, la seule variable thermodynamique est la température qui est simplement limitée à la température de fusion. C'est à dire que l'on impose arbitrairement à la température de ne pas dépasser le point de fusion au cours de la simulation. Ce genre de modèle ne conserve pas l'énergie car les changements de contenu en chaleur latente dans la glace tempérée ne sont pas pris en compte. Un flux d'énergie dans la glace tempérée est donc perdu ou transformé instantanément en fonte basale. L'évolution de la zone tempérée d'un glacier est donc mal représentée avec cette

approximation.

Plus récemment, les travaux de *Aschwanden and Blatter* (2005, 2009); *Aschwanden et al.* (2012) proposent une nouvelle formulation mathématique conservant l'énergie pour la modélisation des glaciers polythermes. Cette approche est basée sur l'utilisation de l'enthalpie comme unique variable thermodynamique du glacier. Elle a le très gros avantage que la CTS n'existe plus comme condition aux limites mais seulement comme isosurface de la variable enthalpie. Cette variable prend en compte la température et le contenu en eau du glacier de manière unifiée (voir partie 1.1) et rend la résolution numérique beaucoup plus simple. Cette méthode a été utilisée par *Wilson and Flowers* (2013) pour simuler tous types de structures thermiques à l'état stationnaire en fonction de différentes conditions aux limites de surfaces pour un glacier type (Figure 1.4).

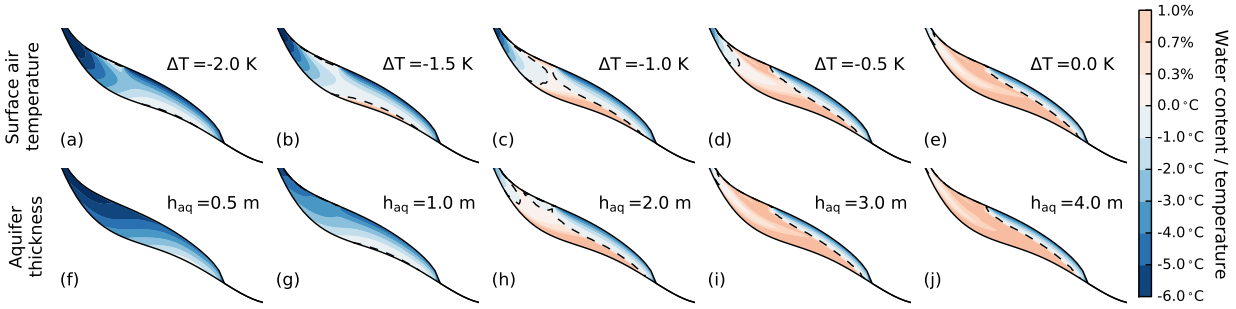

FIGURE 1.4 – Différentes structures thermiques modélisées par la formulation de l'enthalpie pour différentes conditions de surface (température et chaleur latente dans la zone d'accumulation). Source : *Wilson and Flowers* (2013).

Le cas des zones d'accumulation froides pour lesquelles le glacier possède une zone de névé d'épaisseur significative en comparaison de l'épaisseur totale du glacier est un cas particulier et plus complexe de la modélisation du régime thermique. Bien que le glacier soit froid et qu' il n'y ait pas d'eau liquide, le milieu est cette fois compressible et est caractérisé par une densité variable. La conductivité thermique est elle aussi non constante (fonction de la densité) et surtout, la rhéologie du névé doit être prise en compte dans la loi d'écoulement (*Gagliardini and Meyssonnier*, 1997). Ainsi densité, température, épaisseur et vitesse du glacier forment un système de quatre variables couplées qui vont répondre ensemble à un forçage climatique extérieur. Très peu d'études se sont intéressées à ce problème (*Zwinger et al.*, 2007; *Lüthi and Funk*, 2001; *Gagliardini and Meyssonnier*, 1997) et aucune n'a étudié la réponse couplée de ces quatre variables à un changement climatique. *Gagliardini and Meyssonnier* (1997) se sont intéressés seulement à la rhéologie du névé dans un cas isotherme et à l'état stationnaire. *Lüthi and Funk* (2001) sont allés plus loin en incluant la température comme variable et en montrant l'importance de prendre en compte l'état thermique du socle rocheux du glacier.

1.4.2 Apport de cette thèse

La plupart des travaux cités précédemment s'attache à modéliser des structures thermiques de types (a) et (b) qui ne sont pas liées aux conditions de surface mais seulement à la physique interne du glacier. Le climat a peu d'influence sur ces structures thermiques qui ne seront pas directement

modifiées dans un contexte de changement climatique. Un nombre très limité d'études se consacre à l'influence des variations de surface sur le bilan énergétique et l'impact de celle-ci sur le régime thermique. *Wilson and Flowers* (2013) explorent la diversité des structures thermiques possibles en prenant en compte de manière paramétrée la chaleur latente libérée par le regel de l'eau de fonte de surface dans la zone d'accumulation. Cette approche permet effectivement de modéliser de manière conceptuelle différents types de régimes thermiques (Figure 1.4) mais pas de faire le lien entre le climat et le régime thermique. *Zwinger and Moore* (2009) proposent un modèle couplé thermomécanique en régime transitoire qui prend lui aussi en compte la chaleur latente de regel dans la zone d'accumulation mais cette fois aussi de manière paramétrée en utilisant la méthode de *Wright et al.* (2007). Cette méthode se base sur la mesure des profils de température dans la couche active en hiver et à la fin de l'été pour déterminer la quantité d'eau qui a regelé par an. Cette approche permet de travailler au pas de temps annuel et donne une bonne estimation de l'influence de la chaleur latente dans la zone d'accumulation mais n'est pas basée sur des données climatiques et ne peut pas être utilisée pour des scénarios futurs. D'autres approches utilisent des paramétrisations pour relier directement la température de surface du glacier à la température de l'air en moyenne annuelle (*Wohlleben et al.*, 2009).

Le principal problème de toutes les approches existantes jusqu'à présent est qu'elles travaillent à des échelles de temps trop longues (de l'ordre de l'année) pour modéliser explicitement les processus de surface qui contrôlent la température du glacier dans les premiers mètres sous la surface. Il n'est pas possible de modéliser physiquement ces processus à cette échelle de temps et il est donc impossible de relier les variations climatiques et les conditions de surface pour des modèles de régime thermique. Dans cette étude on s'attachera si possible à travailler à une échelle de temps permettant de représenter explicitement des processus de surface comme la percolation et le regel de l'eau de fonte ou l'évolution de l'épaisseur de neige saisonnière et du névé. Dans ce cas, il est possible de forcer un modèle de régime thermique directement par des données météorologiques et d'en étudier les variations dans un contexte de changement climatique. L'objectif de cette thèse est de produire ces modèles pour les appliquer à l'étude des risques glaciaires et de la reconstitution du climat passé.

1.5 Organisation du manuscrit

Ce manuscrit s'organise autour de quatre articles qui concernent plusieurs aspects de la relation entre régime thermique et climat.

- Le premier article est une proposition d'un modèle de surface pour les zones froides fonctionnant à l'échelle journalière. Il est basé sur une étude du bilan énergétique de surface du site du Col du Dôme (4250 m, massif du Mont Blanc, France). Il est utilisé comme schéma de surface pour contraindre un modèle de régime thermique à partir de données météorologiques.

- Le second article est l'application du modèle de surface présenté précédemment pour forcer un modèle couplé thermomécanique pour les zones d'accumulations froides et applicable aux glaciers polythermes. Ce modèle est appliqué au site du Col du Dôme. Densité, surface libre,

vitesse et température sont résolues en régime transitoire en trois dimensions à partir de données météorologiques pour étudier la réponse thermique et dynamique d'un glacier aux variations climatiques. Les perspectives de ce modèle pour l'étude de la stabilité des glaciers froids suspendus sont mises en avant à la fin du chapitre.

- Le troisième article étudie l'influence de l'état de surface du glacier (neige, névé ou glace) sur le régime thermique du glacier. L'évolution saisonnière de la neige et du névé sur le glacier est ainsi modélisée à partir du modèle de neige CROCUS (*Brun et al.*, 1989). Cette variabilité de l'épaisseur de neige et névé est utilisée par la suite dans le modèle de régime thermique en incluant les processus de surface décrits dans le chapitre 1. Cette étude est appliquée au glacier de Tête Rousse pour lequel le régime thermique joue un rôle essentiel dans la formation de grands volumes d'eau potentiellement dangereux pour les habitants de la vallée.

- Enfin le dernier article est une application de la modélisation du régime thermique d'un glacier froid pour la reconstitution du climat passé. Nous présentons un modèle inverse basé sur l'inversion simultanée de plusieurs profils de températures permettant de reconstituer les variations de température atmosphériques du dernier siècle sur le site du Col du Dôme.

Chapitre 2

Sites d'étude, données disponibles et enjeux

L'ensemble des travaux réalisés dans cette thèse concerne plusieurs glaciers du massif du Mt Blanc (France) dont les glaciers de Tête Rousse, de Taconnaz et du Col du Dôme (voir Figure 2.1). Les glaciers de Tête Rousse et de Taconnaz posent des problèmes de risques glaciaires. Le glacier du Col du Dôme est particulièrement intéressant pour les reconstitutions du climat ou de la composition de l'atmosphère. Ces glaciers sont aussi un véritable laboratoire pour l'étude du régime thermique des glaciers de type alpin grâce aux nombreuses données acquises depuis une vingtaine d'année. Les enjeux en termes de risques glaciaires sont très forts car une partie de la population qui vit dans les vallées est menacée ou pourrait l'être dans le futur. Ceci est d'autant plus vrai que la zone concernée est la vallée de Chamonix et St Gervais, au pied du plus haut sommet des Alpes, emblème mondial de l'alpinisme. Le tourisme est la première ressource économique de cette vallée. Aussi, dans ce contexte, prévenir les catastrophes naturelles éventuelles est une préoccupation majeure et le développement d'outils de prédiction est très attendu par les collectivités.

Dans ce chapitre, nous expliquons le contexte de ces études, les données disponibles sur les trois glaciers étudiés et la nécessité de la modélisation du régime thermique de ces glaciers.

2.1 Le Col du Dôme

Le Col du Dôme (Fig. 2.2 et 2.3) est situé à l'altitude de 4250 m. C'est un glacier froid en zone d'accumulation situé sur la voie normale d'accès au sommet du Mt Blanc. L'accumulation de neige a lieu toute l'année et les événements de fonte sont occasionnels. L'écoulement y est très faible avec des vitesses horizontales de surface inférieures à 15 m an^{-1}. Les vents majoritairement forts à dominance Sud-Ouest (Fig. 2.4) sont à l'origine d'une importante redistribution de l'accumulation de neige expliquant la très forte variabilité spatiale de l'accumulation observée sur ce site, de 0.3 à 3.5 m w.e. an^{-1}. L'épaisseur du glacier varie de 40 m au sommet du Dôme du Goûter à 140 m au niveau du site de forage N°2 (Fig. 2.3) où l'épaisseur du névé peut atteindre 60 m à 80 m.

Les premières observations au col du Dôme remontent à la période 1890 - 1920. Elles sont à l'initiative de Joseph Vallot qui fit construire en 1898 l'observatoire qui porte son nom, et encore utilisé actuellement. Par la suite, un premier carottage de 20 m a été réalisé en 1980 dont les échantillons ont été datés par mesures radioactives (*Jouzel and Merlivat*, 1984) puis un autre à 70 m de profondeur en 1986 qui n'a pas atteint le lit rocheux. A partir de 1993, les observations deviennent plus systématiques et complètes. Le site est ainsi instrumenté pour le suivi de l'accumulation de neige et des vitesses de surface depuis 1993 (*Vincent et al.*, 1997). Ce suivi consiste en la maintenance d'un réseau de pieux dont l'émergence et la position sont régulièrement mesurées

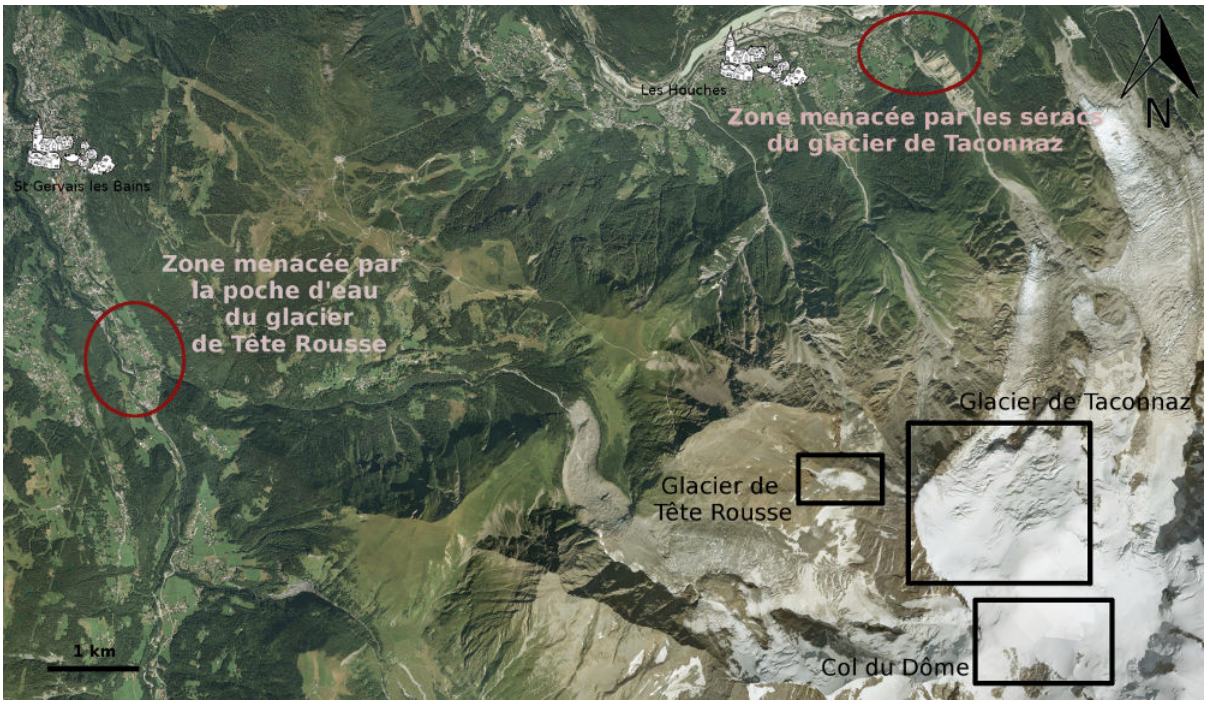

FIGURE 2.1 – Photographie aérienne des sites d'étude. Les trois glaciers étudiés sont encadrés en noir et les zones sensibles aux risques glaciaires en rouge.

par GPS différentiel (Fig. 2.3). Ces mesures permettent une bonne connaissance de la répartition moyenne de l'accumulation sur le site et de la variabilité des vitesses de surface verticales et horizontales (*Vincent et al.*, 2007a). Une station météorologique automatique a fonctionné au col (Fig. 2.3) durant les étés 2009, 2010, 2011, 2012 et 2013 enregistrant des données de vitesse et direction de vent, rayonnement, température et humidité. Une chaîne de thermistances pour la mesure de températures a été installée dans les 16 premiers mètres sous la surface, dans le cadre de cette thèse. Elle a fonctionné en parallèle des mesures météorologiques durant l'été 2012. La topographie du lit rocheux a été acquise en 1993 par mesure radar grâce à nos collègues suisses de Zurich (*Vincent et al.*, 2007a).

FIGURE 2.2 – Photographie du site du col du Dôme en mars 2012 à proximité du site de forage N°1 (sommet du Dôme du Goûter, 4300 m). Au fond le Mt Blanc (4810 m). (cliché A. Gilbert)

Depuis 1994, 9 forages profonds ont atteint le lit rocheux sur trois sites différents du Dôme

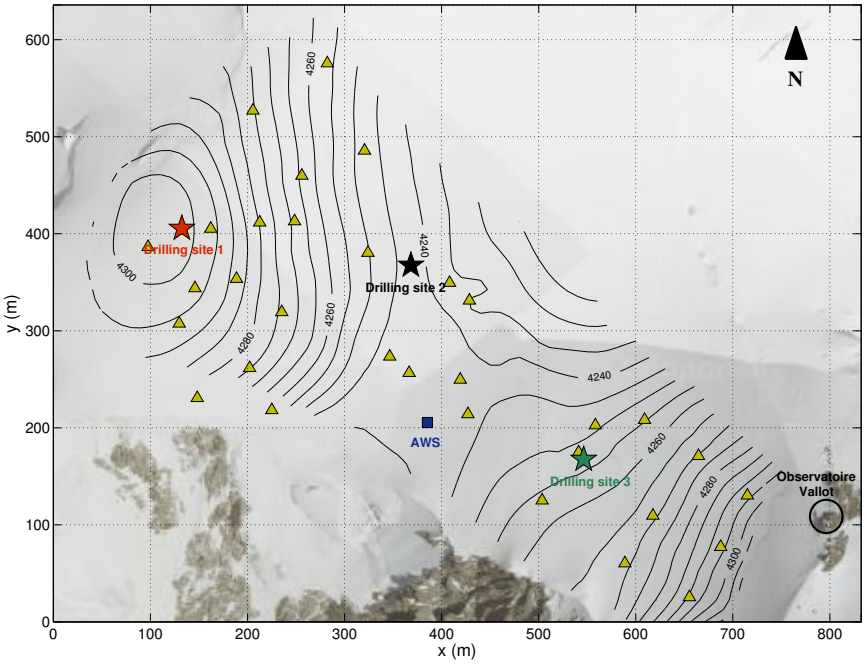

FIGURE 2.3 – Carte du Col Dôme. Les positions des pieux pour les mesures d'accumulation et d'écoulement sont indiquées par des triangles jaunes, le carré bleu montre la position de la station météorologique (AWS) et les étoiles les positions des sites de forages profonds.

du Gouter et du Col du Dôme (site 1, 2 et 3 de la figure 2.3). Le tableau 2.1 résume les mesures effectuées pour chacun de ces forages. Le grand intérêt des mesures de température effectuées dans ces forages profonds est que (i) elles ont été répétées plusieurs fois sur un même site et permettent la quantification de l'évolution de la température du glacier en réponse aux variations climatiques et (ii) ces mesures sont effectuées sur des sites avec différentes accumulations et orientations ce qui permet de bien appréhender l'impact de ces paramètres sur l'évolution du régime thermique du glacier.

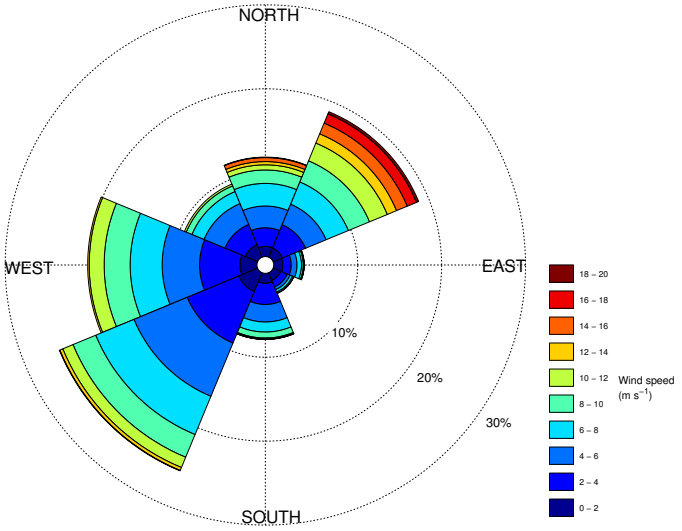

FIGURE 2.4 – Intensité et direction du vent mesurées sur le col du Dôme durant l'été 2012.

Forage N°	Site N°	Profondeur	Année	Type de forage	Température	Densité	Chimie	X	Y	Z
1	2	126 m	1994	mécanique	oui	non	oui	950179	103592	4243
2	2 (à 30 m du forage N°1)	140 m	1994	mécanique	non	oui	oui	-	-	-
3	1	40 m	1999	mécanique	oui	oui	oui	949952	103633	4301
4	3	103 m	1999	mécanique	oui	oui	oui	950366	103395	4251
5	2	113,4 m	2004	eau chaude	oui	non	non	950188	103595	4243
6	2	125,3 m	2009	eau chaude	oui	non	non	950187	103590	4243
7	1	33 m	2011	eau chaude	oui	non	non	949945	103626	4303
8	3	97 m	2011	eau chaude	oui	non	non	950363	103389	4249
9	2	125 m	2012	mécanique	oui	À venir	À venir	-	-	-

Tableau 2.1 – Mesures réalisées dans les 9 forages effectués entre 1994 et 2012. Coordonnées x, y, z en Lambert.

L'enjeu de l'étude réalisée dans cette thèse sur le col du Dôme est double. D'une part, le jeu exceptionnel de données sur ce site a permis de calibrer et valider un modèle thermomécanique du régime thermique pour les glaciers froids de type alpin (Chapitres 3 et 4). Ce modèle thermomécanique permettra l'étude du régime thermique du glacier de Taconnaz dans le futur, dont la stabilité dépend de sa température basale. Une déstabilisation même partielle du glacier aurait de lourdes conséquences sur les populations de la vallée (voir Fig. 2.1 et section 2.3). D'autre part, les nombreuses mesures de températures en profondeur ont permis l'étude des changements climatiques à haute altitude par inversion des profils de température (voir chapitre 6). La quantification des variations climatiques à très haute altitude sur une longue période intéresse la communauté des climatologues. En effet, la question de l'amplification du réchauffement climatique en altitude reste pour l'instant ouverte (*Rangwala and Miller*, 2012) par manque de données à haute altitude.

2.2 Glacier de Tête Rousse

Le glacier de Tête Rousse est un petit glacier orienté Ouest de 0.08 km^2 situé lui aussi sur la voie normale d'accès au Mont Blanc (Fig. 2.1). Il s'étend sur 600 m de long entre 3300 et 3100 m d'altitude. Sa petite taille et son altitude lui donnent la particularité d'avoir une zone d'accumulation de taille très variable en fonction des années (en comparaison de la taille du glacier). Le glacier peut même passer entièrement en zone d'accumulation une année ou entièrement en zone d'ablation une autre année. Le glacier est quasi statique avec une vitesse d'écoulement inférieure à 2 m an^{-1} en surface. Le lit rocheux forme une gorge étroite et profonde de 70 m au centre du glacier.

FIGURE 2.5 – Cavité supérieure de la poche d'eau de 1892 (Cliché Kuss, 13 août 1893)

L'intérêt porté au glacier de Tête Rousse remonte à la catastrophe de la nuit du 12 juillet 1892. Une lave torrentielle dévasta alors une partie du hameau de Bionnay (cercle rouge sur la figure 2.1) et les thermes de Saint Gervais en faisant plus de 175 victimes. Les causes de la catastrophe ont été rapidement identifiées : le torrent de boue avait pour origine la vidange brutale d'une poche

d'eau contenue dans le glacier de Tête Rousse. Suite à la catastrophe de 1892, trois campagnes de reconnaissance et d'exploration ont permis de faire un état des lieux et une description détaillée du glacier et des cavités visibles (*Vallot et al.*, 1892). La partie frontale du glacier avait été arrachée sur environ 40 mètres de hauteur. Dans la paroi de glace de laquelle le front s'était arraché, était visible une grande cavité de 40 mètres de diamètre et 20 mètres de hauteur. De cette cavité inférieure, une reconnaissance permit d'établir qu'un chenal de 85 mètres de long menait, vers l'amont, à une autre cavité de forme cylindrique (Fig. 2.5), de section elliptique ayant 50 mètres comme grand axe et 27 m comme petit axe. Cette cavité supérieure débouchait à ciel ouvert à la surface du glacier, et atteignait 35 à 40 mètres de profondeur. En tenant compte de la glace de la partie frontale arrachée, *Mougin and Bernard* (1922) estimèrent un volume total de 200 000 m3 d'eau et de glace libérées lors de la vidange brutale (*Vincent et al.*, 2012). *Vincent et al.* (2010a) ont réanalysé l'origine de la catastrophe. Ils montrent que l'origine du stockage d'eau dans le glacier à cette époque fut certainement un lac supra-glaciaire.

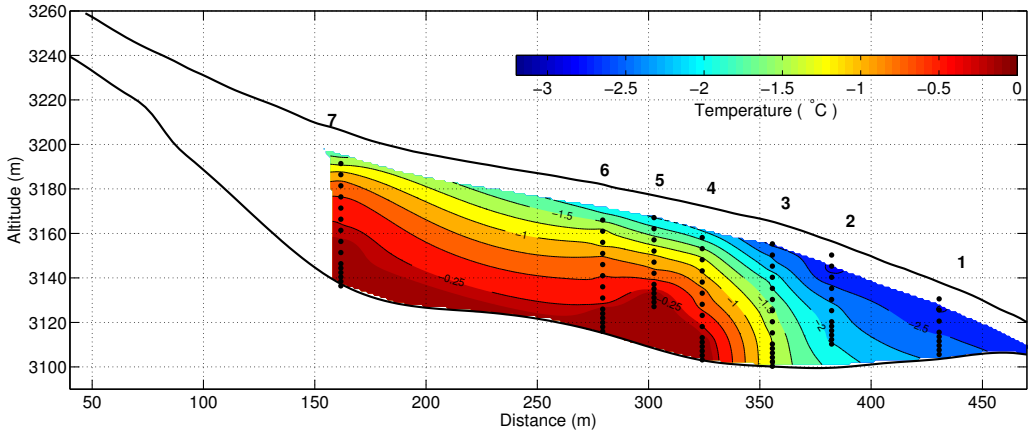

FIGURE 2.6 – Mesures de températures réalisées sur le glacier de Tête Rousse en septembre 2010 interpolées sur une coupe longitudinale du glacier. Les points de mesure dans les sept forages sont indiqués par des points noirs.

Pour drainer toute nouvelle poche d'eau et permettre la vidange de nouvelles crevasses inondées, deux galeries ont été creusées en 1899 et 1904 dans le flanc sud de l'éperon rocheux qui encadre le glacier. Le service de Restauration des Terrains de Montagne (RTM) a poursuivi jusqu'en 2007 l'entretien de la galerie de 1904 qui n'a pourtant jamais servi à drainer d'eau depuis. En 2007, la question de l'utilité de cette galerie s'est posée et le service du RTM confia alors une étude au Laboratoire de Glaciologie de Grenoble (*Vincent et al.*, 2008, 2012c)). Débute alors une vaste campagne de mesures sur ce petit glacier de Tête Rousse. Tout d'abord, les mesures radars révélèrent une anomalie au centre du glacier au niveau du lit rocheux qui laissa suspecter la présence d'eau liquide. Ces soupçons se confirmèrent ensuite en 2010 par la détection d'un volume de 65 000 m^3 d'eau liquide par la méthode de Résonance Magnétique des Protons (RMP) (*Legchenko and Valla*, 2002) et des forages à eau chaude (*Vincent et al.*, 2012). Pour éviter une nouvelle catastrophe, les scientifiques alertèrent la préfecture (*Vincent et al.*, 2010b), ce volume d'eau a été drainé par pompage en août

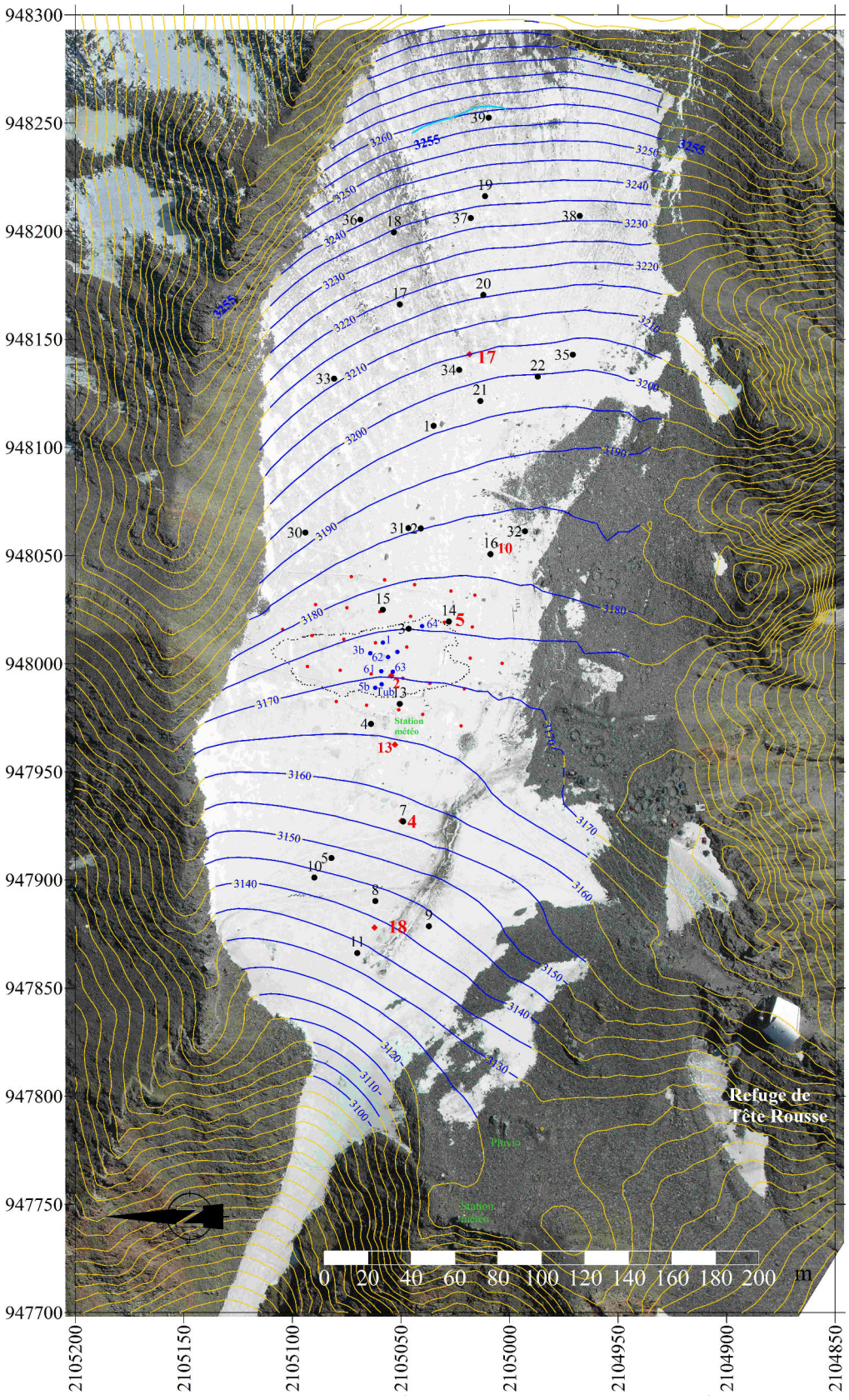

FIGURE 2.7 – Plan d'ensemble du glacier de Tête Rousse avec l'instrumentation utilisée en 2011 : stations météorologiques (vert), thermistances profondes (rouge), balises d'ablation (noir), balises de déformation dans la région de la cavité (rouge). Le trait pointillé noir indique la position de la cavité en 2010. Source : (*Vincent et al.*, 2011)

et septembre 2010. La cavité vide s'est remplie de nouveau au cours des étés suivants. Néanmoins, son volume a diminué chaque année. L'opération de pompage a ainsi été renouvelée en 2011 et 2012 évacuant respectivement 20000 et 9000 m^3 d'eau (*Vincent et al.*, 2010b, 2011, 2012b; *Legchenko et al.*, 2013).

Depuis 2007 le glacier fait ainsi l'objet d'un suivi important qui s'est intensifié après l'été 2010. Le bilan de masse est mesuré par un réseau de balises (en noir sur la figure 6), deux stations météorologiques sont installées depuis 2010 permettant la modélisation de la fonte sur le glacier par bilan d'énergie (en vert sur le figure 2.7). Un réseau dense de pieux installés sur la zone de la poche d'eau permet un suivi topographique des déformations de surface (*Gagliardini et al.*, 2011) (points rouges sur la figure 2.7). 14 forages profonds atteignant le lit rocheux ont permis d'installer 4 piézomètres pour mesurer le niveau d'eau à plusieurs endroits de la cavité (forage 61, 62, 63 et 64 sur la figure 2.7) et 7 chaînes de thermistances sur une coupe longitudinale du glacier (numéros rouges sur la figure 2.7) Ces observations ont mis en évidence la structure thermique du glacier (*Vincent et al.*, 2012). La particularité de la structure thermique du glacier de Tête Rousse est un front froid et une partie amont partiellement tempérée (Fig. 2.6). Le bouchon de glace froide empêche le drainage naturel de l'eau pénétrant en amont au sein du glacier. Ce phénomène est à l'origine de la formation de la poche d'eau découverte en 2007. L'étude du régime thermique et de son lien avec les variations climatiques est donc essentielle pour comprendre l'origine du front froid et estimer l'évolution future du glacier. Le régime thermique joue ici un rôle clef sur la formation des poches d'eau du glacier de Tête Rousse. La modélisation de son évolution passée et future réalisée dans ces travaux de thèse permet de discuter de l'aléa que représente ce volume d'eau, de sa formation et de l'évolution future de cet aléa.

2.3 Glacier de Taconnaz

Le glacier de Taconnaz est situé à quelques centaines de mètre de distance du Col du Dôme (voir Fig. 2.8) et s'étend du sommet du Dôme du Goûter (4300 m) jusqu'à l'altitude de 1700 m environ à l'amont du village du Nant. Globalement orienté au nord, il est scindé en deux parties : une zone supérieure d'accumulation et la langue inférieure. Ces 2 parties sont séparées par une chute de séracs d'une largeur de 600 à 700 m et d'une hauteur maximum de 100 m à environ 3300 m d'altitude (ligne rouge sur la Fig. 2.8). Au dessus de cette barre, c'est un glacier froid en zone d'accumulation. Durant la saison hivernale, lorsque les accumulations de neige sont importantes et que le manteau neigeux est instable, les chutes de séracs sont susceptibles de déclencher des avalanches de neige très importantes et cette masse de neige et de glace peut parcourir toute la langue terminale et atteindre les zones habitées de la vallée de Chamonix (voir Fig. 2.1). La période de retour de ces événements est d'environ 6 mois et ils déchargent environ $1.2 \pm 0.3\ 10^6$ m^3 de glace par an (*Le Meur and Vincent*, 2006).

L'histoire relatée des avalanches de Taconnaz remonte au début du $20^{ème}$ siècle, analysée sur une centaine d'année, l'activité avalancheuse du couloir de Taconnaz est importante : en moyenne, des avalanches atteignent le niveau des lames déflectrices (cote 1245 m) plus d'une fois par an, et le niveau de la digue frontale (cote 1090 m) tous les 7 ans. La cote maximale d'arrivée de la coulée

s'étale généralement entre 1040 m (26/2/1988) et 1100m (1937, 1966). Tous les aménagements (de 1985 à 1991) ont été fortement sollicités et l'ont été encore récemment, en particulier en 1999. L'avalanche du 11 février 1999 a franchi la digue latérale en rive droite et s'est étendue sur la piste de ski de la Côte du Mont. Le téléski longeant la trouée forestière de la Côte du Mont a été détruit dans son tronçon supérieur. L'avalanche s'est prolongée jusqu'aux premiers chalets de la Côte du Mont. La partie amont de la route de desserte de Vers le Nant a aussi été atteinte ainsi que la forêt située à l'Est de la digue frontale. Le volume de neige et de glace total déposé par l'avalanche était d'environ 750 000 m3 (calcul de cubatures à l'aide de restitutions photogrammétriques réalisées avant et après l'événement). Compte tenu de la proportion de glace des dépôts (environ 30%), il a été estimé que cette avalanche avait pour origine la rupture d'un sérac vers 3300 m d'altitude (*Vincent et al.*, 2003).

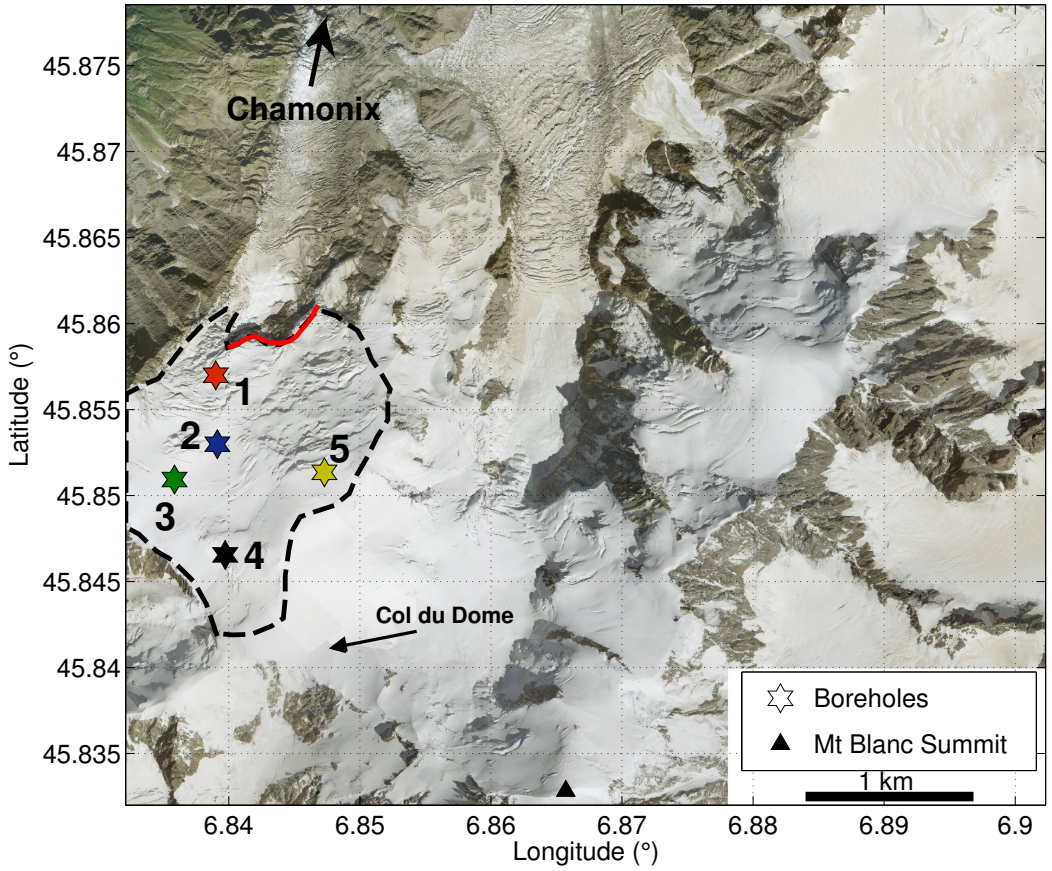

FIGURE 2.8 – Photographie aérienne du Mont Blanc. Le glacier de Taconnaz est délimité par les tirets noirs, la barre de sérac est indiquée par la bande rouge. Les étoiles montrent la localisation des sites de forage avec mesures de températures.

Pour tenter de mieux maîtriser l'aléa associé à la chute de sérac de Taconnaz, des mesures glaciologiques ont débuté en 2001. Ces mesures ont permis entre 2001 et 2003 d'estimer le bilan de masse annuel de la partie supérieure du glacier et la vitesse d'écoulement du glacier pour en déduire une estimation du débit du glacier au niveau de la barre de séracs (*Vincent et al.*, 2003). Les questions sur le régime thermique de la zone de séracs de Taconnaz, de son évolution et des

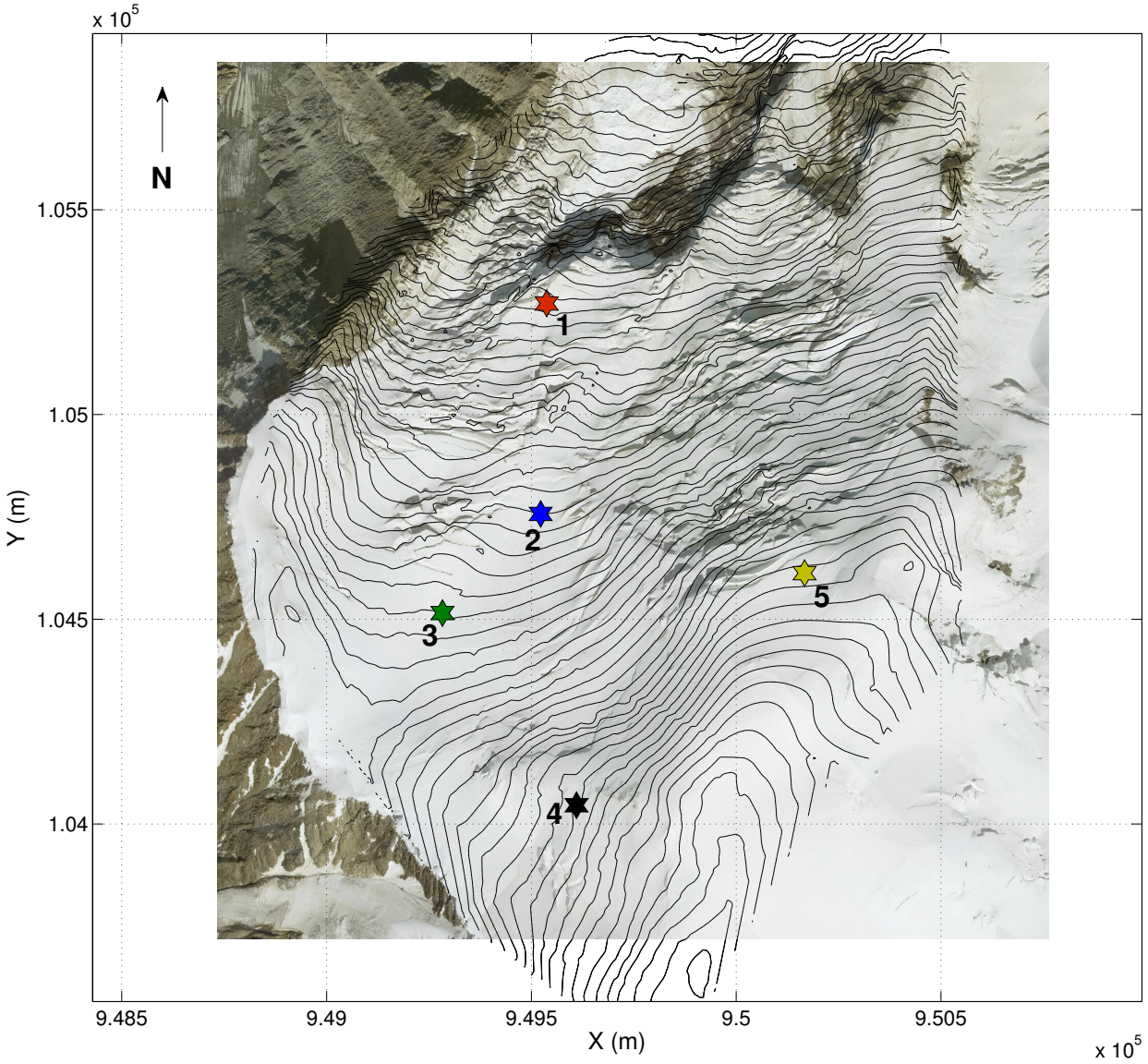

FIGURE 2.9 – Carte du glacier de Taconnaz Les étoiles montrent la localisation des sites de forage avec mesures de températures.

conséquences sur la stabilité de cette zone, se sont posées à la suite de l'observation du réchauffement du glacier du Col du Dôme révélé par les forages de 1993 et 2004 : Le glacier est il tempéré ou froid ? S'il est froid, ne devrait il pas se réchauffer similairement au Col du Dôme ? Dans ce cas, un réchauffement de la base du glacier pourrait il entraîner une déstabilisation d'une partie du glacier si cette base atteint le point de fusion ? Les conséquences pourraient alors être dramatiques dans la vallée quand l'on voit les dégâts que peut provoquer une chute de séracs « normale». Plusieurs profils profonds de température (jusqu'au lit rocheux) ont ainsi été mesurés en 2008, 2012 et 2013 sur cinq différents sites (voir Fig. 2.8, 2.9 et 2.11). Ceux-ci montrent que la température basale du glacier évolue depuis -11°C à son sommet jusqu'à -3°C proche de la barre de sérac (Fig. 2.8). On

remarque aussi que la surface du forage 1 atteint le point de fusion sur plus de 20 m d'épaisseur. C'est le signe que cette zone est dans des conditions de zone d'accumulation tempérée et que seule l'advection de glace froide venant de l'amont maintient des conditions froides à la base du glacier. La question de savoir comment cette structure thermique va évoluer dans un contexte de réchauffement climatique est complexe dans la mesure où le champ de température est extrêmement influencé par l'écoulement du glacier. Cette question est pourtant cruciale. Pour y répondre, les chapitres 3 et 4 de la thèse sont consacrés à l'élaboration d'un modèle pouvant simuler le régime thermique de Taconnaz dans le passé et le futur (selon différents scénarios climatiques).

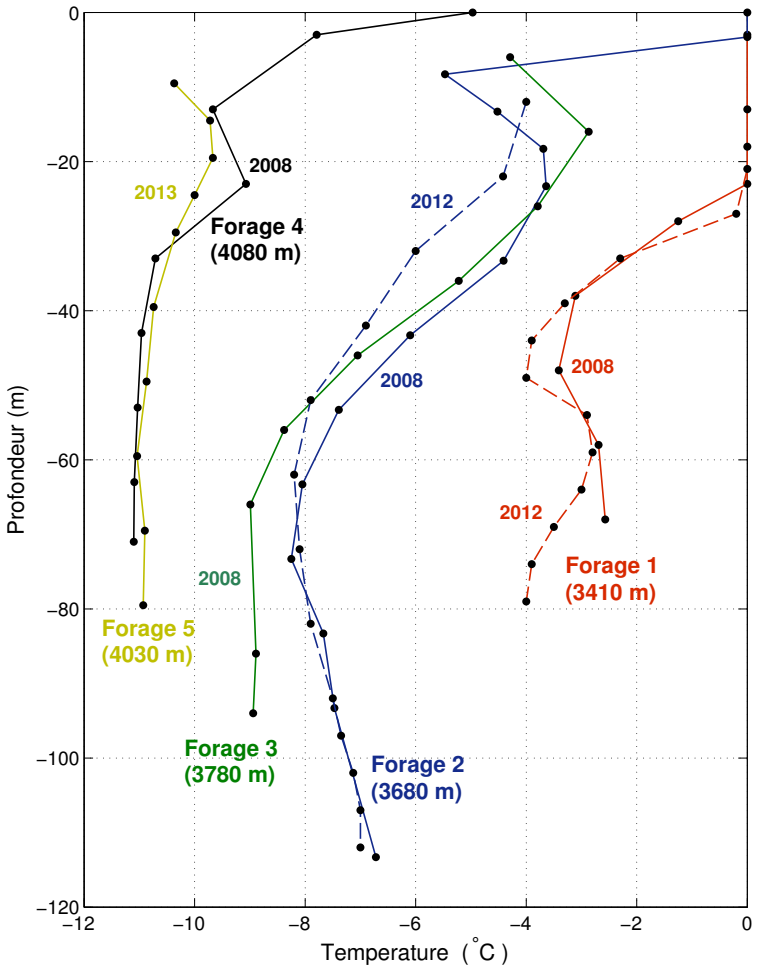

FIGURE 2.10 – Températures mesurées dans les cinq sites de forages (voir les localisations des forages à la figure précédente).

FIGURE 2.11 – Sur le site de forage N° 1 (glacier de Taconnaz). Cliché : A.Gilbert

Chapitre 3

Vers une modélisation du forçage climatique adaptée aux modèles de régime thermique

Introduction

La réponse du régime thermique des glaciers aux forçages climatiques est due à une modification du bilan énergétique de l'ensemble de la surface du glacier ou de son lit rocheux. Elle se traduit par une variation de température et de la fonte en surface du glacier. La modélisation complète des échanges énergétiques entre le glacier et l'atmosphère requiert un grand nombre de données météorologiques à des pas de temps très courts (pas horaire environ). En effet, la modélisation de tous les termes du bilan d'énergie de surface nécessite la mesure des rayonnements incidents et réémis, du vent, de la température et de l'humidité relative. La forte variabilité de ces paramètres météorologiques au cours de la journée impose une mesure au minimum horaire de ces paramètres pour correctement représenter le bilan d'énergie de surface.

De ce bilan résulte une température de surface et une fonte de surface très variables pour le glacier à l'échelle de la journée. Du fait du phénomène de diffusion thermique dans un matériau très isolant (la neige), cette variabilité de surface est rapidement atténuée avec la profondeur dans le glacier et à environ 60 cm de profondeur la température du glacier n'est plus sensible à la variabilité intra-journalière. A environ 10 à 15 m de profondeur, la température du glacier n'est plus sensible à la variabilité intra-annuelle des températures de surface. La couche dans laquelle la température du glacier est sensible à la variabilité journalière et saisonnière est appelée couche active. C'est la variabilité au delà de cette couche qui contrôle finalement l'évolution du régime thermique du glacier avec un temps caractéristique d'évolution de l'ordre de l'année.

C'est pourquoi la plupart des modèles de régime thermique d'un glacier fonctionne à des pas de temps supérieurs à 30 jours et souvent annuels (*Wilson and Flowers*, 2013; *Wilson et al.*, 2013b; *Wohlleben et al.*, 2009; *Zwinger and Moore*, 2009; *Lüthi and Funk*, 2001). Dans ces modèles, le régime thermique du glacier est directement forcé en surface par la Température située en réalité sous la Couche Active (TCA). Il est ainsi nécessaire dans ce cas de paramétrer une relation entre température de surface et TCA. Dans une première approximation, on peut considérer que TCA est égale à la moyenne annuelle des températures de surface mais cette approximation devient fausse dès que de la fonte de surface a lieu dans l'année (*Lliboutry et al.*, 1976). Ainsi, l'utilisation de la TCA comme condition aux limites de surface nécessite l'emploi de paramétrisations empiriques pour relier la TCA aux variations climatiques en prenant en compte l'effet de la chaleur latente ou de l'advection verticale dans les zones de névé (*Hooke et al.*, 1983; *Blatter*, 1987; *Wohlleben et al.*, 2009). Une

telle approche ne permet pas de simuler de façon réaliste l'impact des variations climatiques futures sur le régime thermique des glaciers. En effet, la réponse des températures de surface du glacier aux variations des températures de l'air n'est pas linéaire. Elle est influencée par la modification du bilan d'énergie lorsque la surface atteint le point de fusion et par la percolation et le regel de l'eau de fonte. Pour prendre en compte explicitement ces phénomènes, il est nécessaire d'augmenter la résolution temporelle et spatiale (verticalement), ce qui permet de reproduire correctement la variabilité journalière et saisonnière dans la couche active et forcer correctement le modèle de régime thermique en simulant physiquement la TCA. L'objectif de ce chapitre est de proposer une formulation permettant de forcer à l'échelle journalière un modèle de régime thermique à partir des seules valeurs de températures journalières de l'air et en prenant en compte la variabilité spatiale due à l'orientation et à l'inclinaison de la surface et aux masques du relief. Cette approche, d'une complexité intermédiaire, permet d'une part de simplifier le bilan d'énergie de surface qui réclame un nombre de données trop importantes et souvent non disponibles sur de longues périodes. D'autre part, le pas de temps journalier permet de modéliser explicitement les phénomènes de percolation et regel de l'eau de fonte ainsi que la variabilité de la couche active pour calculer physiquement la TCA.

L'étude qui suit se base sur une étude fine du bilan d'énergie de surface associée à des mesures de température dans la couche active du glacier sur le site du Col du Dôme (voir Chapitre 2) pour déterminer les processus contrôlant la température dans cette couche. Le bilan d'énergie de surface est modélisé à partir données météorologiques collectées sur le site durant l'été 2012. Ces données ont été collectées à partir d'une station automatique installée sur le col et comprennent des mesures de vitesse du vent, de température de l'air, d'humidité et de rayonnement de longues et de courtes longueurs d'onde (voir article pour plus de détails). Le bilan d'énergie est utilisé pour forcer un modèle de transfert de chaleur unidimensionnel prenant en compte la percolation et le regel de l'eau de fonte de surface. Le modèle est validé par la comparaison des températures simulées et mesurées dans la couche active. Ce modèle est ensuite dégradé pour permettre des simulations au pas de temps journalier à partir des températures de l'air seulement. Les performances du modèle dégradé sont évaluées de la même manière par comparaison des températures simulées et mesurées. La variabilité spatiale de la fonte de surface est étudiée à partir de la quantification du regel d'eau liquide sur 14 différents sites répartis sur l'ensemble de la zone du col du Dôme. Ces mesures permettent de spatialiser la fonte de surface en fonction de l'insolation potentielle locale. Enfin, l'utilisation de ce modèle de surface pour simuler l'évolution du régime thermique du Col du Dôme sur trois sites de forage différents pendant le dernier siècle valide cette approche pour rendre compte du forçage climatique sur le régime thermique du glacier.

Modélisation des températures de surface dans le névé des zones froides d'un glacier et application à la modélisation du régime thermique dans un contexte de changement climatique

D'après :

Gilbert, A., C. Vincent, P. Wagnon, D Six and P. Ginot (2013b), Modeling firn near-surface temperature in a cold accumulation zone (Col du Dôme, French Alps) : from physical to semi-parameterized approach, *The Cryosphere Discussion*, submitted

Abstract Analysis of the thermal regime of glaciers is crucial for glacier hazard assessment, especially in a context of a changing climate. In particular, the transient thermal regime of cold accumulation zones needs to be modeled. A modeling approach has therefore been developed to determine this thermal regime using only surface boundary conditions coming from meteorological variables. In a first step, a surface energy-balance (SEB) model accounting for water percolation was applied to identify the main processes that control the subsurface temperatures in cold firn. Results agree well with subsurface temperatures measured at Col du Dôme (4250 m above sea level (a.s.l.), France). In a second step, a simplified model using only daily mean air temperature and potential solar radiation was developed. This model properly simulates the spatial variability of surface melting and subsurface firn temperatures and was used to accurately reconstruct the deep borehole temperature profiles measured at Col du Dôme. Results show that percolation and refreezing are efficient processes for the transfer of energy from the surface to underlying layers. However, they are not responsible for any higher energy uptake at the surface, which is exclusively triggered by SEB changes due to 0°C surface conditions during melting events. The resulting enhanced energy uptake makes cold accumulation zones very vulnerable to air temperature rise.

3.1 Introduction

The thermal regime of glaciers needs to be modeled to study the impact of climate change on ice flow and intraglacial or subglacial hydrology. Indeed, englacial temperatures control ice viscosity and basal sliding (*Paterson*, 1994). They also affect the drainage system (*Ryser et al.*, 2013; *Gilbert et al.*, 2012; *Skidmore and Sharp*, 1999). In addition, most glacier hazard studies require a thorough analysis of the thermal regime of glaciers (*Faillettaz et al.*, 2011; *Gilbert et al.*, 2012; *Huggel et al.*, 2004; *Haeberli et al.*, 1989). Although several mathematical models have already been developed to simulate energy transfer within glaciers (*Wilson and Flowers*, 2013; *Aschwanden and Blatter*, 2009; *Zwinger and Moore*, 2009; *Lüthi and Funk*, 2001; *Funk et al.*, 1994; *Hutter*, 1982), the boundary conditions of these models are often not physically based and not related to external meteorological data, making future transient simulations impossible. This is due to the fact that applied integration times steps are generally longer than those of surface process time-scales such as the percolation/refreezing of surface meltwater. In *Wilson and Flowers* (2013), volumetric heat flux due to meltwater refreezing is calculated using a degree-day model and released in a given firn layer immediately below the surface. This thickness is however determined arbitrary and thus depends on the final result. Another approach, used by *Zwinger and Moore* (2009), is the Wright Pmax-model (*Wright et al.*, 2007). This model quantifies meltwater refreezing heat flux on the basis of englacial temperature measurements in the active layer. Although this formulation gives good results and can be used at an annual time-step, it requires monthly englacial temperature measurements that are very rare. Even more importantly, it cannot be used for future simulations. Furthermore, investigation of the spatial variability of meltwater refreezing heat flux would require extensive temperature measurements, usually not available in the field. Other studies are limited to steady state simulation and do not focus on the relationship between climate and boundary conditions (*Aschwanden and Blatter*, 2009; *Hutter*, 1982) or use only time-dependent surface temperature changes imposed by Dirichlet condition (*Lüthi and Funk*, 2001; *Funk et al.*, 1994).

The aim of this study is to develop a model allowing long-term past and future glacier thermal regime simulations by explicitly taking into account the main surface firn processes such as meltwater percolation and refreezing. To achieve this goal, we could have coupled a thermal regime model to a sophisticated physically-based snow model (e.g. CROCUS (*Brun et al.*, 1989, 1992)). However, this approach requires a considerable amount of meteorological data at a short time-scale (hour), which is not appropriate for simulations to be performed over several decades or centuries. This is why we decided to develop a simple surface temperature model suitable for long term thermal regime simulation based only on daily air temperatures and surface topography parameters. The study site and data are presented in section 3.2. Numerical models are described in section 3.3 and results are shown and discussed in section 3.4. Section 3.4 also explores the spatial variability of surface and englacial temperatures and applies the model to an example involving deep borehole temperature profiles. The last section presents our conclusions and some future perspectives for this work.

3.2 Study site and data

3.2.1 Study site

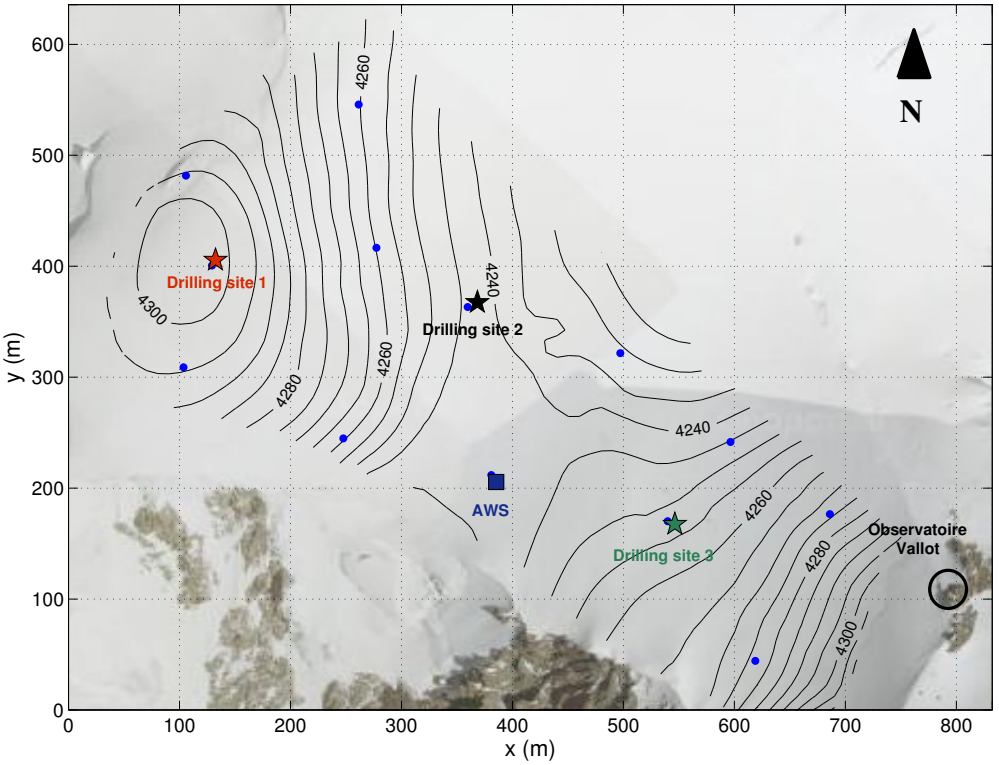

FIGURE 3.1 – Map of Col du Dôme (Mt Blanc range, France) showing the locations of the Automatic Weather Station (AWS ; blue square), density measurement sites (blue dots) and borehole drilling sites (stars).

Col du Dôme is located in the Mont Blanc area at an elevation of 4250 m above sea level (a.s.l.). This is a cold accumulation zone (*Vincent et al.*, 2007b) on a saddle with slopes of various aspects (Fig. 3.1). Snow accumulation rates range from 0.5 m w.e. yr^{-1} (meters of water equivalent per year) to 3.5 m w.e. yr^{-1} over short distances (a few hundreds of meters) and horizontal surface velocities do not exceed 10 m yr^{-1} (*Vincent et al.*, 2007a). The mass balance seems to be stable over the last one hundred years (*Vincent et al.*, 2007a). Mean firn temperature is about -10°C (below the active thermal layer) but has been significantly rising over the last 20 years due to a recent increase in regional air temperature and surface melting (*Gilbert and Vincent*, 2013). These temperature changes are very spatially dependent on local firn advection velocity, slope, aspect and basal heat flux.

3.2.2 Field measurements

3.2.2.1 Meteorological data and firn temperatures

An automatic weather station (AWS) located near the center of the saddle (Fig. 3.1) ran continuously between 3 July and 23 October, 2012. The measurements were carried out within the

surface boundary layer. Wind speed, air temperature, humidity, incident and reflected short-wave radiation and incoming and outgoing long-wave radiation were recorded as half-hourly means of measurements made every 10 seconds. Instantaneous values of surface position and wind direction were collected every half hour. The Vaisala hygro-thermometer was artificially ventilated in the daytime to prevent measurement errors due to radiation.

Five meters from the AWS, 16 thermistors (PT100) were set up in the firn at depths of 0.11 m, 0.24 m, 0.34 m, 0.44 m, 0.65 m, 1 m, 2 m, 3 m, 5 m, 8 m, 12 m and 16 m and at heights of 0.15 m, 0.30 m, 0.45 m and 0.60 m above the surface from 3 July, 2012 to 13 June, 2013. The purpose of the sensors initially located in the air was to measure the subsurface temperature in the even of snow accumulation. Firn temperature was recorded as half hourly means of measurements made every minute. Due to surface melting, the first three sensors were found at the same depth at the end of the melting period, making the first 40 cm deep temperature measurements not reliable after September. Air and surface temperatures were also recorded at this location from 3 July, 2012 to 13 June, 2013. The characteristic and specifications of all sensors are summarized in Table 3.1.

Quantity[1]	Sensor Type (height)	Accuracy according to manufacturer
Air temperature, °C	Vaisala HMP155 – aspirated (1.5 m)	±0.12°C
Relative humidity, %	Vaisala HMP155 – aspirated (1.5 m)	±1% in [0-90%] ±1.7% in [90-100%]
Wind speed[2], m s^{-1}	Young 05103 (2.5 m)	±0.3 m s^{-1}
Wind direction[2], deg	Young 05103 (2.5 m)	±3 deg
Incident short-wave radiation,W m^{-2}	Kipp & Zonen CNR4 (1 m) $0.3 < l < 2.8\mu m$	< 5% for daily sums
Reflected short-wave radiation, W m^{-2}	Kipp & Zonen CNR4 (1 m) $0.3 < l < 2.8\mu m$	< 5% for daily sums
Incoming long-wave radiation, W m^{-2}	Kipp & Zonen CNR4 (1 m) $4.5 < l < 42\mu m$	< 10% for daily sums
Outgoing long-wave radiation, W m^{-2}	Kipp & Zonen CNR4 (1 m) $4.5 < l < 42\mu m$	< 10% for daily sums
Accumulation/Ablation, cm	Campbell Sci SR50	±1 cm
Firn temperature[3], °C	PT100 (16 sensors[4])	±0.05 °C
Surface temperature[3], °C	Campbell Sci IR 120	±0.2 °C
Air temperature[3], °C	PT100 – not aspirated (2 m)	±0.05 °C
Deep borehole temperature, °C	YSI 44031 and PT100 (site 3, 1999)	±0.1 °C

[1] Quantities are recorded as half-hourly means of measurements made every 10 seconds except for wind direction and accumulation/ablation, which are instantaneous values every 30 minutes.

[2] Data measurements were interrupted from 17/07/2012 to 06/08/2012 and from 08/10/2012 to 12/10/2012

[3] Measurement period was 3 July, 2012 to 13 June, 2013

[4] Sensor depths are described in section 3.2.2.1

Tableau 3.1 – List of Different Sensors of AWS with their specifications.

3.2.2.2 Deep borehole temperature profiles

Englacial temperature measurements using a thermistor chain (see Table 3.1) were performed from surface to bedrock in seven boreholes drilled between 1994 and 2011 at three different sites located between 4240 and 4300 m a.s.l. (Fig. 3.1). Ice thicknesses were 40, 126, and 103 m at sites 1, 2, and 3, respectively (see *Gilbert and Vincent* (2013) for more details). Site 1 was measured in January 1999 and March 2012 ; site 2 in June 1994, April 2005 and March 2010 ; site 3 in January 1999 and March 2012.

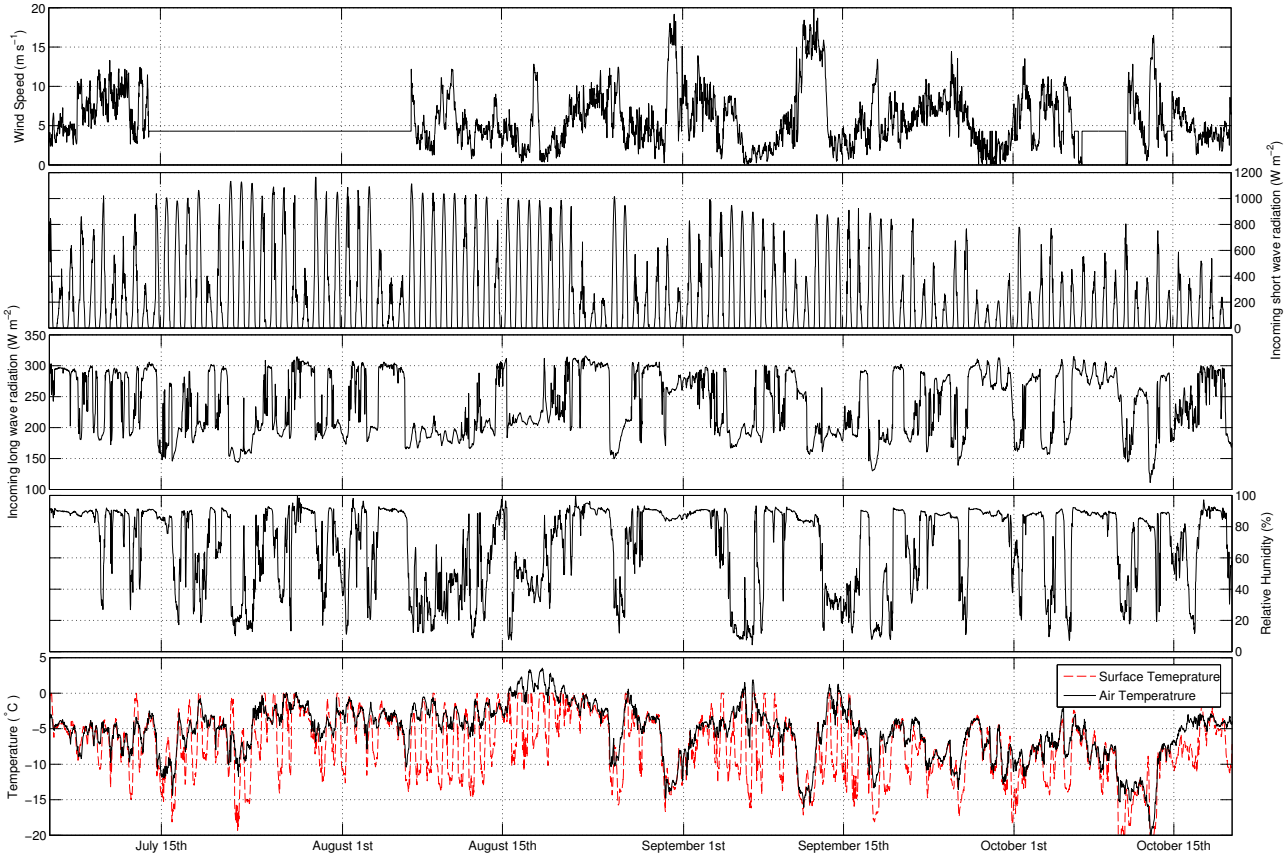

FIGURE 3.2 – Meteorological data recorded by the AWS in summer 2012 and surface temperature calculated using measured infra-red surface emissions

3.2.2.3 Near-surface densities

On 27 September, 2011, density profiles were measured down to a depth of 4 meters at 14 different drilling locations at Col du Dôme using a manual auger device (Fig. 3.1, blue dots).

3.3 Modeling approach

Two distinct one-dimensional and spatially distributed models are used to calculate the near-surface firn temperatures at Col du Dôme. The first is used to calculate the firn surface temperature and melting from a surface energy balance model using the meteorological data recorded by the

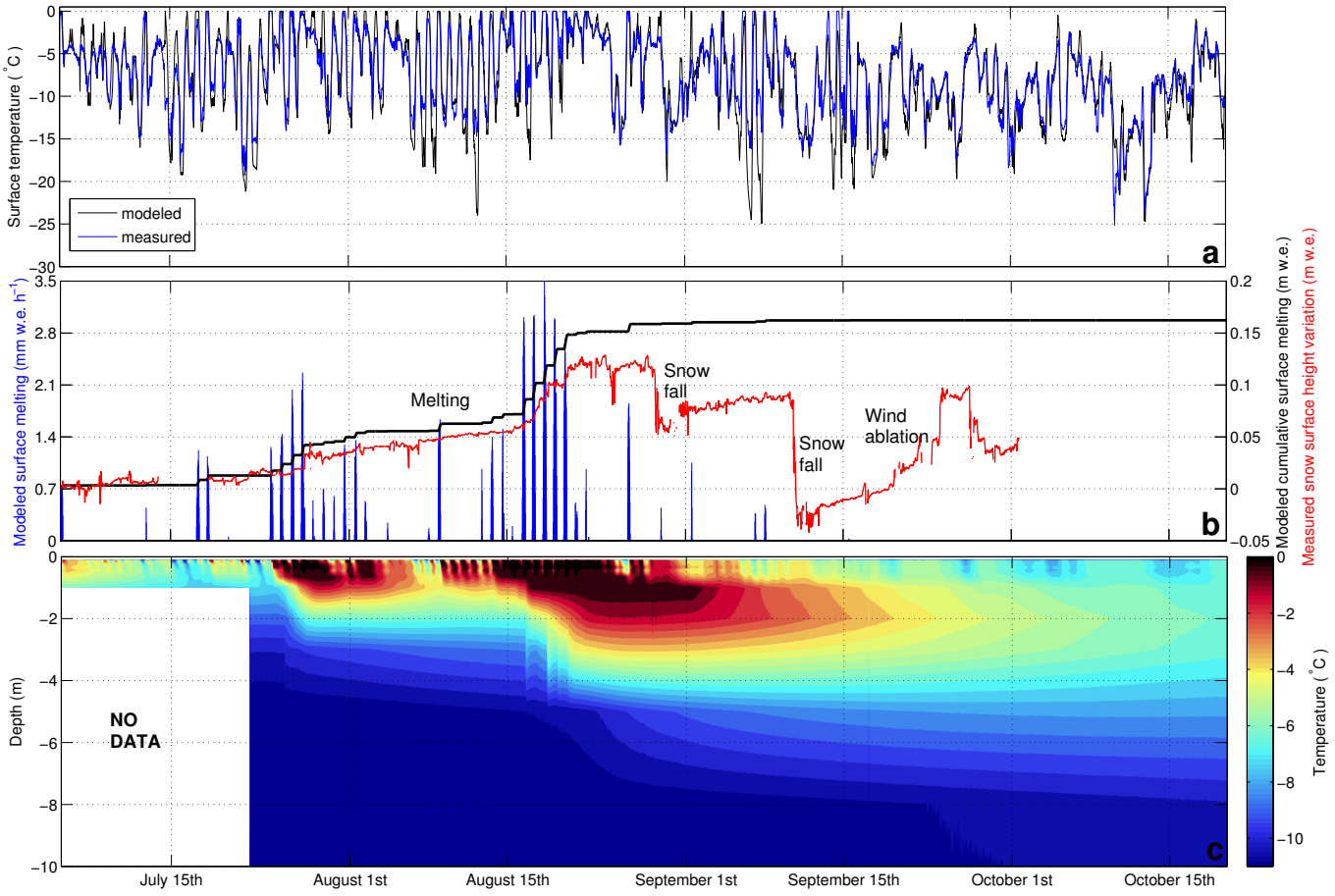

FIGURE 3.3 – (a) Measured (calculated from long-wave radiation emissions) and modeled surface temperature during summer 2012 at the AWS. (b) Modeled surface melting from energy balance (black line) compared to measured snow height (red line). (c) Firn temperature measurements as a function of depth and time during summer 2012.

AWS. The second is a heat flow model coupled to a water percolation model with temperature and melting rate at the surface as input data. This model is used successively with different input datasets obtained first from the energy balance model and then from a parameterized approach.

3.3.1 Model 1 : Surface energy balance

A Surface Energy Balance (SEB) model coupled to a one-dimensional heat flow model was developed in order to determine the energy fluxes within the firn during the measurement period. The SEB equation can be written as (fluxes directed toward the surface are considered positive) (*Oke*, 1992) :

$$R + H + LE + Q = Q_m \tag{3.1}$$

where R is the radiative net balance (W m^{-2}), H the turbulent sensible heat flux (W m^{-2}), LE the turbulent latent heat flux (W m^{-2}), Q the energy flux within the firn (W m^{-2}) and Q_m the

energy flux available for melting. The radiative heat balance is calculated as :

$$R = SW_{in} - SW_{out} + LW_{in} - \sigma T_s^4 \tag{3.2}$$

where SW_{in} is the incident short-wave radiation (W m^{-2}), SW_{out} the reflected short-wave radiation (W m^{-2}), LW_{in} the incoming long-wave radiation (W m^{-2}) and σT_s^4 the outgoing long-wave radiation (W m^{-2}) emitted by the surface (calculated using the modeled surface temperature T_s and the black body law with σ = 5.67x10^{-8} W m^{-2} K^{-4} (*Essery and Etchevers*, 2004). Turbulent fluxes are explicitly calculated using the Bulk aerodynamic approach as proposed by *Essery and Etchevers* (2004).

The SEB model is coupled to a heat diffusion model to determine Q (eq. 3.1). The one-dimensional heat equation is therefore solved over a 16 m deep temperature profile. The upper surface boundary condition is determined by the SEB as a flux condition (Neumann) and we assume no heat flux at 16 m depth over the whole simulation period (125 days) (zero-flux boundary condition). This assumption is supported by the fact that no temperature change is observed at this depth over the measurement period. The time step is set to 5 min (half-hourly meteorological data are linearly interpolated for each time step) and vertical resolution is 4 cm. The heat equation is solved using the Crank-Nicholson scheme. The heat capacity is set to 2050 J K^{-1} kg^{-1} (*Paterson*, 1994). The heat conductivity is calculated from density data using the relation from *Calonne et al.* (2011). The initial temperature profile is taken to be similar to the profile measured at the beginning of the simulation (3 July, 2012).

During the simulation, at every time-step, if the surface temperature Ts exceeds 0°C, Ts is systematically reset to 0°C, and the temperature difference is used to calculate melt energy and the resulting volume of meltwater (*Hoffman et al.*, 2008). This amount of energy is then released in the first underlying cold layer below the surface to simulate water percolation and refreezing.

3.3.2 Model 2 : Coupled water percolation and heat transfer model

In this second model, Dirichlet conditions are assumed at the surface for temperature and the surface boundary condition for percolation is treated as a water flux. Water is assumed to percolate through homogeneous snow. In this way we solve for water saturation in snow using gravity flow theory (*Colbeck and Davidson*, 1973) adapted for dry and cold snow. All symbols used in the following equations (Eq. 3 to 11) are explained in Table 3.2 together with their respective units and values when available. We define the effective water saturation S^* :

$$S^* = \frac{S - S_r}{1 - S_r} \tag{3.3}$$

where S is the water saturation in the snow, S_r is the irreducible water saturation which is permanently retained by capillary forces. If $S < S_r$ there is no water flow and if $S > S_r$, S^* gravitationally advects and we have :

$$\Phi(1 - Sr)\frac{\partial S^*}{\partial t} + n\rho_w g \mu^{-1} K S^{*(n-1)} \frac{\partial S^*}{\partial z} = W \tag{3.4}$$

where Φ is the porosity, n a constant set to 3.3 (*Colbeck and Davidson*, 1973), ρ_w the water density (kg m^{-3}), g acceleration due to gravity (9.81 m s^{-2}), μ the viscosity of water (1.79x10^{-3} kg m^{-1} s^{-1}), K the intrinsic snow permeability (m^2) and W a negative source term coming from liquid water refreezing (s^{-1}). Snow permeability is calculated as a function of snow density ρ and mean grain size d (set to 1.0x10^{-3} m) using the relationship from *Shimizu* (1970) :

$$K = 0.077 d^2 e^{(-7.8\rho)} \tag{3.5}$$

The heat advection/diffusion equation is solved and coupled with the water saturation at each time step :

$$\rho c_p \left(\frac{\partial T}{\partial t} + v_z \frac{\partial T}{\partial z} \right) = \frac{\partial}{\partial z} \left(k \frac{\partial T}{\partial z} \right) + Q \tag{3.6}$$

$$Q = \frac{mL}{dt} = W \left(L \rho_w \Phi (1 - S_r) \right) \tag{3.7}$$

where z is the depth (m), t the time (s), T the temperature (K), c_p the heat capacity of ice (J kg^{-1} K^{-1}), ρ the firn density (kg m^{-3}), v_z the vertical advection velocity (m s^{-1}), k the thermal conductivity of firn (W m^{-1} K^{-1}), Q the latent heat released by refreezing meltwater (W m^{-3}), m the mass of water that freezes per unit volume (kg m^{-3}) during dt and L the latent heat of fusion (J kg^{-1}). Density variations due to meltwater refreezing are neglected.

As proposed by *Illangasekare et al.* (1990), we impose that m is only a fraction of maximum water freezing (m_{max}) allowed by the conservation of heat because in general the time step used in modeling will be small compared to the velocity of freezing processes. So we define :

$$w = S \ \Phi \ \rho_w \tag{3.8}$$

$$m_{max} = \rho \ c_p \ \frac{T_0 - T}{L} \tag{3.9}$$

$$m = \begin{cases} w & \text{if} \quad w < dt \ \tau_f \ m_{max} \\ \\ dt \ \tau_f \ m_{max} & \text{if} \quad w > dt \ \tau_f \ m_{max} \end{cases} \tag{3.10}$$

where w is the snow water content (kg m^{-3}), T_0 the ice melting point (273.15 K), dt the time step (s) and τ_f the freezing calibration constant (s^{-1}, $\tau_f < \frac{1}{dt}$).

The model is run at 30 min time-steps. We assume a zero flux boundary condition at 16 m depth over the entire simulation period (125 days). The initial temperature profile is taken to be similar to the profile measured at the beginning of the measurement period (3 July, 2012). The problem is solved numercially using the Elmer/ice finite element model (*Gagliardini et al.*, 2013) based on the Elmer open-source multi-physics package (see http ://www.csc.fi/elmer for details) that will make it possible to work in three dimensions and perform thermo-mechanical coupling easily in future studies.

	Symbol	Values and units
Water saturation	S	
Effective water saturation	S^*	
Water content	w	kg m^{-3}
Residual Saturation	S_r	0.005
Porosity	Φ	
Water flow constant	n	3.3
Water density	ρ_w	1000 kg m^{-3}
Gravity	g	9.81 m s^{-2}
Water dynamic viscosity at 0°C	μ	1.79 10^{-3} kg m^{-1} s^{-1}
Snow mean grain size	d	1.0 10^{-3} m
Snow intrinsic permeability	K	m^2
Snow temperature	T	K
Temperature of fusion	T_0	273.15 K
Latent heat of fusion	L	3.34 10^5 J kg^{-1}
Snow density	ρ	Kg m^{-3}
Ice heat capacity	c_p	J kg^{-1} K^{-1}
Firn advection velovity	v_z	m s^{-1}
Snow conductivity	k	W K^{-1} m^{-1}
Heat Source	Q	W m^{-3}
Water Source	W	s^{-1}
Maximum water content freezing	m_{max}	kg m^{-3}
Effective water content freezing during dt	m	kg m^{-3}
Freezing calibration constant	τ_f	2.0 10^{-5} s^{-1}

TABLEAU 3.2 – Parameters and variables used in the percolation and heat transport model (model 2), with their respective values when available.

3.4 Results and discussion

3.4.1 Meteorological conditions in summer 2012

AWS measurements from 3 July, 2012 to 23 October, 2012 are reported in Figure 3.2 for wind speed, incoming short- and long-wave radiation, relative humidity, air temperature and firn surface temperature. These measurements show 13 days of positive air temperature events with a more marked event from 15 to 20 August. There were 42 cloudy days and 69 clear sky days. Based on surface elevation measurements, we estimate that three snow falls occurred on 29 August (16 cm), 11 September (30 cm) and 27-28 September (15 cm). Mean wind speed was 5.4 m s^{-1} (half-hourly mean), mainly from the south-west and west ($>$ 50%) with some strong wind events from the north-east.

3.4.2 Surface energy balance (Model 1)

The calculated surface energy balance, surface temperature and surface melt obtained from the SEB model are reported in Figures 3.3 and 3.4. Given that all meltwater refreezes within the cold firn pack, energy is conserved and the cumulative surface energy balance should match the energy content variation of the firn pack. For this purpose, the roughness length for momentum z_0 is tuned

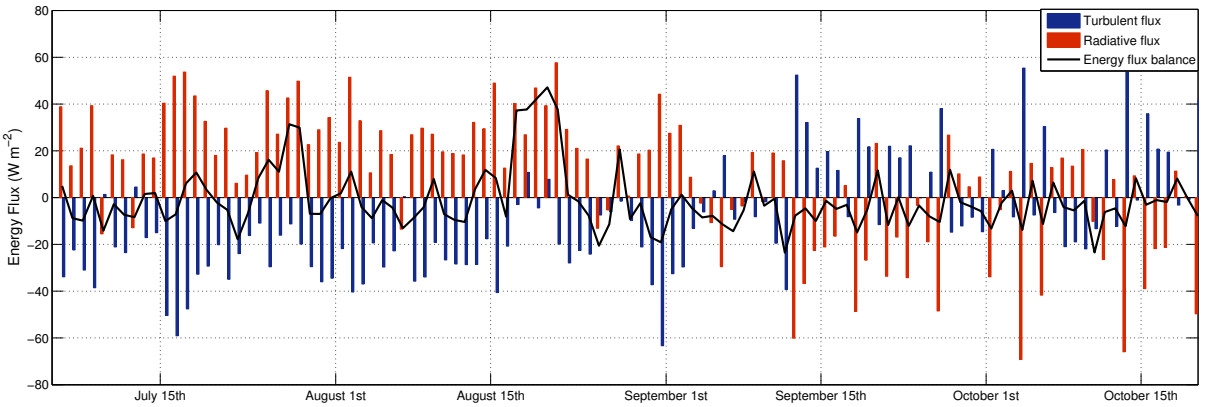

FIGURE 3.4 – Modeled daily mean net turbulent and all-wave radiation fluxes during summer 2012.

to 1.6 mm so that the measured firn internal energy matches the modeled energy input (Fig. 3.5). This value is close to the expected value found in the literature at high-altitude cold sites (*Suter et al.*, 2004; *Wagnon et al.*, 2003). The energy balance is only adjusted for turbulent fluxes (via z_0), given that the radiative fluxes are directly measured in the field and the main uncertainty comes from turbulent fluxes.

The calculated hourly surface melt and corresponding cumulative melt are displayed in Figure 3.3 together with the measured distance between the surface and the SR50 ultrasound sensor expressed as a surface height change in m w.e. Two main melting events (25 July to 4 August, and 16 to 26 August) can be identified and agree fairly well with the surface height variation measurements. The mismatch observed between cumulative surface melt and surface height variations from September 10 to 25 can be attributed to wind erosion. Indeed, strong winds observed just after the large snow fall of September 10 (Fig. 3.2) likely re-mobilized fresh snow into the atmosphere, explaining the ablation without any melting. Modeled surface temperatures also agree well (r^2= 0.80, n= 5326 half-hours) with measured surface temperatures inferred from long-wave radiation emissions (Fig. 3.3), further supporting the ability of the model to efficiently simulate surface melting.

Figure 3.5 compares the integrated thermal energy of the firn pack (red line) obtained from temperature measurements with the cumulative surface energy balance (E_b, blue line) obtained from the model and the modeled firn thermal energy. Firn thermal energy E_{firn} is calculated from :

$$E_{firn} = \int_0^D c_p(z)\rho(z)T(z)dz \tag{3.11}$$

where D (m) is the temperature measurement depth, which is constant over the simulation period i.e. 16 m at Col du Dôme. Figure 3.5a shows that energy is conserved except during the second melting event. In this case, the energy input calculated from the SEB exceeds the firn pack thermal energy. Indeed, part of the energy transferred to the firnpack from the surface is stored as latent heat because some firn layers have reached the melting point. Consequently, liquid water is stored in the firn (Fig. 3.5, blue line). This energy is then released when the water refreezes. This explains why the cumulative surface energy balance is once again equal to the firn pack thermal energy several days after the melting event (Fig. 3.5a).

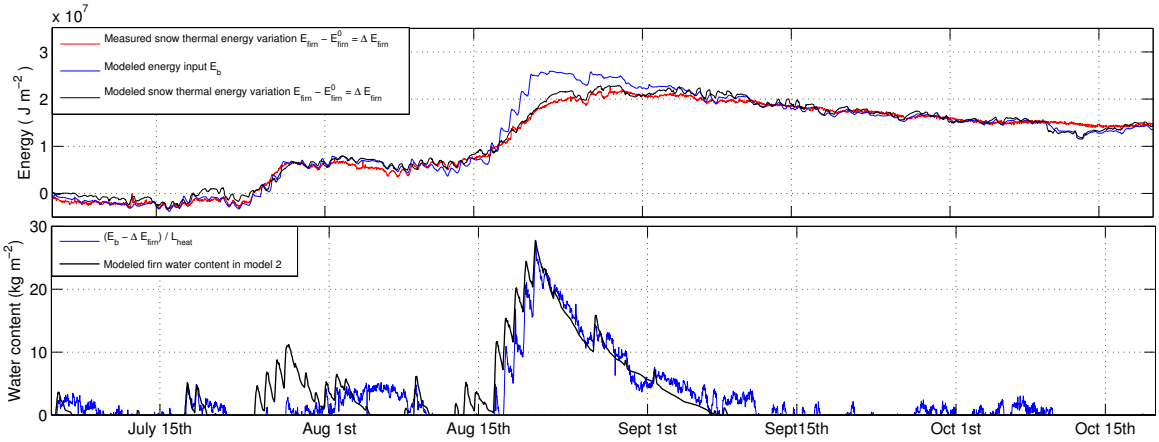

FIGURE 3.5 – (a) Modeled cumulative energy input in firn from surface energy balance (E_b, blue line), measured and modeled firn thermal energy E_{firn} (red and black lines respectively). (b) Energy difference between the energy input calculated from the SEB (E_b) and firn thermal energy (E_{firn}) compared to modeled water content in firn using model 2 (integrated on the vertical axis).

As illustrated in Figure 3.5a, each melting event results in a large energy increase in firn. This means that the surface energy balance is modified during these events. Figure 3.6 focuses on two consecutive days of melting (18 and 19 August). During these two days, we compare the energy flux of two cases : (i) a virtual case for which the surface temperature can exceed 0°C and no melting can occur (dashed lines) and (ii) the true case for which the surface temperature cannot exceed 0°C and melting occurs. In the daytime, for case (i), the short-wave radiative balance is efficiently compensated by the other fluxes due to increasing surface temperature, implying on one hand an enhanced energy loss due to increased outgoing long-wave radiation and on the other hand unstable conditions in the surface boundary layer leading to negative values for sensible heat flux and a strong negative latent heat flux. For case (ii), net short-wave radiation largely dominates the other fluxes because surface temperature cannot exceed 0°C, thereby limiting heat loss through long-wave radiation and maintaining stable conditions inside the surface boundary layer that reduces turbulent fluxes. In this case, a large amount of energy is transferred to the firn. At night, energy fluxes remain unchanged for both cases. Consequently, the energy uptake during melting events is due to the fact that surface temperature is maintained at 0°C by thermodynamic equilibrium between the liquid and solid phases. Note once again that case (i) is a virtual case where meteorological records have been considered unchanged even though surface temperature is allowed to exceed 0°C. In reality, meteorological variables such as air temperature, air vapor pressure, etc. would be modified along with the turbulent fluxes if surface temperature rises above 0°C. Nevertheless, we believe that this simple comparative approach is useful to qualitatively understand the impact of melting on the SEB over cold surfaces.

We conclude that each melting event is associated with a significant energy transfer to the firn pack and the duration of the event therefore has a very strong impact on the total energy balance of the firn pack during summer. With expected higher air temperatures, melting events will be more frequent and the energy will be transferred more efficiently to the firn in the accumulation zones of glaciers. This energy is injected into firn by water percolation and refreezing processes but actually

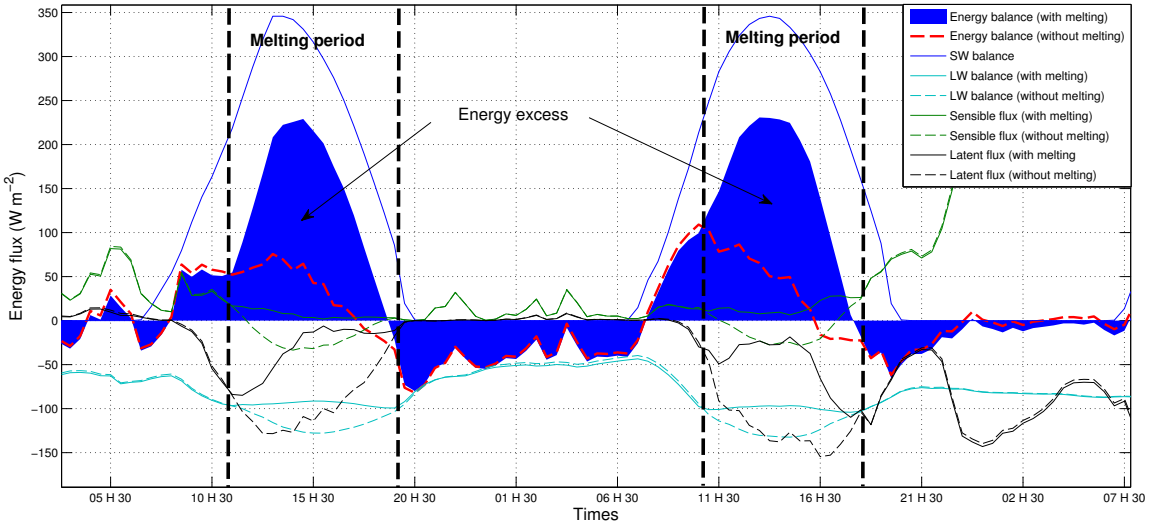

FIGURE 3.6 – Energy fluxes during two consecutive days of melting (18 and 19 August). Comparison between two cases : (i) no phase change is taken into account and firn temperature can artificially exceed 0°C (dashed line) (ii) melting is taken into account (lines and filled blue area).

the strong energy uptake during melting events is less due to these processes than to an energy gain in the SEB due to peculiar conditions of the lower atmosphere-firn surface continuum triggered by a 0°C firn surface. In other words, for similar atmospheric conditions, firn surfaces are able to absorb more energy when the surface temperature is at 0°C than when it is negative, explaining why warming of cold accumulation zones of glaciers is more efficient when melting conditions are encountered than when they are not.

3.4.3 Subsurface temperature and water content (Model 2)

3.4.3.1 Comparison with data

Measured subsurface temperatures during summer 2012 are shown in Figure 3.3c. The influence of surface melting events is clearly visible on the firn temperature data (Fig. 3.3c). These observations reveal two striking features, (i) water percolates into cold firn until 4 to 5 meters deep and (ii) liquid water crosses the cold firn without totally refreezing. Indeed, we observe a step-change in the time evolution of firn temperature between 2 and 5 meters deep on 25-26-27 July and 16-17-18 August. These temperature increases at these dates are too sharp and rapid to come from diffusive processes and are likely due to additional energy supplied by refreezing meltwater.

Model 2 uses the surface temperature and surface melting flux calculated by the SEB model as input data. The only free parameters of the model are the percolation parameters which are not constrained (S_r and τ_f). These two parameters were adjusted to $\tau_f = 2.010^{-5} s^{-1}$ and $S_r = 0.005$ respectively to match the measured temperatures at all depths (Fig. 3.7a-e). Figure 3.5b shows that the modeled water content using model 2 agrees well with the expected value based on the energy balance (see section 3.4.2). However, the value of S_r is one order of magnitude lower than past published values (S_r = 0.03 to 0.07) (*Illangasekare et al.*, 1990). We think that water does not percolate within the cold firn in a uniform manner but more locally using small preferential

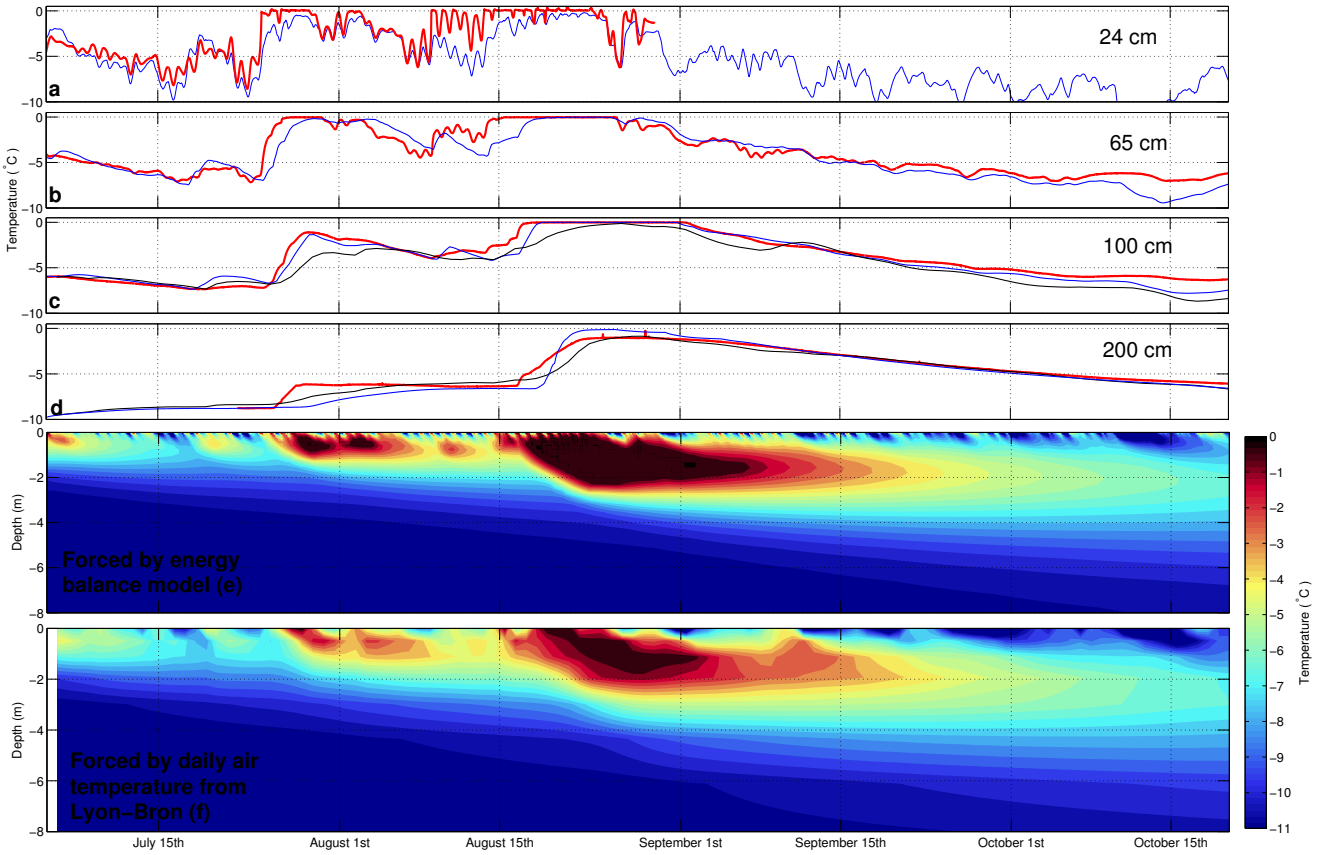

FIGURE 3.7 – Measured (red line) and modeled (blue and black lines) firn temperature at different depths (a, b, c, d). Modeled firn subsurface temperature during summer 2012 using the energy balance model at a 30-min time-step (e, blue line on panels a, b, c, d) compared to modeled temperature using the Lyon-Bron temperature at a daily timescale (f, black line on panels c and d).

pathways (*Harrington et al.*, 1996), explaining why less water is retained by capillarity in this case. Higher values of S_r lead to more liquid water being stored within the first meters of firn below the surface, which prevents water from percolating deep enough to explain the observed firn temperatures. The freezing calibration constant τ_f makes it possible to simulate water percolation in cold firn where only part of the liquid water refreezes between two time steps (30 min here). This parameter is well constrained by temperature measurements. Indeed, if the value of τ_f is too high, the water will not manage to percolate through cold firn and will not influence the temperature field deep enough compared to measurements. Conversely, if the value of τ_f is too low, the firn temperature never reaches 0°C and the energy released by meltwater refreezing is distributed over too large a thickness.

From these results, we can conclude that our subsurface firn temperature model is able to reproduce the water content and the subsurface temperature field accurately (Fig. 3.5b and 3.7). However, this model cannot be applied for simulations over several decades or centuries because the half-hourly data it requires is not available over such long periods. Consequently, a simplified approach has been developed with boundary conditions parameterized using daily air temperature data.

3.4.3.2 Simplified approach

For numerical reasons, in order to use a daily time step, the vertical resolution has been reduced from a few centimeters to about 50 cm. In addition, the previous percolation approach is not meaningful at this space and time scale. For this reason, we now use a constant percolation velocity. The value of 1.0 10^{-6} m s^{-1} provides the best agreement between the results obtained with this simplified approach and those with the previous model using the Colbeck and Davidson formulation (Fig. 3.7). All other parameters remained unchanged.

In this way, the boundary conditions are now parameterized using the daily mean and maximum air temperatures. Daily surface temperature is assumed to vary in the same way as daily mean air temperature. This is confirmed by one year of hourly simultaneous measurements of surface (infra-red camera) and air temperature at this site (Fig. 3.8). From these measurements, the mean difference between daily mean air and surface temperature is estimated at 3.4 K (Fig. 3.8). In order to take into account the enhanced energy uptake during melting events, melting is assumed to occur when daily maximum air temperature reaches 0°C. The daily surface melt flux is calculated using the following degree-day model (*Hock*, 1999) :

$$M = \begin{cases} (T_{max} - T_0)\ a & \text{if} \quad T_{max} > T_0 \\ \\ 0 & \text{if} \quad T_{max} \leq T_0 \end{cases} \tag{3.12}$$

where M is the daily amount of surface melt (m w.e. d^{-1}), a the melt factor (m w.e. d^{-1} K^{-1}), T_0 the melting point (273.15 K) and T_{max} the daily maximum air temperature.

Air temperature data from Lyon-Bron meteorological station located $\sim$ 200 km west of the studied site was selected given that it is one of the longest meteorological series in this region (*Gilbert et al.*, 2012). Comparison between Lyon-Bron air temperature and on-site surface temperature at daily time-steps between 3 July, 2012 and 13 June, 2013 leads to an altitudinal gradient between Lyon air temperature and Col du Dôme surface firn surface temperature of -5.94 10^{-1} K m^{-1}. Although the altitudinal gradient varies significantly between summer and winter (-5.6 10^{-1} K m^{-1} in winter and -6.5 10^{-1} K m^{-1} in summer), we use a constant mean value of -5.94 10^{-1} K m^{-1}. In this way, the following inferred melt factor will be used for simulation over several years that use a mean altitudinal gradient. The melt factor is adjusted to simulate the total melt calculated from the SEB during summer 2012 (3 July, 2012 – 23 October, 2012) and set to 3.3 10^{-1} m w.e. d^{-1} K^{-1}. Calculated temperatures using this simplified approach agree well with in-situ measurements (Fig. 3.7c,d,f) and properly account for the step-change observed during melting events. This reveals that the simple model using daily temperature data from a remote station provides satisfactory results and can be used to simulate long-term firn subsurface temperature variations in a cold accumulation zone.

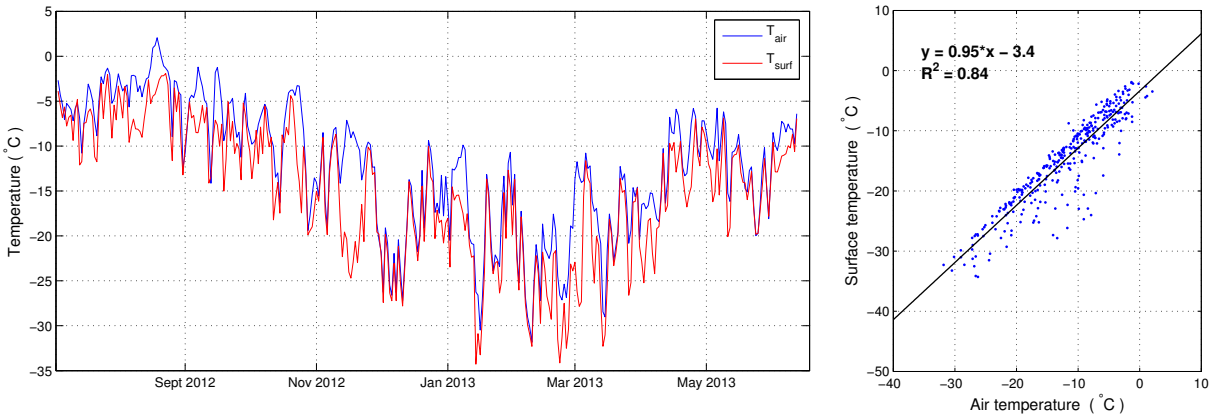

FIGURE 3.8 – Comparison between daily measured air and surface temperature between 3 July, 2012 and 13 June, 2013 at Col du Dôme.

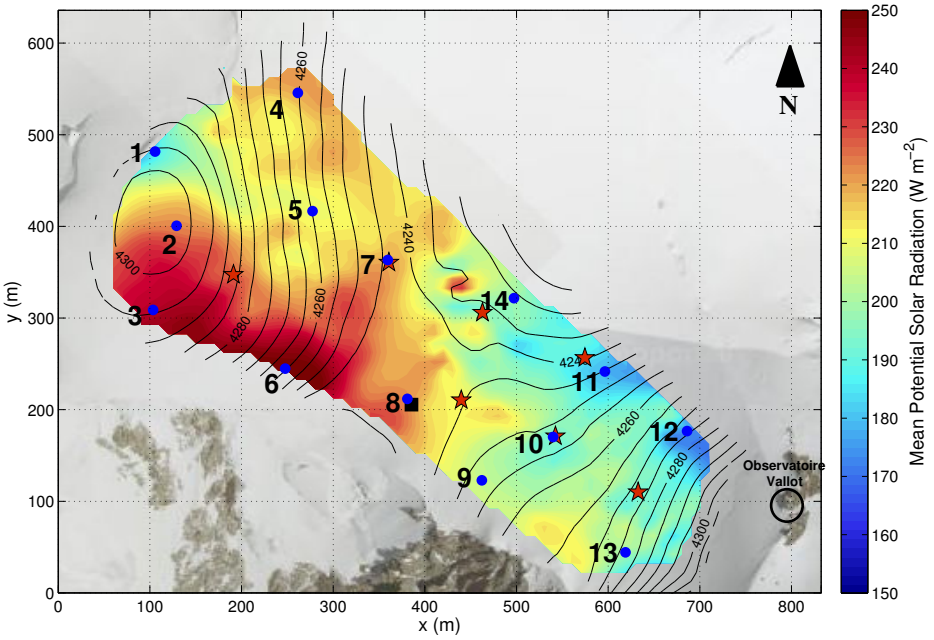

FIGURE 3.9 – Incoming potential solar radiation at Col du Dôme (color scale). Numbers and blue dots indicate the locations of sites where density measurements were performed . Red stars indicate the locations of sites where snow accumulation has been monitored since 2010.

3.4.4 Spatial variability of melting and subsurface temperature

3.4.4.1 Melting spatial variability

In order to quantify melting spatial variability, 14 4-meter deep density profiles were measured in the field on 27 September, 2011 (Fig. 3.9 and 3.10). The amount of meltwater was quantified using the density anomaly related to meltwater refreezing in the firn. This anomaly was quantified in every section of the firn core by comparing the measured density with a computed density obtained from an empirical firn densification model (*Herron and Langway Jr*, 1980). *Gilbert et al.* (2010) (annexe A) successfully applied this method on a high altitude site in the Andes to quantify local melting. (Fig. 3.10, blue line). Uncertainty on melt quantification (error bars in Fig. 3.11) were

computed considering uncertainty from mass, length and circumference measurements on each core section. This Col du Dôme site has been monitored for snow accumulation since 1994 using a well-distributed stake network (*Vincent et al.*, 2007a) that provides a good assessment of the spatial variability of snow accumulation at Col du Dôme. In this way, we were able to spatially extrapolate the snow accumulation monitored since 2010 in the vicinity of the measured density profiles (Fig. 3.9 – red stars). Knowing the accumulation rate, we were then able to accurately date every density profile (Fig. 3.10, dashed lines). The density anomaly above the horizon identified on 28 October, 2010 was been considered here to make sure that we only take into account the refreezing meltwater of summer 2011. The quantified melt at each site is plotted in Figure 3.11 as a function of the mean annual incoming Potential Solar Radiation (PSR) of the corresponding site taking into account the shading effect of the surrounding relief and atmospheric transmissivity (Fig. 3.9).

Although uncertainties related to these measurements are high, we observe a good correlation between PSR and surface melt (Fig. 11). Between 27 June and 26 October, 2011, the AWS ran continuously, allowing us to run the SEB model over the whole summer of 2011 and in turn quantify the corresponding on-site melt values. Results agree well with the melt values obtained from the density anomaly method at site 8, 5 meters from the AWS. In order to model surface melt over the whole site using the SEB model, the measured incoming short-wave radiation at AWS is varied artificially according to PSR before re-running the SEB model. In this way we obtain a relationship between surface melt and PSR for summer 2011 from the SEB model (Fig. 11). A quadratic function provides a reasonable fit for the melt-PSR relationship. The non-linearity can be explained by the fact that increasing short-wave radiation enhances the frequency of melting events which in turn shifts the energy balance towards positive values (see section 3.4.2).

In order to take into account the effect of PSR on the melting intensity in the degree-day formulation, we revise Equation 3.12. PSR is now taken into account in Equation 3.13 proposed by (*Hock*, 1999) and melt is calculated by :

$$M = \begin{cases} (T_{max} – T_0)\ a_{PSR}(x,y) & \text{if} \quad T_{max} > T_0 \\ \\ 0 & \text{if} \quad T_{max} \leq T_0 \end{cases} \tag{3.13}$$

where a_{PSR} is the melt factor as a function of PSR.

Using daily maximum air temperature inferred from Lyon-Bron daily maximum air temperature (using the same gradient as the one obtained between Lyon-Bron air temperature and Col du Dôme surface temperatures in 2012-13) and melt calculated using SEB in summer 2011, we calculate a_{PSR} for different PSR values. We found a quadratic relationship (Fig. 3.11) :

$$a_{PSR} = 3.3\ 10^{-8} \times PSR^2 – 8.23\ 10^{-6} \times PSR + 5.62\ 10^{-4} \tag{3.14}$$

In this way, this relationship can be applied to calculate the surface melt and the firn temperature can be calculated using the above-described simplified model for the whole area. However, this relationship is not likely to be transferable to another site. Indeed, melt factors depend on site characteristics that influence the surface energy balance such as mean albedo, wind speed, humidity and surface roughness. Thus, the relationship between melt factor and PSR needs to be recalibrated for every studied site.

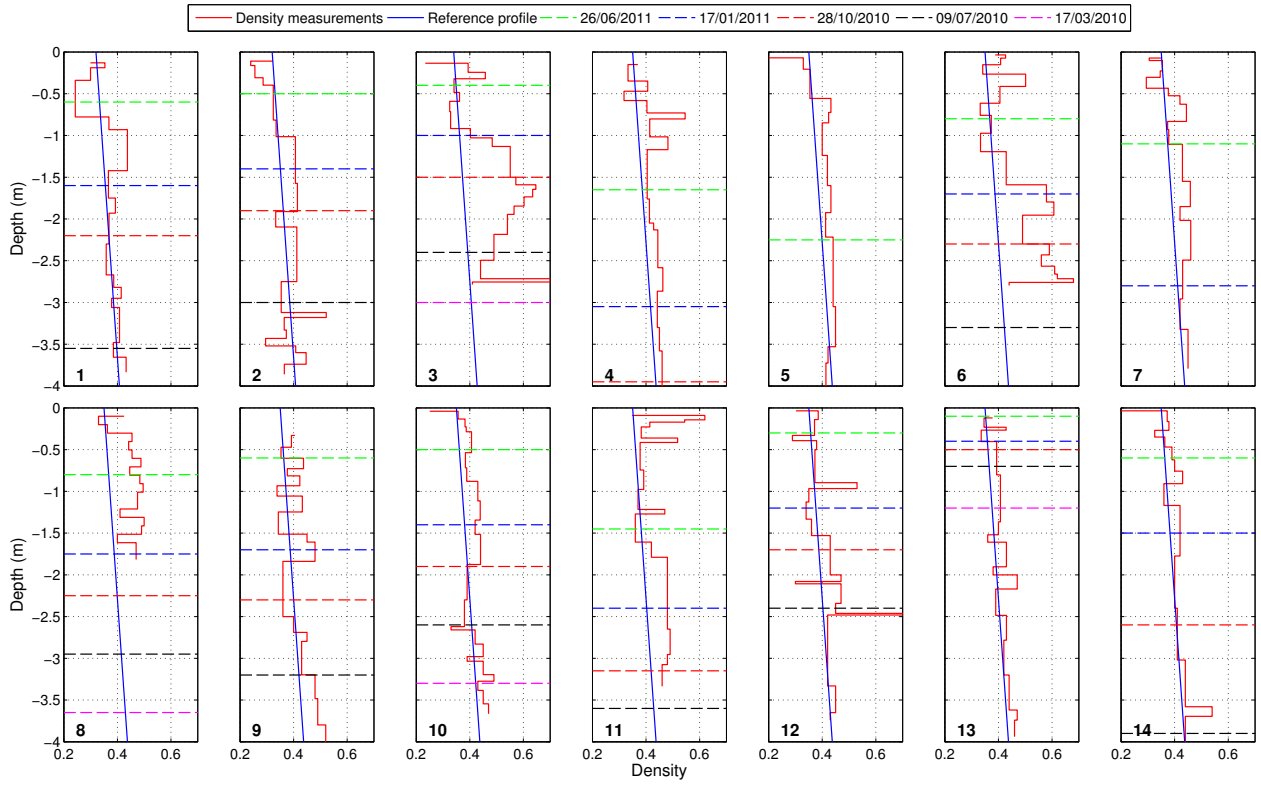

FIGURE 3.10 – Density profiles (red line) measured on 27 September, 2011. Dashed lines correspond to different surface horizons identified at different dates. Blue lines are reference density profiles determined using the empirical model proposed by *Herron and Langway Jr* (1980).

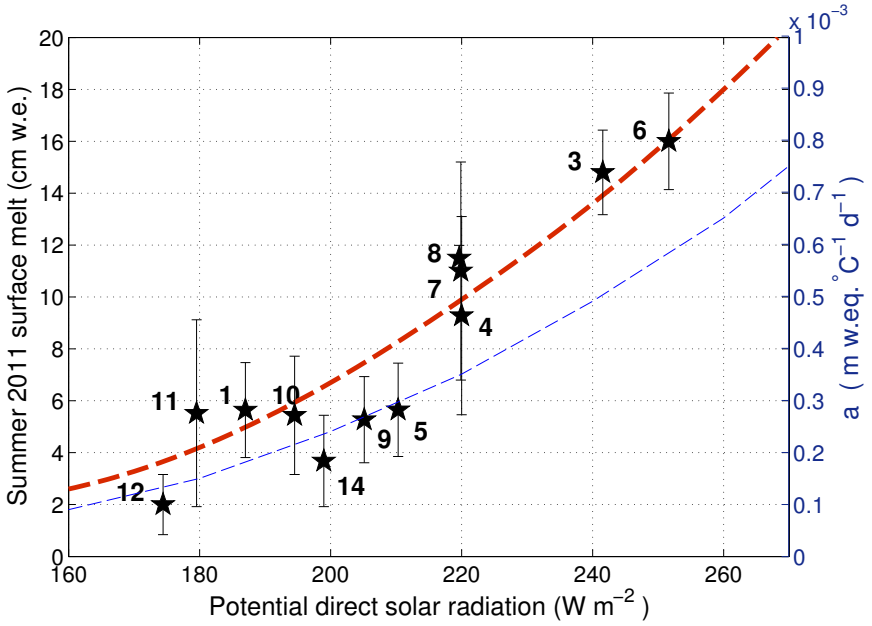

FIGURE 3.11 – Melt obtained from density anomalies (black stars) as a function of potential solar radiation, compared to melt obtained using the surface energy balance model (red dashed line). Corresponding melt factor values in the degree-day model (eq. 3.14) are plotted in blue.

3.4.5 Application of the simplified model at multi-decennial scale to reconstruct deep borehole temperature profiles

The locations of borehole sites 1, 2 and 3 are indicated on the map in Figure 1 and their respective annual PSR values are assessed at 220, 220 and 192 W m^{-2}. Our simplified 1-D model (model 2 using daily temperature from Lyon-Bron station and topographic parameters) was applied to the three sites and run over the period 1907-2012. The vertical advection profile is calculated from the measured surface advection velocity and assumed to vary linearly with depth (*Gilbert and Vincent*, 2013). Basal heat flux is set to 15 10^{-3} W m^{-2} for sites 1 and 2 and set to 30 10^{-3} W m^{-2} for site 3 according to measured basal temperature gradients. The basal heat flux is specified at 150 meters depth in the bedrock because it can be considered to be constant at this depth for the time scale of the simulation (no temperature change is modeled at this depth during the simulation). The thermal properties of the rock (gneiss and granite) are taken from *Lüthi and Funk* (2001) with a thermal conductivity of 3.2 W m K^{-1} m^{-1} , a heat capacity of 7.5 10^2 J kg^{-1} K^{-1} and a density of 2.8 10^3 kg m^{-3}.

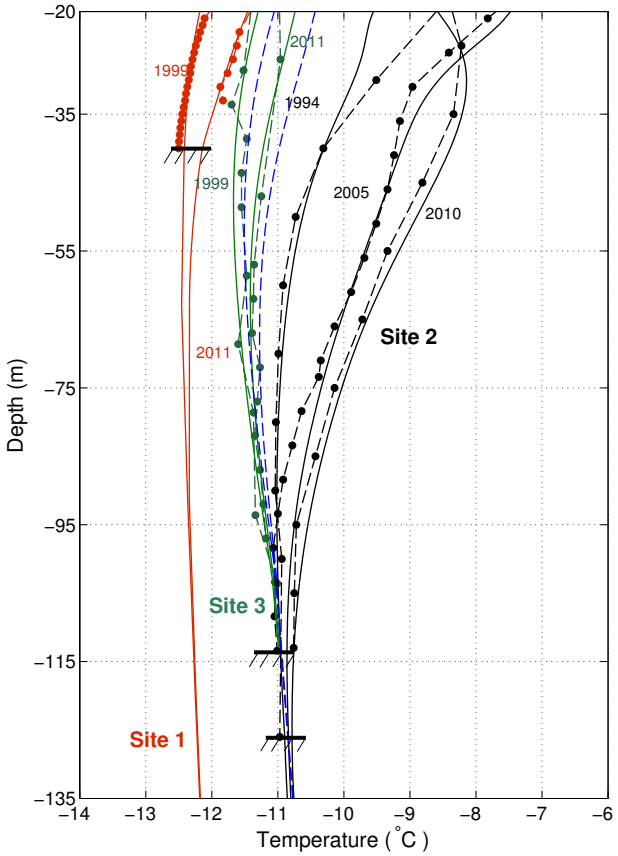

FIGURE 3.12 – Measured (dashed lines and dots) and modeled (solid lines) temperature profiles at the three drilling sites (site 1 = red, site 2 = black, site 3 = green) for different dates. The blue dashed line is the temperature profile modeled at site 3 in 1999 and 2012 for a melt factor set to 2.0x10^{-4} m w.e. d^{-1} K^{-1} according to the relationship with PSR.

For each site, the altitudinal temperature gradient and the melt factor are adjusted to match observed borehole temperatures. We found values of 5.95 10^{-3}, 5.70 10^{-3} and 5.83 10^{-3} K m^{-1}

for the altitudinal temperature gradients and values of 3.5 10^{-4} m w.e. d^{-1} K^{-1}, 3.5 10^{-4} m w.e. d^{-1} K^{-1} and 1.0 10^{-4} m w.e. d^{-1} K^{-1} for the melt factors for sites 1, 2 and 3 respectively. The results plotted in Figure 12 show that temperature differences between the three boreholes can be explained by differences in both surface melt (in agreement with PSR differences) and vertical advection velocities. As already seen, PSR has a strong influence on firn temperature of a cold glacier mainly through surface melt and must be accounted for to simulate the thermal regime of cold glaciers. Indeed, site 2 experiences higher surface melting rates than site 3, leading to a stronger firn temperature rise over the first decade of this century. Differences between the two sites are amplified by stronger vertical advection velocities at site 2. The respective melt factors for sites 1, 2 and 3 derived from PSR values (220, 220 and 192 W m^{-2} respectively Eq (3.14)) are 3.5 10^{-4}, 3.5 10^{-4}, and 2.0 10^{-4} m w.e. d^{-1} K^{-1}, in perfect agreement with adjusted values for sites 1 and 2, but twice as high as the values for site 3, where a lower value is needed to fit the observed temperatures. However, the use of the melt factor specified on the basis of the PSR relationship leads to an englacial warming over-estimation of less than 0.5°C (see blue dashed line in Fig. 3.12), which is acceptable for thermal regime simulation at the glacier scale.

3.5 Conclusions

To simulate the transient thermal regime of a cold glacier, we developed a model based on a surface energy balance and water percolation modeling. The results agree well with in-situ firn temperature measurements for summer 2012.

Our energy balance study highlights the impact of the duration of melting events on cold firn temperature. Once the surface temperature reaches 0°C in summer, cold accumulation zones become extremely sensitive to climate change. Indeed, when surface temperature reaches 0°C, the surface energy balance shifts towards more positive values which means that more energy is transferred to underlying layers through water percolating and then refreezing within cold layers. Consequently, air temperature rise, which contributes to increasing frequency and duration of melting events at high elevations, has a very strong impact on cold glacier temperature profiles. Note that water percolation and refreezing are very efficient processes for energy transfer from the surface to subsurface firn layers, however they are not responsible for a higher energy uptake at the surface, which is mainly due to the fact that temperature is blocked at 0°C.

To perform numerical simulations over several centuries, instead of applying a sophisticated surface energy balance requiring an excessive amount of data, we also developed a simplified approach based only on daily air temperature and topography. Results from this simplified approach agree well with in-situ firn temperature measurements and with results coming from SEB modeling. In addition, if the melt factor is known, this simplified model allows us to reconstruct deep borehole temperature profiles that agree well with measurements.

Our measurements show that the spatial variability of melting is highly dependent on the potential solar radiation. This confirms the results obtained by *Suter* (2002) at these high elevations and we propose a relationship between the melt factor and potential solar radiation at Col du Dôme.

Water percolation study shows that gravity flow theory (*Colbeck and Davidson*, 1973) is sufficient

to reproduce the observed subsurface temperature by taking into account water flow and refreezing. However, residual saturation in firn must be set to a low value given that water does not percolate uniformly into the cold firn. This may be due to the formation of impermeable ice layers capable of driving water through preferential pathways, leaving some parts of the firn pack dry. This results in an apparent residual saturation much lower than expected. However, the gravity flow approach is meaningless at a daily time scale and the use of a constant velocity flow is recommended instead. Although this water percolation scheme is far from reality, it provides good results for subsurface temperature modeling. The same model could be applied in temperate accumulation zones however it would be necessary to determine how the water drains at the firn/ice transition.

As the climate is expected to change in the future (*IPCC*, 2007), cold glacier temperatures will be modified. The response of subsurface firn temperature to air temperature rise will be largely amplified by an increase in the duration and frequency of melt events. This will lead to strong changes in ice temperature fields. Coupling our surface model with a thermo-mechanical model will make it possible to study the transient response of cold glaciers to climate change and investigate glacier hazards related to thermal regime changes, such as cold hanging glacier stability.

Acknowledgments This study was funded by the AQWA European program (212250). We are grateful to G. Picard for providing the SEB code and we thank Météo-France for providing Lyon Bron air temperature data.

Résumé des résultats principaux et conclusions

La modélisation de l'évolution du régime thermique des glaciers dans un contexte de changement climatique nécessite de contraindre les conditions de surface d'un modèle de régime thermique à partir de variables climatologiques. On a proposé ici une méthode pour établir ces conditions de surface à partir des seules températures atmosphériques journalières. L'étude effectuée sur le site du Col du Dôme valide cette méthode.

L'analyse du bilan énergétique du glacier durant l'été 2012 montre l'impact extrêmement important de la durée des événements de fonte sur le bilan énergétique des zones froides. En effet, on montre que, lorsque la surface du névé atteint son point de fusion (0°C), le bilan énergétique de surface devient très positif. Le fait que la température de surface soit limitée à 0°C par équilibre thermodynamique entre les phases solide et liquide limite l'intensité des flux évacuant de l'énergie. L'intensité du rayonnement infra-rouge réémis est ainsi limitée à $LW_{out} = \sigma T_m^4 = 315$ W m^{-2} (T_m = 273,15 K), la pression partielle en vapeur d'eau à la surface est limitée à la pression partielle saturante à 0°C ce qui limite la sublimation (à cause de la diminution du gradient de pression de vapeur d'eau entre la surface et l'air). L'absorption du rayonnement courte longueur d'onde reste en revanche inchangée voire amplifiée par une diminution de l'albedo due au grossissement des grains soit par la fonte/regel soit par métarmorphisme de la neige humide. Le flux turbulent de chaleur sensible devient encore plus positif avec l'augmentation du gradient de température entre la surface (bloquée à 0°C) et l'air (dont la température est généralement positive pendant les événements de fonte). L'énergie absorbée pendant ces événements est convertie en eau de fonte qui, dans les zones froides, percole et regèle. L'énergie est dans ce cas conservée par le glacier. Dans les zones tempérées ou en zone d'ablation, cette eau de fonte est généralement évacuée (en partie) car l'eau percole complétement le névé tempéré et/ou ruisselle à la surface de la glace généralement imperméable et quitte le glacier, ce qui fait que l'énergie absorbée pendant ces événements n'a pas d'impact sur le bilan énergétique du glacier. On montre en revanche que, à l'échelle journalière, tant que la température de surface reste sous le point de fusion, elle varie de manière similaire à la température de l'air. Dans ce cas, on peut simuler le bilan énergétique du glacier par le forçage de sa température de surface.

A partir de ces conclusions, nous avons proposé de forcer le modèle de régime thermique par deux composantes : (i) la température de surface qui varie similairement à la température de l'air et (ii) un flux d'eau liquide qui simule l'excédent d'énergie absorbée pendant les événements de fonte. Ceci implique que le modèle de régime thermique doit modéliser le transport et le regel éventuels de l'eau. Pour cela, deux approches ont été testées et comparées : (i) la théorie du flux gravitaire dans la neige homogène (*Colbeck and Davidson*, 1973) et (ii) l'utilisation d'une vitesse de percolation constante en prenant en compte la saturation résiduelle de l'eau dans la neige. L'approche (i) est testée au pas de temps semi-horaire avec une fonte calculée par bilan d'énergie. L'approche (ii) est utilisée au pas de temps journalier avec une fonte de surface calculée par un modèle degré jour. On montre que les deux approches permettent une bonne simulation de l'impact thermique de la percolation et du regel de l'eau de fonte de surface. L'échelle journalière offre l'avantage d'utiliser des données météorologiques simples et accessibles sur le long terme (les moyennes journalières des

températures de l'air mesurées à Lyon) et ce pas de temps peut être utilisé pour des simulations du régime thermique sur de longues durées. Les mesures de fonte réalisées sur plusieurs sites avec différentes expositions montrent une bonne corrélation entre la fonte de surface et l'insolation potentielle qui permet de spatialiser la fonte en calculant l'intensité du facteur degré jour comme une fonction de l'insolation potentielle (*Hock*, 1999).

Cette approche est utilisée pour forcer un modèle de régime thermique sur trois sites de forage différents à partir d'une série de température journalière mesurée depuis 1907 sur la station de Lyon-Bron (à environ 200 km à l'ouest du site) afin de reconstituer l'évolution des températures sur une centaine d'années. La comparaison avec plusieurs mesures de profils profonds de température sur chacun des sites permet de valider les simulations à l'échelle du siècle par cette méthode. Nous montrons ainsi que le forçage climatique est bien représenté de cette manière et que la méthode peut être utilisée comme condition de surface pour un modèle de régime thermique fonctionnant au pas de temps journalier. On représente correctement l'impact du climat sur les conditions de surface du glacier. Cela permet d'étudier l'impact climatique sur le régime thermique et dynamique du glacier et donc d'étudier les conséquences des variations climatiques en termes de risque glaciaire.

Chapitre 4

Réponse des zones d'accumulation froides aux variations climatiques : couplage thermomécanique

Introduction

Le régime thermique des zones d'accumulation froides est très sensible aux variations climatiques, notamment lorsque la fréquence et la durée des événements de fonte augmentent. Certaines de ces zones, du fait de leur altitude modérée, peuvent être proches du point de fusion avec des températures faiblement négatives (par exemple de -1°C à -3°C). Dans ce cas, une variation climatique peut, à l'échelle de quelques années ou quelques décennies, faire basculer localement le régime thermique du glacier d'un état froid à un état tempéré. Les conséquences sur la stabilité des glaciers suspendus peuvent être très importantes. L'aléa glaciaire peut être appréhendé grâce à la modélisation de la réponse thermique de ces glaciers à un changement climatique.

Dans le chapitre 3, nous avons développé un modèle de surface permettant de fournir les bonnes conditions aux limites pour forcer un modèle de régime thermique à partir des variations des températures atmosphériques. L'article qui suit présente le couplage du précédent modèle avec un modèle thermomécanique complet appliqué au glacier du col du Dôme en trois dimensions. Ce modèle résout, en régime transitoire, l'évolution de la surface libre, des champs de vitesse et de pression, du champ de densité et du champ d'enthalpie de manière entièrement couplée. Il se base principalement sur les travaux de *Gagliardini and Meyssonnier* (1997), *Lüthi and Funk* (2001) et *Zwinger et al.* (2007) en prenant notamment en compte la rhéologie du névé en fonction de la densité. Ces précédentes études se sont peu intéressées au régime transitoire. En effet, *Gagliardini and Meyssonnier* (1997) font l'hypothèse d'un glacier isotherme à l'état stationnaire. *Zwinger et al.* (2007) résolvent l'équation de la chaleur mais toujours pour un état stationnaire. *Lüthi and Funk* (2001) ont effectué des simulations en régime transitoire sur le site du col Gnifetti (4500 m, massif du Mont Rose, Suisse) mais en utilisant une paramétrisation très simple entre température de surface et température de l'air sans tenir compte de la fonte de surface. Leur modèle était forcé en surface par les variations de températures calculées à partir d'une moyenne glissante sur 9 ans des températures annuelles mesurées à la station météorologique du col du Grand St Bernard. De plus, aucun couplage entre dynamique et thermique n'avait été pris en compte en régime transitoire. Dans l'étude qui suit, le modèle thermomécanique est couplé au modèle de surface présenté au chapitre 3. Le couplage avec le modèle de surface permet alors des simulations en régime transitoire prenant en compte l'impact des événements de fonte et la variabilité spatiale de ces événements. Le couplage entre thermique et dynamique permet d'appréhender l'impact des changements de viscosité dus à

la variabilité du régime thermique sur la géométrie et l'écoulement du glacier en régime transitoire. Afin de simuler correctement la formation de glace tempérée en profondeur, une formulation de l'enthalpie (*Aschwanden et al.*, 2012) pour le transfert d'énergie est implémentée dans le modèle.

La résolution du modèle mathématique est effectuée à l'aide du «solver» de type élément fini Elmer/ice (*Gagliardini et al.*, 2013). Cet outil, développé sur la base du « solver» multi-physique Elmer (http ://www.csc.fi/elmer), permet la résolution d'un certain nombre d'équations différentielles utilisées en glaciologie dont l'équation de Stokes, de transfert de la chaleur, de conservation de la masse et de la surface libre. Dans cette thèse, un module de résolution de la percolation de l'eau liquide et du couplage avec le champ de température (regel) ainsi qu'un module de transfert d'énergie suivant la formulation enthalpique ont été développés. Chaque module résout une équation en faisant éventuellement appel aux variables d'autres modules permettant ainsi de résoudre de manière entièrement couplée le système d'équation du modèle mathématique.

Le modèle est ainsi appliqué au site du Col du Dôme, bien instrumenté depuis presque 20 ans (voir chapitre 2). L'évolution dynamique et thermique du glacier du Col du Dôme est ainsi simulée sur l'ensemble du $20^{ème}$ siècle et dans le futur. Les résultats sont comparés aux mesures de vitesses, de températures et de densité disponibles. Le grand nombre de mesures disponibles au Col du Dôme permet de valider le modèle dans l'objectif de l'appliquer à d'autres glaciers du même type.

Un modèle thermomécanique à trois dimensions pour la simulation du régime thermique des glaciers froids et polythermaux d'altitude en régime transitoire (application au glacier du Col du Dôme)

D'après :

Gilbert, A., O. Gagliardini, C. Vincent, and P. Wagnon (2013c), A 3-D thermal regime model suitable for cold accumulation zones of polythermal mountain glaciers, *J. Geophys. Res.*, in prep

Abstract Analysis of the thermal and mechanical response of high altitude glaciers to climate change is crucial to assess future glacier hazards associated with thermal regime changes. Indeed, the stability of many hanging glaciers in mountainous regions depends on the persistence of a cold basal thermal regime. What will happen in the future in a context of global warming ? We present a new fully thermo-mechanically coupled transient model including enthalpy transport, firn densification, full-Stokes porous flow, free surface evolution, strain heating and surface melt water percolation and refreezing. The model runs at a daily timescale and is forced by daily air temperature data. The mathematical model is solved using the Elmer/ice finite element code and applied to the Col du Dôme area (Mt Blanc range, 4250 m a.s.l., France) where a unique and very complete dataset is available. The results show that the model is capable of reproducing flow characteristic as well as the thermal evolution of the glacier. The strong spatial variability of englacial temperature change observed on the site is well reproduced. This spatial variability is mainly due to the variability of the slope aspect of glacier surfaces and snow accumulation. Results support the use of this model to study the influence of climate change on cold accumulation zones, in particular to estimate where and under what conditions glaciers will become temperate in the future.

4.1 Introduction

The thermal regime of glaciers influences both their dynamics and their hydrology. Indeed, many glacier characteristics such as basal sliding, ice viscosity and liquid water permeability depend on temperature (*Paterson*, 1994). Although the relationship between glacier mass balance and climate has been widely investigated, fewer studies have focused on the response of the thermal regime of glaciers to climate change. This is however a key to understanding dynamical and hydrological changes in glaciers and improving glacier hazard analysis (*Gilbert et al.*, 2012; *Faillettaz et al.*, 2011; *Huggel et al.*, 2004; *Haeberli et al.*, 1989) and the reconstruction of paleoclimatic records (*Gilbert et al.*, 2010; *Gilbert and Vincent*, 2013) (annexe A). Cold accumulation zones are particularly sensitive to climate change due to the influence of surface melting (*Gilbert et al.*, 2013) and the glacier response to these changes is therefore complex. Indeed, glacier velocity, temperature, density and thickness are all linked and form a coupled system. For instance, velocity and temperature interact through the dependence of viscosity on temperature, strain heating and advective energy transport (*Paterson*, 1994). Density and velocity fields are linked through mass conservation and firn rheology, which depends on density (*Gagliardini and Meyssonnier*, 1997). Glacier thickness depends on the velocity field and the surface mass balance. Investigation of the impact of climate change on a cold firn dominated glacier therefore needs to take into account every component of this coupled system.

In this study, we solve this system by coupling a full-Stokes thermo-mechanical model including firn rheology (*Zwinger et al.*, 2007; *Lüthi and Funk*, 2000; *Gagliardini and Meyssonnier*, 1997) to a firn model accounting for surface processes *Gilbert et al.* (2013) in order to establish the surface boundary conditions with respect to climatic changes. This is the first time such a model has been forced by physical surface boundary conditions including melt-water percolation and refreezing processes. Boundary conditions are therefore determined by both surface temperature and liquid water flux. The thermal model is based on the work of *Aschwanden et al.* (2012) using the enthalpy variable instead of temperature. It makes it possible to properly take into account the presence of temperate ice.

The model is then applied to Col du Dôme Glacier, already studied by *Gagliardini and Meyssonnier* (1997). These authors focused only on the flow law for firn along a two dimensional flow line and assumed isothermal conditions. They validated the firn rheology used in the present study by comparing modeled and measured density profiles, surface velocities and firn dating from ice core analysis. *Lüthi and Funk* (2001) extended this work by including thermal model coupling in a study at Col Gnifetti (Swiss Alps). They have shown the importance of taking into account the past thermal history of the rock below the glacier to adequately model heat flux at the glacier base. Transient simulations were carried out assuming a parameterized surface temperature increase and a constant velocity field. They conclude that their model simulates the observed englacial temperature well. In the present study, three mains points are improved to allow reliable modeling of future transient thermal regimes : (i) surface melt water and its spatial variability are included as model inputs, (ii) the transient response of velocity, density, free surface and temperature are solved in a fully coupled manner and (iii) the enthalpy method makes it possible to account for temperate ice

in an energy conservative manner by taking into account water moisture (*Hutter*, 1982). Including melt water as input is essential because the thermal regime of a cold glacier is extremely dependent on surface melt intensity that induces strong spatial variability in firn temperature and non-linear englacial temperature warming in comparison to air temperature rise (*Suter*, 2002; *Gilbert et al.*, 2013).

The next section of this study (section 4.2) describes the model. Section 4.3 presents the application of the model to Col du Dôme (Mt Blanc range, France) and investigates glacier evolution over the 20th century and in the future. In the final section, we discuss the results and model limitations before providing our conclusions and some perspectives for future work.

4.2 Model description

The thermo-mechanical model is mainly based on the work of *Zwinger et al.* (2007), *Lüthi and Funk* (2000, 2001) and *Gagliardini and Meyssonnier* (1997) with two main improvements in the mathematical formulation :(i) Instead of glacier temperature, the enthalpy variable is used (*Aschwanden and Blatter*, 2009) to specifically take into account the temperate ice (at 0°C). (ii) A surface water percolation scheme has been implemented to account for melt water transport and refreezing in firn (*Gilbert et al.*, 2012, 2013), making it possible to carry out reliable transient simulations in cold firn using meteorological data (*Gilbert et al.*, 2013). The enthalpy variable is used to model the appearance of temperate ice in the future according to various climatic scenarios. It makes it possible to study the potential development of a temperate basal layer below cold hanging glaciers for which the current basal temperature is cold but close to the melting point. This issue is crucial to assess the stability of such glaciers and the related hazards.

4.2.1 Field equations

4.2.1.1 Water percolation

Water percolation through the firn is assumed to be uniform and at constant velocity and water saturation S is calculated from the purely advective equation. We define the effective water saturation S^* (*Colbeck and Davidson*, 1973) :

$$S^* = \frac{S - S_r}{1 - S_r} \tag{4.1}$$

where S (dimensionless) is the water saturation in the firn and S_r the irreducible water saturation that is permanently retained by capillary forces. If $S < S_r$, there is no flow of water ($S^* = 0$) and if $S > S_r$, S^* is gravitationally advected according to the following equation :

$$\frac{\partial S^*}{\partial t} + v_w \frac{\partial S^*}{\partial z} = 0 \tag{4.2}$$

where v_w is the water percolation velocity (m s^{-1}). At each time step, the amount of refrozen liquid water is directly taken into account via the water saturation S by removing from S the amount of refreezing water (see section 4.2.2.2).

4.2.1.2 Enthalpy transport

Among polythermal schemes, the main advantages of the enthalpy method is that it describes the Cold-Temperate Transition Surface (CTS) as a set level of the enthalpy variable. No explicit surface representation scheme is required and no a priori restrictions apply to CTS shape (*Aschwanden et al.*, 2012). This makes it possible to take moisture content in temperate ice into account in a relatively simple manner and easily compute it in a numerical model. Enthalpy is calculated as proposed by *Aschwanden et al.* (2012), neglecting heat flux arising from melting point temperature gradient :

$$\rho\left(\frac{\partial H}{\partial t}+\vec{v}\cdot\overrightarrow{\nabla H}\right)=\nabla(\kappa\overrightarrow{\nabla H})+tr(\sigma\dot{\epsilon})+Q_{lat} \tag{4.3}$$

where ρ is firn density (kg m^{-3}), H enthalpy (J kg^{-1}), v the velocity field, κ enthalpy diffusivity (m2), $tr(\sigma\dot{\epsilon})$ strain heating (J m^{-3} s^{-1}) and Q_{lat} (J m^{-3} s^{-1}) a source term coming from melt water refreezing.

4.2.1.3 Stokes equations and mass conservation

Neglecting the acceleration terms in the momentum balance yields the Stokes equations :

$$\nabla\sigma+\rho g=0 \tag{4.4}$$

where σ is the stress tensor (Pa) and g acceleration due to gravity (m s^{-2}). By neglecting densification due to water percolation and refreezing, mass conservation reads :

$$\frac{\partial\rho}{\partial t}+\nabla(\rho\overrightarrow{v})=0 \tag{4.5}$$

The assumption that refreezing water does not significantly influence the density field is only true at very high altitudes where little melt water refreezing occurs. At lower altitudes, densification by percolation and refreezing of melt water is the dominant process (*Vallon et al.*, 1976) and a source term must be added in equation 4.5. This source term is equal to $\frac{Q_{lat}}{L}$ (eq. 4.3) where L is the latent heat of fusion (3.34 10^5 J kg^{-1}).

4.2.1.4 Free surface

The elevation of the free surface is computed by solving :

$$\frac{\partial s}{\partial t}+u\frac{\partial s}{\partial x}+v\frac{\partial s}{\partial y}-v_z=a_\perp \tag{4.6}$$

where $s(x,y,t)$ is the free surface elevation (m), u, v ,v_z are the surface velocity (m yr^{-1}) components on axes x, y and z respectively and $a_\perp$ the surface snow accumulation (m yr^{-1}).

4.2.2 Constitutive equations

4.2.2.1 Flow law

We adopt the flow law for compressible firn described in *Zwinger et al.* (2007), *Lüthi and Funk* (2000) and *Gagliardini and Meyssonnier* (1997). This rheological law expresses the relationship

between the deviatoric parts ($\boldsymbol{\tau} = \sigma - \frac{tr(\sigma)}{3} I$ and $\dot{\boldsymbol{e}} = \dot{\epsilon} - \frac{tr(\dot{\epsilon})}{3} I$) and the isotropic parts (p and $\dot{\epsilon}_m$) of the stress and those of the strain-rate, such as :

$$\boldsymbol{\tau} = \frac{2}{a} B_n^{-1/n} \dot{\epsilon}_D^{(1-n)/n} \dot{\boldsymbol{e}} \tag{4.7}$$

$$\dot{\epsilon}_m = -b B_n \sigma_D^{n-1} p \tag{4.8}$$

where a and b are only functions of the relative density ($D = \frac{\rho}{\rho_{ice}}$), B_n is the fluidity parameter that depends on the temperature ($B_n(T) = 2A(T)$ with $A(T)$ the flow rate factor in the Glen's flow law), n is the Glen's law exponent and $\dot{\epsilon}_D$ and σ_D are invariants for the strain-rate and the stress defined by :

$$\dot{\epsilon}_D^2 = \frac{\gamma_e^2}{a} + \frac{\dot{\epsilon}_m^2}{b}, \quad \gamma_e^2 = 2tr(\dot{\boldsymbol{e}})^2 = 2\dot{e}_{ij}\dot{e}_{ij} \tag{4.9}$$

$$\sigma_D^2 = a\tau^2 + bp^2, \quad \tau^2 = \frac{1}{2}\, tr\, \boldsymbol{\tau}^2 = \frac{1}{2}\tau_{ij}\tau_{ij} \tag{4.10}$$

Factors a and b are calculated using the analytical solution proposed by (*Duva and Crow*, 1994) for high relative densities ($0.81 < D < 1.0$) :

$$a_0(D) = \frac{1 + 2(1-D)/3}{D^{2n/(n+1)}}, \quad b_0(D) = \frac{3}{4}\left(\frac{(1-D)^{1/n}}{n\left(1-(1-D)^{1/n}\right)}\right)^{2n/(n+1)} \tag{4.11}$$

In this way, the limiting case where $D = 1.0$ (ice density) gives $a = 1.0$ and $b = 0.0$ and the previous flow law (eq. 4.7 and 4.8) becomes simply the classical incompressible Glen's flow law. For smaller relative densities, we use the parameterization for a and b proposed by *Zwinger et al.* (2007) that reads :

$$a(D) = \begin{cases} e^{13.22240 - 15.78652D} & \text{if} \quad 0.4 < D < 0.81, \\ \\ a_0(D) & \text{if} \quad 0.81 < D < 1, \end{cases} \tag{4.12}$$

$$b(D) = \begin{cases} e^{15.09371 - 20.46489D} & \text{if} \quad 0.4 < D < 0.81, \\ \\ b_0(D) & \text{if} \quad 0.81 < D < 1, \end{cases} \tag{4.13}$$

This relationship (eq.4.12 and 4.13) gives acceptable results for simulated density profiles and surface velocities at Col du Dôme (see next section). Numerical experiments at Col du Dôme show that the parameterization used by *Lüthi and Funk* (2000) leads to high values of a and b for relative densities less than 0.45, making surface velocities extremely sensitive to surface density and producing excessively fast densification in comparison with measurements. The *Zwinger et al.* (2007) parameterization is therefore recommended.

Flow rate dependence on temperature is calculated using the Arrhenius law with the activation energy and pre-exponential factors values recommended by *Paterson* (1994).

4.2.2.2 Thermodynamic settings

Enthalpy is defined as a function of the water content ω and the temperature T (K) by :

$$\Delta H(T,\omega) = \begin{cases} \int_{T_0}^{T} c_p(T)dT & \text{if} \quad \Delta H < \Delta H_f(p) \\ \\ \int_{T_0}^{T_m(p)} c_p(T)dT + \omega L & \text{if} \quad \Delta H \geq \Delta H_f(p) \end{cases} \tag{4.14}$$

where c_p is the heat capacity (J K^{-1} kg^{-1}), T_0 is the reference temperature for enthalpy (set to 200 K), L the latent heat of fusion (= 3.34 10^5 J kg^{-1}), p the pressure (Pa) and ΔH_f the enthalpy of fusion (J kg^{-1}). ΔH_f is defined from the temperature of fusion T_m (K) according to the Clausius-Clapeyron relationship :

$$T_m = T_f - \beta(p - p_0) \tag{4.15}$$

$$\Delta H_f(p) = \int_{T_f}^{T_m(p)} c_p(T)dT \tag{4.16}$$

where β is the Clausius-Clapeyron constant ($\beta = 9.745610^{-8} KPa^{-1}$), p_0 (Pa) the atmospheric pressure at the surface and T_f (K) the temperature of fusion at pressure p_0. c_p is calculated as a function of temperature (*Paterson*, 1994) :

$$c_p = 152.5 + 7.122\ T \tag{4.17}$$

The enthalpy diffusivity is expressed as :

$$\kappa = \begin{cases} \frac{k(\rho,T)}{C_p(T)} & \text{if} \quad H < H_f(p) \\ \kappa_0 & \text{if} \quad H \geq H_f(p) \end{cases} \tag{4.18}$$

where k is the thermal conductivity and κ_0 the moisture diffusivity in temperate ice. The conductivity is calculated using the relationship proposed by *Calonne et al.* (2011) :

$$k = 2.5\ 10^{-6}\ \rho^2 - 1.23\ 10^{-4}\ \rho + 0.024 \tag{4.19}$$

Temperature dependence on ice conductivity is expressed as (*Paterson*, 1994) :

$$k_{ice} = 9.828e^{-5.710^{-3}\ T} \tag{4.20}$$

It is assumed that the thermal conductivity of firn shows the same temperature dependence, which is taken into account with a multiplicative factor in the equation below.

In the percolation zone ($\rho < 700$ kg m^{-3}), enthalpy is limited to enthalpy of fusion H_f and water content is taken into account by the water saturation term from the percolation equation (eq. 4.1 and 4.2). At each time step, the maximum liquid water that can refreeze (S_{max}) is calculated as :

$$S_{max} = \frac{(H_f - H)\rho}{L\Phi\rho_w} \tag{4.21}$$

where Φ is the porosity and ρ_w the water density (kg m^{-3}). This gives :

$$Q_{lat} = \begin{cases} S\Phi\rho_w L/dt \quad \text{and} \quad S = 0 & \text{if} \quad S < S_{max} \\ S_{max}\Phi\rho_w L/dt \quad \text{and} \quad S = S - S_{max} & \text{if} \quad S > S_{max} \end{cases} \tag{4.22}$$

where dt is the time step.

4.2.3 Boundary conditions

4.2.3.1 Surface

We assume a Dirichlet condition for the enthalpy $H = H(T_s)$ where T_s is the surface temperature and using the same condition for density, i.e. $\rho = \rho_s$ where ρ_s is the surface density. A melt flux fw (kg m^{-2} s^{-1}) is specified to solve the percolation equation (eq. 4.2). The surface is treated as a stress-free boundary for the Stokes equation (eq. 4.4).

4.2.3.2 Bedrock

As pointed out by *Lüthi and Funk* (2001), the thermal state of the rock below the glacier must be taken into account. Rock is therefore included in the model and a basal heat flux f_b (W m^{-2}) is defined several meters below the glacier base. Sliding is neglected at the bedrock interface.

4.2.4 Numerical solution using Elmer/Ice

All these equations have been implemented in the Elmer/Ice finite element code (*Gagliardini et al.*, 2013) based on the Elmer open-source multi-physics package (see http ://www.csc.fi/elmer for details).

4.2.4.1 Steady state simulations

A steady state is calculated using the following method. An initial diagnostic simulation is performed using a constant initial density field and surface elevation, solving the steady state temperature and velocity fields. The initial density field for this first step is estimated as a function of depth using the 1-D densification model of *Herron and Langway Jr* (1980) and the surface elevation is set to the measured DEM. This first diagnostic run is then used as an initial condition for a transient simulation where density, surface elevation and velocity evolve until all variables reach a quasi-equilibrium. This equilibrium is reached after 50 years when both density and free surface no longer change. The time step for this transient simulation is set to one year. The resulting density field and surface elevation are then used to run a new diagnostic simulation (similar to the first one) to obtain a new temperature field. This process is repeated until all variables reach equilibrium (see schema in Fig. 4.1).

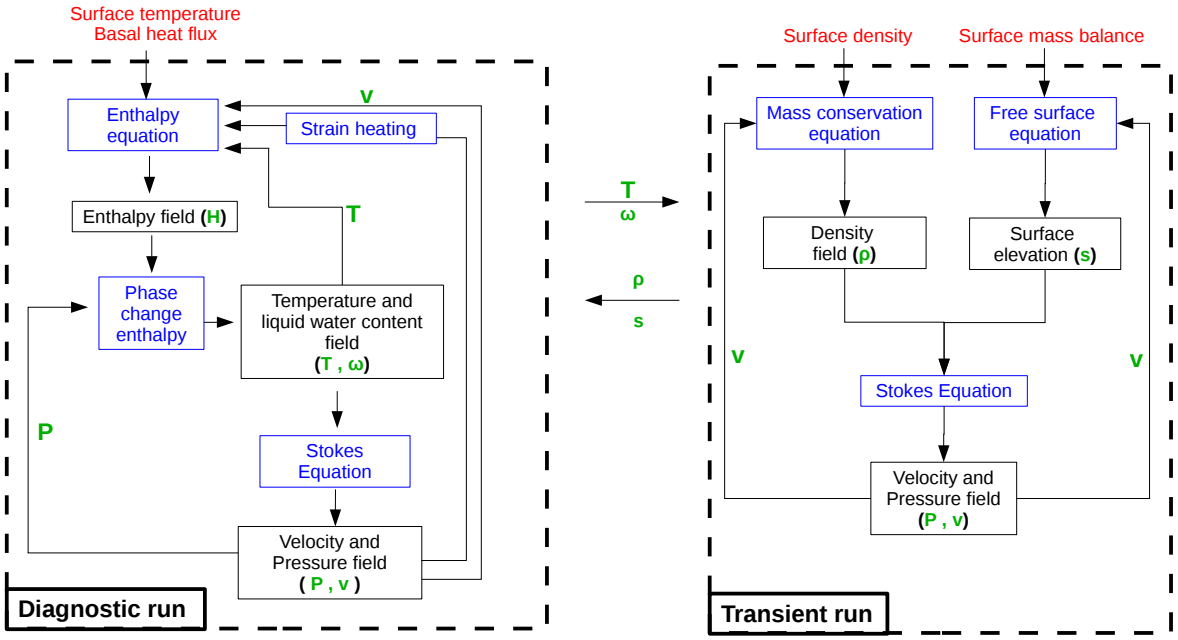

FIGURE 4.1 – Diagram of the steady state solution. In red : steady state boundary condition input. In blue : solved equation. In green : solved variables.

4.2.4.2 Transient simulations

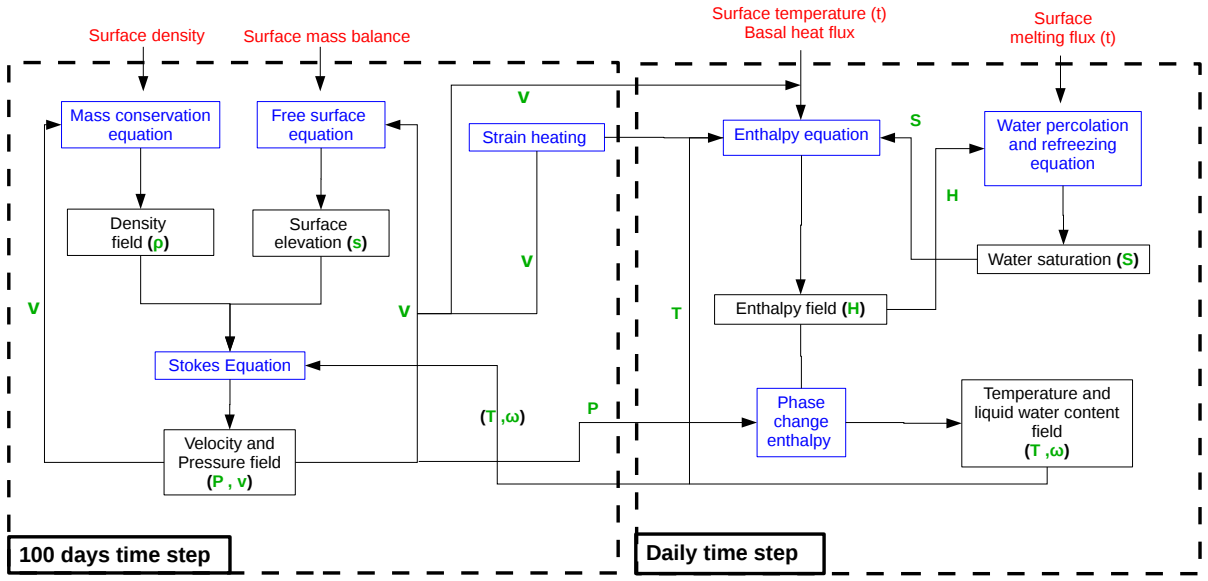

FIGURE 4.2 – Diagram of the transient simulation solution. In red : boundary condition input. In blue : solved equation. In green : solved variables. Note that the only time dependent boundary conditions are the surface temperature and the surface melt flux.

Because of the high computational time-cost of solving the Stokes equation, the velocity field cannot be calculated for a daily time step. Transient simulations therefore use two different time steps, one of 100 days to update the velocity, density and surface elevation and another of one day to calculate water percolation and heat flow (see Fig. 4.2). Each 100 days, the new temperature field is used to calculate a new velocity field and adjust the free surface and density field. Time dependent boundary conditions are the surface temperature and the melt water input, varying on a daily timescale.

4.3 Application : investigation of climate change impact on a cold accumulation zone (Col du Dôme, Mont Blanc area, France)

4.3.1 Studied site

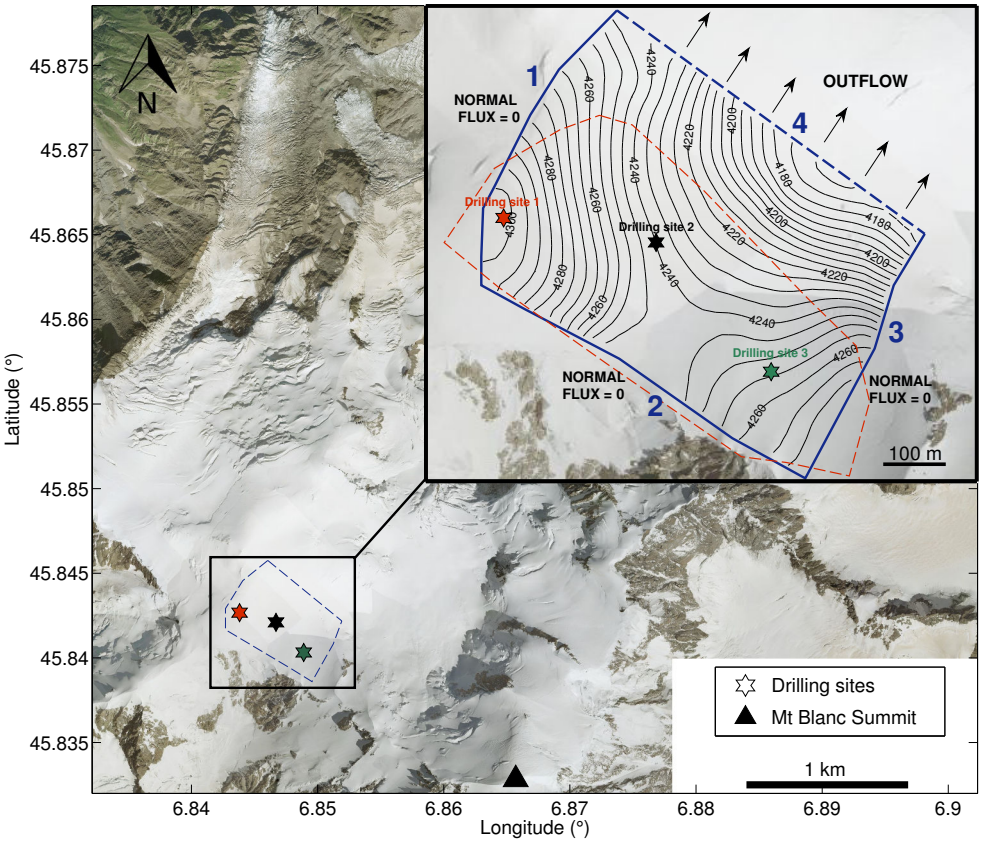

FIGURE 4.3 – Map of the studied area. Stars are the locations of the drilling sites. The blue line of the enlarged inset map is the periphery of the three dimensional model. The red dashed line shows the area of measured bedrock elevations.

The Col du Dôme is a cold accumulation zone located at 4250 m above sea level (a.s.l.) near the Mt Blanc summit (Fig. 3). This site has been instrumented for many years and provides a valuable opportunity to validate our thermo-mechanical model. Indeed, snow accumulation and surface velocities have been monitored since 1994 (*Vincent et al.*, 1997, 2007a) as well as local meteorology

over 3 summers (*Gilbert et al.*, 2013). Several drillings since 1973 have provided englacial temperature and density data at different locations. Moreover radioactive horizons have been determined in these boreholes to provide ice age information (*Gilbert and Vincent*, 2013; *Vincent et al.*, 1997, 2007a; *Preunkert et al.*, 2000). Surface and bedrock Digital Elevation Models (DEMs) have also been determined. The Col du Dôme is thus a suitable site with sufficient available data to calibrate and validate the proposed model in a first step before applying it to other similar glaciers with fewer measurements.

4.3.2 Field data

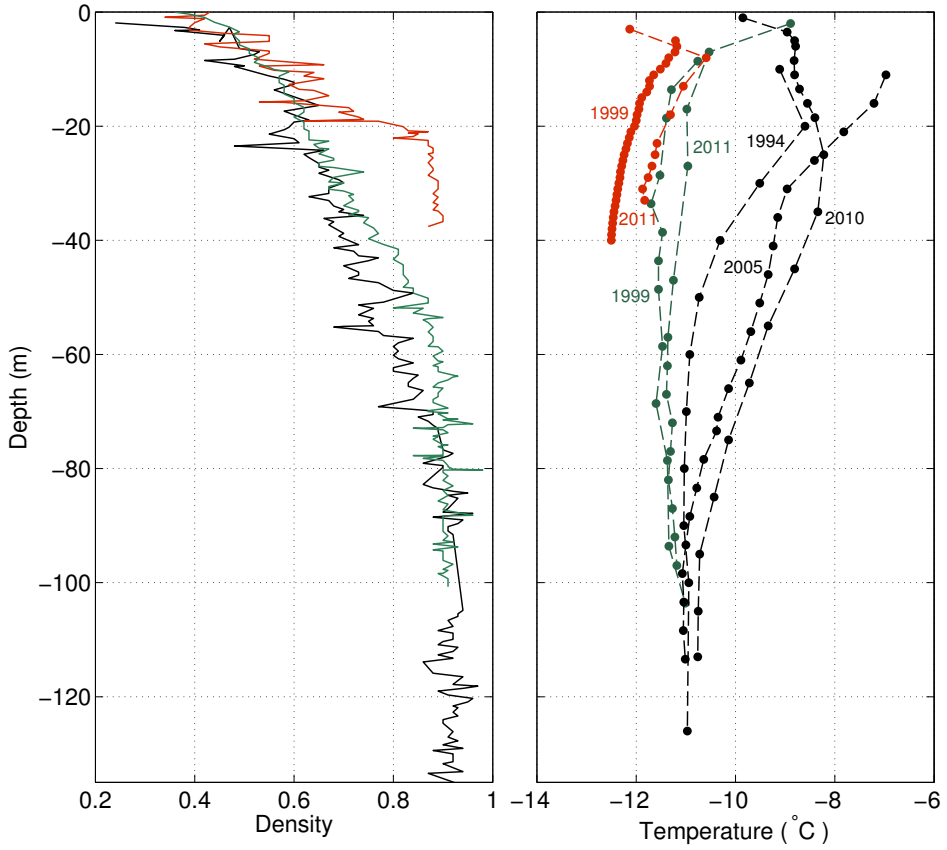

FIGURE 4.4 – Density and temperature measurements at sites 1, 2 and 3 (in red, black and green respectively)

4.3.2.1 Temperature and density

Englacial temperature measurements (Fig. 4.4) were performed from the surface to bedrock in seven boreholes drilled between 1994 and 2011 at three different sites located between 4240 and 4300 m a.s.l. (Fig. 4.3). Ice thicknesses were 40, 126, and 103 m at sites 1, 2, and 3, respectively (see *Gilbert and Vincent* (2013) for more details). Density profiles (Fig. 4.4) were measured along ice cores extracted in 1994 (site 2) and 1999 (sites 1 and 3). Note that the density profile reported for site 2, where temperature was measured, comes from another 140-m drilling performed also in

1994 but 30 m from site 2. Given that the mean surface melt over the period 1907-2012 does not exceed 12 cm w.e. yr^{-1} at Col du Dôme (deduced from our degree day model), densification due to the refreezing of melt water could only have a significant impact on the part of the accumulation area experiencing very low snow accumulation as well as high surface melt. The annual proportion of spatialized mean surface melt compared to yearly snow accumulation does not exceed 5% except along the southern boundary of the modeled area (boundary n° 2 in Fig. 4.3) where the ratio can reach 15 to 20% due to low snow accumulation (Fig. 4.5). This leads to an increase in the near-surface density from < 20 kg m^{-3} to 50 or 80 kg m^{-3} near the southern boundary of our studied area.

4.3.2.2 Velocity fields and DEMs

Surface velocity fields were determined from a stake network surveyed by D-GPS since 1994 (*Vincent et al.*, 2007a). Fig. 5a shows the mean horizontal surface velocity field (over the period 1994-2012) interpolated over the entire stake network. Subsidence velocities (Fig. 4.5b) are calculated by removing the vertical velocities due to slope from the total vertical velocities measured by D-GPS. For a steady state mass balance, subsidence velocities are equal to the mean snow accumulation (*Vincent et al.*, 2007a). Comparison between mean snow accumulation and subsidence velocities confirm that the surface is close to a steady state mass balance (*Vincent et al.*, 2007a) and subsidence velocities can be considered as the mean surface mass balance.

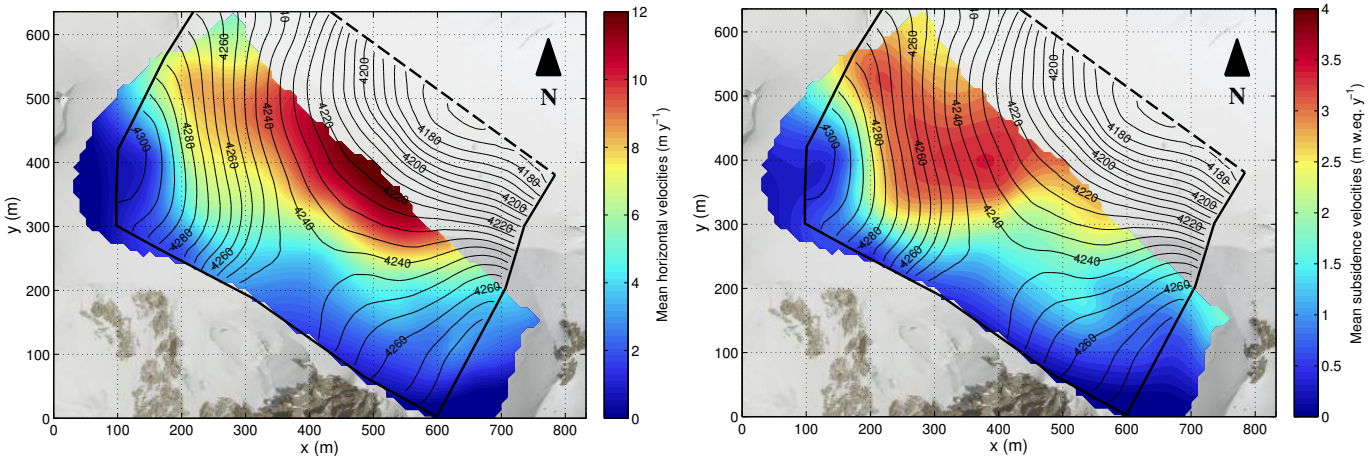

FIGURE 4.5 – Mean measured surface flow velocity fields over the period 1994-2004. Horizontal and subsidence velocities are plotted on the left and right panels respectively.

The surface DEM was measured in 2005 by D-GPS and the bedrock DEM was determined by GPR measurements in 1993 and 1994 (*Vincent et al.*, 1997, 2007a). Bedrock measurements (red dashed line in Fig. 4.3) do not cover the entire modeling zone. Bedrock elevations were therefore extrapolated in the outflow zone (inset in Fig 4.3).

4.3.2.3 Radioactive dating

The radioactive fallout from atmospheric thermonuclear tests (*Picciotto and Wilgain*, 1963), conducted mainly in 1954 and 1961-62, and from the Chernobyl accident in 1986 (*Pourchet et al.*, 1988) provide well-known radioactive levels in glaciers and enable absolute dating. Gamma radioactivity analysis in ice cores drilled in the Col du Dôme has been used to locate these events and date the corresponding ice core levels (*Pinglot and Pourchet*, 1995). Dating was carried out on the 1994 ice core from site 2 and the 1999 ice core from site 3.

4.3.2.4 Meteorological data

Daily maximum and minimum air temperatures used to perform transient simulations on the glacier come from the Lyon-Bron meteorological station located 200 km west of the glacier. These data are available from 1907 to present and are well correlated with air temperature variations at Col du Dôme (*Gilbert and Vincent*, 2013).

Future climatic scenarios come from the ENSEMBLES climate scenario database (www.ensembles-eu.org) (*Van der Linden and Mitchell*, 2009). Climate scenarios were produced by Regional Climate Models (RCM) forced by Global Circulation Models (GCM) using the A1B scenario (*Nakicenovic and 26 others*, 2000). For our study, a 100-yr time series (1951–2050) for daily mean, minimum and maximum air temperatures was produced. As regional climate models are known to suffer from systematic errors, an empirical-statistical error correction method (quantile mapping (*Themessl et al.*, 2011)) was applied over a 29-year calibration period (1981–2009) to adjust regional model results to local-scale observations. Daily observational data from the Col du Grand Saint Bernard meteorological station located at 2469 m a.s.l. and 50 km east of the glacier were used to adjust the regional model. From the final transient time series, three were selected for the present study (with the short label used hereafter in brackets) : CNRM-RM5.1_ARPEGE (ARPEGE), METNOHIRHAM_HadCM3Q0 (HadCM3Q0) and MPI-M-REMO_ECHAM5 (ECHAM5).

4.3.3 Model settings

4.3.3.1 Geometry and meshing

Surface elevation contour for meshing are shown in the inset in Fig. 4.3 and follow the glacier flow lines except for the front (dashed line in the inset in Fig. 4.3) and the south-east part of the periphery (limit n°2 and 3 in Fig. 4.3). A three dimensional mesh is obtained by extrusion of an unstructured triangular 2D mesh (Fig. 4.6, 50 m resolution) and has 4515 nodes and 35 vertical layers. This makes it possible to obtain aligned nodes in the vertical dimension, which is specifically required to solve the water percolation equation. The mesh is refined up to 50 cm along the vertical axis close to the surface to solve the heat and water percolation equations on a daily time scale (see Fig. 4.6).

4.3.3.2 Boundary conditions

Our domain is delimited by 5 boundaries which are the glacier surface, the lateral boundaries, the outflow limit, the bedrock interface and the rock base (Fig. 4.3 inset and Fig. 4.6).

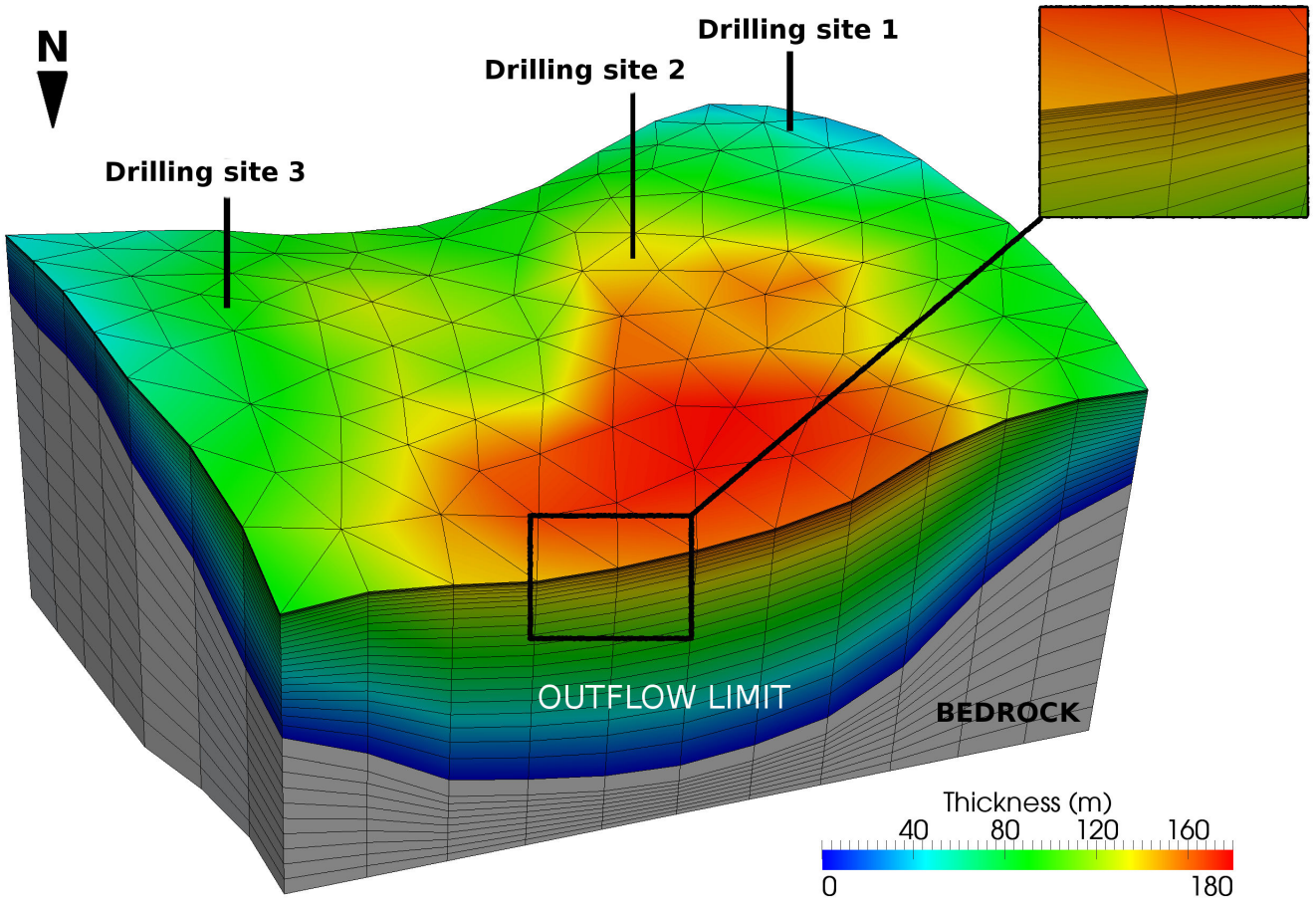

FIGURE 4.6 – Glacier topography and mesh used in the 3D model. The three drilling sites from Fig. 4.3 are shown. Ice and firn are shown in color and bedrock in gray.

Outflow and lateral limits The outflow limit is shown in Fig. 4.3 and Fig. 4.6. The boundary condition for the Stokes equation is given as a pressure set to the hydro-static pressure. A zero-flux boundary condition is assumed for the other equations on the outflow boundary. Given that lateral boundary n° 1 is perpendicular to the elevation contours (Fig 4.3) and the horizontal velocity is very close to zero (< 3 m yr^{-1}) on boundaries n° 2 and 3 (Fig. 4.5), a zero-flux boundary condition is assumed for all equations on these boundaries. However, temperature simulations show that lateral boundary n° 1 near the drilling site 1 seems to be influenced by a negative lateral heat flux coming from the north-facing side of Dôme du Goûter. Indeed, during transient simulations, a comparison with temperature measurements in the deeper part of borehole n° 1 shows that englacial temperature seems to be influenced by excessively strong bedrock warming although surface temperature is well modeled. We therefore introduce a negative heat flux, called Flat (set to -10.0 10^{-3} W m^{-2}) , as a boundary condition on this side (throughout the whole thickness). This flux influences only the temperature field close to boundary n° 1.

Surface and basal conditions At the surface, steady state simulations assume a constant density and enthalpy (as a function of surface temperature) set as Dirichlet conditions for mass conser-

vation (eq. 4.5) and enthalpy equation (eq. 4.3). A free surface condition is used for the Stokes equation (eq. 4.4). Spatial variability of the surface temperature is calculated using :

$$T_s(x,y) = T_{steady} - g_T(x,y) \times (z(x,y) - z_0) \tag{4.23}$$

where (x,y) are horizontal coordinates, $T_s(x,y)$ the surface temperature, T_{steady} the steady state temperature at the altitude z_0, $z(x,y)$ the surface elevation and g_T(x,y) the local lapse rate defining the gradient between air temperature at altitude z_0 and surface temperature at Col du Dôme. T_{steady} is set to 11.4°C (mean air temperature recorded at Lyon-Bron meteorological station over the period 1907-1917) and z_0 is set to 200 m a.s.l. (altitude of Lyon-Bron station). *Gilbert et al.* (2013) found that g_T is equal to 5.95, 5.70 and 5.83 10^{-3} K m^{-1} at sites 1, 2 and 3 respectively. Assuming that these values may depend on mean local wind speed which is the main driver controlling local snow accumulation, g_T was correlated to mean snow accumulation using measured accumulations at the three drilling sites. The obtained linear relationship between mean snow accumulation and g_T (R^2 = 0.97, n = 3) was used to extrapolate g_T over the entire studied area. Assuming that the glacier surface remained approximately unchanged over the last century (*Vincent et al.*, 2007a), the surface mass balance is set to the measured subsidence velocities to solve the free surface equation. The surface mass balance is set to the modeled steady state subsidence velocities using the measured surface elevation where no measurements are available.

For transient simulations, only the enthalpy and water percolation equations have time dependent boundary conditions. Surface temperature is variable as a function of time :

$$T_s(x,y,t) = T_{air}(t) - g_T(x,y) \times (z(x,y) - z_0) \tag{4.24}$$

where T_{air} (t) is the daily mean air temperature measured at altitude z_0. Liquid water input comes from a melt water flux calculated according to *Gilbert et al.* (2013) using a degree-day model :

$$M(x,y,t) = \begin{cases} (T_{max}(x,y,t) - T_0)\ m_f(x,y) & \text{if} \quad T_{max}(x,y,t) > T_0 \\ \\ 0 & \text{if} \quad T_{max}(x,y,t) \leq T_0 \end{cases} \tag{4.25}$$

where M is the daily amount of surface melt (m w. e. d^{-1}), m_f (x,y) the melt factor (m w. e. d^{-1} K^{-1}) , T_0 the temperature of fusion (273.15 K) and T_{max} the daily maximum temperature. The melt factor m_f is calculated as a function of potential solar radiation using the relationship given by *Gilbert et al.* (2013). Daily maximum temperature T_{max} (x,y,t) is calculated using equation 4.24.

A constant basal heat flux is specified at the base of the rock domain. The heat flux is set to 1.5 10^{-2} W m^{-2} in order to match the measured basal temperature at the three drilling sites. No sliding condition is assumed at the bedrock interface.

4.3.3.3 Thermal regime in the bedrock

The enthalpy equation is solved in the whole domain including the rock. In order to avoid a discontinuity of the enthalpy field due to a discontinuity in the heat capacity, we use the heat

capacity of ice for the rock. We compensate for this by using an "apparent" density ρ_a for the rock set to :

$$\rho_a = \frac{\rho_{rock}\ c_{prock}}{c_p} \tag{4.26}$$

where ρ_{rock} and $c_{p_{rock}}$ are respectively the density and heat capacity of rock. Diffusivity κ_{rock} is set to :

$$\kappa_{rock} = \frac{k_{rock}}{c_p} \tag{4.27}$$

The thermal properties of the rock (gneiss and granite) are not well known. We use a thermal conductivity krock of 3.2 W m^{-1} K^{-1}, a heat capacity Cprock of 7.5 10^2 J kg^{-1} K^{-1} and a density of 2.8 10^3 kg m^{-3} as proposed by *Lüthi and Funk* (2001) at Col Gnifetti. The resulting bedrock temperature is then used as a Dirichlet condition to solve a purely diffusive heat equation in the rock and obtain the temperature field in the rock.

4.3.4 Results

4.3.4.1 Steady state simulation

This subsection present the results obtained for steady state run following the method described in section 4.2.4.1.

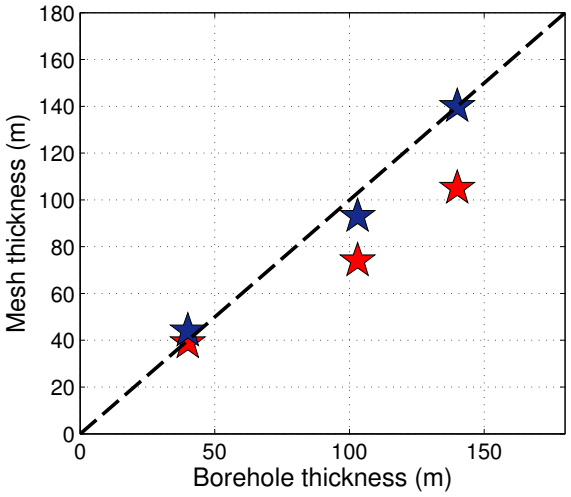

FIGURE 4.7 – Comparison between measured glacier thickness in the three boreholes (borehole thickness) and the mesh thickness in the model before (red stars) and after (blue stars) the bedrock correction assuming an unchanged surface elevation.

Free surface For given surface and bedrock topography, modeled subsidence velocities in a steady state simulation indicate the required accumulation to maintain constant geometry. However, the bedrock topography is not known as accurately as the surface topography or the accumulation. Therefore, the bedrock topography is adjusted iteratively so that the accumulation obtained to

keep the surface geometry constant matches the observed accumulation. As shown in Fig. 4.7, the modified glacier thickness is in better agreement with borehole measurements than was the initial measured thickness. This new bedrock DEM will be used for all the following applications.

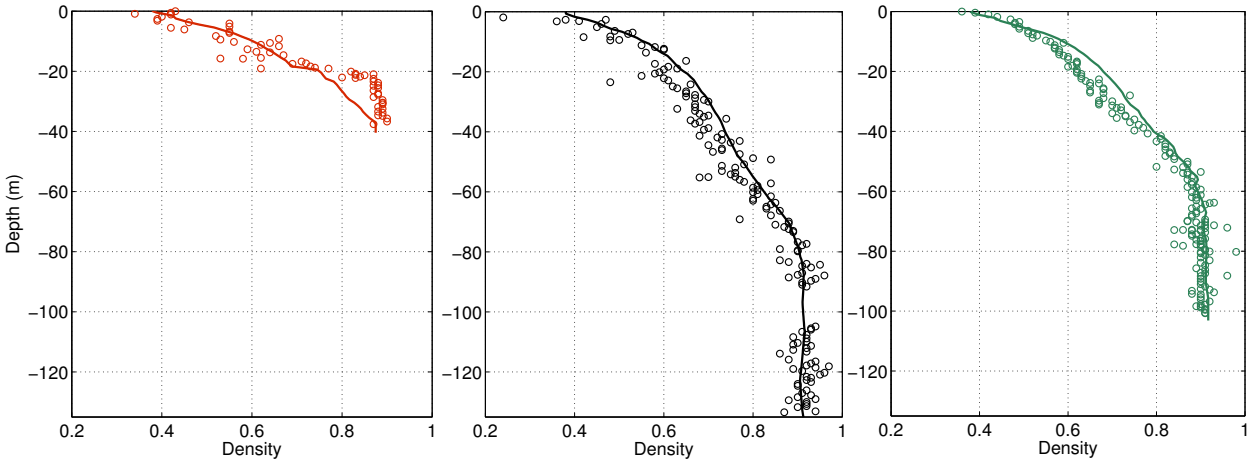

FIGURE 4.8 – Measured (circles) and modeled (lines) firn density at drilling site 1, 2 and 3 (from left to right respectively)

Density and velocity fields Starting from the diagnostic run using parameterized density fields (see section 4.2.4.1), a steady state for density and velocity fields was reached after 50 years. Results are shown in Fig.4.8 and 4.9. Comparisons between measured and modeled density profiles at the three drilling site show good agreement. This confirms that the rheology of firn is adequately taken into account by the firn rheological model as already noted by *Lüthi and Funk* (2000) and *Gagliardini and Meyssonnier* (1997). Parameterization of a and b as a function of the relative density proposed by *Zwinger et al.* (2007) seems to give satisfactory results for the snow and firn conditions prevailing at Col du Dôme.

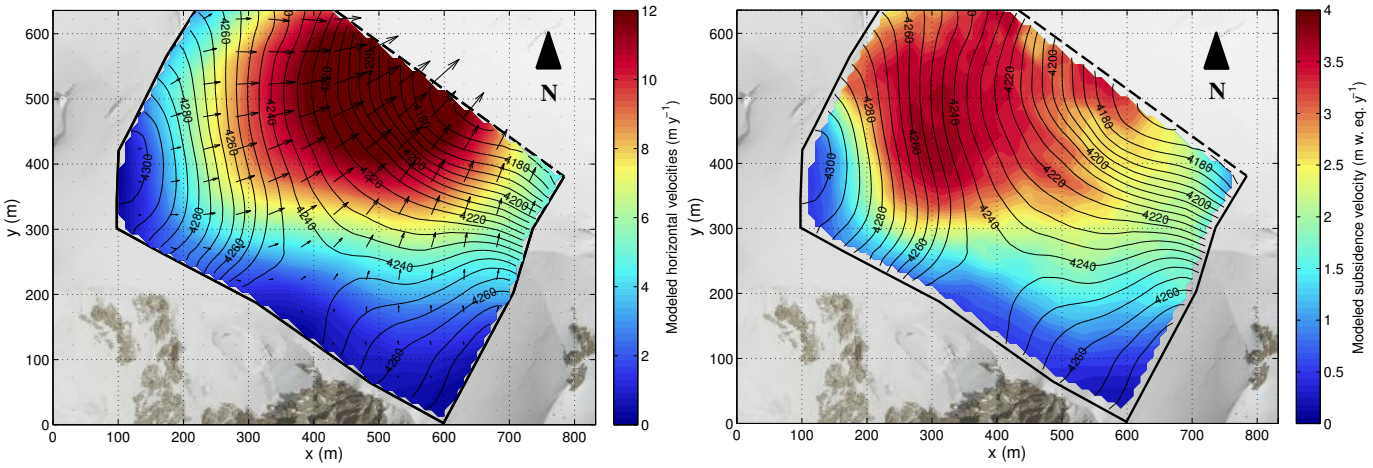

FIGURE 4.9 – Modeled surface flow velocities. Horizontal and subsidence velocities are plotted on the left and right panels respectively.

Modeled subsidence velocities are in good agreement with the measurements because the free surface has been adjusted accordingly. However, the fact that modeled glacier thicknesses are consistent with measured thicknesses at the drilling sites corroborates the modeled subsidence velocities. Comparison between measured and modeled horizontal surface velocities reveals a mean difference of – 0.71 m yr^{-1} with a standard deviation of 1 m yr^{-1}, also supporting the model. Consistency between modeled and measured firn dating at sites 2 and 3 (Fig. 4.10) confirms the validity of the modeled three-dimensional velocity field.

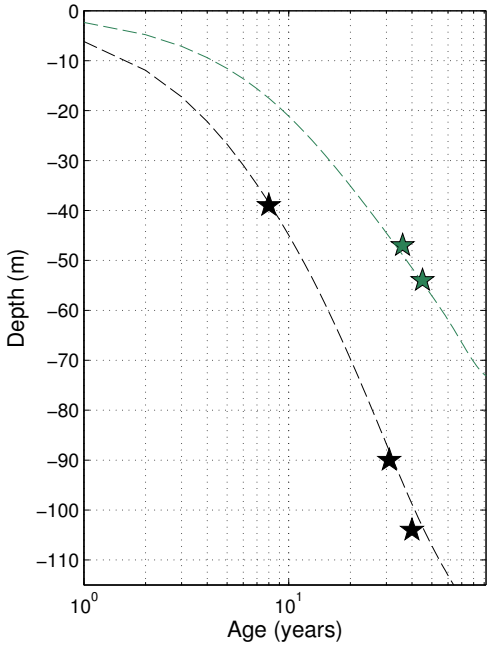

FIGURE 4.10 – Modeled depth/age relationship at site 2 (black dashed line) and site 3 (green dashed line) compared to radioactive dating (black and green stars respectively). X-axis in log-scale.

Strain heating influence In order to assess the influence of strain heating on the temperature field, we performed two steady state simulations taking and not taking into account strain heating. Temperature differences between the two simulations are shown in Fig. 4.11 and reveal that strain heating is far from negligible, inducing temperature warming greater than 1°C at some locations. However strain heating is localized at the bottom of the glacier and numerical experiments show that it can be taken into account by artificially increasing the basal heat flux (from 15 10^{-3} to 30 10^{-3} W m^{-2} here). This explains the stronger basal heat flux inferred by *Gilbert and Vincent* (2013) using one-dimensional heat flow simulation and neglecting strain heating. Heat production from strain heating is estimated to be between 1 10^{-3} and 5 10^{-3} W m^{-3} at the bottom of the glacier.

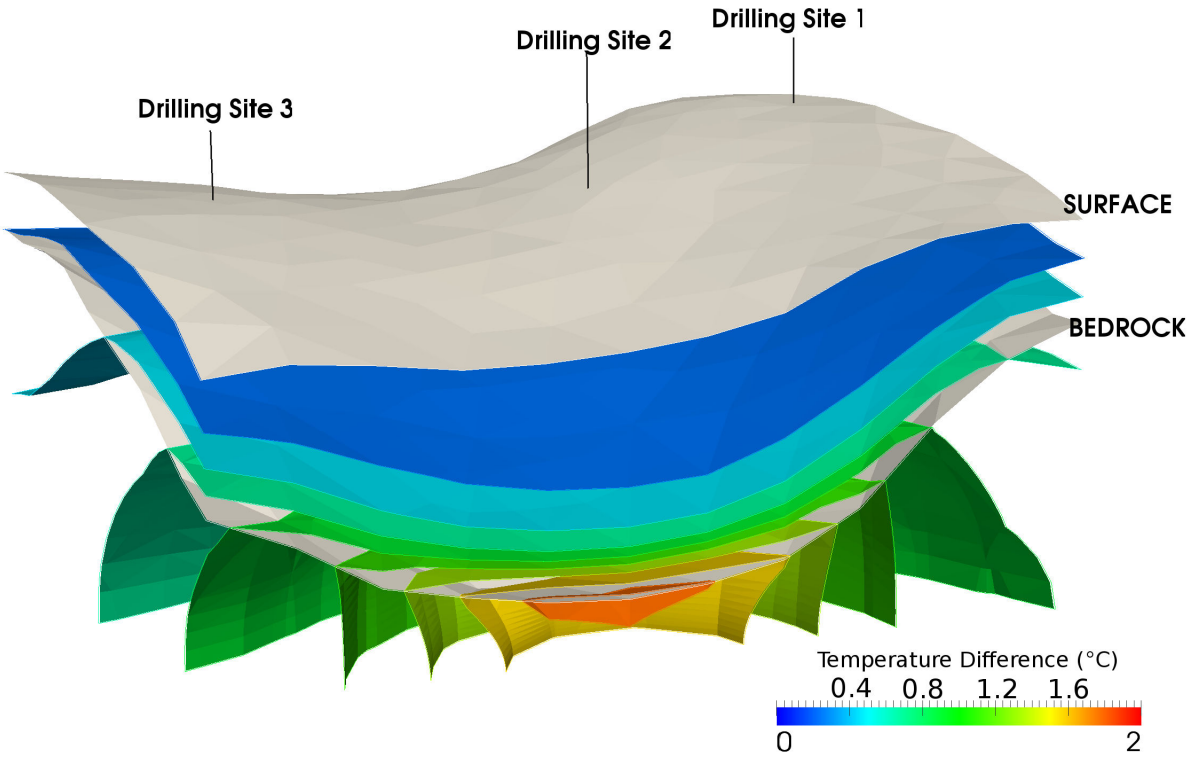

FIGURE 4.11 – Iso-temperature-difference between two steady state simulations taking and not taking strain heating into account.

4.3.4.2 Transient simulation from 1907 to 2012

We assume that at the beginning of the 20th century, the thermal regime at Col du Dôme was close to equilibrium (*Gilbert and Vincent*, 2013). We therefore used the previous calculated steady state as the initial condition for transient modeling. The surface mass balance is assumed to be constant after this date (*Vincent et al.*, 2007a) and we use the same surface mass as used for steady state calculations.

Temperature change over the last century Transient simulations have been performed over the period 1907-2012 for a daily time step with updating of the density, velocity and free surface every 100 days (see section 4.2.4.2). Melting occurs each summer as a result of supplementary energy input (*Gilbert et al.*, 2013) and produces melt water percolation and refreezing. These phenomena are taken into account in the model to simulate water inside firn every summer. Water percolates one to four meters deep each summer depending on the amount of melt water. This is in agreement with on-site percolation events already observed by *Gilbert et al.* (2013) during summer 2012.

Results are in good agreement with measured temperature profiles at each date and site (Fig. 4.12). It highlights the strong spatial variability of englacial temperature response to climate change (see Fig. 4.13). This variability is due to different flow patterns and slope aspects of the surface that induce surface melt spatial variability. So far, the bedrock temperature has been almost unaffected by climate warming except in areas of low glacier thickness such as on Dôme du Goûter summit

in the Mt Blanc range (temperature increase of 1°C) or in areas experiencing strong vertical flow advection where basal temperature increased by 0.5°C.

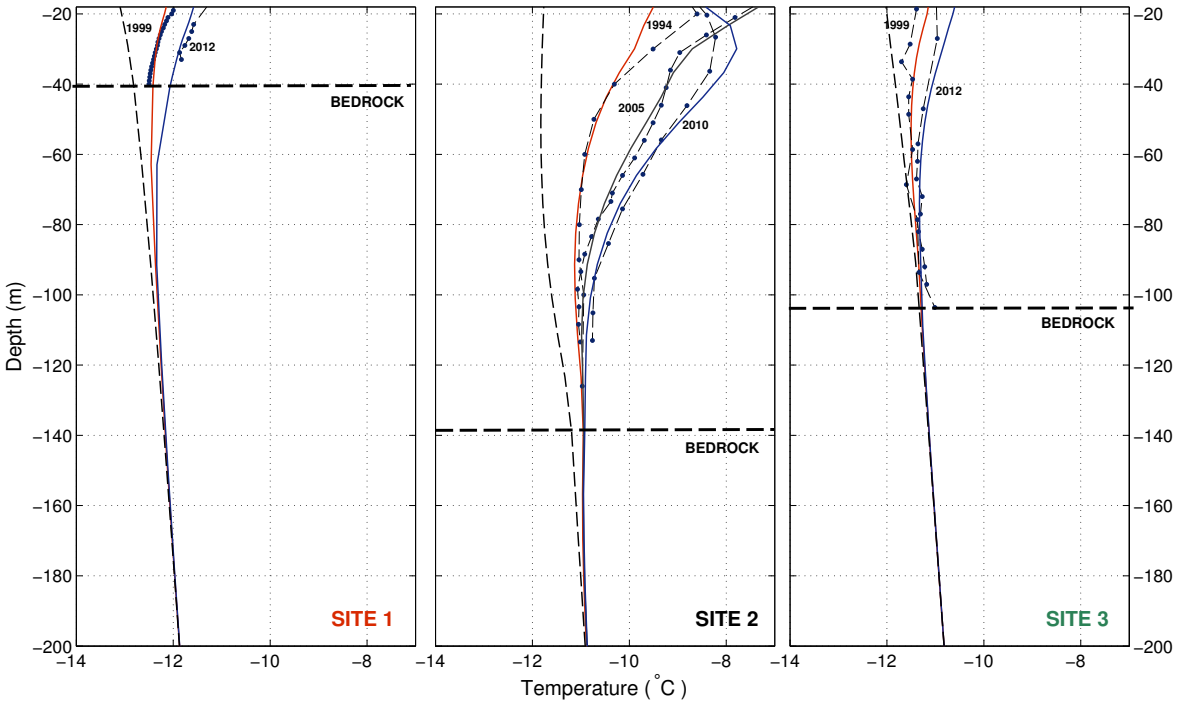

FIGURE 4.12 – Modeled (blue lines) and measured (black dots) temperature profiles at drilling sites 1, 2 and 3 for the different dates indicated in the figure. The modeled steady state profile is shown in blue dashed line.

4.3.4.3 Simulations with future climatic scenarios (until 2050)

To investigate future thermal regime changes at Col du Dôme, we performed three transient simulations using the different climatic scenarios described in section 4.3.2.4. The resulting future daily air temperatures are then used to force our model between 2013 and 2050 (see Fig. 4.14). Future temperatures were adjusted to Lyon-Bron temperature so that the mean Lyon temperature for 2012

Temperature changes Expected englacial temperature changes at site 2 for the three scenarios are plotted in Fig. 4.15. Fig. 4.16 shows temperature changes between today and 2050 below a depth of 40 m over the entire modeled domain. The three scenarios give similar results and show that the temperature at a depth of 40 m will reach -6°C to -5°C by 2050 at site 2. However, basal temperature rises slowly and will not exceed -10°C until 2050.

Stronger englacial warming is localized where ice/firn flow is the fastest because surface temperature anomalies can be quickly advected deep inside the glacier. Warming in this part could reach 2°C (yellow and orange iso-surface in Fig. 4.16) below a depth of 40 m whereas it is not expected to exceed 1°C around site 3.

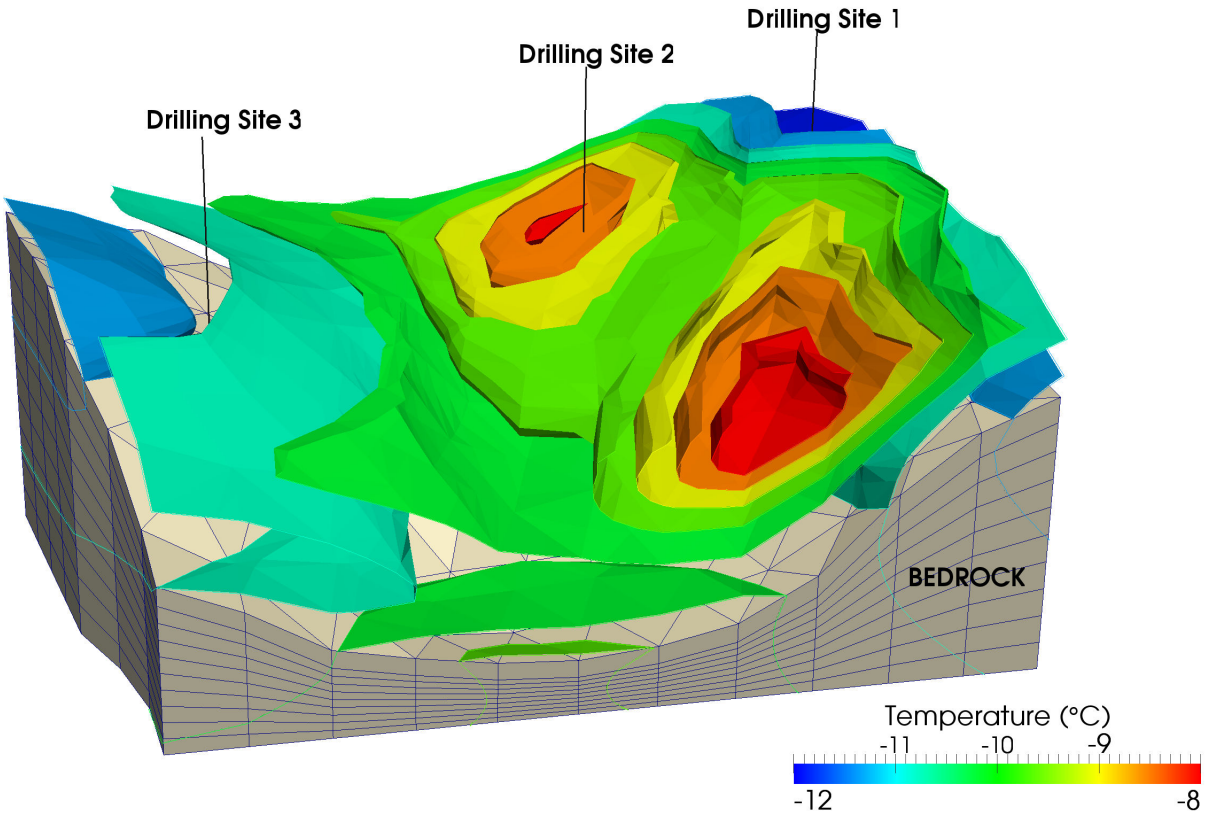

FIGURE 4.13 – Isothermal surfaces modeled in 2012 from transient simulation performed between 1907 and 2012.

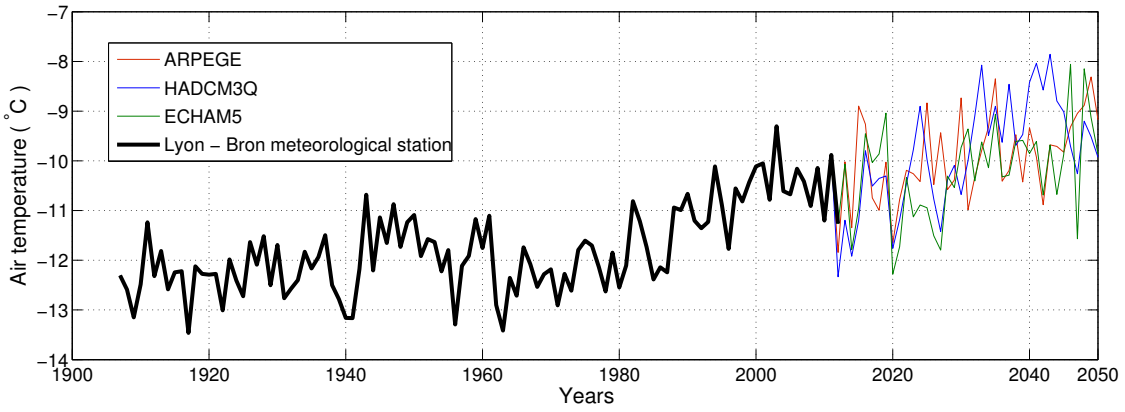

FIGURE 4.14 – Annual mean air temperature from Lyon-Bron meteorological station extrapolated to Col du Dôme (black thick line) and future climatic scenarios (see section 4.3.2.4).

Surface elevation, density and velocity field changes As mentioned in the introduction, temperature, velocity, density fields and glacier thicknesses are coupled. We use the simulation with the ARPEGE climatic scenario to compare surface velocity, glacier thickness and density changes between 1980 and 2050 (Fig. 4.17 and 4.18). These results reveal that decreasing ice viscosity due to increasing englacial temperature has an impact on the flow velocity (Fig. 4.17). This effect is however partially compensated by a density increase and a glacier thickness decrease (Fig. 4.18)

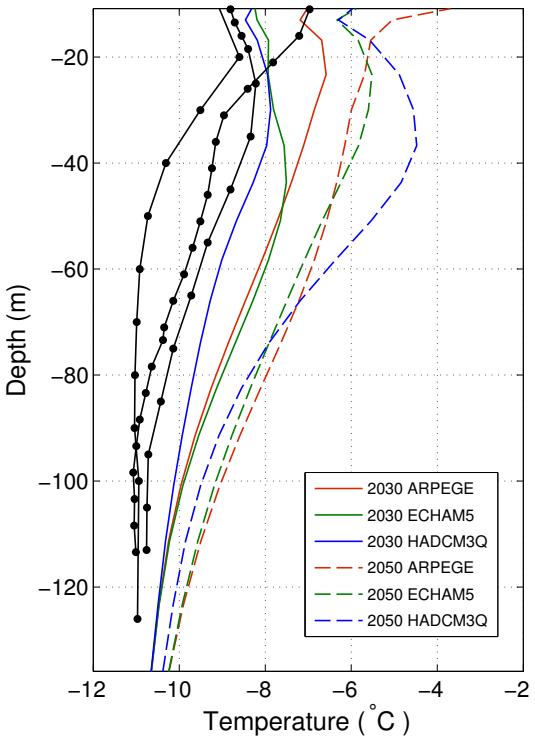

FIGURE 4.15 – Measured temperature profiles in 1994, 2005 and 2010 and modeled future temperature profiles in 2030 and 2050 at site 2 for the different climatic scenarios. Black lines with dots refer to measured temperature profiles (see Fig. 4.13 caption for dates)

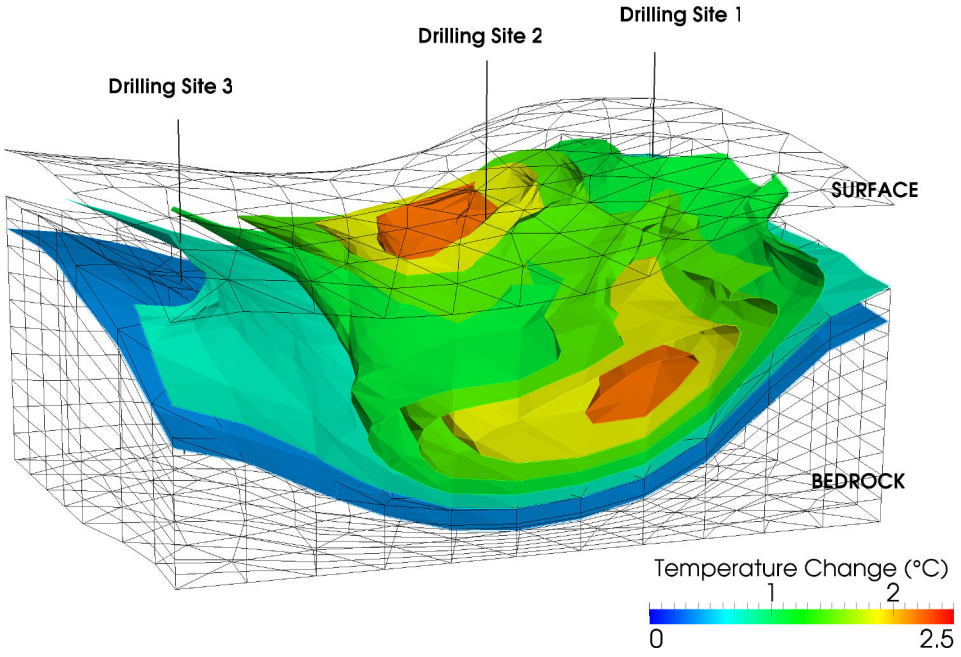

FIGURE 4.16 – Modeled temperature changes between 2012 and 2050 below a depth of 40 m for the ARPEGE climatic scenario.

that both tend to reduce glacier flow. The surface velocity increase is estimated to be 12 to 15% in the zone the most impacted by temperature change. This represents a velocity increase that does not exceed 1 to 2 m yr^{-1}, which is difficult to detect by direct measurements. However, surface elevation variations associated with these changes are expected to reach 8 to 15 m and could be measured using a D-GPS survey of the zone. A yearly fine surveillance of the surface topography could provide a suitable indicator of englacial warming in cold accumulation zones if the mean surface balance can be considered constant (which is the case at Col du Dôme since 1900 (*Vincent et al.*, 2007a)). However, inter-annual variability of the snow accumulation introduces strong surface elevation inter-annual variability. Glacier thickness simulations performed by taking into account a surface accumulation variability reconstructed using precipitation records in the valley (see section 3.2.4.) is shown at site 2 by the dashed green line in Fig. 18 (bottom panel). It reveals that surface elevation changes due to snow accumulation inter-annual variability amount to about 5 to 8 meters at site 2. Very long term elevation measurements (up to 40 years) are therefore needed to identify a surface elevation trend related to englacial temperature warming.

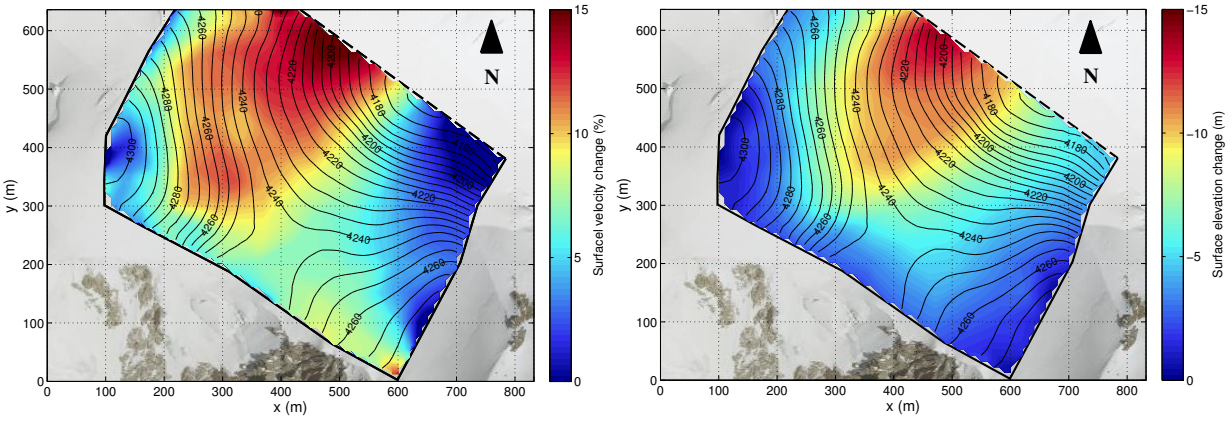

FIGURE 4.17 – Expected horizontal velocity (left panel) and surface elevation changes (right panel) between 1980 and 2050 due to englacial temperature warming modeled using the ARPEGE climatic scenario.

4.4 Conclusions and perspectives

In this study, we introduce a new three dimensional polythermal glacier thermal regime model especially adapted to transient simulation in cold accumulation zones of mountain glaciers. The model were constructed using the conclusions of previous studies that showed the importance of taking into account firn rheology (*Gagliardini and Meyssonnier*, 1997; *Lüthi and Funk*, 2000, 2001; *Zwinger et al.*, 2007), bedrock thermal regime (*Lüthi and Funk*, 2001) and water content in the temperate ice (*Hutter*, 1982; *Aschwanden et al.*, 2012; *Wilson and Flowers*, 2013). It therefore includes enthalpy transport, firn densification, full-Stokes porous flow, free surface evolution and strain heating. However, as pointed out by *Lüthi and Funk* (2001) and *Zwinger et al.* (2007), surface boundary conditions were poorly determined and it was largely unclear how climate forcing could

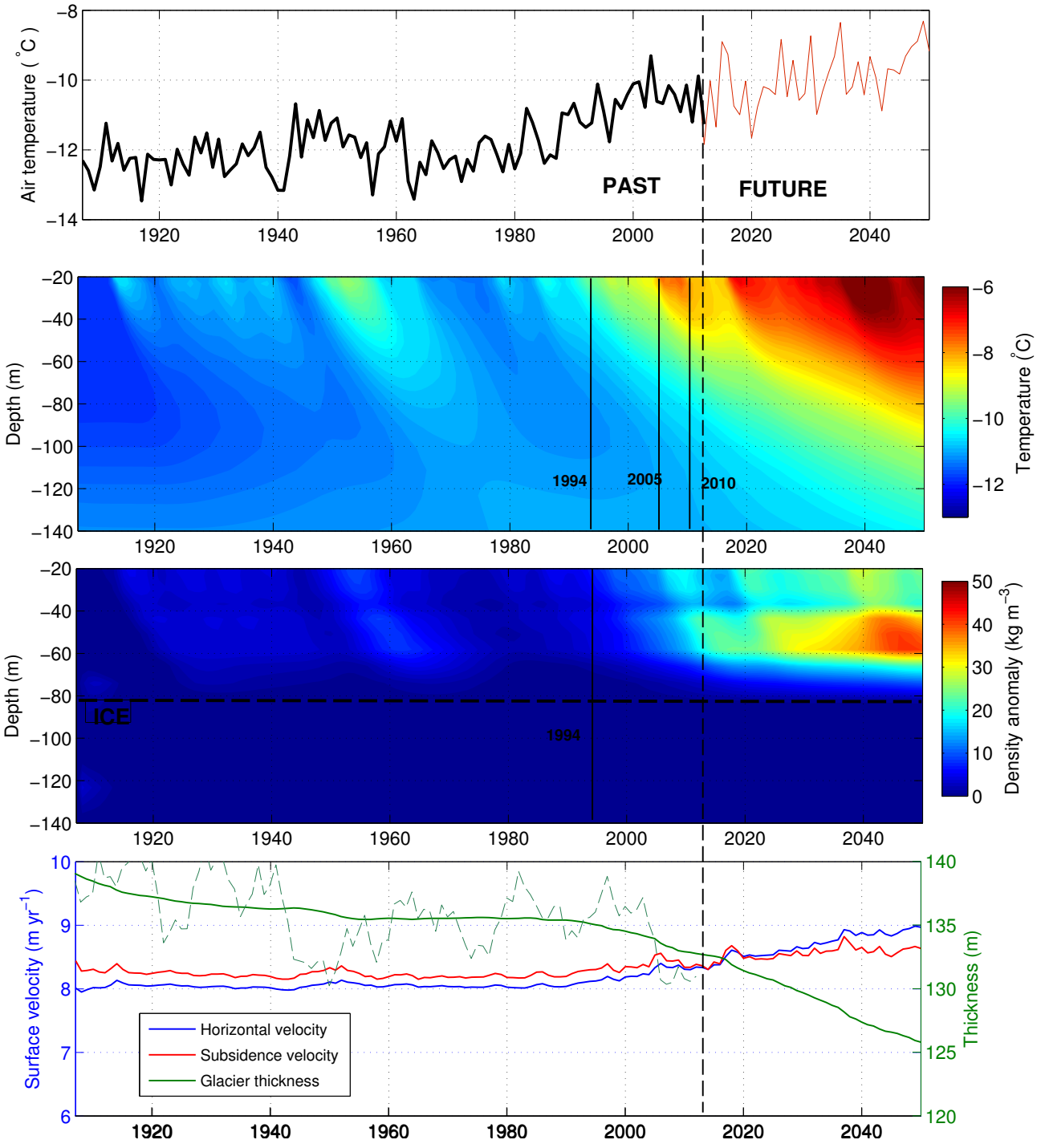

FIGURE 4.18 – Air temperature, englacial temperature, density, surface velocity and thickness evolution modeled from 1907 to 2050 at site 2 using the ARPEGE climatic scenario for the period 2012-2050. Borehole measurements are indicated by black lines. The vertical dashed line shows the transition between the past and the future with respect to the simulation. In the bottom panel, the green dashed line shows the evolution of modeled glacier thickness taking into account the inter-annual variability of snow accumulation.

be used as input to a thermal regime model. The main improvement of our model is the use of physically addressed surface boundary conditions in order to use climate forcing as input to the transient model. Using the formulation developed by *Gilbert et al.* (2013), climatic forcing is inferred from daily air temperature to provide surface temperature and melt water input to the thermal regime model that also includes water percolation and refreezing processes. For the first time, the response of glaciers to climate change is totally physically addressed by coupling temperature, density, flow velocity and free surface elevation in transient simulations.

The model was successfully applied to simulate the response of Col du Dôme glacier to climatic changes. This glacier constitutes a very good validation site due to a rare and very complete dataset that includes surface velocities, ice core dating, deep borehole temperatures and density profiles and radar measurements. In this way, thermal regime variations over the past 100 years and for the coming 40 years were reconstructed in 3D. This application has demonstrated the importance of taking into account the surface melt spatial variability and strain heating. It has also revealed the strong spatial variability of englacial temperature change that can be observed over short distances (several tenths of meters) in a glacier with various slopes aspects and strongly spatially variable snow accumulation. Future climatic scenarios until 2050 show that Col du Dôme will stay entirely cold although some parts of the glacier below a depth of 40 m could experience a 3°C temperature rise. The glacier flow response to englacial temperature warming is partially compensated by increasing density and decreasing glacier thickness, assuming an unchanged mass balance. Impact on glacier flow is therefore estimated to be low with a surface velocity increase of less than 15%, which will be hard to detect by a GPS survey. Expected surface elevation changes associated with englacial temperature warming could reach 8 to 15 m, which is not very significant compared to the surface elevation inter-annual variability that could reach 5-8 m as estimated in this study.

This model will provide a valuable tool to study how cold glaciers will warm in the future. This is essential to assess future stability of cold hanging glaciers that is clearly linked to their basal thermal regime (*Faillettaz et al.*, 2011). This kind of glacier is quite common in the Alps (e.g. Taconnaz glacier, South Face of Grande Jorasses, Weisshorn, Atels glacier) and represents a true glacial hazard. For example, in 1965, a major part of the Allalin glacier (Switzerland) broke off and killed 88 employees on the Mattmark dam construction site (*Röthlisberger*, 1981; *Raymond et al.*, 2003). Ice-falls on Taconnaz glacier were responsible for important infrastructure damage in the Chamonix valley (France) in February, 1999. Thermal regime changes due to climatic variations are clearly suspected to be the cause of the gigantic break-off of the Atels hanging glacier in 1895. Associating our model with a gravity-driven instability model, such as the one developed by *Faillettaz et al.* (2010), could provide an effective means to predict hanging glacier instability.

Résumé des résultats et conclusions

Cette étude valide un nouveau modèle de régime thermique à trois dimensions pour les zones d'accumulation froide d'un glacier alpin. Il permet la simulation de la réponse couplée dynamique et thermique du glacier à une variation climatique.

Les résultats confirment la bonne prise en compte de la rhéologie du névé comme l'avaient déjà conclu *Lüthi and Funk* (2000) et *Gagliardini and Meyssonnier* (1997). En effet, les simulations montrent un très bon accord avec les mesures de vitesses de surface, les mesures de densité dans les profils profonds et les datations obtenues à l'aide d'horizons radioactifs sur deux sites de forage différents. La comparaison des températures simulées et mesurées dans les trois sites de forage montre la capacité du modèle à reproduire l'importante variabilité spatiale observée dans les variations de température du glacier. Cette variabilité est due à la variabilité de l'accumulation de surface et de la fonte selon l'orientation et la pente.

Des simulations futures ont été effectuées à partir de différents scénarios climatiques à l'horizon 2050 pour évaluer l'évolution future du glacier tant au niveau thermique que dynamique. Les résultats mettent en avant la grande variabilité spatiale du réchauffement du glacier. On montre que l'altitude de la surface libre, le champ de densité et le champ de vitesse répondent simultanément à la diminution de la viscosité de la glace associée au réchauffement du glacier. Le changement de viscosité affecte l'écoulement du glacier. Néanmoins, les vitesses d'écoulement du glacier seront peu affectées (augmentation de 10 à 15%) car cet effet est compensé par les modifications de la densité et la diminution d'épaisseur du glacier. La conséquence la plus visible est l'affaissement de la surface qui pourrait atteindre une quinzaine de mètres d'ici 2050. Suivant les différents scénarios utilisés, le glacier devrait rester froid, au moins jusqu'à cette date malgré un réchauffement pouvant atteindre 3°C en profondeur, dans certaines zones du glacier (voir Figure 4.16).

La résolution du couplage entre les processus de surface (percolation/regel), la température et l'écoulement dans un climat variable permet de simuler correctement la réponse du glacier aux changements climatiques. L'application au site du Col du Dôme illustre les capacités du modèle à reproduire correctement les observations. Ce modèle pourra être appliqué à l'étude du régime thermique des glaciers froids suspendus qui pourraient présenter un risque dans le futur, à cause du réchauffement basal. En particulier, il permettra de réaliser une étude approfondie en trois dimensions de l'impact des variations climatiques sur le glacier de Taconnaz pour lequel la vulnérabilité à l'aval est importante (voir Chapitre 2).

Perspective

Des premières simulations de l'écoulement et du régime thermique du glacier de Taconnaz en régime stationnaire ont été effectuées en supposant une température de surface constante (Figure 4.19). Les résultats présentés ici restent préliminaires. Nous avons utilisé, en données d'entrée du modèle, la topographie de surface mesurée par lidar ainsi que la topographie du lit rocheux mesurée par radar héliportées en 2012. L'altitude de la surface libre n'est pas calculée (supposée égale à la topographie de surface mesuré en 2012). Le champ de densité est lui aussi supposé

constant et initialisé à partir d'un modèle de *Herron and Langway Jr* (1980) en utilisant le champ d'accumulation reconstitué par *Le Meur and Vincent* (2006).

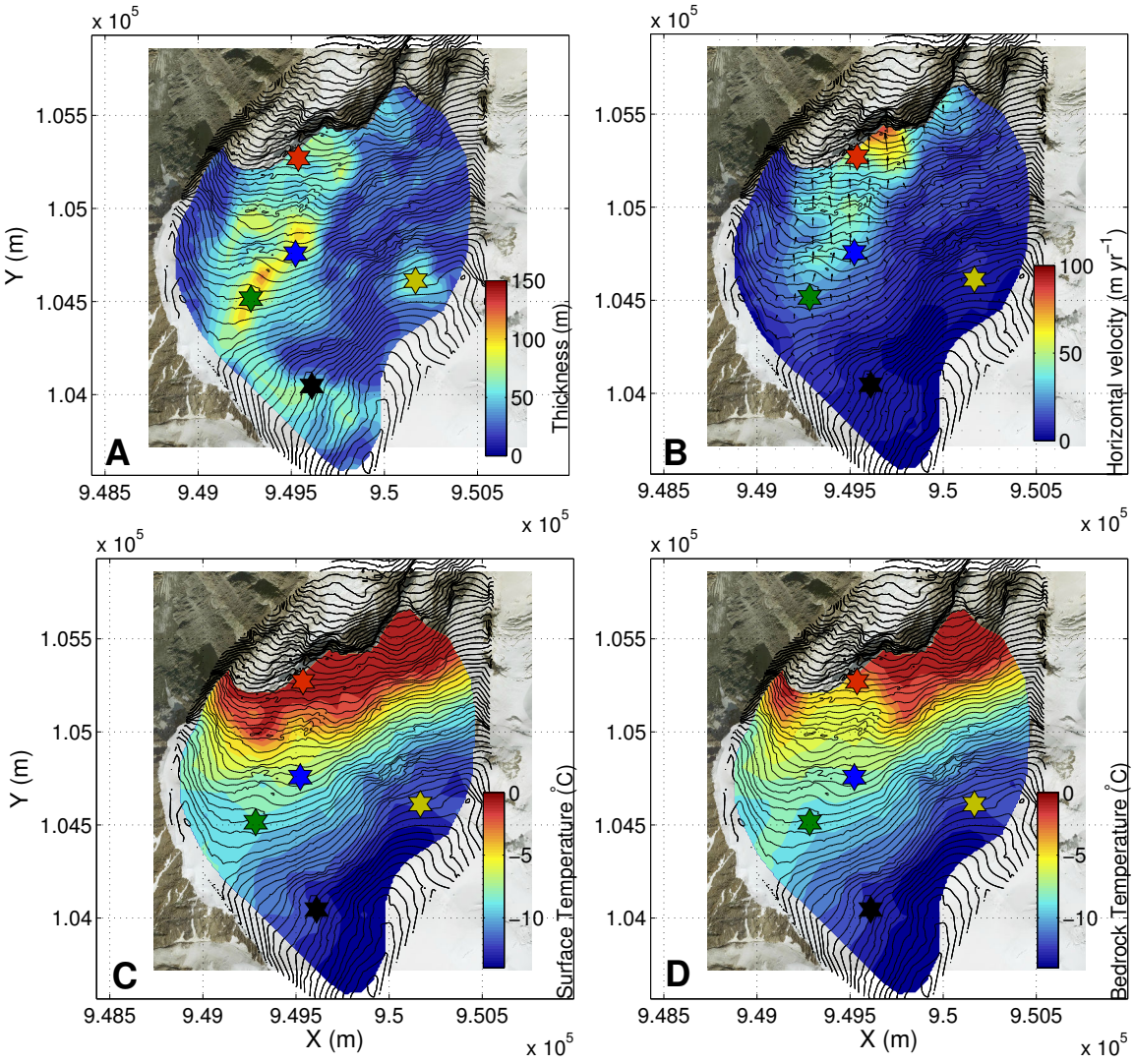

FIGURE 4.19 – Simulation à l'état stationnaire du glacier de Taconnaz utilisant une température de surface constante (figure C). En A l'épaisseur du glacier mesurée par radar, en B la vitesse horizontale de surface modélisée, en C la température de surface imposée et en D la température simulée au niveau de l'interface avec le lit rocheux.

Ces résultats offrent déjà une bonne approximation du champ de vitesse mesuré (*Vincent et al.*, 2003; *Le Meur and Vincent*, 2006) (voir figure 4.20). On remarque ainsi que l'écoulement du glacier est inférieur à 20 m an^{-1} sur une majeure partie du glacier sauf dans la zone entre les forages 1 et 2 où les vitesses atteignent 50 à 100 m an^{-1} juste avant de franchir la barre de séracs (Fig 4.19B et 4.21). Le modèle confirme que l'advection de glace froide est suffisante pour maintenir la base du glacier à température négative au niveau du forage 1 (Fig 4.19D) malgré des conditions de surface tempérées (Fig 4.19C). En revanche, ces résultats préliminaires montrent qu'une grande partie de la barre de séracs serait tempérée pour des conditions de surface tempérées comme celles utilisées

dans la simulation. Ceci est dû à une advection de glace froide moins importante sur la partie Est de la barre. Ces résultats sont très dépendants de la taille de la zone supposée tempérée en surface qui est très mal contrainte ici et ont besoin d'être confirmés. De plus, aucune simulation en régime transitoire n'a été effectuée sur ce glacier durant cette thèse mais les résultats encourageants obtenus sur le Col du Dôme sont prometteurs quant à la capacité du modèle à pouvoir simuler les changements futurs des températures basales du glacier de Taconnaz. Ces travaux seront réalisés à la suite de cette thèse.

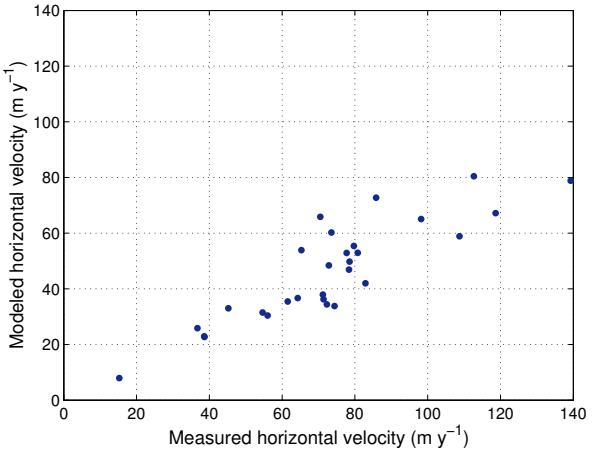

FIGURE 4.20 – Comparaison entre vitesse mesurée et simulée sur le glacier de Taconnaz

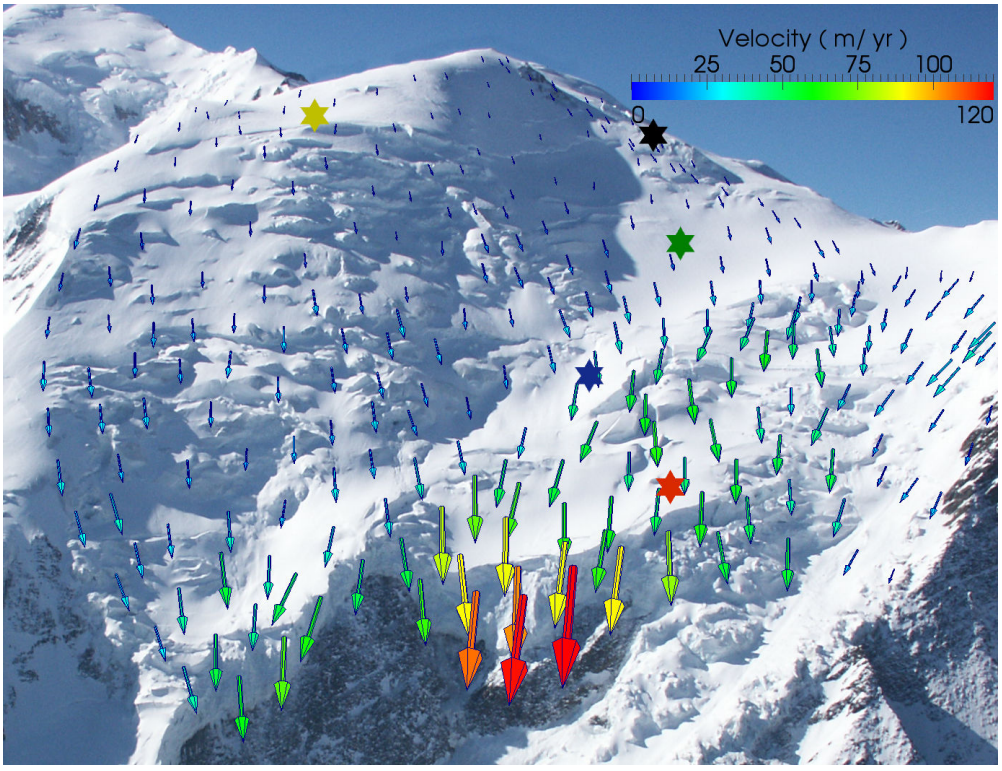

FIGURE 4.21 – Champ de vitesses modélisées sur le glacier de Taconnaz. Les sites de forages sont indiqués par des étoiles avec les couleurs correspondant à la figure 4.19

Chapitre 5

Réponse des zones de transition accumulation/ablation aux variations climatiques : sensibilité à la couverture de neige/névé et variabilité du régime thermique (cas du glacier de Tête Rousse)

Introduction

Les structures thermiques de types c, e et f (voir Chapitre 1, Fig. 1.1) sont dues aux changements d'état de surface du glacier entre la zone d'ablation et la zone d'accumulation (névé, neige ou glace). Les surfaces en neige et névé permettent la percolation de l'eau de fonte en été alors que la glace est globalement imperméable. La zone d'accumulation reçoit ainsi beaucoup plus d'énergie que la zone d'ablation où la majeure partie de l'eau de fonte est évacuée par ruissellement en surface. C'est pourquoi, selon le climat local, une zone tempérée peut exister en zone d'accumulation d'un glacier froid et inversement il peut exister une zone froide en zone d'ablation d'un glacier tempéré. La couverture neigeuse et de névé à la surface du glacier joue donc un rôle très important sur les échanges énergétiques entre le glacier et l'atmosphère. Notamment, autour de la ligne d'équilibre du glacier, des zones peuvent passer facilement d'un état froid à un état tempéré ou inversement selon l'évolution de l'altitude de la ligne d'équilibre (*Delcourt et al.*, 2012). Ainsi dans un contexte de réchauffement climatique, l'élévation de la ligne d'équilibre du glacier peut impliquer localement un refroidissement du glacier (*Rippin et al.*, 2011).

Le cas du glacier de Tête Rousse est un cas un peu particulier car du fait de la petite taille du glacier et de son altitude, il peut être entièrement en ablation ou entièrement en accumulation pour des faibles variations climatiques. Il en résulte des changements importants de régime thermique au cours du temps. L'étude présentée dans l'article qui suit couple des simulations d'épaisseur de neige et névé par le modèle CROCUS (*Brun et al.*, 1989, 1992) appliqué au glacier de Tête Rousse, avec un modèle de régime thermique. La résolution numérique utilise une méthode de type éléments spectraux sur un profil longitudinal à deux dimensions. Les conditions aux limites pour le modèle de régime thermique sont les mêmes que dans le modèle 3D présenté dans le chapitre précédent en prenant en compte la percolation et le regel de la fonte de surface. Seule la glace est supposée étanche à la percolation d'eau liquide. L'étude se base sur des observations de terrain réalisées entre 2007 et 2010 (bilan de masse, profils de température) (*Vincent et al.*, 2011) sur l'utilisation de

photographies aériennes collectées depuis 1939 (Institut Géographique National) et sur des données climatologiques provenant des bases de données HISTALP (*Auer et al.*, 2007) et SAFRAN (*Durand et al.*, 2009) et de la station météorologique de Lyon-Bron (Météo France). L'évolution du régime thermique du glacier est ainsi modélisée depuis le 19ème siècle jusqu'en 2010 pour étudier le rôle du régime thermique du glacier dans la formation de poches d'eau (Chapitre 2) et mettre en évidence l'influence thermique de la couverture de neige et du névé.

Influence de l'épaisseur de neige/névé sur le régime thermique du glacier de Tête Rousse (Massif du Mt Blanc, 3200 m) : conséquences sur le stockage d'eau, les risques de laves torrentielles et la réponse du glacier aux changements climatiques

D'après :

Gilbert, A., C. Vincent, P. Wagnon, E. Thibert and A. Rabatel (2012), The influence of snow cover thickness on the thermal regime of Tête Rousse Glacier (Mont Blanc range, 3200 m a.s.l.) : consequences for outburst flood hazards and glacier response to climate change, *J. Geophys. Res.*, 117, F04018, doi :10.1029/2011JF002258

Abstract Tête Rousse Glacier (French Alps) was responsible for an outburst flood in 1892 that devastated the village of St Gervais-Le Fayet close to Chamonix, causing 175 fatalities. Changes in the hydrothermal configuration of the glacier are suspected to be the cause of this catastrophic outburst flood. In 2010, geophysical surveys of this glacier revealed a subglacial lake that was subsequently drained artificially. The processes controlling the thermal regime of the glacier have been investigated on the basis of measurements and snow/firn cover and heat flow models using meteorological data covering the last 200 years. Temperature measurements show a polythermal structure with subglacial water trapped by the cold lowest part of the glacier (-2°C). The modeling approach shows that the polythermal structure is due to temporal changes in the depth of the snow/firn cover at the glacier surface. Paradoxically, periods with negative mass balances, associated with warmer air temperature, tend to cool the glacier whereas years with colder temperatures, associated with positive mass balances, tend to increase the glacier temperature by increasing the firnpack depth and extent. The thermal effect of the subglacial lake is evaluated and shows that the lake was formed around 1980. According to future climate scenarios, modeling shows that the glacier may cool again in the future. This study provides insights into the thermal processes responsible for water storage inside a small almost static glacier which can lead to catastrophic outburst floods such as the 1892 event or potentially dangerous situations as in 2010.

Keywords Polythermal glacier, outburst flood hazard, englacial temperatures, Tête Rousse Glacier, French Alps

5.1 Introduction

In all mountainous glaciated area, polythermal structures can be observed on glaciers. Many studies have described this kind of glacier in the Alps (*Eisen et al.*, 2009), Greenland (*Loewe*, 1966), Alaska (*Rabus and Echelmeyer*, 2002; *Harrison et al.*, 1975), the Rockies (*Paterson*, 1972; *Clarke and Goodman*, 1975), the Himalayas (*Maohuan*, 1990; *Gulley et al.*, 2009), the Peri-Antarctic Islands (*Navarro et al.*, 2009), the Canadian Arctic (*Copland et al.*, 2003; *Blatter*, 1987), Svalbard (*Jania et al.*, 1996; *Odegard et al.*, 1992; *Rippin et al.*, 2005) and the Scandinavian mountains (*Holmlund and Eriksson*, 1989). In fact, all glaciers with wet accumulation areas (*Paterson*, 1994) and ablation areas with a mean annual temperature below zero are polythermal with a temperate accumulation area and a partially cold ablation area. This is a well understood process caused by the refreezing of meltwater in the porous firnpack in the accumulation area, releasing latent heat that quickly removes the winter cold content while meltwater is evacuated by surface runoff in the ablation area (*Hooke et al.*, 1983; *Blatter and Hutter*, 1991; *Pettersson et al.*, 2003, 2007; *Gusmeroli et al.*, 2012).

Thus, in such glaciers, temperate ice (at the pressure melting temperature) coexists with cold ice. This structure affects mechanical (*Aschwanden and Blatter*, 2009; *Copland et al.*, 2003) and hydrological (*Skidmore and Sharp*, 1999; *Jansson*, 1996; *Boon and Sharp*, 2003; *Flowers and Clarke*, 2002) properties within the glacier. Subglacial hydrology can be influenced by the thermal barrier formed by cold basal ice in the glacier tongue (*Rippin et al.*, 2005; *Copland et al.*, 2003), sometimes leading to potentially dangerous configurations of water storage when water is dammed by a cold ice barrier which can suddenly break. In the case of John Evans Glacier (Canada), it has been shown that basal water can be trapped at the cold/temperate ice interface and lead to local high water pressure (*Copland et al.*, 2003). This was also the case of Tête Rousse Glacier, which displays a polythermal structure and houses a subglacial water-filled cavity detected by field surveys carried out from 2007 to 2010 (*Vincent et al.*, 2012; *Legchenko et al.*, 2011) and artificially drained in September and October 2010 to avoid any possibility of a catastrophic outburst flood event. *Vincent et al.* (2012) have shown that the thermal regime of the glacier likely plays a key role in the formation of such a cavity. The modeling of processes that lead to such a polythermal structure is therefore a key issue to prevent subglacial lake outburst flood hazards. Furthermore, thermal regime of the glacier can change in response to climate change (*Rabus and Echelmeyer*, 2002; *Pettersson et al.*, 2003; *Wohlleben et al.*, 2009; *Rippin et al.*, 2011; *Gusmeroli et al.*, 2012). The main objective of this study is to investigate the thermodynamic processes responsible for the polythermal structure of Tête Rousse Glacier under varying climate conditions in order to simulate thermal regime variations of the glacier. The aim is to improve our understanding of water storage inside the glacier and the associated lake outburst flood hazards.

The data and model used are described in sections 5.2 and 5.3, respectively. Section 5.4 presents the results and the interpretation of the englacial temperature distribution in order to discuss the conditions that could lead to water storage inside the glacier (section 5.5). Section 5.6 explores the expected future changes of the thermal regime of Tête Rousse Glacier according to various climate scenarios and our conclusions are presented in section 5.7.

5.2 Study site and data

5.2.1 Study site

Tête Rousse Glacier is located in the Mont Blanc range (French Alps, 45°55'N, 6°57'E). The normal route to access the summit of the Mont Blanc crosses this glacier. Its surface area was 0.08 km^2 in 2007. This west-facing glacier is approximately 0.6 km long, and extends from about 3300 m above sea level (a.s.l.) to 3100 m a.s.l. with a maximum thickness of 70 m (*Vincent et al.*, 2010a) (Figure 5.1). The size of the accumulation area varies significantly from one year to another. At the end of the hydrological year, the glacier may be completely snow-covered or snow-free. The mean Equilibrium Line Altitude (ELA) observed over the last 20 years is around 3195 m (Figure 5.1). The mean annual air temperature measured by an automatic weather station in the vicinity of the glacier (3100 m a.s.l) over the period 1 July 2010 to 30 June 2011was -2.84°C.

One peculiarity of Tête Rousse Glacier comes from its location below the west face of the Aiguille du Goûter (3863 m a.s.l.) peak. Snow accumulation at the glacier surface comes partly from avalanches from this 500 m high face, which explains the high accumulation gradient observed in the upper reaches of the glacier. This location also results in considerable shading by surroundings slopes. This has been quantified by measuring the skyline elevation angle as a function of the azimuth angle at the center of the glacier and applying the calculation method proposed by *Oerlemans* (2001). In comparison with solar radiation at the top of the atmosphere, shading reduces the mean annual direct solar radiation by -16% on Tête Rousse Glacier, with a maximum of -20% for winter daily means and a minimum of -9% during the ablation season (mid-May to mid-October).

5.2.2 Field measurements

All the field measurements used in this study will be briefly described here. The reader is invited to refer to *Vincent et al.* (2010a, 2012) for more details.

5.2.2.1 Mass balance and surface velocity

Geodetic measurements were carried out in 1901 and 1950 using a theodolite and in 2007 using differential GPS instruments. The differences between the Digital Elevation Models (DEM) resulting from the 1901 and 2007 surveys show that the glacier thinned by 15 to 20 m on average over the whole period (*Vincent et al.*, 2010a).

Surface ice-flow velocities were calculated at the end of the ablation season in 2007 and 2009 (September) from the displacement of five ablation stakes on a longitudinal section of the glacier. Ice-flow velocities range from 0.4 to 0.6 m yr^{-1} (*Vincent et al.*, 2010a). In addition, many ice-flow velocity measurements were carried out between 1901 and 1903 (*Mougin and Bernard*, 1922). These ice-flow velocities were also very low, ranging from 0.2 m yr^{-1} close to the edge of the glacier to 1.1 m yr^{-1} at the central flow line.

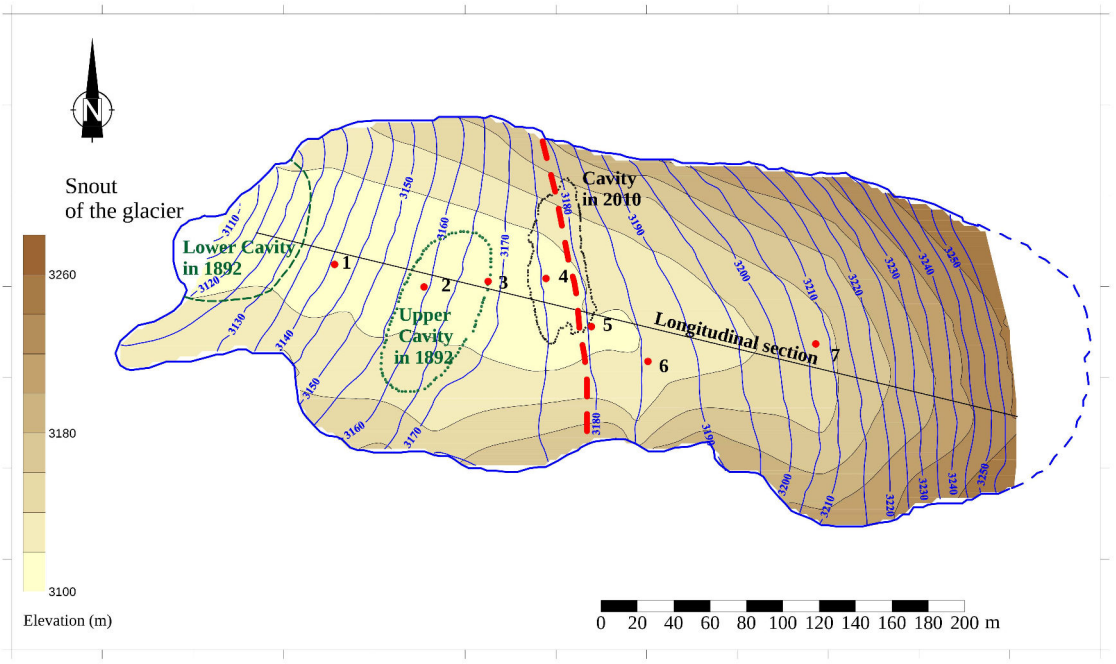

FIGURE 5.1 – Map of Tête Rousse Glacier showing surface (blue contours) and bedrock topography (color scale) in 2007. The 1892 upper and lower cavities are represented in green and the 2010 cavity is plotted in black. Red points show the location of borehole temperature measurements. The black line is the longitudinal section used for 2-D temperature simulations. The bold dashed red line shows the approximate location of mean Equilibrium Line Altitude (ELA) over the last 20 years.

5.2.2.2 Bedrock topography and subglacial lake detection

The bedrock topography of Tête Rousse Glacier was determined in 2007 from Ground Penetrating Radar (GPR) data using a 250 MHz shielded antenna (*Vincent et al.*, 2010a) and also from 20 direct borehole measurements conducted in summer 2010 (Figure 5.1, only shows the location of the boreholes with temperature sensors). Some uncertainties remain due to considerable radar energy dispersion in the deepest part of the glacier that prevents clear recognition of the radar returns from the ice/rock interface . Both methods (radar and boreholes) were used together to locate the glacier bedrock.

GPR images from 2007 also show a peculiar pattern, with very clear, bright reflectors visible 40 m deep in the middle of the glacier, over a distance of 20 m along the central profile. These large reflectors are located approximately 170 m up from the snout. These reflectors suggest the possible presence of a subglacial water reservoir (*Vincent et al.*, 2012). In 2010, additional measurements on 18 cross sections and four longitudinal sections using 250 MHz and 100 MHz antennas confirmed the results obtained from 2007 measurements. Finally, 3D images of the water reservoir inside the glacier were obtained by surface nuclear magnetic resonance imaging (SNMR) performed in 2009 (*Legchenko et al.*, 2011). The minimum total volume of water stored in the glacier was estimated to be 45 000 m^3.

5.2.2.3 Temperature profiles

Figure 5.1 shows the location of seven thermistor chains installed in boreholes in July 2010 along a central longitudinal section of the glacier at 3141 m a.s.l. (34 m depth), 3159 m a.s.l. (57 m depth), 3168 m a.s.l. (65 m depth), 3176 m a.s.l. (70 m depth), 3181 m a.s.l. (70 m depth), 3186 m a.s.l. (66 m depth) and 3207 m a.s.l. (70 m depth). In each borehole, temperature was measured by the thermistors through the entire thickness of the ice. Boreholes were made by hot water drilling, resulting in a temporary local disturbance of englacial temperatures. Consequently, measurements were repeated 5 times between July and September 2010 (accuracy of ± 0.1 °C) to be sure that thermal equilibrium had been reached. Little change was observed between the last two measurements, 10 days apart ($\pm$ 0.1°C), indicating that thermal equilibrium had been reached.

5.2.3 Meteorological data

In order to simulate glacier surface changes, meteorological data over the two last century are required. The different sources for each kind of data are described bellow.

5.2.3.1 Air temperature

Daily maximum and minimum air temperatures on the glacier were reconstructed using data from the Lyon-Bron meteorological station located ~200 km west of the glacier. These data are available from 1907 to present. Before this date, we used homogenized temperature data over the north-west Alps from (*Böhm et al.*, 2001).

5.2.3.2 Precipitation

Precipitation data are available from 1907 for Besse-en-Oisans meteorological station located 150 km south of the Mont Blanc range in the Grandes Rousses range at 1525 m a.s.l. *Vincent et al.* (2007a) found a good correlation between Besse-en-Oisans and Chamonix precipitation records (close to our study site) using 5-year running averages over the 1938-2007 period. We therefore decided to use the Besse-en-Oisans series rather than the closer Chamonix series because it began 31 years earlier. Surface accumulation was assessed from this precipitation record using a multiplication factor ranging from 1.5 to 3.3 depending on the location on the glacier. These factors were calibrated to fit the winter accumulation measured on Tête Rousse Glacier for the hydrological years 2007/2008, 2008/2009 and 2009/2010. Snow accumulation is strongly influenced by local effects which result in a negative gradient (-0.012 m w.e. m^{-1}) from 3120 m a.s.l. to 3170 m a.s.l. and a positive gradient (+0.011 m w.e. m^{-1}) from 3170 m a.s.l. to 3275 m a.s.l. Indeed, at an annual time-scale, higher accumulation rates have been observed on the tongue of the glacier, mainly due to site effects (the lowest part of the tongue is surrounded by slopes, forming a basin that traps precipitation). Before 1907 we used homogenized precipitation data over the north-west Alps from *Auer et al.* (2007). These data are inferred from instrument-based time series of monthly mean precipitation.

5.2.3.3 Radiation, wind speed, humidity and cloudiness

In addition to air temperature and precipitation, the CROCUS model used for snow and firn thickness simulations (section 5.3.1) requires the following input meteorological data at an hourly time-scale : 10-m wind speed, 2-m air relative humidity, incoming direct and diffuse solar radiation, incoming long-wave radiation, and cloudiness. These data are provided by the SAFRAN disaggregated meteorological model (*Durand et al.*, 1993) and are available from 1958 for each mountain range of the French Alps according to aspect and altitude (every 300 m). SAFRAN reanalysis assimilates large scale meteorological fields obtained from meteorological modeling and local information provided by weather stations and direct observations at ski resorts (*Durand et al.*, 1993). In the vicinity of Tête Rousse Glacier, an automatic weather station has been operating at 3100 m a.s.l since 1 July 2010, recording 30-min averages of air temperature and relative humidity, wind speed and incoming solar and long wave radiation. Comparison between SAFRAN reanalysis and daily mean data from the weather station over July, August and September 2010 shows good agreement in mean and daily variability for humidity and incoming direct radiation (n=93 days and r^2=0.66 and 0.80 respectively). We found r^2=0.19 and r^2=0.23 for wind speed and long wave incoming radiation respectively. Wind speed is effectively influenced by local topography and cannot be well represented by large scale data. Similarly, long wave radiation depends on nebulosity which can also vary locally. Nevertheless, these data are used because we consider that mean variations over larger time scales are well represented. Indeed, long wave radiations trends mainly depend on air temperature trends which are well reconstructed by SAFRAN (comparison with the glacier station gives r^2=0.95). Furthermore, mean cloudiness (that also influences long wave radiation) did not change too much over the period of interest (*Durand et al.*, 2009).

Before 1958, we consider that mean wind speed, air relative humidity, incoming direct and diffuse solar radiation and cloudiness remain unchanged and we use a 10-year time-series from 1958 to 1968 provided by SAFRAN reanalysis to reconstruct these data over the 1800-1958 period. Indeed, the relative humidity of the atmosphere can be considered to be roughly constant, even if air temperatures show large seasonal variations (*Hartmann*, 1994). Analysis of year to year variations in wind speed from SAFRAN data does not indicate any specific trend and the mean wind speed is around 2.7 m s^{-1}. SAFRAN reanalysis indicates that cloud cover has not significantly changed either, remaining at about 44%. This is also confirmed at a larger scale from the HISTALP data set (*Auer et al.*, 2007). Considering that atmospheric solar transmissivity mainly depends on cloud cover, we consider global radiation to be constant, neglecting dimming and brightening of solar radiation due to changes in atmospheric aerosol content. We assume the associated error to be negligible since, based on the long record from Davos (Switzerland) (*Ohmura and Lang*, 1989), global solar radiation has not presented any marked changes since 1949. Incoming long-wave radiation was estimated from air temperature, vapor pressure and cloudiness using (*Brutsaert*, 1975) :

$$L_w = 1.24\left(1 + an^b\right)\left(\frac{e}{T}\right)^{1/7}\sigma T^4 \tag{5.1}$$

where L_w (W m^{-2}) is the incoming long-wave radiation, e (Pa) the partial pressure of water vapor,

T (K) the air temperature, σ the Stephan Boltzman constant (σ = 5.67 10^{-8} W m^{-2} K^{-4}), n the cloudiness (in tenths), and a and b are two dimensionless parameters. These parameters a and b were tuned to obtain the best agreement between estimated hourly long-wave radiation derived from equation (1) and SAFRAN data (r^2=0.55 over one randomly selected year (2009) at an hourly time scale) : $a = 0.3$ and $b = 3.14$. Tests performed on other years gave the same result.

5.2.4 Aerial photographs and satellite images

In order to assess the validity of the snow cover model (section 5.3) and to correct possible discrepancies, modeling results were compared with observations. Generally, the snow line on a glacier is easy to discern from aerial photographs and satellite images (*Rabatel et al.*, 2005), as illustrated in Figure 5.2, and offers a good way to constrain our snow cover model. Thus, the end-of-summer snowline was identified on Tête Rousse Glacier using 38 aerial photographs and satellite images (Table 5.1). These data cover the 1939-2009 period with an almost annual resolution since the early 80s. All the aerial photographs and satellite images were geometrically corrected on the basis of the same image used as a reference (SPOT 5 image from 2003) and using a 25 m resolution DEM from the French National Geographical Institute (IGN) The snow line was delineated manually and its elevation was computed using the IGN DEM.

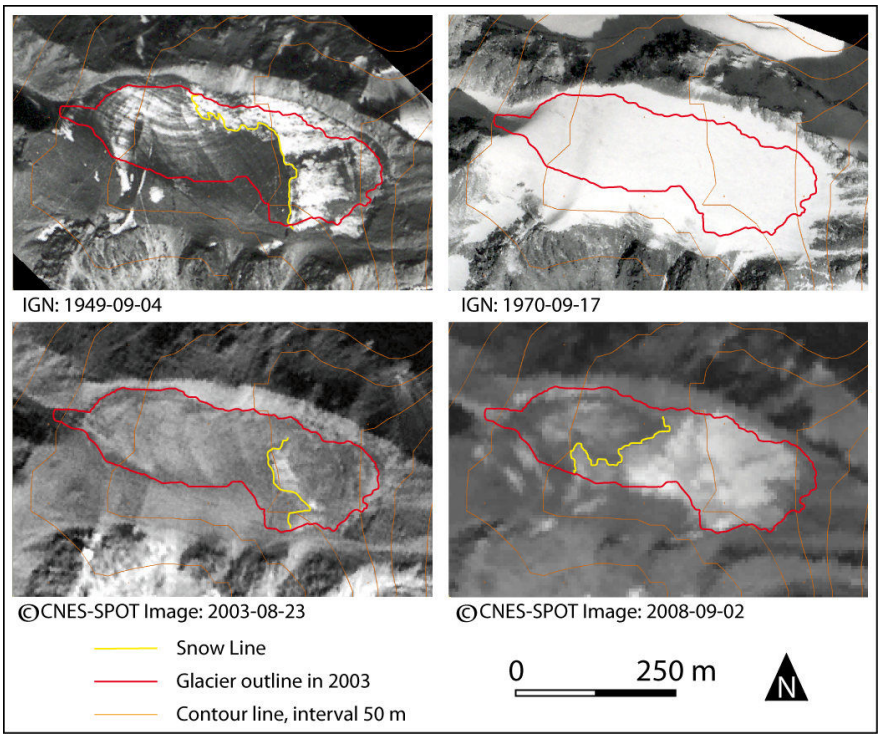

FIGURE 5.2 – Aerial photographs (1949 and 1970) and satellite images (2003 and 2008) of Tête Rousse Glacier in summer. For each year, the glacier outline in 2003 is indicated in red and the snowline in yellow

Date Source	Path/Row	Scale or resolution	Snow cover on the glacier (Partial or Total)	Mean snow line elevation (m)
1939-07-03Aerial Photograph	N/A	1 :20,000	T	-
1949-09-04Aerial Photograph	N/A	1 :26,000	P	3200
1952-07-27Aerial Photograph	N/A	1 :25,000	P	3180
1958-07-31Aerial Photograph	N/A	1 :25,000	T	-
1961-08-29Aerial Photograph	N/A	1 :25,000	T	-
1966-09-08Aerial Photograph	N/A	1 :25,000	T	-
1970-09-17Aerial Photograph	N/A	1 :30,000	T	-
1979-09-05Aerial Photograph	N/A	1 :30,000	T	-
1982-09-26Aerial Photograph	N/A	1 :30,000	T	-
1984-07-09Aerial Photograph	N/A	1 :15,000	T	-
1984-08-31Landsat 5 TM	196-028	30 m	T	-
1985-08-11Landsat 5 TM	195-028	30 m	T	-
1986-09-09Landsat 5 TM	196-028	30 m	T	-
1987-09-09Landsat 5 TM	196-028	30 m	P	3150
1988-07-26Aerial Photograph	N/A	1 :30,000	T	-
1988-09-12Landsat 4 TM	195-028	30 m	P	3160
1989-09-20SPOT 1	052-258	10 m	T	-
1990-09-10Landsat 5 TM	195-028	30 m	P	3180
1991-08-30SPOT 2	051-258	10 m	P	3220
1992-08-05Landsat 5 TM	196-028	30 m	T	-
1993-08-11Aerial Photograph	N/A	1 :20,000	P	3170
1993-09-02Landsat 5 TM	195-028	30 m	T	-
1994-08-09SPOT 3	052-258	10 m	P	3180
1998-08-30SPOT 4	052-258	20 m	P	3150
1999-09-11Landsat 7 ETM+	195-028	15 m	T	-
2000-08-01Aerial Photograph	N/A	1 :25,000	T	-
2000-08-26SPOT 1	051-257	10 m	P	3180
2001-08-13Aerial Photograph	N/A	1 :25,000	P	3170
2001-07-30Landsat 7 ETM+	195-028	15 m	T	-
2002-08-18Landsat 7 ETM+	195-028	15 m	T	-
2003-08-23SPOT 5	051-257	2.5 m	P	3200
2005-08-10Landsat 7 ETM+	195-028	15 m	P	3150
2006-09-05Aerial Photograph	N/A	1 :20,000	T	-
2006-09-05Landsat 7 ETM+	196-028	15 m	T	-
2007-07-31Landsat 7 ETM+	195-028	15 m	T	-
2008-09-02SPOT 5	051-257	5 m	P	3180
2009-08-15SPOT 5	052-258	10 m	P	3200

Tableau 5.1 – List of aerial photographs (from the French National Geographic Institute) and satellite images.

5.3 Methodology : numerical modeling

Englacial temperatures are derived from heat flow and water content modeling taking into account meltwater percolation through snow and firn as well as moisture diffusion in the temperate

ice. This numerical modeling needs to simulate both spatial and temporal changes of the thickness and extent of snow and firn on the glacier. First, the thickness changes are modeled using the CROCUS model (see section 5.3.1). Second, modeled firnpacks and snowpacks are used as inputs to the heat and water transfer models described in section 5.3.2.1 and 5.3.3. The heat and water transfer models also work independently but water content and temperature are coupled at each time step as explained in Section 5.3.4.

5.3.1 Snow and firn thickness modeling

The presence of snow affects the physical properties of the glacier surface layers. Indeed, thermal conductivity strongly depends on density. The porosity of snow also allows water percolation and storage at the snow/ice interface (*Fountain and Walder*, 1998). Consequently, the heat input during the summer season strongly depends on the snow thickness. When the glacier surface is snow covered, heat is stored by percolation (and refreezing) of surface meltwater. Conversely, when the glacier surface is snow-free, this latent heat is lost due to meltwater runoff over the impermeable surface.

To estimate snow thickness changes over the last 200 years, we use the CROCUS snow model developed by Météo-France (*Brun et al.*, 1989, 1992). This one-dimensional multilayer physical model was initially developed for seasonal snow modeling and avalanche forecasting in the French Alps. It explicitly evaluates mass and energy exchanges between the snowpack and the low-level atmosphere at 15-min time steps as a function of meteorological conditions, including turbulent heat flux, moisture surface transfers and ground heat flux. CROCUS computes the heat transfer within the snowpack and also the grain types, snow temperature, density and liquid-water content of each snow layer. Snow and firn albedo is derived from grain characteristics (optical diameter) and from the age of the surface layer. CROCUS has been successfully applied to glaciers in the French Alps for mass balance modeling (*Gerbaux et al.*, 2005). As suggested by *Gerbaux et al.* (2005), we added a 200 m thick ice layer below the initial snow profile to start the simulations. The reason for this is that, in the ablation zone where mass is lost yearly, an initial 200 m thick ice layer makes it possible to preserve ice throughout the simulation. The thickness of this ice layer does not have any influence on the results and is simply used to maintain the presence of ice below the snow. Ice albedo was set to 0.23 in the 0.3-0.8 μm band, 0.15 in the 0.8-1.5 μm band, and 0.06 in the 1.5-2.8 μm band, according to measurements performed on St Sorlin Glacier (French Alps) (*Gerbaux et al.*, 2005). In the accumulation zone, we consider that snow to ice compaction is completed when simulated firn density reaches 800 kg m^{-3}. Indeed, CROCUS is a seasonal snow model and it can not reproduce the firn

densification until the ice (913 kg m^{-3}). We use the value of 800 km m^{-3} as threshold for the firn/ice transition. At the elevation of Tête Rousse Glacier, densification processes mainly come from percolation and refreezing of surface meltwater. Given that the firn is approximately 30 m thick at 3550 m a.s.l. in the Mont Blanc range (*Vallon et al.*, 1976), we assume that the firn thickness is less (20 m) in the accumulation zone of Tête Rousse Glacier due to the lower elevation of the site.

The CROCUS model also calculates temperature, heat flow and water percolation within the

snowpack. However CROCUS is a one-dimensional model developed for seasonal snowpack simulations and therefore cannot be used to simulate the thermal regime of a glacier with a peculiar geometry. Consequently, only the snow thicknesses modeled by CROCUS are used and the thermal regime of the glacier is modeled by the model presented below.

5.3.2 Heat flow and water content modeling

Field temperature measurements performed along a longitudinal section (Figure 5.1) are assumed to be representative of the temperature distribution within the glacier. We assume that the relevant physical processes are laterally invariant and that the lateral heat fluxes coming from the glacier sides are negligible because the central longitudinal section we use is located 80-120 m from the glacier edges. Physical equations are integrated on a 2D-grid using the spectral element method (*Patera*, 1984) (see appendix D) with tetragonal polygons. Temperature and water content are computed at a 8-hour time-scale and spatial resolution varies from 0.8 m to 2 m. We consider that glacier thickness remains constant over the whole 20^{th} century (equal to the measured thickness in 2007 (*Vincent et al.*, 2010a)) and over the whole 19th century (equal to the measured thickness in 1901 (*Mougin and Bernard*, 1922)). This approximation does not influence modeled temperature since the changes in the glacier thickness (-15 m over 104 years) is not significant in comparison with heat transfer velocity by diffusive and advective processes.

5.3.2.1 Heat flow model

The temperature field in the cold part of the glacier is calculated solving the heat transfer equation within a cold glacier (including ice, firn and snow) which can be written as follows (*Malvern*, 1969; *Hutter*, 1983) :

$$\rho C_p \left[\frac{\partial T}{\partial t} + \vec{v} \cdot \vec{\nabla} T \right] = \nabla \cdot (k \nabla T) + Q \tag{5.2}$$

where T (K) is the temperature, ρ (kg m^{-3}) the density, C_p (J kg^{-1} K^{-1}) the specific heat and k (W m^{-1} K^{-1}) the thermal conductivity of the firn/ice, $\vec{v}$ (m s^{-1}) the glacier flow velocity vector, t (s) the time, and Q (W m^{-3}) a volumetric heat source. Heat dissipation by ice deformation was neglected given that we observed very low ice-flow velocities. The heat source associated with the refreezing of percolating water is discussed in section 5.3.4 and is treated separately from the volumetric source, so Q is set to zero.

Ice advection has been taken into account. For this purpose, the ice-flow velocities have been calculated using steady-state three-dimensional full-Stokes simulation proposed by *Gagliardini et al.* (2011). For these numerical simulations, we used (i) the 1901 topography (maximum surface velocity of about 1.1 m yr^{-1}) for the period 1800-1901 and (ii) the 2007 topography (maximum surface velocity about 0.6 m yr^{-1}) for the period 1901-2010. For the period during which the subglacial water-filled cavity is presen (see Section 5.4.2.2), (iii) we take into account of the water-filled cavity influence on the velocity field. In this way, the calculated surface velocities are in

agreement with the easurements. However, heat advection due to firn densification is ignored because heat transport into the firn is largely dominated by meltwater percolation and refreezing.

Furthe more, in this wet accumulation zone, densification is mainly due to refreezing of surface melt water (*Vallon et al.*, 1976) involving very fast densification of fir and therefore very low vertical advection.

Changing snow thickness is included in the model by changing density profile each month supposing a constant surface elevation (to avoid a re-mesh calculation each month). Given that CROCUS model is developed for seasonal snowpack, it is not able to simulate correctly firn densification into ice. Consequently, according to the fact that, at 3500 m a.s.l. in the Mont Blanc area, the firn density increases linearly as a function of depth (*Vallon et al.*, 1976), density is updated every month from snow thicknesses modeled by CROCUS using equation (3) :

$$\rho(x,z) = \begin{cases} \rho_{surf} + \frac{z}{z_{max}}(\rho_{ice} - \rho_{surf}) & if\ z < z_{snow(x)} \\ \rho_{ice} & if\ z > z_{snow(x)} \end{cases} \tag{5.3}$$

where x (m) is the horizontal distance from the upper limit of the glacier, z (m) the depth from the surface, z_{max} (m) the maximum firn thickness (set to 20 m), ρ_{surf} the surface density (set to 400 kg m^{-3}, in agreement with field observations), ρ_{ice} the ice density (913 kg m^{-3}) and z_{snow} (m) the snow thickness given by the CROCUS model. zmax represent the firn thickness needed to transform firn into ice. Although CROCUS model gives firn thickness superior to zmax, firn thickness can not exceed this value. Indeed, CROCUS model is not developed to simulate correctly firn densification into ice.

Thermal conductivity is inferred from snow and firn density using the relationship provided by *Sturm et al.* (1997) :

$$k = 0.138 - 1.01\rho + 3.233\rho^2 \tag{5.4}$$

Ice conductivity is set to 2.1 W m^{-1} K^{-1} (*Paterson*, 1994). Surface temperatures are inferred from air temperature using a constant lapse rate (Table 5.2) and determine the surface boundary condition. This approximation has shown good results in heat flow modeling carried out for the Col du Dôme, 1000 m above the study site (*Vincent et al.*, 2007b) and for Mount Illimani (6350 m a.s.l.) in Bolivia (*Gilbert et al.*, 2010) (annexe A). At the glacier bedrock, the basal heat flux is assumed to be constant in time and space (flux boundary condition). Due to local topography (Tête Rousse Glacier is located on a large spur on the west face of Aiguille du Goûter), the horizontal component of the heat flux through the bedrock between the south-facing side of the spur to the north-facing side is probably greater than the vertical component (*Noetzli et al.*, 2007). Consequently, since the basal flux is in any case low, we derived the basal flux from the basal temperature gradient observed at the borehole in the cold tongue of the glacier, yielding a value of 20±10 10^{-3} W m^{-2}. The englacial temperature in this borehole is not influenced by the subglacial lake, as opposed to the temperature in boreholes 2 and 3 (see section 5.4.2.2).

Assuming a thermodynamic equilibrium between ice and water, the temperature of the water reservoir is set to 0°C. Note that this is consistent with our temperature measurements performed in 2010 in boreholes 4 and 5.

When ice or firn become temperate, temperature is set to the melting point temperature T_0 and liquid water can be stored (section 5.3.3).

5.3.3 Water content modeling

Processes involving meltwater percolation from the surface and refreezing have a strong influence on englacial temperature (*Greuell and Oerlemans*, 1989; *Lüthi and Funk*, 2001; *Vincent et al.*, 2007b; *Gilbert et al.*, 2010; *Humphrey et al.*, 2012). We therefore coupled our heat flow model with a model of water percolation within the snow/firn layers of the glacier and a model of moisture diffusion in the temperate ice (*Hutter*, 1982; *Aschwanden and Blatter*, 2009).

We assume that the surface meltwater percolates vertically through the snow and firn at a constant velocity of 3.0 10^{-5} m s^{-1} as observed by *Vallon et al.* (1976) in the accumulation zone of the Mer de Glace (3550 m a.s.l., Mont Blanc range), although this value is somewhat higher than theoretical values for water percolation through homogeneous snow (values close to 10^{-6} m s^{-1} (*Colbeck and Davidson*, 1973)). Neglecting non-continuous sources of water transport like water channels within the ice or crevasses, the transport equation for water is expressed as follow :

$$\frac{\partial \omega}{\partial t} + v_z \frac{\partial \omega_{advec}}{\partial z} = K \Delta \omega \tag{5.5}$$

where ω (kg m^{-3}) is the water content, v_z (m s^{-1}) is the percolation velocity, ω_{advec} (kg m^{-3}) the water available for percolation and K (m2 s^{-1}) is the moisture diffusivity (*Hutter*, 1982) set to 5 10^{-4} m^2 s^{-1} if $\rho = \rho_{ice}$ (*Aschwanden and Blatter*, 2009) and set to zero if $\rho < \rho_{ice}$. We assume that cold or temperate ice is totally impermeable to liquid water percolation (*Fountain and Walder*, 1998). Therefore v_z is set to 0 as soon as the density sets by equation 5.3 reaches the ice density (913 kg m^{-3}). As water is partly retained in the snow by capillarity (*Colbeck and Davidson*, 1973), we define :

$$\omega_{advec} = \omega - s_r \omega_{sat} \tag{5.6}$$

where ω (kg m^{-3}) is the total water content, s_r the residual saturation (ranging from 0.03 to 0.07 (*Illangasekare et al.*, 1990)) and ω_{sat} the maximum water content which depends on the snow porosity and related to snow density by :

$$\omega_{sat} = \rho_{water} \left(1 - \frac{\rho_{snow}}{\rho_{ice}}\right) \tag{5.7}$$

where ρ_{water} is the water density and ρ_{snow} (kg m^{-3}) the snow density. If water content exceeds ω_{sat}, we assume that this water is drained by runoff. In the temperate ice, maximum water content is set to 10 kg m^{-3} in temperate ice (*Pettersson et al.*, 2004). When this maximum water content is reached, we assume that water can not enter anymore into the body of the glacier.

Surface boundary condition is a water flux Ω_{source} (kg m^{-2} s^{-1}) coming from surface melting and we assume a zero-flux basal boundary condition. Surface melting is estimated from daily maximum air temperature by a degree-day model as done by *Vincent et al.* (2007b) for the Col du Dôme in the Mont Blanc range because meteorological data like wind speed, direct and diffuse short-wave radiation, incident long-wave radiation, cloudiness and relative humidity are not sufficiently accurate before 1958 (SAFRAN reanalysis data are not available, see section 3.1) to apply a full energy balance model like CROCUS.

Parameter	Label	Values	Units
Latent heat of ice fusion	L	3.35 10^5	J kg^{-1}
Basal flux	F_b	15 10^{-3}	W m^{-2}
Thermal conductivity	k	[0.25 ; 2.1]	W m^{-1} K^{-1}
Specific heat of ice	C_p	2.05 10^3	J kg^{-1} K^{-1}
Surface temperature lapse rate	dT/dz	-6.5 10^{-3}	K m^{-1}
Degree day factor	D_{day}	3.0 10^{-3}	m K^{-1} day^{-1}
Percolation velocity	v_z	3.0 10^{-5}	m s^{-1}
Residual saturation	s_r	0.03	
Moisture diffusivity	K	5 10^{-4}	m^2 s^{-1}
Maximum water content in temperate ice	ω_{ice}	10	kg m^{-3}
Precipitation correction factor	P	[1.5 3.3]	-
Long wave radiation (cloudiness corrections)	$a; b$	0.3 ; 3.14	-
Snow thickness	z_{snow}	from CROCUS model	m
Maximum snow thickness	z_{max}	20	m
Density	ρ	[400 ; 913]	kg m^{-3}

Tableau 5.2 – List of parameters used in the model.

5.3.4 Coupling water content and temperature field

Water content is coupled with the heat flow model by assuming that water refreezes and produces latent heat in the cold firn at each time step. This induces a temperature increase given by :

$$\Delta T = \frac{\omega\, L}{\rho_{snow}\, c_p} \tag{5.8}$$

as long as the snow temperature T (K) remains below the ice melting point (where L (J kg^{-1}) is the latent heat of fusion of ice). This total refreeze of the liquid water content results in $\omega = 0$. If the temperature reaches the melting point T_0, T is set equal to T_0 and the content of water which remains liquid is given by :

$$\omega = \omega_i - (T_0 - T_i)\frac{\rho_{snow}\, c_p}{L} \tag{5.9}$$

where ω_i and T_i are respectively the initial water content and firn temperature. Energy released when the refrozen meltwater is cooled to the temperature of the surrounding firn is not accounted for. Given that the firn temperature is not lower than -4°C (Section 4), this source is therefore less than 5% of the latent heat (ratio between latent heat of fusion and energy lost by cooling the refrozen meltwater of 4K) and its contribution can be neglected.

5.4 Results

Englacial temperatures along a 2D longitudinal section of Tête Rousse Glacier were simulated over the whole 1800-2010 period, using different data sets depending on the considered period (cf.

Section 5.2.2). At the beginning of the simulation period, in 1800, the glacier was considered to be uniformly cold (-2.5°C). This initial temperature corresponds to the mean simulated englacial temperature for the first 50 years. The initial snow thickness was arbitrarily set to 10 m at 3125 m a.s.l., 5m at 3175 m a.s.l., 20 m at 3225 m a.s.l. and 20 m at 3275 m a.s.l. These choices do not affect simulated temperatures after 1850.

5.4.1 Snow cover : validation and correction using satellite images and aerial photographs

The aerial photographs and satellite images show that the portion of the glacier covered by snow at the end of summer can vary from almost none to all (Figure 5.2, Table 5.1). Indeed, the 1949 aerial photography shows that almost the whole surface of the glacier showed exposed ice on September 4^{th} whereas it was entirely snow covered from 1960 to 1990.

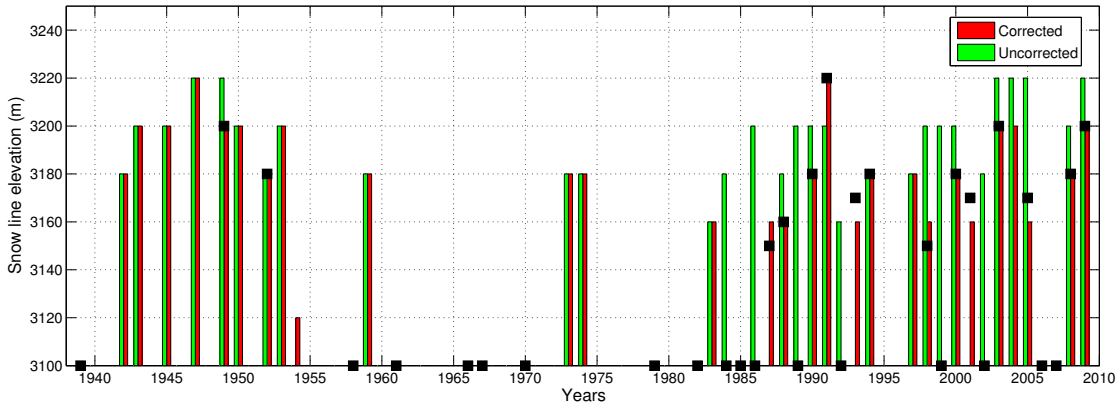

FIGURE 5.3 – Modeled (bars) and observed (squares) snow line elevations. Modeled snow line elevations on the dates from Table 1 are shown after and before correction using aerial photographs and satellite images (red and green bars respectively). Black squares are snow line elevations estimated from satellite images and photographs. For years without available satellite images or photographs, the snow lines modeled for 15th September are plotted. Note that differences between measurements and the corrected model results are due to the elevation resolution of the model (set to 20 m). A snow line at 3100 m means that the entire glacier is snow covered. There is no ablation zone during these periods.

Figure 5.3 shows that snow line elevations from the model and images/photographs are in good agreement over the period 1940-2010 except for nine years (1984, 1986, 1987, 1989, 1992, 1993, 1999, 2001, 2002). Due to the fact that snow and firn thicknesses are simulated during 200 years, potential model errors accumulate from year to year after each winter accumulation /summer melting cycle even if the model performs correctly for most of annual runs. Therefore, hourly snow thicknesses modeled by CROCUS are corrected by incorporating information from satellite images and aerial photographs. The aim of this correction is to have the best possible unbiased snow and firn thicknesses evolution since 200 years for our heat transport model. Thus, in the event of disagreement between the model and the images/photographs, snow thickness is reinitialized at the date of the image/photograph. For such dates, the snow thickness at given elevation is deduced from the difference between that elevation and the snow line elevation, i.e. it is set to zero below

the snow line and is calculated from the measured accumulation gradient used for precipitation corrections (see section 5.2.2) above the snow line. However, the glacier may often remain totally snow covered during the whole year, as shown in Figure 5.2 for 1970. In such a case, because images and photographs cannot provide any information on snow thickness, the images are only used to correct the CROCUS model if it calculates an exposed ice surface on the glacier. Thus, in this case, we impose a minimum of 1 meter of snow at 3160 m (where snow thickness is generally minimal) and we use the measured accumulation gradient to complete the snow cover thickness over the glacier.

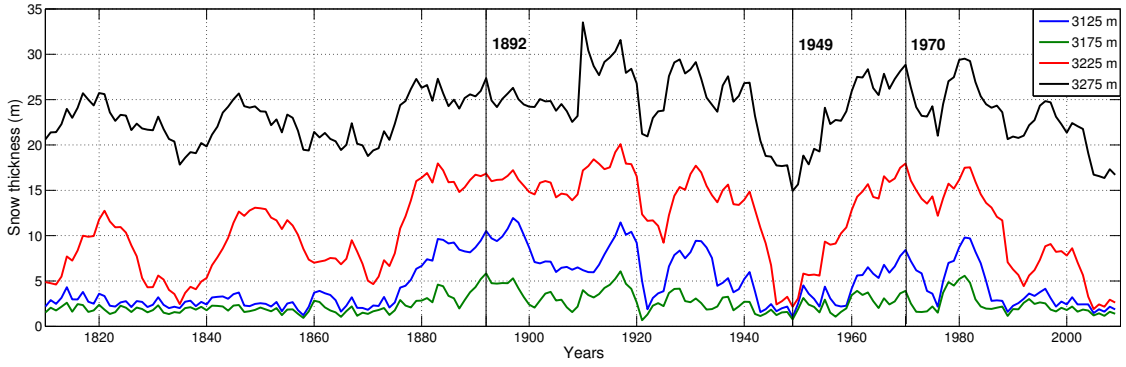

FIGURE 5.4 – Mean annual firn+snow thicknesses on Tête Rousse Glacier modeled by CROCUS at four different elevations (3275 m a.s.l. in black, 3225 m a.s.l. in red, 3175 m a.s.l. in green and 3125 m a.s.l. in blue) for the period 1810-2010. The years 1892, 1949 and 1970 correspond respectively to the date of the first outburst flood and the date of the two first photographs shown in Figure 5.2.

Snow cover modeling results presented in Figure 5.4 show rapid and large changes of snow thickness over the last 200 years. From the beginning of the study period to 1878, the snow cover thickness on the glacier was lower than over the 20^{th} century. Between 1878 and 1892, periods of positive mass balance increased the snowpack thickness by about 4 m (at 3175 m a.s.l.) to 10 m (at 3225 m a.s.l.). The snowpack then remained thick until 1930 and the glacier was snow covered all year round with a thickness ranging from 3 to 20 m (except between 1921 and 1926). Due to a period of strong negative mass balances during the forties, Tête Rousse Glacier quickly lost its snow cover to become snow-free on a large part of the glacier in 1949 (see Figure 5.2). Snow cover increased again between 1955 and 1985 before returning to a state where permanent snow cover was limited to the highest part of the glacier (see Figure 5.3).

5.4.2 Thermal regime

5.4.2.1 Comparison with observations in 2010

Measured and simulated temperature distributions for September 2010 along the longitudinal section are shown in Figure 5.5. Measurements and simulation are in very good agreement (Figure 5.5b) and show a polythermal structure with a cold tongue and temperate ice in the upper part of the glacier. Advection of temperate ice is not sufficient to impact significantly the cold temperature

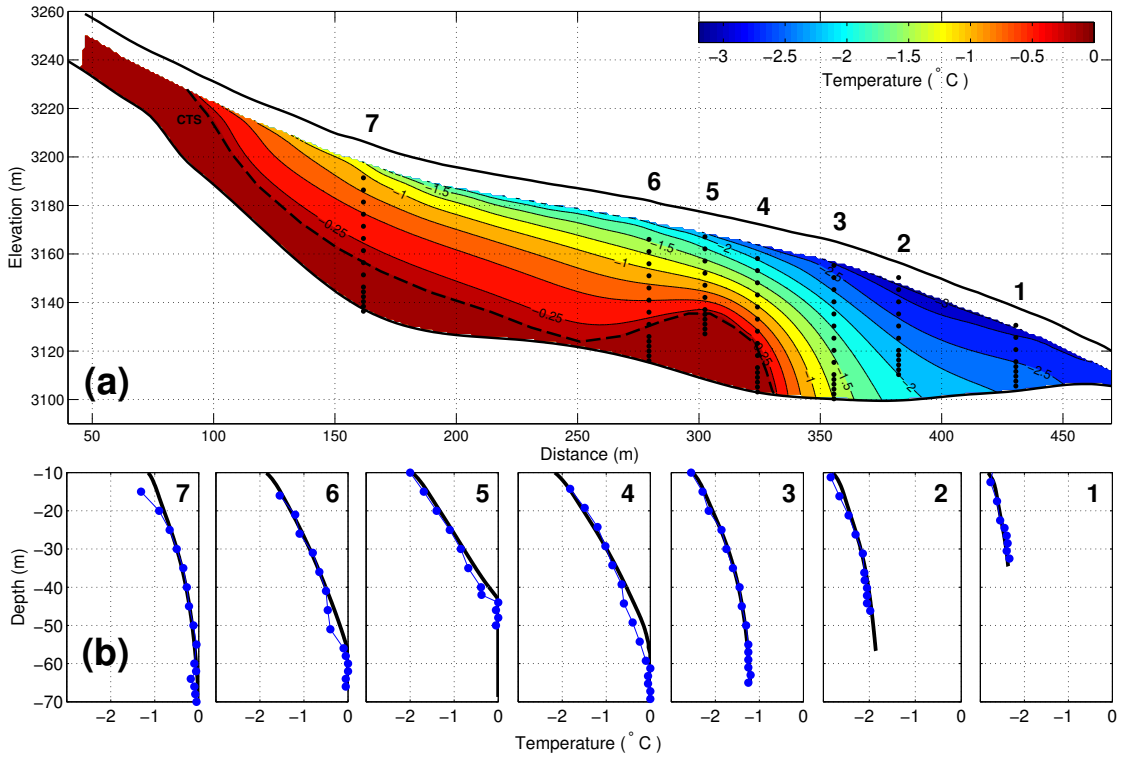

FIGURE 5.5 – (a) Modeled englacial temperatures in 2010 for Tête Rousse Glacier. Black dots show thermistor locations in the boreholes. (b) Comparison between measurements (blue dots) and simulation (black bold line) at each borehole. The borehole numbers are indicated in (a) and (b). The cold temperate transition surface (CTS) is indicated with a dashed line.

of the glacier tongue. Surface temperatures (between 0 and 10 m deep) are not plotted in Figure 5.5 given that they are influenced by seasonal changes. The temperate zone at the center of the glacier, between distance 280 m and 330 m, is due to the 55,000 m^3 water reservoir drained in 2010 (*Vincent et al.*, 2012) and fixed in the boundary conditions since 1980. The date of appearance of this water-filled cavity and its thermal influence will be discussed in section 5.4.2.2.

Simulation Numbers	Modified parameters	New Values
1 and 2	F_b	0 and 30 10^{-3}
3 and 4	dT/dz	$^{-6}$ 10^{-3} and -7 10^{-3}
5 and 6	D_{day}	1 10^{-3} and 5 10^{-3}
7	v_z	3.0 10^{-6}
8	s_r	0.1
9 and 10	ω_{ice}	4 and 16
11 and 12	z_{snow}	$z_{snow} = z_{snow}$ +1 and $z_{snow} = z_{snow}$ - 1
13 and 14	z_{snow}	$z_{snow} = z_{snow}\times 2$ and $z_{snow} = z_{snow}/2$
15	z_{max}	40

TABLEAU 5.3 – List of simulation performed for sensitivity test. One parameter is modified from Table 2 in each simulation.

We performed sensitivity tests for the main parameters of the model by comparing 2010 englacial

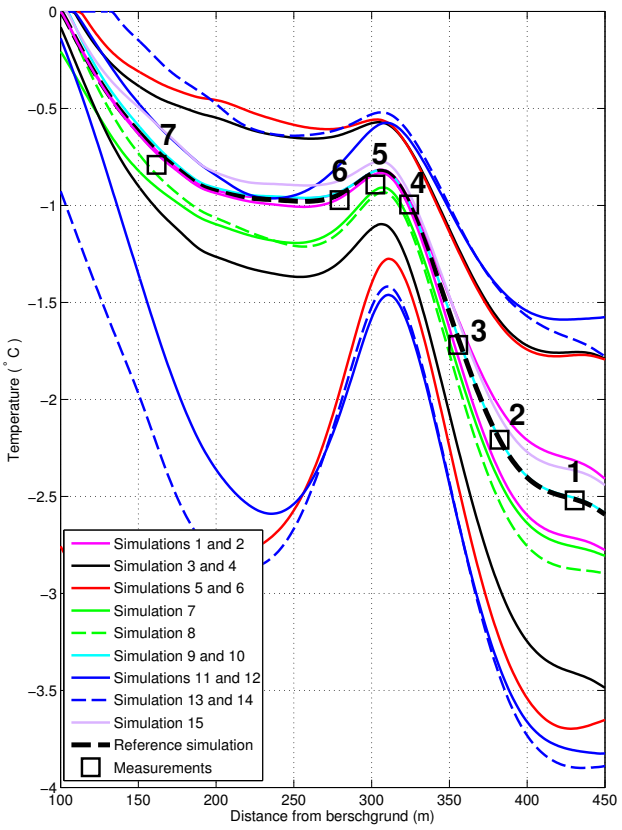

FIGURE 5.6 – Simulated 30-m depth englacial temperatures along the central longitudinal section (red dashed line in Figure 5.7a) for different parameter sets. Squares represent the measurements (with borehole numbers from Figure 5.1) and the black dashed line shows model results using the reference parameter set (see Table 5.2). Other curves show the modeled englacial temperatures with other parameter values summarized in Table 5.3.

temperatures simulated using a given set of reference parameters with temperatures obtained when varying each parameter from its maximum to its minimum values (Table 5.3) taken from the literature (see section 3.2) and/or field observations. Figure 5.6 shows the results along a one-dimensional longitudinal profile at about 30 m depth (red dashed line in Figure 5.7a). The most sensitive parameters are the degree-day factor (red line), snow cover thickness (blue and dashed blue lines) and surface temperature (the air temperature gradient, black line). The other parameters (temperate ice porosity, water percolation velocities, basal flux, maximum snow thickness, residual water saturation in snow and maximum water content in ice) are less sensitive, and do not imply a temperature difference exceeding 0.5°C along the considered one-dimensional longitudinal profile. The sensitivity to snow cover is investigated by observing the impact of snow persistence throughout the year and snow thickness separately. Note that adding or removing just one meter of snow to the annual snowpack has the same impact as multiplying or dividing the snow thickness by two. Consequently, the persistence of snow all year round, which turns into firn, is the most important process controlling the thermal regime of the glacier in comparison with winter snow thickness.

The tongue of the glacier remains cold irrespective of the parameter set used for the simulation. This means that current climatic conditions lead undoubtedly to a polythermal glacier. Transfor-

mation to a temperate glacier would require persistence of snow cover exceeding 7 to 8 m over the whole glacier surface for several consecutive years.

5.4.2.2 Thermal influence of the subglacial water-filled cavity

The temperature inside the subglacial water-filled cavity is set to 0°C assuming thermodynamic equilibrium between the liquid and solid phases. As surrounding ice temperature is negative (Figure 5.5a and 5.5b), heat conduction largely contributes to warming the glacier around the cavity. Because of the low velocity of heat transfer in ice, this warming effect is very dependent on the date on which the cavity formed, i.e. if thermal equilibrium has been reached or not. In this section, "steady state" or "thermal equilibrium" will mean that the subglacial lake no longer has an influence on ice temperatures change. We have therefore analyzed the thermal effect of the subglacial lake to answer two questions : Is the observed (2010) temperature field at steady state ? How is the age of the cavity related to the observed temperatures ?

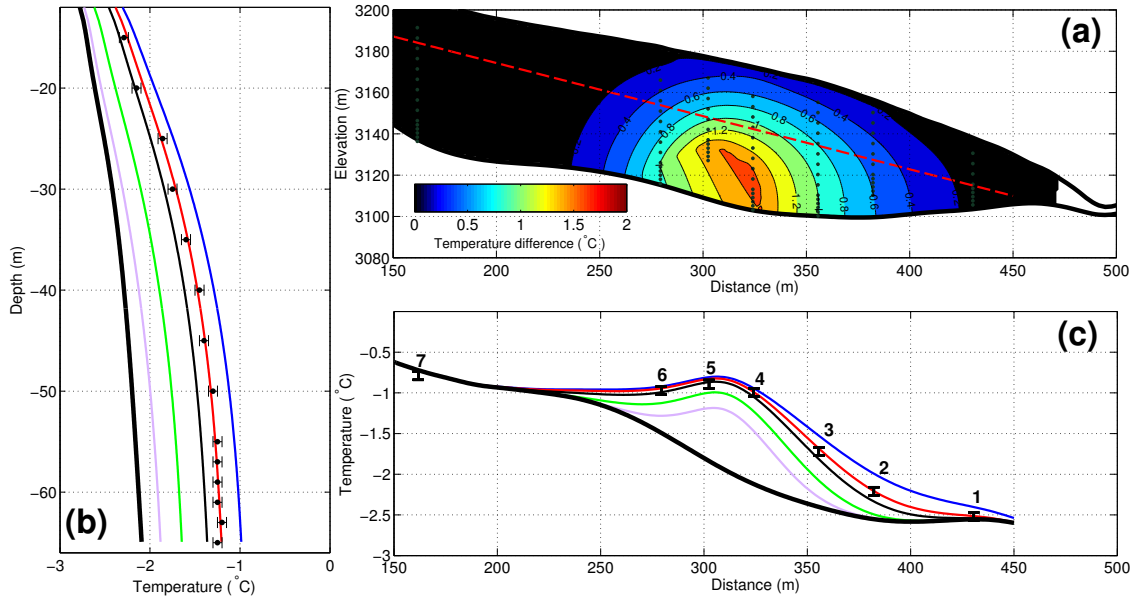

FIGURE 5.7 – (a) Differences in steady state temperature between the glacier with and without a subglacial lake. (b) Temperatures measured and modeled in borehole 3 for different dates of lake formation. Error bars represent measurements, the black bold line is the modeled temperature without the lake and the blue line is the modeled temperature with a lake at thermal equilibrium with the surface of the glacier. Purple, green, black and red curves are the thermal states for a lake formed respectively in 2005, 2000, 1990 and 1980. (c) Borehole temperature measured and modeled along the red dashed line in Figure 5.7a for different dates of lake formation. The fit with red curve means that the lake was likely formed in 1980. Error-bars represent measurements (with borehole numbers from Figure 5.1). The curve legend is the same as for Figure 5.7b.

To investigate steady state conditions, we consider this subglacial cavity to be formed as far as possible in the past, i.e. in 1907 (beginning of the Lyon-Bron air temperature time series). Starting the simulation in 1907 allows us to make sure that a steady state is reached. Indeed, our simulations show that thermal equilibrium between the surface of the glacier and the 0°C zone is reached after

60 years. To determine how the subglacial lake modifies the temperature field at steady state, an additional simulation with no subglacial reservoir was performed. This simulation shows that the thermal effect of the subglacial reservoir in the surrounding cold ice is only significant (difference $> 0.1°C$) at a distance less than 100 m downstream of the cavity and less than 70 m upstream of the cavity (due to ice-flow advection). A very small influence is therefore detected at borehole 1. Average temperatures at boreholes 2 and 3 increase by $+0.5°C$ and $+0.8°C$, respectively (Figure 5.7a). Comparing the steady state simulation (cavity created in 1907) to the temperature profiles measured in boreholes 2 and 3 (Figure 5.7b and 5.7c), we note that the observed temperatures disagree with this steady state ($r^2 = 0.72$). This suggests that thermal equilibrium between the surface and the cavity was not yet reached in the thermal state observed in 2010.

From the previous conclusion, a remaining question is the age of the subglacial lake required to reach the temperatures observed in 2010. To determine this, the thermal effect of the 0°C-volume was investigated by making it appear at different dates. Simulations were performed considering a subglacial water-filled cavity appearing in 2005, 2000, 1990 and 1980 respectively. The modeling experiments reported in Figure 5.7b and 5.7c show that temperatures measured in boreholes 2 to 6 can only be explained by a cavity that is 30 years old ($r^2 = 0.99$).

The dependency of this conclusion on the parameter values used in the simulation was checked with a sensitivity test. The temperature profile measured in borehole 1 is effectively sensitive to all model parameters (Figure 5.6) although it is very little thermally influenced by the water-filled cavity (Figure 5.7a). Thus, if we assume that the cavity appeared after 1980, and that the warming simulated in boreholes 2 to 6 is due to changing parameters, simulated temperatures in borehole 1 would have also been modified, and would disagree with the data. This is not the case and leads us to conclude that our model parameters are well constrained by borehole 1 temperature data. Therefore temperature measurements in boreholes 2 to 6 suggest the existence of a subglacial water reservoir for 30 years. This result is obtained assuming constant cavity geometry, i.e. not taking into account any cavity growth. This means that the thermal influence of the cavity could be overestimated and that the cavity may have started to grow a few years before 1980.

5.4.2.3 Thermal regime variability over the last two centuries

Figure 5.8 shows the temperature distribution at six different dates in 1860, 1892, 1920, 1950, 1980 and 2010. Simulated englacial temperatures in 1860 are not very sensitive to initial conditions in 1800 (cold glacier at -2.5°C throughout). Indeed, a simulation performed with an initial temperate glacier in 1800 gives similar results as of 1860 with the same extent of the temperate zone and less than a 1°C temperature difference in the cold zone. To set relevant boundary conditions, we also assume the existence of a supraglacial lake as of 1870, at the level of the upper cavity in 1892 (*Vincent et al.*, 2010a), and the existence of a subglacial cavity since 1980 as presented in the previous section. Results show that the extent of the temperate part of such a small and thin glacier can change significantly over a 15 to 20–year period. Figures 5.9a, 5.9b and 5.9c shows that the extent of the temperate part is clearly linked to the snow thickness on the glacier. Consequently, the expansions of temperate parts of the glacier are negatively correlated to air temperature variations. Higher accumulation can lead to temperate conditions at the glacier tongue as observed in the late

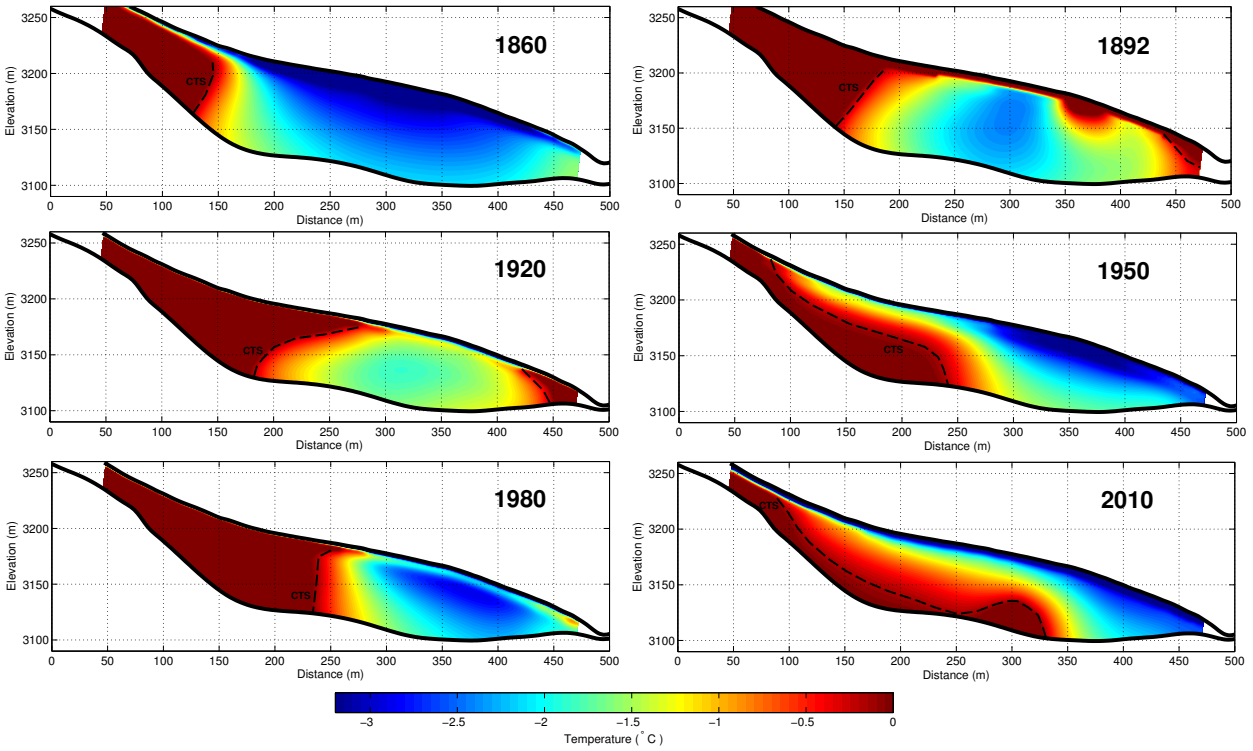

FIGURE 5.8 – Englacial temperature for Tête Rousse Glacier for six different dates over the last 200 years.

19th century (Figure 5.8). Although the central part of the glacier has remained cold over the whole period of simulation, the temperate part included as much as half of the total volume of the glacier in 1920 and 1980. Our simulations show that Tête Rousse Glacier has been a polythermal glacier since the beginning of our study period. This is in disagreement with the conclusion of *Mougin and Bernard* (1905). These authors reported measurements performed at different times in the ice at 15 and 20 m depth at the level of the 1892 upper cavity (Figure 5.1) and concluded that the glacier was temperate in 1903. Their measurements were made 11 years after the 1892 event and were probably influenced by a local warming effect caused by meltwater infiltration into the old upper cavity, the inner central part of the glacier remaining cold.

The last 25 years are known as a period of strong negative mass balances for Alpine glaciers, mainly explained by an increase in summer air temperatures (*Vincent*, 2002) (Figure 5.9a). A paradoxical consequence on Tête Rousse Glacier is the glacier cooling effect caused by reduction of the surface firn cover (Figures 5.9b and 5.9c). However, no trend in winter snow accumulation is observed (Figure 5.9c), which shows that the cooling effect mainly comes from increased summer melting (which reduces the firn thickness). The influence of winter snow precipitation is not significant in comparison to the influence of firn depth and extent. Our model clearly indicates that the temperate part of the glacier has shrunk over the last 25 years (Figure 5.9b). Thus, deep temperate ice observed in the upper part of the glacier in 2010 is likely to come from the temperate accumulation zone simulated between 1955 and 1980 and is now cooling.

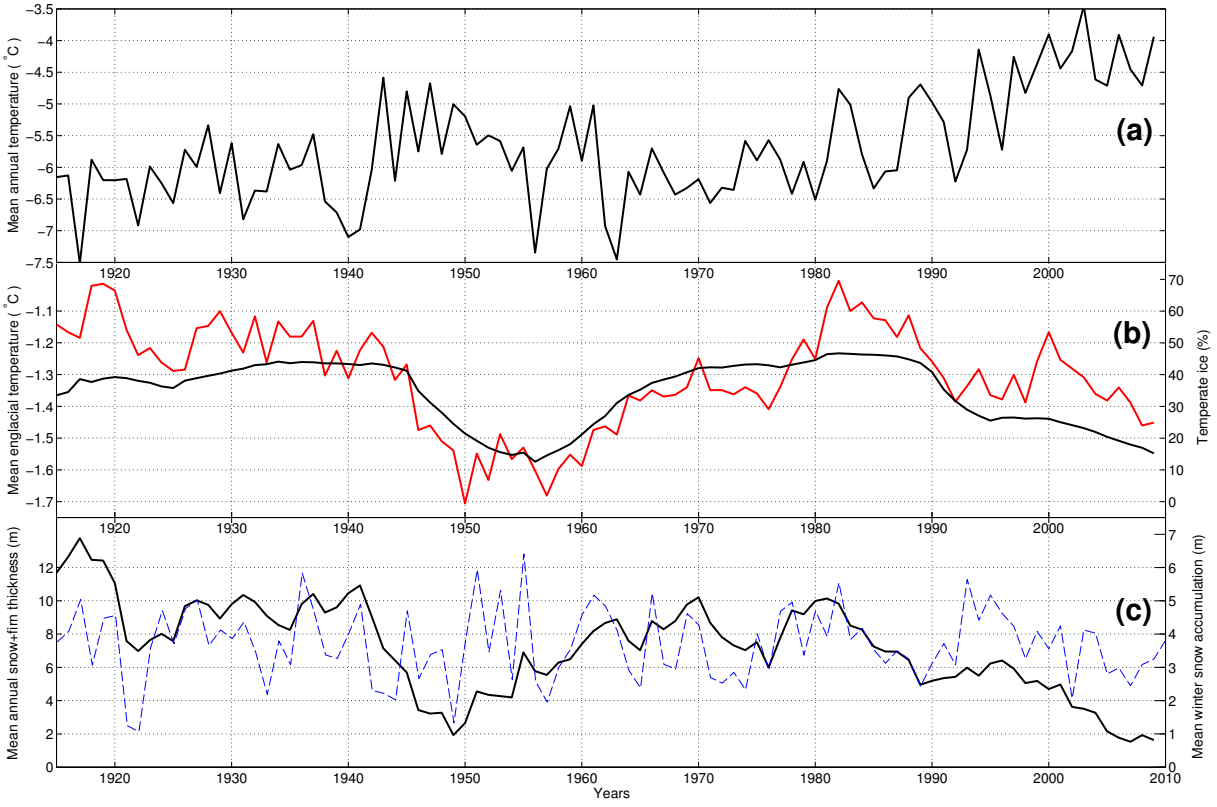

FIGURE 5.9 – (a) Mean annual air temperature measured at Lyon-Bron meteorological station and extrapolated to Tête Rousse Glacier. (b) Mean englacial temperature of Tête Rousse Glacier (red curve) and proportion of the temperate part of the glacier (black curve). (c) Mean annual snow thickness simulated on Tête Rousse Glacier (black line) and mean winter snow accumulation (blue dashed line) from December to April.

5.5 Discussion

5.5.1 Thermal regime

Simulations shows that the polythermal structure of the glacier is strongly influenced by the snow and firn cover which control englacial temperature distribution within the glacier. Two processes are involved here, the refreezing of meltwater (process (a)) and the thermal insulation provided by this snow and firn cover (process (b)). Process (a) releases latent heat that warms up the snowpack (and firnpack). This process occurs when surface meltwater percolates into the cold snowpack or when stored liquid water refreezes in winter. This process warms the snow and firn up to 0°C each year during summer and also stores energy by trapping liquid water which can potentially refreeze later. This mechanism does not appear on snow-free surfaces of the ablation area because, in this case, the surface meltwater is lost by runoff. Process (b) reduces the heat loss by thermal diffusion during winter as a function of snow/firn thickness. Owing to the extremely low thermal conductivity of the snow (values of ∼0.2 to 0.4 W m^{-1} K^{-1}, (*Sturm et al.*, 1997)), the upper snow/firn layers act as an insulating layer that efficiently limits the diffusion of the cold

wave through the snowpack from the surface towards the older underlying layers. The efficiency of this process depends on the snow thickness. We show in our model that below 7 to 8 m, the firn formed during previous years always remains at 0°C and all the water stored sufficiently deep in the firn layers of the glacier cannot refreeze and keep the upper ice layer of the glacier temperate all year round. The contribution of these two processes is not the same over the whole glacier surface because snow thickness is spatially variable. This can explain the observed thermal structure of Tête Rousse Glacier.

The accumulation zone of Tête Rousse Glacier corresponds to a "wet snow" accumulation zone (*Paterson*, 1994) i.e. all the snow accumulated during winter reaches 0°C in summer mainly due to process (a). After that, meltwater is lost by runoff or trapped by an impermeable surface (ice layer or interface between firn and ice). Consequently, in the accumulation zone, when the entire snowpack accumulated during winter has reached 0°C, water percolates through the firnpack down to the waterproof ice surface, forming a water-saturated layer at the firn/ice interface. Due to latent heat released when it refreezes, this water-saturated layer keeps the upper ice layer of the glacier temperate. Furthermore, if the snow cover is sufficiently thick (> 8 m), process (b) prevents refreezing of all the water stored in deep firn layers of the glacier and keeps the upper ice layer of the glacier temperate all year round.

In the ablation zone, because of the absence of snow/firn at the glacier surface during summer, the meltwater cannot be trapped and is evacuated by runoff over the impermeable ice surface. Therefore, no latent heat can be released by refreezing and energy from process (a) is lost and does not warm up the glacier. Process (b) is also less efficient because the snow thickness does not exceed the winter accumulation.

Consequently, englacial temperature strongly depends on the respective sizes of the accumulation and ablation zones which have significantly changed in the past as shown by our snow/firn thickness simulation over the last 200 years (Figure 5.4). As a consequence the polythermal structure of Tête Rousse Glacier observed in 2010 results from snow and firn thickness changes in the past.

The consequences of the recent decreasing firn cover due to climate warming is a cooling of Tête Rousse Glacier. This result conflicts with most of the studies showing that glaciers are warming in a warming climate, not only in their accumulation zone (*Vincent et al.*, 2007b; *Gilbert et al.*, 2010; *Hoelzle et al.*, 2011) but also in their ablation zone (*Pettersson et al.*, 2003; *Gusmeroli et al.*, 2012; *Rabus and Echelmeyer*, 2002). Cooling may only occur in the vicinity of the fluctuating firn. In the case of Tête Rousse Glacier, due to its small elevation range (150 m), the whole glacier is located within the fluctuating firn zone, explaining why the entire glacier is cooling although air temperatures are rising. This specific behaviour of Tête Rousse Glacier is due to its small size as well as its altitudinal location.

5.5.2 Water storage in the glacier

5.5.2.1 Case of the outburst flood in 1892

In the analysis of the 1892 outburst flood, *Vincent et al.* (2010a) concluded that water had been stored in a supraglacial lake formed in the 1860-70s and covered afterwards by the heavy annual snowfalls of the winters of the 1880s. Englacial and subglacial conduits may have drained the water towards the glacier terminus where a watertight cavity was formed in contact with the bedrock. However the causes of the bursting of the terminus still remain unclear. Two possible explanations were considered by these authors. First, the glacier terminus could have burst due to the water pressure against the thinning ice roof of the lower cavity. Another possibility could be linked to a thermal regime change. Simulations performed in the present study support the second hypothesis.

Indeed, most of the glacier was comprised of cold ice for more than 20 years before 1880 (Figure 5.8). This favored the formation of a supraglacial lake filled with meltwater trapped over an ice-impermeable surface (*Boon and Sharp*, 2003) in the context of a flat topography. Furthermore, the formation of the lower cavity required a cold tongue frozen to bedrock to avoid any water drainage through subglacial conduits (*Vincent et al.*, 2010a). Between 1878 and 1892, successive years with positive mass balances were responsible for a sufficiently high snow accumulation to produce temperate conditions in the lower part of the glacier tongue (Figure 5.8, 1892 panel). The temperature rise of the glacier sole linked with snow accumulation was probably the process responsible for the 1892 rupture. However, the formation of the englacial conduits from the upper to lower cavity remains unclear for the case of cold ice as simulated in our study (between -1.5°C and -1°C here). Only mechanical fracturing of the ice could explain water drainage in such a case (*Fountain and Walder*, 1998; *Van der Veen*, 2007).

5.5.2.2 Cold/temperate interface : a trap for subglacial water

The processes explaining the subglacial water-filled cavity discovered in 2010 are different than those explaining the 19th century lake. Results presented in section 5.4.2.2 tend to support the existence of a 30-year old internal cavity and Figure 5.8 shows that the upper part of Tête Rousse Glacier was generally made up of temperate ice over the last century. In this zone, surface meltwater can drain to the glacier bedrock through small englacial conduits or crevasses (*Fountain and Walder*, 1998; *Fountain et al.*, 2005). Water can also enter below the glacier along the rock-ice interface from the Aiguille du Goûter western face and form subglacial water streams. These streams can contribute to melting of the ice, creating channels descending along the sloping bedrock (*Fountain and Walder*, 1998) due to pressure-induced melting (*Paterson*, 1994). This subglacial water is then trapped by the cold and impermeable lower part of the glacier, creating a water-filled cavity. How the cavity was formed remains unclear but high water pressure measured in 2010 in the cavity suggests mechanical processes involving hydraulically driven fracturing and ice deformation around a high water pressure zone (*Vincent et al.*, 2012). Energy transfer through the roof of the cavity, as low as -1.9 10^{-1} W m^{-2} according to our simulations, is not sufficient to refreeze the stored water. Indeed, with such an energy flux, refreezing of 1 m of the cavity wall would take ∼55 years (2 cm yr^{-1}). Thus, the location of the cavity observed in 2010 corresponds to the lowest elevation ever

reached by the trapped water, which is the same as the location of the temperate part of the glacier at the end of the seventies. In case of regression of the temperate part as indicated by simulations over the last 30 years, the cavity cannot move upward and is progressively surrounded by cold ice as observed in 2010.

The minimum volume of this subglacial water reservoir was estimated to be 45,000 m^3 in 2010 (*Legchenko et al.*, 2011; *Vincent et al.*, 2012). The roof of the northern part of the cavity was about 6 m below the surface and the hydrostatic water pressure was close to the overburden pressure (*Vincent et al.*, 2012). Consequently, to prevent the subglacial lake from outbursting, it was totally artificially drained in early fall 2010.

5.6 Future evolution

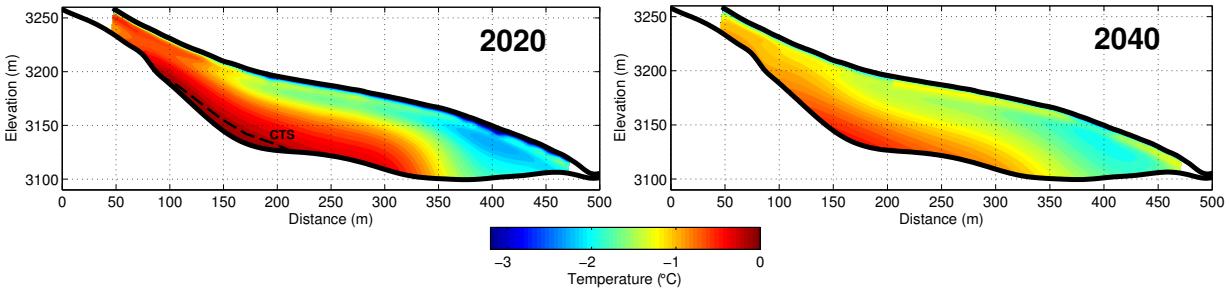

FIGURE 5.10 – Future temperature distributions for Tête Rousse Glacier in 2020 and 2040 assuming an air temperature warming of 2°C over the next 100 years and a constant precipitation rate.

The future evolution of the thermal regime of Tête Rousse Glacier was investigated by testing two scenarios and assuming no change in the snow precipitation rate. Meteorological conditions over the next 30 years were considered similar to those of the last 10 years, except for air temperature, assumed to increase linearly at a rate of 2°C and 5°C per 100 years. The results for the two scenarios are very similar and only the first is reported in Figure 5.10. In both cases, the glacier will be totally in the ablation zone and will remain comprised of cold ice with a deeper residual temperate part in 2020 and entirely cold in 2040 (Figure 5.10). Despite strongly differing temperature conditions, both scenarios have roughly the same impact on the glacier thermal state. The greater surface warming for the +5°C scenario is partly counteracted by the effect of surface temperature cooling related to the greater diminution of snow cover extent for this scenario, leading to an overall similar effect on englacial temperatures for both scenarios. In conclusion, in the coming decades, the glacier will become completely cold, gradually preventing water from snow melt to percolate through the glacier and therefore limiting the possibilities of subglacial water-filled cavity formation. Note that in both scenarios, we did not take into account glacier thinning that could accelerate cooling and the snow precipitation rate is maintained constant. According to our numerical modeling, a 30% increase in the precipitation rate could maintain the temperate part of the glacier. For atmospheric warming scenarios higher than + 3°C from present, the local mean annual air temperature will be positive after 2080.

5.7 Conclusion

The thermal regime of Tête Rousse Glacier is characterized by a temperate accumulation area and a predominantly cold ablation area. This polythermal structure is explained by the presence of a wet accumulation area and a negative mean annual air temperature. This cover insulates the glacier in winter and warms it up to the melting point in summer by releasing latent heat from the refreezing of meltwater. The absence of a firn layer in the lower part leads the glacier to reach a temperature close to the local mean annual temperature (-2.8°C) below a depth of nearly 10 m which englacial temperature are not influenced by the seasonal temperature change. Due to the very low glacier dynamics, the gravitational temperate ice advection from the upper part of the glacier cannot balance this thermal equilibrium likely present over the last 30 years. Heat flow modeling shows that each summer, snow and firn reach 0°C due to meltwater refreezing. Moreover, when the snow cover exceeds a thickness of 7-8 m, a water saturated layer subsists at the firn-ice interface during winter, maintaining the temperature of the surface layers at 0°C. Thus, the englacial temperature distribution directly depends on the snow cover thickness distribution and changes. Simulations of snow cover and englacial temperatures over the last 200 years show that the glacier was cold before 1870 but then gradually warmed up until 1920 due to a snow thickness increase. During this period, the glacier was almost entirely temperate except for its central deeper part which remained cold. The 1892 outburst flood event may have been triggered by a change from cold to temperate conditions at the glacier tongue. The temperate part was large until 1980, allowing water to percolate through the glacier until becoming trapped at the cold-temperate interface. From the comparison of modeled and observed temperatures, we show that water had probably been stored for around 30 years in the subglacial water-filled cavity discovered inside the glacier in 2010. This confirms a probable cavity formation between 1970 and 1980. The future evolution of the thermal regime and the associated water storage of Tête Rousse Glacier depend on the future mass balance trend. According to atmospheric temperature increase scenarios of +2°C and +5°C for the coming century, snow cover will become very thin and spatially reduced and most of the glacier will become cold. Finally, assessment of the outburst flood hazard associated with the water cavity will require further investigations regarding the mechanisms of water percolation through temperate ice. Cavity formation, filling and bursting will also need to be better understood. Dye tracing experiments will be performed in a near future to better understand the internal hydrological network of the glacier and the origin of the internal water cavity.

Acknowledgements This study was funded by Le Service de Restauration des Terrains en Montagne (RTM) of Haute Savoie (France), the city of Saint Gervais (France) and the Joseph Fourier University – Grenoble (Pôle TUNES program). Funding was also provided by the European "GlaRiskAlp" Alcotra Program. We thank P. Possenti for conducting the drilling operations and the USGS-EDC for providing free access to Landsat images. SPOT images were provided through the CNES/SPOT-Image ISIS program, contracts 405 and 435. Finally, we thank R. Böhm for providing the homogenized instrument temperature data going back to 1760 in the Alps and Météo-France for providing meteorological data for the 20th century. We also thank A. Gusmeroli, J. Walder and

an anonymous reviewer for helpful comments and suggestions and we are grateful to H. Harder who revised the English of this manuscript.

Résumé des résultats et conclusions

Dans ce chapitre, on montre que l'épaisseur de la neige saisonnière et du névé autour de la ligne d'équilibre du glacier contrôle très largement le régime thermique du glacier dans cette zone. Dans la mesure où les conditions climatiques locales le permettent (moyenne annuelle des températures de l'air entre -5°C et 0°C), le glacier peut varier d'un état froid à un état tempéré simplement en réponse à une variation de l'épaisseur totale du névé. Sur le glacier de Tête Rousse, les résultats, en très bon accord avec les observations, montrent que le modèle de surface présenté en chapitre 3 peut être adapté aux zones d'accumulation tempérées.

Les simulations effectuées mettent en évidence que le volume de glace tempérée sur le glacier de Tête Rousse est très variable dans le temps et varie avec l'épaisseur du névé. On montre que l'épaisseur de névé plus importante dans la partie haute du glacier comparativement à celle de la zone d'ablation explique la structure thermique particulière du glacier de Tête Rousse (fig 5.5). Cette structure, associée à la topographie du lit rocheux, permet de piéger efficacement de l'eau liquide dans le glacier. L'eau de fonte de surface atteint le socle rocheux par percolation dans la partie amont tempérée du glacier avant d'être retenue par la langue de glace froide et collée à son socle de la partie aval du glacier. On montre que le volume de glace tempérée du glacier diminue progressivement depuis 1990 en réponse à la diminution de l'épaisseur du névé associée aux bilans de masse négatifs des deux dernières décennies (fig 5.9). Les simulations dans le futur montrent que le glacier devrait continuer à se refroidir dans l'hypothèse d'un réchauffement climatique de 2°C ou 4°C à l'horizon 2100 (fig 5.10). Ceci s'explique par la disparition progressive du névé (le glacier devient alors entièrement en ablation dans ces scénarios). Le glacier devrait devenir entièrement froid d'ici 2040. La reconstitution de l'évolution du régime thermique du glacier de Tête Rousse depuis 1860 nous éclaire sur les processus responsables de la catastrophe de 1892 (voir chapitre 2) et de la formation de la poche d'eau découverte en 2007. En effet, au milieu du 19ème siècle, le glacier était certainement froid en grande partie, avec une topographie de surface différente. Un lac supra-glaciaire a pu se former comme l'attestent *Vincent et al.* (2010a) avant d'être recouvert par des couches de neige et former une poche d'eau sous glaciaire proche du front du glacier. La rupture du front du glacier en 1892 fait suite à une série de bilans de masse très positifs qui ont augmenté de manière importante l'épaisseur de la couverture neigeuse. Les simulations montrent alors que le front du glacier est devenu tempéré. Ce réchauffement pourrait être la cause de la rupture de la langue frontale, à l'origine de la catastrophe (fig 5.8).

La modélisation de la perturbation thermique de la poche d'eau découverte en 2007 dans la glace froide qui l'entoure montre que cette poche existe depuis au moins 30 ans (fig 5.7). Cette période à correspond une époque où la taille de la zone tempérée était conséquente (45% du glacier), ce qui a pu permettre le développement d'importants chenaux interglaciaires dans la partie amont du glacier. Ces chenaux ont facilité la formation de la poche d'eau découverte en 2007. On pense que la poche s'est formée progressivement par déformation de la glace sous la pression de l'eau (lors des premiers forage en 2010 la poche d'eau était de type artésienne). Aujourd'hui le problème de la poche d'eau de Tête Rousse reste d'actualité et les autorités font face à des questions délicates : peut-on envisager une solution pérenne (drainage artificiel permanent) ? Faut-il continuer de pomper régulièrement ?

Faut -il maintenir un système d'alerte ? Une expertise réalisée par des équipes du LGGE, du LTHE, de Isterre et d'Irstea (*Vincent et al.*, 2011), à laquelle cette thèse a contribué, a permis d'apporter des éléments pour aider les autorités publiques à prendre des décisions pertinentes. L'étude a montré que les trois pompages successifs des étés 2010, 2011 et 2012 ont conduit à une diminution très significative du volume de la cavité. Cette diminution s'explique par le fluage de la glace et les effondrements à l'intérieur de la cavité, le volume passant ainsi de 53 000 m^3 en 2010 à environ 12 000 m^3 en 2012. En revanche une cavité subsiste et se remplit à nouveau très rapidement chaque été. Plusieurs expériences de traçage ont été effectuées dans le cadre de cette thèse pour identifier les points d'alimentation en eau de la cavité (cf annexe B). Ces expériences semblent montrer que l'essentiel de l'eau de fonte de surface atteint la cavité en pénétrant dans le glacier au niveau de la rimaye supérieure du glacier à l'altitude 3260 m. Ainsi, même si le glacier a tendance à se refroidir dans le futur, il est possible que des chenaux d'alimentation partant de la rimaye se maintiennent chaque année avec la fonte et continuent d'alimenter l'intérieur du glacier en eau. En revanche, si la cavité et son réseau d'alimentation finissent par se refermer, le refroidissement du glacier devrait à terme empêcher la formation d'une nouvelle poche d'eau. Le drainage artificiel de l'eau, même par pompage ponctuel, permet la fermeture de la cavité et peut donc solutionner le problème. La question est de savoir combien de pompages seraient nécessaires à la fermeture totale de la cavité et à quelle vitesse celle-ci pourrait s'ouvrir sous la pression d'eau. On estime dans cette étude que la poche avait déjà une taille importante en 1980.Le processus d'ouverture semble donc être très lent alors que la fermeture est relativement rapide (le volume est divisé par 4 en 3 ans). On peut donc penser que quelques pompages annuels pourraient apporter une solution durable ou même définitive si le glacier se refroidit.

Chapitre 6

Régime thermique et reconstitutions climatiques : modélisation inverse

Introduction

Ce dernier chapitre définit une méthode de reconstitution des températures atmosphériques dans le passé à partir de mesures ponctuelles (dans le temps) de profils de température dans le glacier. Il s'agit de résoudre le problème inverse qui lie la température du glacier et la température atmosphérique dans le passé.

L'inversion des profils de températures dans les trous de forages terrestres est une approche qui a déjà été largement utilisée pour les reconstitutions climatiques (*Beltrami*, 2002; *Beltrami and Harris*, 2001; *Pollack et al.*, 1996; *Huang et al.*, 2000). Elle a permis de quantifier les changements de températures au cours des 500 dernières années. Par nature, la diffusion thermique lisse les perturbations de surface : plus une variation a une périodicité courte, plus elle est atténuée rapidement avec la profondeur. Ainsi, seules les tendances sont enregistrées par la température du sous-sol et il n'est pas possible de reconstruire la variabilité climatique haute fréquence. La figure 6.1 illustre par exemple l'atténuation d'une oscillation périodique d'une anomalie de température de surface (ΔT_0) en fonction de sa période d'oscillation et de la profondeur dans le sol. Ainsi, on constate que les variations décennales ne sont plus visibles à 60 m de profondeur (atténuées d'un facteur 100) et les variations centennales ne le sont plus à environ 200 m. La méthode reste en revanche robuste pour reconstruire des tendances à long terme et quantifier une variation climatique moyenne (*González-Rouco et al.*, 2006).

Les calottes de glace offrent des profils de températures profonds allant jusqu'à plus de 3000 m au Groenland ou en Antarctique. On peut ainsi reconstruire des tendances climatiques sur 50 000 à 100 000 ans (*Dahl-Jensen et al.*, 1998; *Salamatin et al.*, 1994). Cependant, il est nécessaire de prendre en compte l'advection due à l'écoulement de la calotte, ce qui induit des incertitudes supplémentaires dans la reconstruction. L'advection verticale de la température permet en revanche de limiter le filtrage haute fréquence de variations climatiques et de reconstruire les variations de plus courte période en comparaison à celles que l'on pourrait reconstruire avec de la diffusion pure seulement. En effet, une perturbation de surface qui est advectée en profondeur peut être conservée plus longtemps car elle ne va pas être «effacée» par une nouvelle perturbation de surface. La figure 6.2 montre un exemple de propagation d'une anomalie de température de surface d'une périodicité de 10 ans avec ou sans advection verticale. La présence d'advection permet d'avoir des informations sur plusieurs cycles alors qu'avec de la diffusion pure, cette information est réduite au dernier cycle d'où l'intérêt des profils glaciaires par rapport aux profils dans le sol.

Ces méthodes appliquées à des profils de température dans des glaciers de type alpin restent en

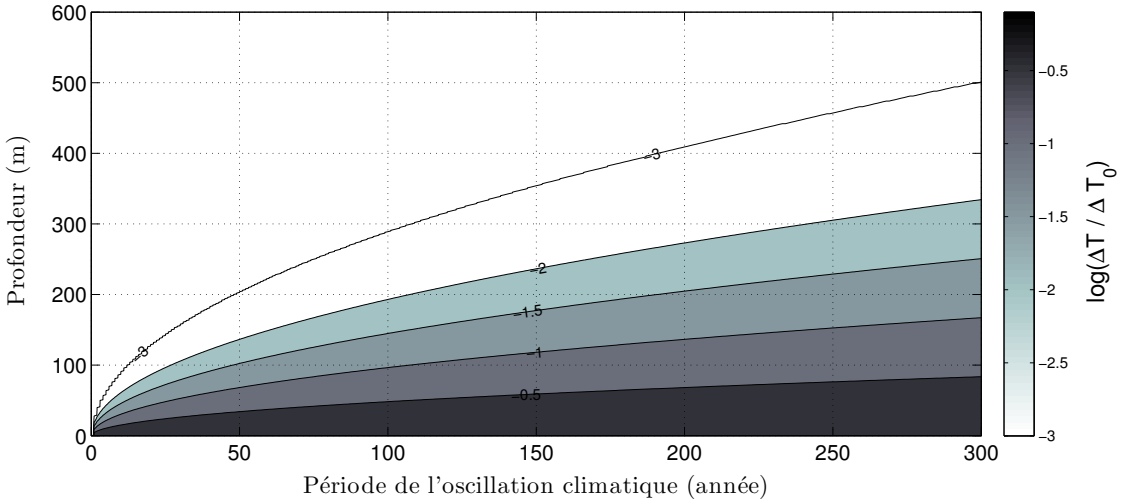

FIGURE 6.1 – Atténuation d'une variation de température de surface périodique dans la glace en fonction de la profondeur et de la période de cette variation.

revanche très peu utilisées car la faible profondeur des profils ne permet que des reconstitutions sur des périodes courtes (de l'ordre d'un siècle). Et surtout, la relation entre la température de surface du glacier et la température de l'air est plus complexe à déterminer car elle est très perturbée par la fonte de surface. De telles reconstitutions nécessitent généralement une quantification indépendante de la fonte de surface si l'on veut obtenir la variabilité des températures atmosphériques et non des températures de surface du glacier (*Gilbert et al.*, 2010) (en annexe). L'intérêt de ces reconstitutions est pourtant réel car elles permettent de quantifier les changements climatiques récents à hautes altitudes où aucune mesure n'est disponible sur de longues périodes. Dans ce chapitre, on propose une nouvelle méthode qui permet la reconstitution des températures atmosphériques à partir de profils de températures dans des glaciers froids subissant de façon occasionnelle des événements de fonte. Aucune mesure complémentaire de fonte ou d'accumulation sur le site n'est nécessaire pour mettre en oeuvre cette méthode. Elle se base sur l'inversion simultanée de plusieurs profils de températures provenant de plusieurs sites avec différentes expositions et donc différents taux de fonte de surface. La méthode est appliquée au Col du Dôme où 7 profils de températures acquis sur plusieurs sites au cours du temps sont inversés simultanément pour en déduire les variations de températures atmosphériques locales sur le dernier siècle.

On utilise une méthode de type Monte-Carlo et une approche probabiliste de type Bayésienne pour déterminer une fonction de probabilité pour chaque paramètre du modèle que l'on souhaite inverser. Le modèle direct est un modèle de régime thermique 1D inspiré du modèle présenté en chapitre 3. En revanche, du fait que seules les tendances sont utilisées comme données de forçage en surface, le modèle utilise un pas de temps d'intégration de un an (les variabilités journalière et même inter-annuelle ne sont pas connues). L'impact de la fonte est ici complètement paramétrée et les processus de percolation/regel ne sont pas explicitement modélisés. Ainsi, les paramètres de vitesse verticale de surface, de fonte de surface, de flux basal et de température moyenne de la surface avant perturbation climatique (température de l'état stationnaire) sont reconstitués pour chaque site de forage. En revanche, la variation des températures atmosphériques du passé est inversée de

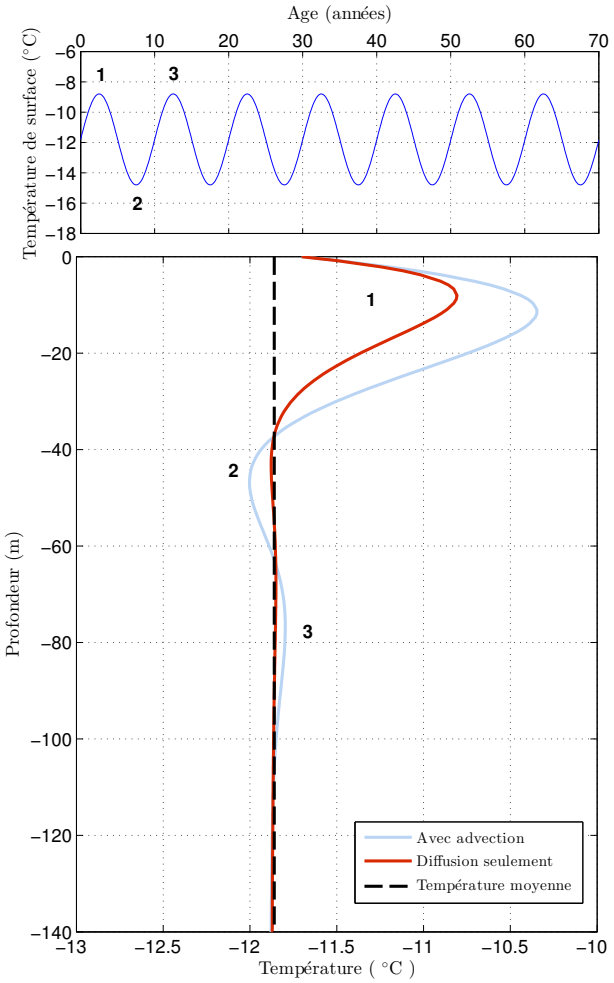

FIGURE 6.2 – Température simulée par un modèle 1D de transfert de chaleur dans la glace à partir d'un forçage périodique en surface d'une période de dix ans (figure du haut). En rouge, une simulation sans advection, en bleu avec advection.

manière commune à tous les sites de forage. Cette méthode est validée par l'inversion de profils de température synthétiques produit par le modèle utilisé en chapitre 3. Ces profils sont produits pour différentes caractéristiques du site de forage (accumulation et fonte de surface) à partir d'une même série temporelle de températures atmosphériques. La comparaison des résultats d'inversion de ces profils synthétiques avec la série temporelle qui a permis de les créer permet d'évaluer les performances de la méthode d'inversion utilisée. Nos résultats permettent de reconstruire de manière robuste le climat passé sur le dernier siècle sur un site à haute altitude pour lequel aucune mesure météorologique de longue durée n'existe. En outre, cette étude apporte un éclairage nouveau sur la question controversée de l'amplification du réchauffement climatique avec l'altitude dans les Alpes (*Rangwala and Miller*, 2012).

Variations des températures atmosphériques sur le 20ème siècle à haute altitude dans les Alpes Européennes à partir des températures glaciaires

D'après :

Gilbert, A. and C. Vincent (2013a),Atmospheric temperature changes over the 20^{th} century at very high elevations in the European Alps from englacial temperatures, *Geophys. Res. Lett.*, 40, doi :10.1002/grl.50401

Abstract Given the paucity of observations, a great deal of uncertainty remains concerning temperature changes at very high altitudes over the last century. Englacial temperature measurements performed in boreholes provide a very good indicator of atmospheric temperatures for very high elevations although they are not directly related to air temperatures. Temperature profiles from seven deep boreholes drilled at three different sites between 4240 and 4300 m a.s.l. in the Mont Blanc area (French Alps) have been analyzed using a heat flow model and a Bayesian inverse modeling approach. Atmospheric temperature changes over the last century were estimated by simultaneous inversion of these temperature profiles. A mean warming rate of 0.14°C/decade between 1900 and 2004 was found. This is similar to the observed regional low altitude trend in the northwestern Alps, suggesting that air temperature trends are not altitude dependent.

Keywords High elevation temperature change ; Bayesian methods ; Borehole temperature inversion ; Cold glacier ; Englacial temperature

6.1 Introduction

The altitude dependency of temperature trends is a key issue for climate change studies (*IPCC*, 2007). It has been suggested that high altitude regions may be more sensitive to global scale climate change than other land surfaces at the same latitudes (*Messerli and Ives*, 1997; *Beniston et al.*, 1997). In the Alps, several studies using climate models have shown an elevation-dependent climate response (*Giorgi et al.*, 1996; *Im et al.*, 2010). In contrast, studies based on ground observations in the Alps do not show a clear elevation dependency (*Ceppi et al.*, 2010; *Rangwala and Miller*, 2012; *Beniston and Rebetez*, 1996; *Jungo and Beniston*, 2001). However, most long-term meteorological data come from altitudes that do not exceed 3000 m a.s.l. In addition, several studies (*Ceppi et al.*, 2010; *Pepin and Lundquist*, 2008) mention that the altitude dependency of surface temperature trends obtained from observations is likely to be influenced by local effects such as snow-albedo feedback and is not representative of temperature trends at a more global scale. Given that there is no long-term temperature series in the Alps for altitudes greater than 3500 m a.s.l. for which this feedback can be neglected (because of snow persistence all year round) the trends obtained from temperature data are difficult to interpret. The temperature-dependency question remains unsolved and, in their review, *Rangwala and Miller* (2012) suggest that both observations and models are currently inadequate to provide a clear understanding of climate change in high elevation regions.

An essential requirement is to increase climate monitoring at very high elevation sites. Mountain summits or isolated saddles located above the 0°C isotherm all year round are the best locations to quantify climate change at high elevations because they are less influenced by topography or urbanization and the snow-albedo feedback does not change significantly at these altitudes (*Pepin and Lundquist*, 2008). Englacial temperatures within cold glaciers provide an excellent tool to investigate climate change in these areas and can be used as a proxy for temperature change where meteorological data are almost inexistent (*Lüthi and Funk*, 2001; *Vincent et al.*, 2007b; *Gilbert et al.*, 2010). In the Mont Blanc (France) and Monte Rosa area (Switzerland, 4500 m a.s.l), englacial temperature observations show that temperature profiles are far from a steady state and show a strong warming since 1980 (*Lüthi and Funk*, 2001; *Vincent et al.*, 2007b; *Hoelzle et al.*, 2011). The near surface firn temperatures depend on complex mass and energy exchanges at the snow surface but are mainly driven by air temperature and meltwater refreezing. This is physically based on the fact that firn surface temperature variations are similar to air temperature variations and energy transport into the firn mainly comes from heat advection/diffusion and water percolation (*Suter*, 2002; *Vincent et al.*, 2007b). The amount of melt energy depends on the surface energy balance which, given the high relevance of shortwave radiation, is highly dependent on elevation, slope, aspect and albedo. The resulting near-surface firn temperature is therefore highly spatially variable (*Suter et al.*, 2001). Consequently, a very high spatial variability in firn or ice temperatures is observed at these very high elevation areas (*Hoelzle et al.*, 2011). In addition to these factors, the deep englacial temperatures also depend on ice and firn advection, firn conductivity and basal heat flux (*Lüthi and Funk*, 2001).

A major challenge of reconstructing past temperatures from ice temperature profiles is the separation of thermal changes due to air temperature from those due to other sources. *Gilbert et al.*

(2010) successfully reconstructed air temperature over the last century at Illimani (Bolivia, 6340 m a.s.l.) from one single englacial temperature profile using complementary data such as ice core density and stratigraphy to quantify the melting intensity and firn advection.

In this study, we reconstruct an air temperature signal over the last century from seven englacial temperature profiles at very high altitudes between 4240 and 4300 m a.s.l. in the Mont Blanc area. This reconstruction is compared to air temperatures observed at lower altitudes. This method was also used to identify criteria that can be used to select the best drilling sites to infer past air temperatures from englacial temperatures.

6.2 Measurements

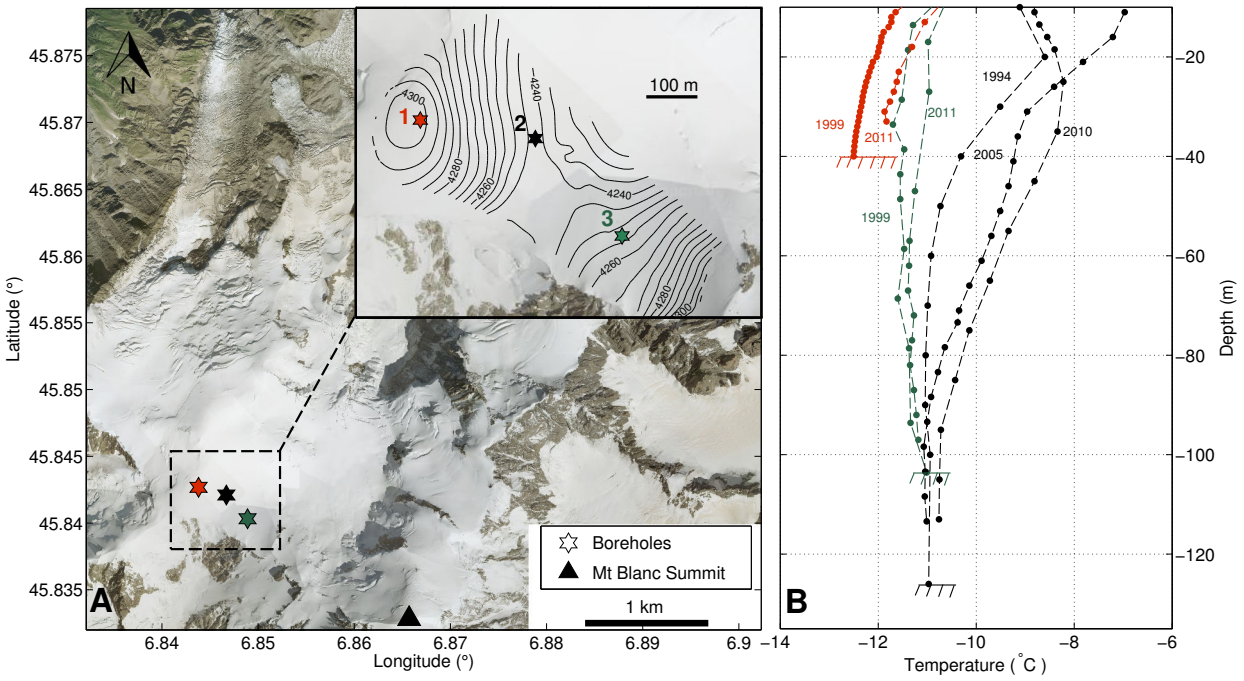

FIGURE 6.3 – A) Aerial view of the studied area with a zoom on the drilling site. Numbers indicate the three borehole drilling sites. B) Ice temperature measurements in boreholes shown in Figure 6.3A with corresponding colors.

Englacial temperature measurements were performed from the surface to bedrock in seven boreholes drilled between 1994 and 2011 at three different sites in the Mont Blanc area located between 4240 and 4300 m a.s.l. (Figure 6.3). At 4240 m, the mean annual air temperature is -10°C and summer temperatures rarely exceed 0°C. Ice thicknesses were 40 m, 126 m and 103 m at sites 1, 2 and 3 respectively. The accuracy of all temperature sensors was better than ±0.1°C except for the 1999 profile at site 3 for which the accuracy was ±0.3°C due to a calibration problem. The boreholes were drilled using electro-mechanical equipment up to 1999 (included) and subsequently by hot water drilling. Measurements were repeated in each borehole several times after drilling until a thermal equilibrium (+/-0.05°C) was reached. The ice temperature measurements are shown in Figure 6.3 and the aspect, slope and elevation of the borehole locations are reported in Table 6.1.

The ice temperature changes exhibit a high spatial variability. Indeed, although sites 2 and 3 are very close (250 m) and at the same elevation (about 4250 m a.s.l.), temperature changes over the last 10 years are very different, for example 0.4°C and 1.2°C at 40 m depth for sites 3 and 2 respectively.

Firn and ice densities were measured on ice cores at all three sites from the surface to bedrock. Horizontal and vertical velocities (v_h and v_0 respectively) were measured by differential GPS surveys over the period 1993-2010 at all 3 sites (Table 6.1). The high spatial variability of snow accumulation is responsible for the very high spatial variability of the subsidence velocity (*Vincent et al.*, 2007a).

Site N°	Elevation (m a.s.l.)	Depth (m)	Firn thickness (m)	Aspect	Slope °	Measurement dates	Horizontal velocities (m year^{-1})	Subsidence velocities (m w.e. year^{-1})
1	4300	40	20	E	8	1999/2011	1.2	0.7
2	4245	126	80	E	10	1994/2005/2010	7.9	3.2
3	4255	103	60	NW	10	1999/2011	3.5	1.3

TABLEAU 6.1 – Borehole site characteristics.

6.3 Methodology

6.3.1 Forward model

To reconstruct the past atmospheric temperature changes, we used a forward model to simulate englacial temperatures from air temperature variations (*Gilbert et al.*, 2010). We assume that horizontal heat advection can be neglected due to very low horizontal velocity (Table 6.1). This assumption is supported by three dimensional numerical experiments (see appendix C). Therefore, we solve the heat diffusion/advection problem at each site in firn and ice in one dimension by solving the heat transfer equation (*Malvern*, 1969; *Hutter*, 1983) :

$$\rho c_p \left(\frac{\partial T}{\partial t} + v_z \frac{\partial T}{\partial z} \right) = \frac{\partial}{\partial z} \left(k \frac{\partial T}{\partial z} \right) + Q_{lat} \tag{6.1}$$

where z is the depth (m), t the time (s), T the temperature (K), c_p the heat capacity of ice (= 2030 J kg^{-1} K^{-1}), ρ the firn density (kg m^{-3}), v_z the vertical advection velocity (m s^{-1}), k the thermal conductivity of firn (W m^{-1} K^{-1}) and Qlat the latent heat released by refreezing meltwater (W m^{-3}). Equation 6.1 is solved using the spectral element method (*Patera*, 1984) (see appendix D) with a time step of one year. We use measured densities at sites 1, 2 and 3. Conductivity is inferred from density using the relationship given by *Calonne et al.* (2011) based on experimental measurements and numerical simulation using microtomographic images. The basal heat flux fb is given at 800 m depth in the bedrock. At this depth, the basal heat flux is assumed to be constant during time of the simulation (see appendix supplementary material). The thermal properties of the bedrock (gneiss and granite) are not well known. We use a thermal conductivity of 3.2 W m^{-1} K^{-1}, a heat capacity of 7.5 102 J kg^{-1} K^{-1} and a density of 2.8 103 kg m^{-3} as proposed by *Lüthi and Funk* (2001). The annual surface temperature Ts is assumed to vary in the same way as the mean annual air temperature (*Gilbert et al.*, 2010). The latent flux from refreezing of meltwater is

released at the surface and calculated from an annual temperature anomaly :

$$Q_{lat} = \frac{a(T_s - T_{ref})}{h\ L\ \rho_w} \tag{6.2}$$

where T_{ref} (K) is equal to the steady state temperature T_0 (K) (see next section), L (3.34 105 J kg^{-1}) is the latent heat of fusion, a (m w.e. K^{-1} s^{-1}) a melting factor (different for each site), ρ_w (= 1.0 103 kg m^{-3}) the water density and h (m) a scale factor representing the thickness of the layer influenced by latent heat over one year (h = 10 m here). The vertical advection profile is calculated from the surface advection velocity v_0 (m w.e. yr^{-1}) and assumed to vary linearly with depth (*Vincent et al.*, 2007b) :

$$v_z(z) = \frac{v_0 \rho_w}{\rho(z)} \left(1 - \frac{z}{D}\right) \tag{6.3}$$

where z is depth (m), D the bedrock depth (m), ρ_w the water density (kg m^{-3}) and ρ(z) the firn density.

6.3.2 Inverse problem

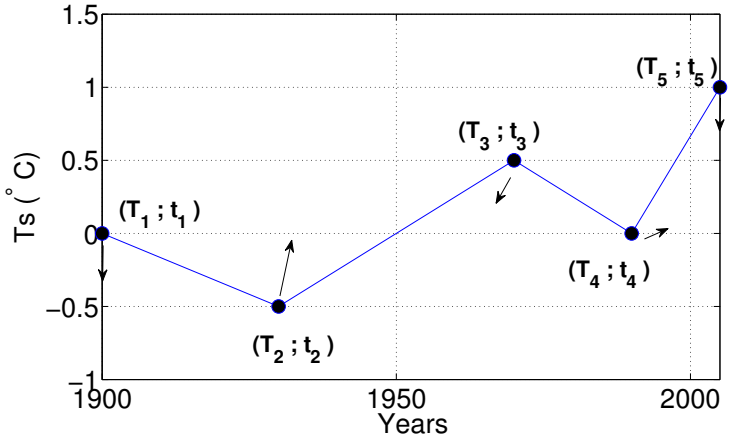

FIGURE 6.4 – Surface temperature evolution as represented by the vector **Ts**

The inverse problem is solved using Bayesian inference (*Hopcroft et al.*, 2007) via the method used by *Gilbert et al.* (2010). We use a Reversible Jump Markov Chain Monte Carlo (RJ-MCMC) algorithm to explore the parameter space and randomly draw the posterior Probability Density Function (PDF) of each parameter. At every site, five different parameters are explored : the surface temperature evolution vector **Ts**, the melting factor a (Equation 6.2), the basal flux f_b, the surface advection velocity v_0 and the steady state surface temperature T_0 used to compute the initial profile. As proposed in other studies (*Lüthi and Funk*, 2001), a long past temperature history is used to calculate the initial temperature profile in 1900 (see figure 6.5). For this purpose, numerical modeling experiments start in the year 800 for which we assume a steady state profile. Numerical experiments have shown that this past temperature history has a very small influence on the temperature inversion (see appendix C). This initial profile is calculated for every iteration

of the RJ-MCMC algorithm using T_0 and v_0. The surface temperature evolution is represented by a series of linear segments with the nodes of these segments being the model parameters **Ts**, i.e., **Ts** = (T_k,t_k ; k=1,5), where T_k is temperature and t_k is time (see figure 6.4). Posterior PDF is calculated for each parameter set sampled by the RJ-MCMC algorithm following the Bayesian approach :

$$P_{post} \propto P_{prior} \times P(\mathbf{d} \mid \mathbf{m}) \tag{6.4}$$

where P_{post} is the posterior PDF, P_{prior} is the prior PDF and $P(\mathbf{d} \mid \mathbf{m})$ is the probability of observing the data **d** for a given parameter set **m**. Details on the calculation of the posterior PDF are given in the appendix C.

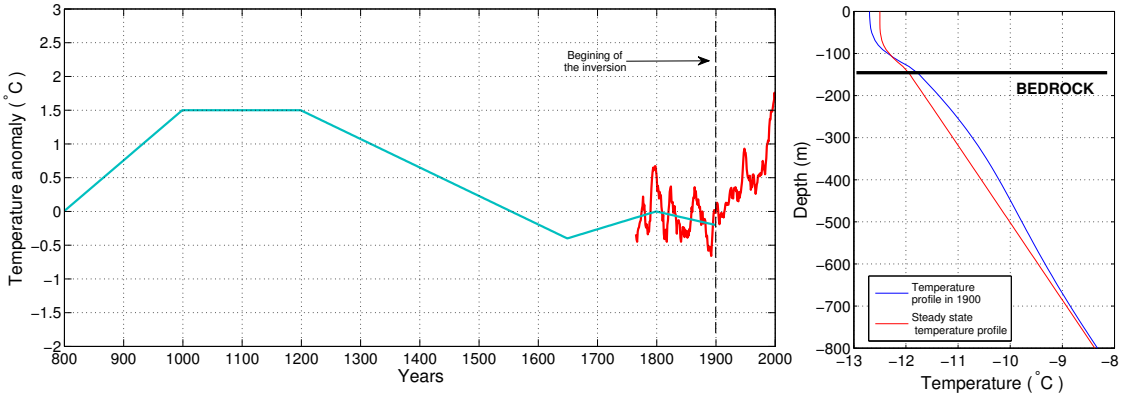

FIGURE 6.5 – Past temperature history used to calculate the initial profile in 1900 (in blue). The reconstitution HISTALP (*Auer et al.*, 2007) is shown in red.. The steady state profile is compared to the profile in 1900 at site 2 in the graph on the right.

In order to deal with the 3 sites simultaneously, the surface temperature is defined as a deviation from the steady state temperature T_0 (different at each site). The surface temperature evolution vector Ts is the same for all sites and the surface temperature at each site is given by :

$$\mathbf{Ts}^i = \mathbf{Ts} + T_0^i \tag{6.5}$$

where $\mathbf{Ts}^i$ is the surface temperature at site i and T_0^i the steady state temperature at site i. Data likelihood is calculated as the product of the data likelihood at each site :

$$P(\mathbf{d}_{i=1,3} \mid \mathbf{m}_{i=1,3}) = \prod_{i=1}^{3} P(\mathbf{d}_i \mid \mathbf{m}_i) \tag{6.6}$$

where $\mathbf{d}_i$ is the data on site i and $\mathbf{m}_i$ the parameters set for site i.

6.4 Results

6.4.1 Individual inversion at each site

Atmospheric temperature reconstruction at each site is shown in Figure 6.6. Ten million iterations were needed to reach a steady posterior PDF. The mean value of the posterior PDF (black

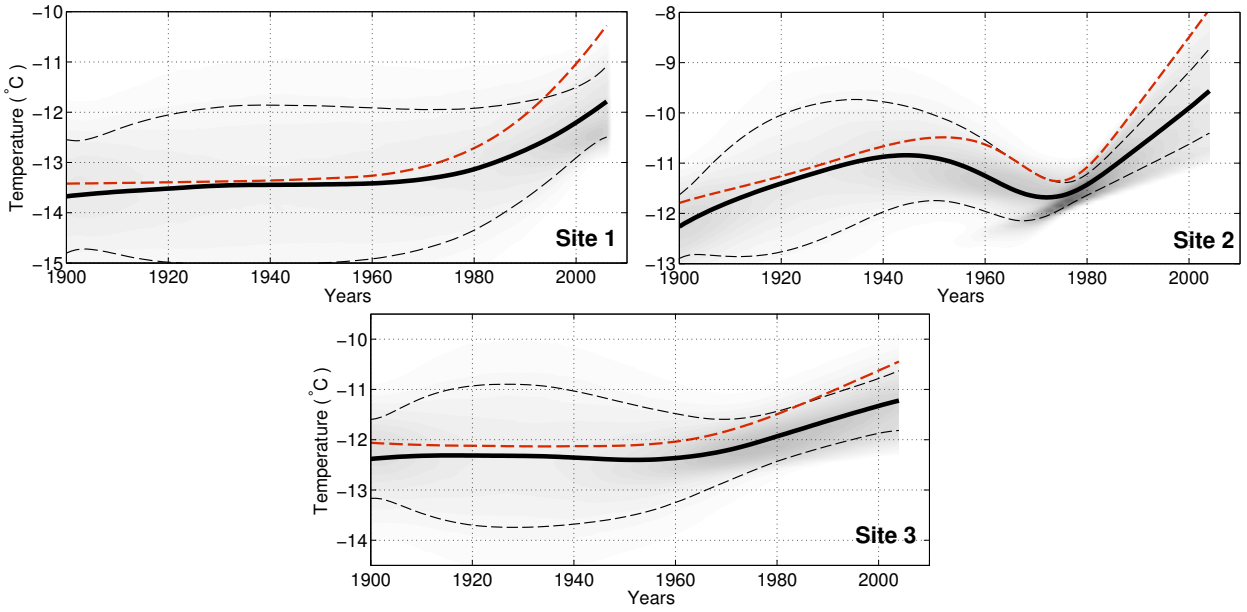

FIGURE 6.6 – Posterior PDF of air temperature sampled by RJ-MCMC algorithm for each borehole. The thick line shows the mean posterior PDF and the dashed line is the standard deviation. The red dashed line shows mean posterior PDF for inversion of firn surface temperature.

bold line) is interpreted as the expected value given by the inversion. The standard deviation (or 68% credible interval) gives the uncertainty (thin dashed line). The three inversions exhibit an air temperature rise starting between 1960 and 1980. The mean warming amplitude between 1960 and 2004 is 1.4°C with a warming of 1.6°C, 1.4°C and 1.1°C for sites 1, 2 and 3 respectively. The sites are too close to experience such different air temperature warming and the differences observed here are clearly due to uncertainties inherent to the method. The uncertainty of these reconstructions remains high due to the uncertainties associated with the melting intensity and advection velocity at each site. Our analysis shows that repeated measurements at the same site and at different times significantly improve the accuracy of reconstruction. For instance, the 3 measurements performed in 1994, 2005 and 2010 at site 2 provide the most accurate reconstruction of air temperatures (Figure 6.6). Moreover, the high advection velocity and melting intensity found at this site increase the impact of the atmospheric temperature change on englacial temperatures and provides a better reconstruction. Note that the englacial temperature measurements carried out in this borehole make it possible to detect the warm period of the forties. The reconstruction from borehole 1 temperatures does not provide any information before 1970 due to the low thickness of the glacier at this site. For site 3, high-frequency climate variations are filtered out by diffusion as a result of the low advective heat transfer. No trace of the forties warm period can therefore be detected from temperature profiles measured at site 3.

A second set of inversion experiments were performed assuming no melting/refreezing processes at the surface (i.e. a=0 in Equation 6.2), making it possible to reconstruct surface firn temperature variations (Figure 6.6, red dashed curve). Comparison with the atmospheric temperature reconstruction (Figure 6.6, black bold curve) shows the occurrence of surface melting at each site when

atmospheric and firn temperature variations deviate. At site 2, the reconstructed surface firn temperature rises by 3.3°C over the last 30 years while reconstructed atmospheric temperature rises by 1.8°C. This confirms the strong impact of increasing melting on englacial temperature in cold glaciers as already demonstrated by other studies (*Vincent et al.*, 2007b; *Suter et al.*, 2001; *Lüthi and Funk*, 2001; *Gilbert et al.*, 2010).

6.4.2 Simultaneous inversion

Simultaneous inversion provides a way to reduce uncertainties related to the melting intensity inference and greatly increases the reliability of the reconstruction (see the numerical experiments performed with the synthetic englacial dataset, in section 6.5). Simultaneous inversion results are shown in Figure 6.7 and Table 6.2 (mean posterior PDF and standard deviation of all parameters for each site) assuming the same temperature changes at the three sites. Posterior PDFs of a, v_0, f_b and T_0 are shown in the appendix C. The surface temperature is given here as a deviation from steady state temperature T_0 at each site (Equation 6.5). This method improves the accuracy of the reconstruction and reduces the uncertainty of parameter estimation given that the same temperature evolution explains englacial temperature changes for all the three sites. Fifty million iterations were needed to reach a steady posterior PDF.

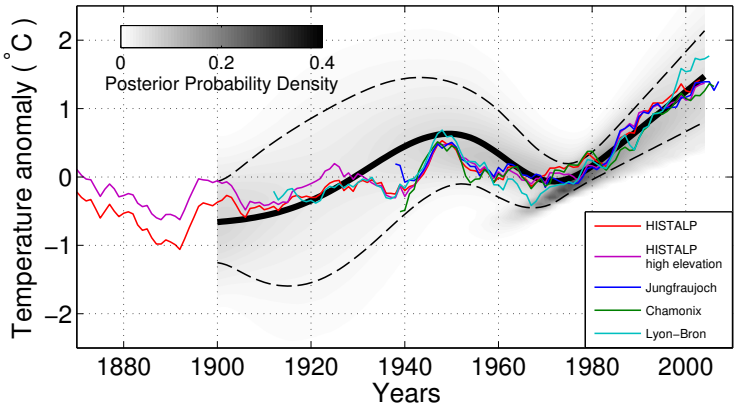

FIGURE 6.7 – Air temperature variations in the Mont Blanc area over the last century from simultaneous inversion using all boreholes (black bold line). The colored curves are the time series of the ten year moving averages of air temperature from Chamonix (1050 m a.s.l.), Lyon-Bron (200 m a.s.l.) and Jungfraujoch (3570 m a.s.l.) meteorological stations and from HISTALP and HISTALP high elevation (1500 to 3500 m a.s.l.) reconstitutions in the northwestern Alps (*Auer et al.*, 2007).

Results exhibit a 1.2°C warming between 1900 and 1950, a cooling period of 0.7°C between 1950 and 1975 and a recent 1.6°C warming between 1975 and 2004. For each site, the inferred surface vertical velocity (v_0, Table 6.2) has been compared with GPS measurements (*Vincent et al.*, 2007a) (Table 1). This comparison shows good agreement for the three sites. Variation of melting intensity is linked to the slope and aspect of the site that influence the incoming potential solar radiation (*Suter*, 2002). Thus, sites 1 and 2 are more subject to surface melting than site 3. This is consistent with our inversion results (Table 6.2) that show less energy released by refreezing of meltwater at site 3.

The reconstructed basal flux values seem to show a stronger basal flux at site 3. This could be due to topographical effects related to the influence of the south face of Mont Blanc.

Site N°	Steady state temperature T_0 (°C)	Mean latent flux Q_{lat} (mW m^{-3})	Subsidence velocities v_0 (m w.e. yr^{-1})	Basal heat flux f_b (10^{-3} W m^{-2})
1	-14.4 ± 0.5	30 ± 16	0.6 ± 0.4	25 ± 16
2	-12.4 ± 0.5	32 ± 16	3.7 ± 0.2	26 ± 16
3	-12.7 ± 0.5	7 ± 10	1.1 ± 0.4	36 ± 12

TABLEAU 6.2 – Posterior PDF means and standard deviations of mean latent heat (Q_{lat}), subsidence velocities (v_0) , basal heat flux (f_b) and steady state temperature (T_0) as sampled by the RJ-MCMC algorithm in the simultaneous inversion.

6.5 Sensitivity and reliability of temperature reconstructions

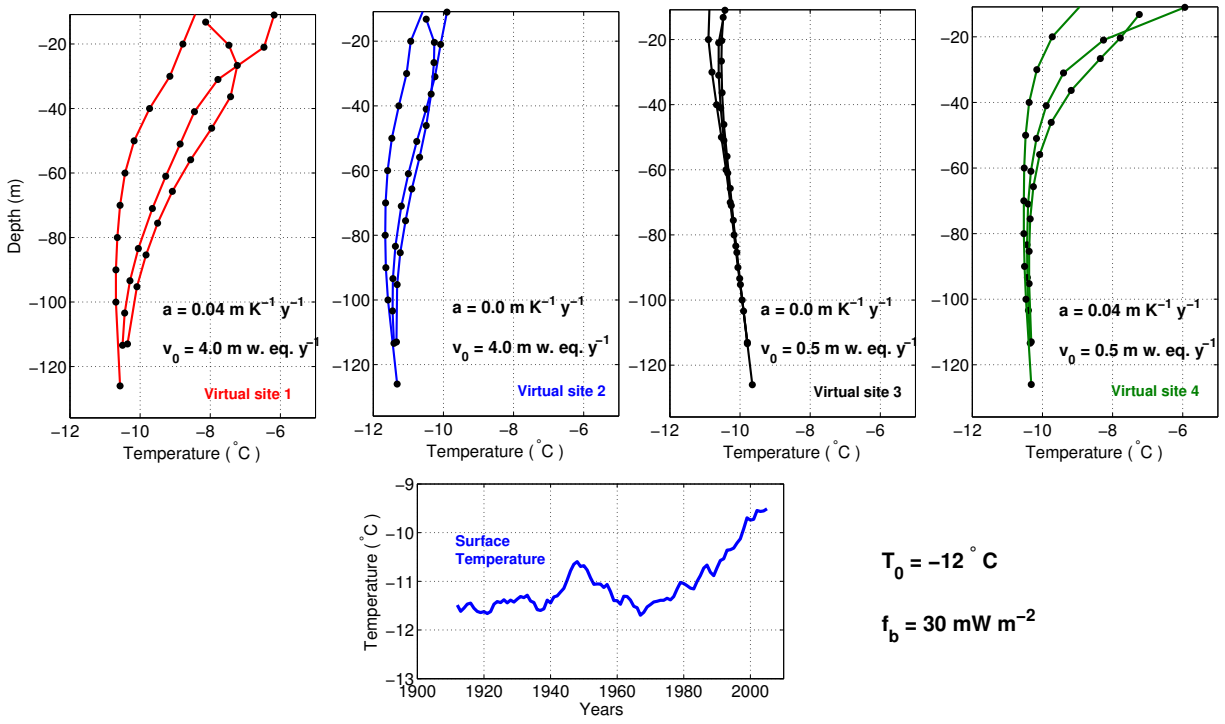

FIGURE 6.8 – Synthetic temperature profiles created in each virtual site using the indicated a, v_0, T_0 and f_b values. At the bottom, Lyon-Bron air temperature signal used to create synthetic profiles is shown

The accuracy of temperature reconstructions is very sensitive to the choice of drilling sites. As shown in section 6.4.1, the main parameters that influence the reconstruction are the melting intensity driven by the local incoming potential solar radiation (*Suter*, 2002) and the firn vertical advection velocity driven by the seasonal distribution of accumulated snow (*Vincent et al.*, 2007a).

In order to test the reliability of our reconstruction, we investigated the influences of melting intensity and vertical advection velocity using a synthetic englacial dataset. This dataset was obtained from the forward model forced by the daily air temperature measured at Lyon-Bron meteorological station and different values of vertical advection velocity and melting intensity. Melting is calculated using the classical degree-day method at a daily time scale (*Hock*, 2003). Four virtual sites were created using low and high vertical advection (set to 0.5 and 4.0 m w.e. yr^{-1} respectively) and low and high melting intensity (with degree-day factor set to 0 and 4.0 mm K^{-1} day^{-1} respectively). For each virtual site, we modeled 3 virtual 126 m deep englacial temperature profiles (in 1994, 2005 and 2010) (see Figure 6.8). Then air temperature was reconstructed from these profiles using the inverse method and compared with the temperatures from Lyon-Bron (Figure 6.9a to 6.9d). The deviation between reconstructed profiles and Lyon-Bron daily temperatures allows us to assess the reliability of the reconstruction. Results show high differences between Lyon-Bron temperature and reconstructions from individual inversion at each virtual site. These differences are due to the high uncertainty on the melting intensity which leads to a high uncertainty on the temperature reconstruction. In contrast, the use of simultaneous inversions at the four virtual sites reconstructs past temperature variations accurately (Figure 6.9e) and give good estimation of the other inverted parameters (Figure 6.10). In addition, our numerical experiments show that repeated measurements at the same site reduce significantly the uncertainty of the reconstruction (Figure 6.9e).

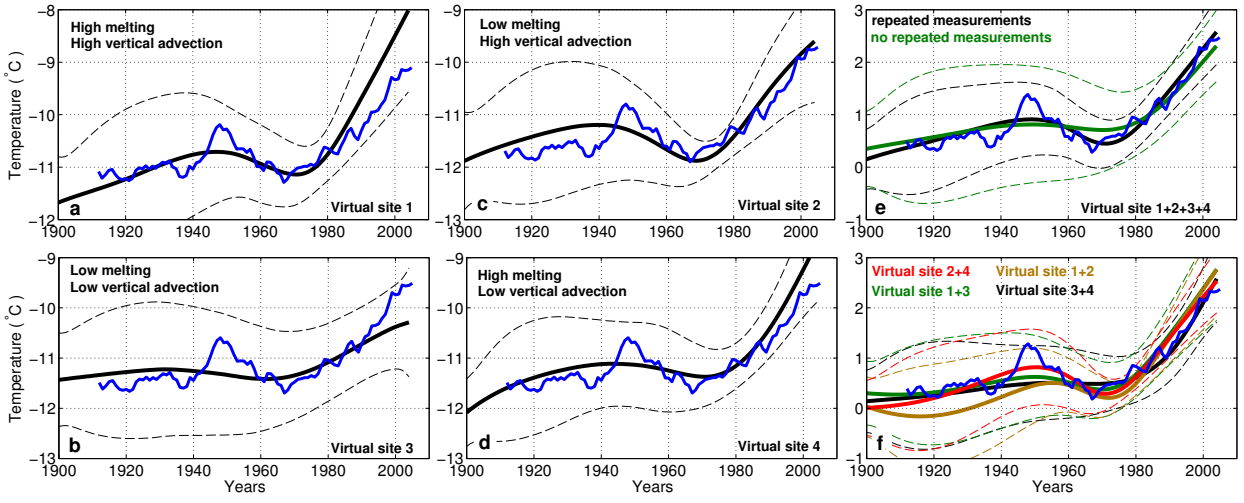

FIGURE 6.9 – Inversions of synthetic englacial temperature profiles created from the forward model forced by daily air temperature measured at Lyon-Bron and using different melting intensities and advection velocities. Bold lines are the mean posterior PDF and dashed lines are the standard deviation of each inversion. The blue line is the ten year moving average of Lyon-Bron temperature

Some further experiments were performed to test the best combination of measurements for temperature reconstruction (Figure 6.9f). These experiments show that the use of only two sites is sufficient to obtain reliable temperature reconstruction. They also reveal that the best reconstruction is obtained from sites with contrasting melting intensity and accumulation (Figure 6.9f). The use of two sites overcomes the difficulty of inferring melting from englacial temperature measurements. Conversely, reconstructions based on only one site require independent calibration of

melting factor from direct measurements or from an energy balance model using on-site automatic weather station data. In addition to a sensitivity analysis, these numerical modeling experiments show that the air temperature reconstruction shown in Figure 6.7 is relevant.

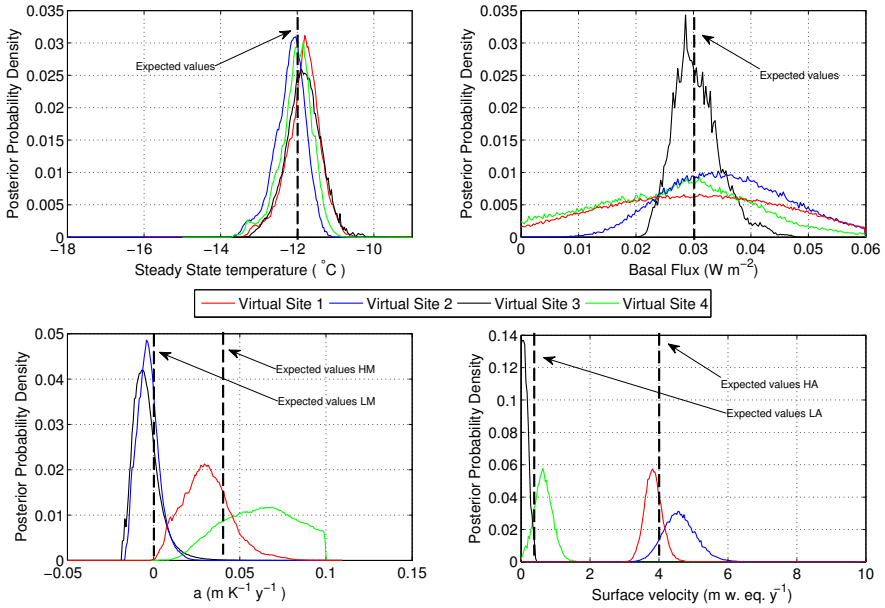

FIGURE 6.10 – Posterior PDF of T_0, f_b , v_0 and a at each virtual site from simultaneous inversion of all synthetic temperature profiles compared to the expected values given in figure 6.8

6.6 Discussion and conclusions

	Elevation range	Localization	Type of data	Linear trend 1900-2004 (K decade^{-1})	Linear trend 1960 – 2004 (K decade^{-1})	Linear trend 1980 – 2004 (K decade^{-1})
HISTALP	0-3500 m a.s.l.	NW Alps	Homogenized records	0.14	0.36	0.58
HISTALP (high elevation)	1500-3500 m a.s.l.	Alps	Homogenized records	0.12	0.36	0.50
Jungfraujoch	3570 m a.s.l.	46° 32' 7° 58'	Meteorological station	-	0.35	0.52
Lyon-Bron	200 m a.s.l.	45° 72' 4° 94'	Meteorological station	-	0.46	0.72
Chamonix	1042 m a.s.l.	45° 93' 6° 88'	Meteorological station	-	0.31	0.51
This study	4250 m a.s.l.	45° 84' 6° 84'	-	**0.14±0.06**	**0.33±0.02**	**0.55±0.15**

TABLEAU 6.3 – Comparison of atmospheric temperature trends from the different datasets.

For the first time, atmospheric temperatures over 100 years were reconstructed at a very high elevation using multiple englacial temperature profiles. This reconstruction does not depend on any air temperature record from lower elevations. Our results exhibit a warming of 2.0 ± 0.6 °C with a linear trend of 0.14 ± 0.06 °C/decade at around 4300 m a.s.l. in the Mont Blanc area between 1900 and 2004. The 2°C warming corresponds to the reconstructed temperature difference between 1900 and 2004. This confirms that 20^{th} century warming in the Alps was greater than the

global and hemispheric average (*Beniston et al.*, 1997). These results have been compared to local meteorological data and temperature reconstructions from HISTALP (*Auer et al.*, 2007) (Figure 6.7). Local meteorological data have been recorded in the valley at Chamonix (1050 m a.s.l.) since 1934, in the plain at Lyon-Bron meteorological station (200 m a.s.l.) since 1907 (located 200 km west of the glacier) and at Jungfraujoch meteorological station (3570 m a.s.l., Switzerland) since 1933. *Auer et al.* (2007) used measurement instrument series (mostly located below 1500 m. a.s.l.) of monthly mean temperature to estimate the homogenized long-term temperature evolution in the Alps. The means for the northwestern Alps and the selected high elevation dataset temperatures (1500 to 3500 m a.s.l.) are reported in Figure 6.7 together with the inversion results. Temporal temperature trends relative to these series are shown in Table 6.3. We can conclude that our reconstruction is in good agreement with the temperature trends of all these data over all the different periods 1900-2004, 1960-2004 and 1980-2004. Only Lyon-Bron temperature trend seems to be stronger over the periods 1960-2004 and 1980-2004. A possible effect of urbanization could affect this series (*Pepin and Lundquist*, 2008). The good agreement with temperatures trends from HISTALP confirms that temperature change at very high elevations in the Mont Blanc area is representative of a regional climate change and it is not biased by local effects. We conclude that atmospheric temperature trends detected on Mont Blanc above 4000 m a.s.l. agree fairly well with the trends recorded at lower elevations or reconstructed at regional scale, even though they have been obtained fully independently from these records. This suggests that, in the Alps, warming is not increasing at very high elevations above the 0°C isotherm.

These results seem to conflict with modeling studies using future scenarios that have shown an elevation-dependent climate response (*Giorgi et al.*, 1996; *Im et al.*, 2010). However, it is difficult to compare our results with other results from large scale atmospheric modeling and simulations for the future. Studies based on ground observations during the 20^{th} century show no overall agreement concerning the elevation dependency of atmospheric temperature trends (*Ceppi et al.*, 2010; *Rangwala and Miller*, 2012; *Beniston and Rebetez*, 1996; *Jungo and Beniston*, 2001). Our study suggests that there is a similar air temperature trend at low and very high altitudes over the last one hundred years.

Englacial temperature measurements provide a way to infer air temperature changes at very high elevations. We show that temperature reconstructions from englacial temperatures need a minimum of two neighboring measurement sites with contrasting surface melting and snow accumulation. This facilitates differentiation between the fraction of the englacial warming coming from increasing air temperature and the fraction coming from increasing surface melting. This method could be applied to other high elevation glaciated areas where meteorological data are non-existent.

Acknowledgments This study was funded by the AQWA European program (n° 212250). We thank P. Possenti and P. Ginot for conducting the drilling operation. We thank HISTALP project members for providing the homogenized instrument data in the Alps. We thank MétéoSwiss and Météo-France for providing air temperature data.

Résumé des résultats et conclusions

La reconstitution climatique à partir de la température des glaciers froids de haute montagne est un moyen de quantification des changements climatiques dans des régions de très haute altitude pour lesquelles les mesure directes sont quasi inexistantes. Ces reconstitutions nécessitent cependant des forages sur des sites particuliers, à températures négatives, dont l'épaisseur de glace est importante (> 100 m) et dont la vitesse d'écoulement horizontale est très faible. Les dômes, plateaux et cols glaciaires de haute altitude sont donc des sites privilégiés.

Dans cette étude, les caractéristiques et le nombre de site de forage ainsi que la nécessité de répéter les mesures sur un même site sont analysés de manière à obtenir la meilleure reconstitution climatique par inversion de profils de température. Les résultats montrent qu'un minimum de deux sites de forage doit être utilisé. Ces sites doivent présenter des caractéristiques d'accumulation de neige et d'exposition différentes. L'utilisation de deux sites avec deux expositions différentes permet de quantifier efficacement l'impact de la fonte de surface sur le profil de température pour en déduire la variation des températures atmosphériques qui nous intéresse. L'utilisation d'un site unique ne peut permettre une reconstitution valable sans une quantification indépendante de la fonte de surface (figure 6.9). On montre aussi que la répétition des mesures sur un même site à plusieurs années d'intervalles (10 ans typiquement) permet de diminuer efficacement les incertitudes sur la reconstitution.

Les résultats obtenus sur le site du Col du Dôme par inversion simultanée de 7 profils de température sur 3 sites différents révèlent un réchauffement atmosphérique de 0.14 °C/décennie entre 1900 et 2004 et 0.55°C/décennie entre 1980 et 2004. La comparaison de ces résultats avec des données météorologiques de basse altitude sur l'ensemble de la région alpine montre que le réchauffement est similaire entre les hautes et les basses altitudes. A l'altitude du Col du Dôme, l'épaisseur et l'étendue de la couverture neigeuse n'est pas affectée par le réchauffement climatique et l'enregistrement reconstitué n'est donc pas influencé par des effets locaux dus à la diminution de la durée d'enneigement. En effet, plusieurs études invoquent la diminution de la durée d'enneigement comme une cause de réchauffement local et saisonnier d'une certaine tranche d'altitude dues aux rétroactions liées au changement d'albédo (*Ceppi et al.*, 2010). Nos résultats sont donc indépendants de cet effet et montrent que de manière plus globale, le réchauffement climatique semble se comporter de manière similaire à haute et basse altitude dans les Alpes.

Chapitre 7

Conclusions générales et perspectives

La modélisation du régime thermique des glaciers est primordiale pour l'étude de l'écoulement glaciaire et de l'hydrologie intra ou sous-glaciaire. Elle est nécessaire à l'étude des aléas d'origine glaciaire et ouvre de nouvelles perspectives sur la reconstitution du climat passé à haute altitude. D'une part, la simulation du régime thermique dans un climat changeant est le seul moyen d'identifier des configurations glaciaires potentiellement dangereuses pour les populations à l'aval. D'autre part, le champ de températures des glaciers froids contient des informations climatiques du passé qu'il est possible d'extraire à l'aide d'outils de modélisation.

Le régime thermique d'un glacier résulte à la fois des processus physiques internes liés aux propriétés thermodynamiques et mécaniques de la glace et des processus d'échanges avec le milieu extérieur le long des deux surfaces d'échanges que sont le lit rocheux et la surface libre. Il est nécessaire de prendre en compte l'ensemble de ces processus pour simuler le régime thermique du glacier et son évolution.

Ces travaux de thèse abordent plusieurs aspects de la modélisation du régime thermique des glaciers à travers des études de cas dans le massif du Mont Blanc, pour lesquelles nous disposons de nombreuses observations. Nous avons mis l'accent sur la modélisation des échanges de surface entre le glacier et l'atmosphère pour deux raisons : d'une part, c'est la principale lacune des études existantes relatives au régime thermique, et, d'autre part, c'est par ces échanges que le climat contrôle le régime thermique glaciaire. Cette thèse tente d'aller plus loin que les précédentes études de la modélisation thermomécanique des zones d'accumulation froides des glaciers de haute altitude. Pour la première fois, les champs de vitesses, de températures, de densités et la surface libre du glacier sont couplés dans un climat changeant.

L'impact d'un réchauffement climatique est très important sur les glaciers froids. Dans les Alpes, les glaciers froids sont généralement situés à très haute altitude et en zone d'accumulation. C'est pourquoi la majeure partie de la thèse est consacrée à l'étude de l'impact climatique sur les zones d'accumulation froides d'altitude. Ces régions glaciaires contiennent des informations climatiques du passé. En outre, certains de ces glaciers froids de haute altitude localisés sur des pentes très abruptes sont sujettes à un fort réchauffement qui pourrait conduire à leur déstabilisation. Le site du Col du Dôme permet d'établir la réponse thermique de ces glaciers aux variations climatiques. L'étude réalisée sur ce site met en évidence la forte variabilité spatiale de cette réponse et identifie les causes de cette variabilité. Elle permet d'identifier les processus à prendre en compte pour relier le régime thermique aux conditions météorologiques. Nous avons développé un modèle 3D thermomécanique pour la simulation de la réponse thermique et dynamique d'un glacier froid en zone d'accumulation aux variations climatiques. Les principales conclusions concernant les zones d'accumulation froides sontles suivantes :

- La modification du bilan d'énergie de surface pendant les événements de fonte permet l'absorption d'un surplus d'énergie par le glacier, qui le rend très sensible à la durée totale des événements de fonte. Cette énergie est convertie en eau de fonte qui percole puis regèle en profondeur

- Cette énergie doit être prise en compte dans les modèles de régime thermique en tenant compte de la fonte de surface et de la percolation/regel de cette eau

- La variabilité spatiale de la fonte de surface induit une forte variabilité du régime thermique et doit être prise en compte. Cette variabilité est corrélée aux variations d'insolation solaire qui dépend de la pente, de l'orientation et des masques du relief.

- La réponse du glacier à une diminution de viscosité due au réchauffement du glacier se traduit par un abaissement de la surface du glacier, une augmentation de la vitesse d'écoulement et une densification plus rapide. On estime à l'horizon 2050, au Col du Dôme, un abaissement de la surface pouvant atteindre 15 m pour une augmentation des vitesses horizontales de surface de 10 à 15%.

A plus basse altitude, la zone d'accumulation finit par atteindre le point de fusion à cause de l'augmentation de la fonte estivale et de la percolation, malgré des températures de l'air qui peuvent être négatives en moyenne annuelle. Dans cette zone, les variations climatiques ont surtout un impact sur le bilan de masse. En revanche, à proximité de la ligne d'équilibre, les variations d'épaisseur de névé en réponse aux variations climatiques peuvent être importantes et influencer considérablement le régime thermique du glacier. C'est ce que montre l'étude réalisée sur le glacier de Tête Rousse. Elle permet d'étendre la modélisation du régime thermique développée pour les zones d'accumulation froides au reste du glacier. On montre que l'épaisseur de neige saisonnière et du névé a une influence déterminante sur le régime thermique du glacier. La modélisation du régime thermique dans la zone d'ablation et la zone d'accumulation tempérée doit donc prendre en compte les changements d'état de surface du glacier (neige/névé ou glace) et nécessite donc un couplage avec un modèle d'enneigement. Dans notre approche, le modèle de surface reste le même que pour les zones d'accumulation froide avec une différence notable : l'état de surface du glacier peut évoluer et l'eau ne peut pas percoler dans la glace. Cette méthode montre de très bons résultats sur le glacier de Tête Rousse pour lequel la couverture de neige/névé contrôle principalement le régime thermique du glacier. Ces travaux de thèse proposent donc une méthode de modélisation physique du régime thermique forcée par des données météorologiques et applicable à tous types de glacier. Le modèle tri-dimensionnel présenté en chapitre 4 peut en effet être étendu à un glacier dans son intégralité en le couplant à un modèle de bilan de masse et d'enneigement.

L'étude réalisée sur les cas particuliers du glacier de Tête Rousse et du Col du Dôme n'a pas seulement permis d'identifier les processus physiques qui conditionnent le régime thermique et de construire des modèles numériques. Elle a aussi permis de répondre à des questions relatives à la gestion opérationnelle de risques. En effet, l'étude du régime thermique de Tête Rousse a permis :

- d'identifier les processus responsables de la formation de la poche d'eau

- de dater la formation de la poche d'eau découverte en 2008/2009 à 1980.
- d'apporter des éléments supplémentaires à l'explication de la catastrophe de 1892
- d'estimer que l'évolution future de l'aléa de formation de poche d'eau devrait diminuer pour cause de refroidissement de la partie amont du glacier

Ces conclusions font partie du rapport remis aux autorités publiques (Préfecture de Haute Savoie et mairie de Saint Gervais) le 30 décembre 2011 sur le glacier de Tête Rousse et sa poche d'eau.

Sur le Col du Dôme, l'étude du régime thermique associée au développement d'une méthode d'inversion de profils de températures a permis de quantifier la variation climatique sur le dernier siècle à très haute altitude. Ces résultats contribuent à répondre à la question de l'amplification du réchauffement climatique à haute altitude. Nos résultats semblent montrer au contraire un comportement similaire du réchauffement à haute et basse altitude dans les Alpes. Ils révèlent un réchauffement atmosphérique de 0.14 °C/décennie entre 1900 et 2004 et 0.55°C/décennie entre 1980 et 2004. Ceci correspond à réchauffement supérieur à celui observé en moyenne dans l'hémisphère nord mais correspond bien à celui observé régionalement dans les Alpes. La méthode inverse développée dans cette thèse est innovante et permet de s'affranchir des effets de la fonte et de l'accumulation pour la reconstitution des températures atmosphériques à partir de profils de températures mesurées sur des glaciers froids de montagne. La condition pour réaliser ces reconstitutions est de disposer de plusieurs profils de températures sur différents sites ayant subi le même forçage atmosphérique. Cette méthode pourrait être appliquée à un grand nombre de sites comme le Col Gnifetti en Suisse où de nombreuses mesures de températures sont déjà disponibles, ou dans les Andes ou en Himalaya.

Ces travaux de thèse ouvrent de nouvelles perspectives sur la quantification du réchauffement climatique à haute altitude par les mesures de températures dans les glaciers froids de montagne. Ils mettent en évidence la nécessité de systématiquement mesurer la température dans les forages réalisés pour d'autres finalités (analyse chimique des carottes de glace). Les outils de modélisation du régime thermique développés dans cette thèse permettent la simulation des températures des glaciers froids à partir de données climatiques et permettent d'étudier leurs évolutions à partir de scénarios climatiques. L'aboutissement des travaux réalisés au col du Dôme est la réalisation d'un modèle à trois dimensions opérationnel pour l'étude de l'évolution thermique des glaciers suspendus pouvant présenter un risque. Dans le cadre de ces travaux de thèse, nous avons débuté une étude préliminaire de l'évolution de la température basale du glacier de Taconnaz. Cette étude sera poursuivi dans le but de déterminer sous quelle condition la base du glacier pourrait atteindre le point de fusion dans le futur. La perspective d'utiliser ce modèle de régime thermique pour contraindre les conditions basales d'un modèle d'endommagement (*Faillettaz et al.*, 2010) donnerait un véritable outil de prédiction de déstabilisation de glaciers suspendus dans un contexte de réchauffement climatique. De la même manière, le couplage du régime thermique avec un modèle d'hydrologie de type GlaDs (*Werder et al.*, 2013) pourrait permettre d'estimer l'impact de variations du régime thermique sur l'hydrologie sous-glaciaire. Il serait intéressant de voir comment une zone de glace froide influence

la formation de chenaux sous-glaciaire et peut mener à la formation d'une poche d'eau comme celle observée sur le glacier de Tête Rousse. L'application au glacier de Tête Rousse peut permettre de déterminer pour quelle condition de température la formation de chenaux de drainage naturel est possible.

Références bibliographiques

Aschwanden, A. (2008), Mechanics and Thermodynamics of Polythermal Glaciers, Ph.D. thesis, ETH Zurich.

Aschwanden, A., and H. Blatter (2005), Meltwater production due to strain heating in Storglaciären, Sweden, *Journal of Geophysical Research : Earth Surface (2003–2012)*, *110*(F4).

Aschwanden, A., and H. Blatter (2009), Mathematical modeling and numerical simulation of polythermal glaciers, *Journal of Geophysical Research : Earth Surface (2003–2012)*, *114*(F1).

Aschwanden, A., E. Bueler, C. Khroulev, and H. Blatter (2012), An enthalpy formulation for glaciers and ice sheets, *Journal of Glaciology*, *58*(209), 441–457.

Auer, I., R. Böhm, and other (2007), HISTALP - historical instrumental climatological surface time series of the Greater Alpine Region, *Int. J. Climatol.*, *27*(1), 17–46, doi :10.1002/joc.1377.

Beltrami, H. (2002), Climate from borehole data : Energy fluxes and temperatures since 1500, *Geophysical Research Letters*, *29*(23), 2111.

Beltrami, H., and R. N. Harris (2001), Foreword : Inference of climate change from geothermal data, *Global and Planetary Change*, *29*(3), 149–152.

Beniston, M., and M. Rebetez (1996), Regional Behavior of Minimum Temperatures in Switzerland the Period 1979-1993, *Theor. Appl. Climatol.*, *53*, 231–243.

Beniston, M., H. Diaz, and R. Bradley (1997), Climatic change at high elevation sites : an overview, *Climatic Change*, *36*(3-4), 233–251.

Blatter, H. (1987), On the thermal regime of an Arctic valley glacier : a study of White Glacier, Axel Heiberg Island, NWT, Canada, *J. Glaciol*, *33*(114), 200–211.

Blatter, H., and K. Hutter (1991), PolytherlIlal conditions in Arctic glaciers, *Journal of Glaciology*, *37*(126).

Böhm, R., I. Auer, M. Brunetti, M. Maugeri, T. Nanni, and W. Schöner (2001), Regional temperature variability in the European Alps : 1760–1998 from homogenized instrumental time series, *International Journal of Climatology*, *21*(14), 1779–1801.

Boon, S., and M. Sharp (2003), The role of hydrologically-driven ice fracture in drainage system evolution on an Arctic glacier, *Geophysical Research Letters*, *30*(18), 1916.

Braithwaite, R. J., and Y. Zhang (2000), Sensitivity of mass balance of five Swiss glaciers to temperature changes assessed by tuning a degree-day model, *Journal of Glaciology*, *46*(152), 7–14.

Brun, E., E. Martin, V. Simon, C. Gendre, and C. Coleou (1989), An energy and mass model of snow cover sidtable for operational avalanche forecasting, *Journal 0/Glaciology*, *35*(12), 1.

Brun, E., P. David, M. Sudul, and G. Brunot (1992), A numerical model to simulate snow-cover stratigraphy for operational avalanche forecasting, *Journal of Glaciology*, *38*(128).

Brutsaert, W. (1975), On a derivable formula for long-wave radiation from clear skies, *Water Resources Research*, *11*(5), 742–744.

Bueler, E., J. Brown, and C. Lingle (2007), Exact solutions to the thermomechanically coupled shallow-ice approximation : effective tools for verification, *Journal of Glaciology*, *53*(182), 499–516.

Calonne, N., F. Flin, S. Morin, B. Lesaffre, S. Rolland du Roscoat, and C. Geindreau (2011), Numerical and experimental investigations of the effective thermal conductivity of snow, *Geophys. Res. Lett.*, *38*(L23501), doi :10.1029/2011GL049234.

Ceppi, P., S. Scherrer, A. Fischer, and C. Appenzeller (2010), Revisiting Swiss temperature trends 1959-2008, *Int. J. Climatol.*, *32*, 203–213.

Clarke, G., and R. Goodman (1975), Radio echo soundings and ice-temperature measurements in a surge-type glacier, *Journal of glaciology*, *14*, 71–78.

Colbeck, S., and G. Davidson (1973), Water percolation through homogeneous snow, *The Role of Snow and Ice in Hydrology (Proc.Banff Symp.)*, *1*, 242–257.

Copland, L., M. J. Sharp, and P. W. Nienow (2003), Links between short-term velocity variations and the subglacial hydrology of a predominantly cold polythermal glacier, *Journal of Glaciology*, *49*(166), 337–348.

Dahl-Jensen, D., K. Mosegaard, N. Gundestrup, G. D. Clow, S. J. Johnsen, A. W. Hansen, and N. Balling (1998), Past temperatures directly from the Greenland ice sheet, *Science*, *282*(5387), 268–271.

Delcourt, C., B. Van Liefferinge, F. Pattyn, and M. Nolan (2012), The climate memory of an Arctic polythermal glacier, *Journal of Glaciology*, submitted.

Durand, Y., E. Brun, L. Merindol, G. Guyomarc'h, B. Lesaffre, and E. Martin (1993), A meteorological estimation of relevant parameters for snow models, *Annals of Glaciology*, *18*, 65–71.

Durand, Y., M. Laternser, G. Giraud, P. Etchevers, B. Lesaffre, and L. Mérindol (2009), Reanalysis of 44 Yr of climate in the French Alps (1958-2002) : methodology, model validation, climatology, and trends for air temperature and precipitation, *Journal of Applied Meteorology and Climatology*, *48*(3), 429–449.

Duva, J., and P. Crow (1994), Analysis of consolidation of reinforced materials by power-law creep, *Mechanics of materials*, *17*(1), 25–32.

Eisen, O., A. Bauder, M. Luthi, P. Riesen, and M. Funk (2009), Deducing the thermal structure in the tongue of Gornergletscher, Switzerland, from radar surveys and borehole measurements, *Annals of Glaciology*, *50*(51), 63–70.

Essery, R., and P. Etchevers (2004), Parameter sensitivity in simulations of snowmelt, *Journal of Geophysical Research : Atmospheres (1984–2012)*, *109*(D20).

Faillettaz, J., D. Sornette, and M. Funk (2010), Gravity-driven instabilities : Interplay between state-and velocity-dependent frictional sliding and stress corrosion damage cracking, *Journal of Geophysical Research : Solid Earth (1978–2012)*, *115*(B3).

Faillettaz, J., D. Sornette, and M. Funk (2011), Numerical modeling of a gravity-driven instability of a cold hanging glacier : reanalysis of the 1895 break-off of Altelsgletscher, Switzerland, *Journal of Glaciology*, *57*(205), 817–831.

Flowers, G. E., and G. K. Clarke (2002), A multicomponent coupled model of glacier hydrology 2. Application to Trapridge Glacier, Yukon, Canada, *Journal of Geophysical Research*, *107*(B11), 2288.

Fountain, A. G., and J. S. Walder (1998), Water flow through temperate glaciers, *Rev. Geophys.*, *36*(3), 299–328.

Fountain, A. G., R. W. Jacobel, R. Schlichting, and P. Jansson (2005), Fractures as the main pathways of water flow in temperate glaciers, *Nature*, *433*(7026), 618–621.

Fowler, A., and D. Larson (1978), On the flow of polythermal glaciers. I. Model and preliminary analysis, *Proceedings of the Royal Society of London. A. Mathematical and Physical Sciences*, *363*(1713), 217–242.

Funk, M., K. Echelmeyer, and A. Iken (1994), Mechanisms of fast flow in Jakobshavns Isbrae, West Greenland : Part II. Modeling of englacial temperatures, *Journal of Glaciology*, *40*(136).

Gagliardini, O., and J. Meyssonnier (1997), Flow simulation of a firn-covered cold glacier, *Annals of Glaciology*, *24*, 242–248.

Gagliardini, O., F. Gillet-Chaulet, G. Durand, C. Vincent, and P. Duval (2011), Estimating the risk of glacier cavity collapse during artificial drainage : The case of Tête Rousse Glacier, *Geophysical Research Letters*, *38*(10).

Gagliardini, O., et al. (2013), Capabilities and performance of Elmer/Ice, a new generation ice-sheet model, *Geoscientific Model Development Discussions*, *6*(1), 1689–1741.

Gerbaux, M., C. Genthon, P. Etchevers, C. Vincent, and J. Dedieu (2005), Surface mass balance of glaciers in the French Alps : distributed modeling and sensitivity to climate change, *Journal of Glaciology*, *51*(175), 561–572.

Gilbert, A., and C. Vincent (2013), Atmospheric temperature changes over the 20th century at very high elevations in the European Alps from englacial temperatures, *Geophysical Research Letters*, pp. 1–7.

Gilbert, A., P. Wagnon, C. Vincent, P. Ginot, and M. Funk (2010), Atmospheric warming at a high elevation tropical site revealed by englacial temperatures at Illimani, Bolivia (6340 m a.s.l., 16°S, 67°W), *J. Geophys. Res.*, *115*(D10109), doi :10.1029/2009JD012961.

Gilbert, A., C. Vincent, P. Wagnon, E. Thibert, and A. Rabatel (2012), The influence of snow cover thickness on the thermal regime of Tête Rousse Glacier (Mont Blanc range, 3200 m asl) : Consequences for outburst flood hazards and glacier response to climate change, *Journal of Geophysical Research : Earth Surface (2003–2012)*, *117*(F4).

Gilbert, A., C. Vincent, D. Six, P. Wagnon, L. Piard, and P. Ginot (2013), Modeling firn surface temperature in cold accumulation zone : from physical to semi-parameterized approach, *The Cryosphere discussion*.

Giorgi, F., J. Hurrell, M. Marinucci, and M. Beniston (1996), Elevation Dependency of the Surface Climate Change Signal : A Model Study, *J. Climate*, *10*, 288–296, doi :10.1175/1520-0442(1997)010⟨0288:EDOTSC⟩2.0.CO;2.

González-Rouco, J., H. Beltrami, E. Zorita, and H. Von Storch (2006), Simulation and inversion of borehole temperature profiles in surrogate climates : Spatial distribution and surface coupling, *Geophysical Research Letters*, *33*(1).

Greuell, W., and J. Oerlemans (1989), *The evolution of the englacial temperature distribution in the superimposed ice zone of a polar ice cap during a summer season*, Kluwer.

Greve, R. (1997), Application of a polythermal three-dimensional ice sheet model to the Greenland ice sheet : response to steady-state and transient climate scenarios, *Journal of Climate*, *10*(5), 901–918.

Gulley, J., D. Benn, D. Muller, and A. Luckman (2009), A cut-and-closure origin for englacial conduits in uncrevassed regions of polythermal glaciers, *Journal of Glaciology*, *55*(189), 66–80.

Gusmeroli, A., P. Jansson, R. Pettersson, and T. Murray (2012), Twenty years of cold surface layer thinning at Storglaciaren, sub-Arctic Sweden, 19892009, *Journal of Glaciology*, *58*(207), 3–10.

Haeberli, W., J. Alean, P. Müller, and M. Funk (1989), Assessing risks from glacier hazards in high mountain regions : some experiences in the Swiss Alps, *Annals of Glaciology*, *13*, 77–101.

Harrington, R. F., R. C. Bales, and P. Wagnon (1996), Variability of meltwater and solute fluxes from homogeneous melting snow at the laboratory scale, *Hydrological processes*, *10*(7), 945–953.

Harrison, W., L. Mayo, and D. Trabant (1975), Temperature measurements on black rapids glacier, Alaska, 1973, *Climate of the Arctic. Fairbanks, AK, University of Alaska. Geophysical Institute*, pp. 350–352.

Hartmann, D. L. (1994), *Global physical climatology*, vol. 56, Academic press.

Herron, M. M., and C. C. Langway Jr (1980), Firn densification : An empirical model, *Journal of Glaciology*, *25*, 373–385.

Hock, R. (1999), A distributed temperature-index ice-and snowmelt model including potential direct solar radiation, *J. Glaciol.*, *45*(149), 101–111.

Hock, R. (2003), Temperature index melt modelling in mountain areas, *Journal of Hydrology*, *282*(1), 104–115.

Hock, R., and B. Holmgren (2005), A distributed surface energy-balance model for complex topography and its application to Storglaciaren, Sweden, *Journal of Glaciology*, *51*(172), 25–36.

Hoelzle, M., G. Darms, M. P. Lüthi, and S. Suter (2011), Evidence of accelerated englacial warming in the Monte Rosa area, Switzerland/Italy, *The Cryosphere*, *5*(1), 231–243, doi : 10.5194/tc-5-231-2011.

Hoffman, M. J., A. G. Fountain, and G. E. Liston (2008), Surface energy balance and melt thresholds over 11 years at Taylor Glacier, Antarctica, *Journal of Geophysical Research*, *113*(F04014).

Holmlund, P., and M. Eriksson (1989), The cold surface layer on Storglaciären, *Geografiska Annaler. Series A. Physical Geography*, pp. 241–244.

Hooke, R. l. B., J. Gould, and J. Brzozowski (1983), Near-surface temperatures near and below the equilibrium line on polar and subpolar glaciers, *Zeitschrift für Gletscherkunde und Glazialgeologie*, *19*(1), 1–25.

Hopcroft, P. O., K. Gallagher, and C. C. Pain (2007), Inference of past climate from borehole temperature data using Bayesian reversible jump Markov Chain Monte Carlo, *Geophys. J. Int.*, *171*, 1430–1439, doi :10.1111/j.1365-246X.2007.03596.x.

Huang, S., H. N. Pollack, and P.-Y. Shen (2000), Temperature trends over the past five centuries reconstructed from borehole temperatures, *Nature*, *403*(6771), 756–758.

Huggel, C., W. Haeberli, A. Kääb, D. Bieri, and S. Richardson (2004), An assessment procedure for glacial hazards in the Swiss Alps, *Canadian Geotechnical Journal*, *41*(6), 1068–1083.

Humphrey, N. F., J. T. Harper, and W. T. Pfeffer (2012), Thermal tracking of meltwater retention in Greenland's accumulation area, *Journal of Geophysical Research : Earth Surface (2003–2012)*, *117*(F1).

Hutter, K. (1982), A mathematical model of polythermal glaciers and ice sheets, *Geophysical & Astrophysical Fluid Dynamics*, *21*(3-4), 201–224.

Hutter, K. (1983), *Theoretical Glaciology : Material Science of Ice and the Mechanics of Glaciers and Ice Sheets*, D. Reidel, Dordrecht, Netherlands.

Hutter, K., H. Blatter, and M. Funk (1988), A model computation of moisture content in polythermal glaciers, *Journal of Geophysical Research*, *93*(B10), 12,205–12.

Illangasekare, T. H., R. J. Walter, M. F. Meier, and W. T. Pfeffer (1990), Modeling of meltwater infiltration in subfreezing snow, *Water Resour. Res.*, *26*(5), 1001–1012.

Im, E.-S., E. Coppola, F. Giorgi, and X. Bi (2010), Local effects of climate change over the Alpine region : A study with a high resolution regional climate model with a surrogate climate change scenario, *Geophys. Res. Lett.*, *37*(L05704), doi :10.1029/2009GL041801.

IPCC (2007), *Climate Change 2007 : The Physical Science Basis. Contribution of Working Group I to the Fourth Assessment Report of the Intergovernmental Panel on Climate Change*, Cambridge Univ. Press, Cambridge, U. K.

Irvine-Fynn, T. D., A. J. Hodson, B. J. Moorman, G. Vatne, and A. L. Hubbard (2011), Polythermal glacier hydrology : a review, *Reviews of Geophysics*, *49*(4), RG4002.

Jania, J., D. Mochnacki, and B. Gadek (1996), The thermal structure of Hansbreen, a tidewater glacier in southern Spitsbergen, Svalbard, *Polar Research*, *15*(1), 53–66.

Jansson, P. (1996), Dynamics and hydrology of a small polythermal valley glacier, *Geografiska Annaler. Series A. Physical Geography*, pp. 171–180.

Jouzel, J., and L. Merlivat (1984), Deuterium and oxygen 18 in precipitation : Modeling of the isotopic effects during snow formation, *Journal of Geophysical Research : Atmospheres (1984–2012)*, *89*(D7), 11,749–11,757.

Jungo, P., and M. Beniston (2001), Changes in the anomalies of extreme temperature anomalies in the 20th century at Swiss climatological stations located at different latitudes and altitudes, *Theor. Appl. Climatol.*, *69*, 1–12.

Klok, E., and J. Oerlemans (2002), Model study of the spatial distribution of the energy and mass balance of Morteratschgletscher, Switzerland, *Journal of Glaciology*, *48*(163), 505–518.

Le Meur, E., and C. Vincent (2006), Monitoring of the Taconnaz ice fall (French Alps) using measurements of mass balance, surface velocities and ice cliff position, *Cold regions science and technology*, *46*(1), 1–11.

Legchenko, A., and P. Valla (2002), A review of the basic principles for proton magnetic resonance sounding measurements, *Journal of Applied Geophysics*, *50*(1), 3–19.

Legchenko, A., M. Descloitres, C. Vincent, H. Guyard, S. Garambois, K. Chalikakis, and M. Ezersky (2011), Three-dimensional magnetic resonance imaging for groundwater, *New Journal of Physics*, *13*(2), 025,022.

Legchenko, A., et al. (2013), Monitoring water accumulation in a glacier using magnetic resonance imaging, *The Cryosphere Discussions*, *7*(3), 2119–2151.

Lliboutry, L., M. Briat, M. Creseveur, and M. Pourchet (1976), 15 m deep temperatures in the glaciers of Mont Blanc (French Alps), *J. Glaciol*, *16*(74), 197–203.

Loewe, F. (1966), The temperature of the Sukkertoppen ice cap, *Journal of Glaciology*, *6*, 179–179.

Lüthi, M., and M. Funk (2000), Dating ice cores from a high Alpine glacier with a flow model for cold firn, *Annals of Glaciology*, *31*(1), 69–79.

Lüthi, M., and M. Funk (2001), Modelling heat flow in a cold, high-altitude glacier : Interpretation of measurements from Colle Gnifetti, Swiss Alps, *J. Glaciol.*, *47*(157), 314–324, doi :10.3189/172756501781832223.

Malvern, L. E. (1969), *Introduction to the Mechanics of Continuous Medium*, Monograph, Prentice Hall, Englewood Cliffs, N. J.

Maohuan, H. (1990), On the temperature distribution of glacier in China, *Journal of Glaciology*, *36*(123).

Messerli, B., and J. Ives (1997), *Mountains of the world : a global priority*, The Parthenon Publishing Group.

Mougin, P., and C. Bernard (1905), Études exécutées au glacier de Tête Rousse, *Annales de l'observatoire du Mont-Blanc. Joseph Vallot*, Tome VI.

Mougin, P., and C. Bernard (1922), *Etude sur le glacier de Tête-Rousse*, Etudes glaciologiques, Imprimerie Nationale IV.

Nakicenovic, N., and 26 others (2000), *IPCC Special Report on Emissions Scenarios*, Cambridge University Press : Cambridge, United Kingdom and New York.

Navarro, F., J. Otero, Y. Macheret, E. Vasilenko, J. Lapazaran, A. Ahlstrom, and F. Machio (2009), Radioglaciological studies on Hurd Peninsula glaciers, Livingston Island, Antarctica, *Annals of Glaciology*, *50*(51), 17–24.

Noetzli, J., S. Gruber, T. Kohl, N. Salzmann, and W. Haeberli (2007), Three-dimensional distribution and evolution of permafrost temperatures in idealized high-mountain topography, *Journal of Geophysical Research*, *112*(F2), F02S13.

Odegard, R. S., S.-E. Hamran, P. Bø, B. Etzelmuller, G. Vatne, and J. L. Sollid (1992), Thermal regime of a valley glacier, Erikbreen, northern Spitsbergen, *Polar Research*, *11*(2), 69–79.

Oerlemans, J. (1991), The mass balance of the Greenland ice sheet : sensitivity to climate change as revealed by energy-balance modelling, *The Holocene*, *1*(1), 40–48.

Oerlemans, J. (2001), *Glaciers and climate change*, Taylor & Francis.

Oerlemans, J., and J. Fortuin (1992), Sensitivity of Glaciers and Small Ice Caps to Greehouse Warming, *Science*, *258*(5079), 115–117.

Ohmura, A., and H. Lang (1989), Secular variation of global radiation in Europe, in *IRS*, vol. 88, pp. 298–301.

Ohmura, A., M. Wild, and L. Bengtsson (1996), A possible change in mass balance of Greenland and Antarctic ice sheets in the coming century, *Journal of Climate*, *9*(9), 2124–2135.

Oke, T. R. (1992), *Boundary layer climates*, vol. 5, Psychology Press.

Patera, A. T. (1984), A Spectral Element Method for Fluid Dynamic Laminar Flow in a Channel Expansion, *J. Comput. Phys.*, *54*(3), 468–488.

Paterson (1994), *The physics of glaciers*, Butterworth-Heinemann.

Paterson, W. (1972), Temperature distribution in the upper layers of the ablation area of Athabasca Glacier, Alberta, Canada, *Journal of Glaciology*, *11*, 31–41.

Pattyn, F., M. Nolan, B. Rabus, and S. Takahashi (2005), Localized basal motion of a polythermal Arctic glacier : McCall Glacier, Alaska, USA, *Annals of glaciology*, *40*(1), 47–51.

Payne, A., et al. (2000), Results from the EISMINT model intercomparison : the effects of thermo-mechanical coupling, *Journal of Glaciology*, *46*(153), 227–238.

Pellicciotti, F., B. Brock, U. Strasser, P. Burlando, M. Funk, and J. Corripio (2005), An enhanced temperature-index glacier melt model including the shortwave radiation balance : Development and testing for Haut Glacier d'Arolla, Switzerland, *Journal of Glaciology*, *51*(175), 573–587.

Pepin, N. C., and J. D. Lundquist (2008), Temperature trends at high elevations : Patterns across the globe, *Geophys. Res. Lett.*, *35*(L14701), doi :10.1029/2008GL034026.

Pettersson, R., P. Jansson, and P. Holmlund (2003), Cold surface layer thinning on Storglaciären, Sweden, observed by repeated ground penetrating radar surveys, *Journal of Geophysical Research : Earth Surface (2003–2012)*, *108*(F1).

Pettersson, R., P. Jansson, and H. Blatter (2004), Spatial variability in water content at the cold-temperate transition surface of the polythermal Storglaciären, Sweden, *J. Geophys. Res.*, *109*(F02009), doi :10.1029/2003JF000110.

Pettersson, R., P. Jansson, H. Huwald, and H. Blatter (2007), Spatial pattern and stability of the cold surface layer of Storglaciaren, Sweden, *Journal of Glaciology*, *53*(180), 99–109.

Picciotto, E. a., and S. Wilgain (1963), Fission products in Antarctic snow, a reference level for measuring accumulation, *Journal of Geophysical Research*, *68*(21), 5965–5972.

Pinglot, J., and M. Pourchet (1995), Radioactivity measurements applied to glaciers and lake sediments, *Science of the total environment*, *173*, 211–223.

Pollack, H. N., P. Y. Shen, and S. Huang (1996), Inference of ground surface temperature history from subsurface temperature data : Interpreting ensembles of borehole logs, *pure and applied geophysics*, *147*(3), 537–550.

Pourchet, M., J. Pinglot, L. Reynaud, and G. Holdsworth (1988), Identification of Chernobyl fallout as a new reference level in Northern Hemisphere glaciers, *Journal of Glaciology*, *34*(117), 183–187.

Preunkert, S., D. Wagenbach, M. Legrand, and C. Vincent (2000), Col du Dôme (Mt Blanc Massif, French Alps) suitability for ice-core studies in relation with past atmospheric chemistry over Europe, *Tellus B*, *52*(3), 993–1012.

Rabatel, A., J. P. Dedieu, and C. Vincent (2005), Using remote-sensing data to determine equilibrium line altitude and mass-balance time series : validation on three French glaciers, 1994-2002, *Journal of Glaciology*, *51*(175), 539–546.

Rabus, B. T., and K. A. Echelmeyer (2002), Increase of 10 m ice temperature : climate warming or glacier thinning ?, *Journal of Glaciology*, *48*(161), 279–286.

Rangwala, I., and J. R. Miller (2012), Climate change in mountains : a review of elevation-dependent warming and its possible causes, *Climatic Change*, *114*(3-4), 527–547, doi :10.1007/s10584-012-0419-3.

Raymond, M., M. Wegmann, and M. Funk (2003), *Inventar gefährlicher Gletscher in der Schweiz.*, Mitt. VAW/ETH 182.

Rippin, D., I. Willis, N. Arnold, A. Hodson, and M. Brinkhaus (2005), Spatial and temporal variations in surface velocity and basal drag across the tongue of the polythermal glacier midre Lovenbreen, Svalbard, *Journal of Glaciology*, *51*(175), 588–600.

Rippin, D. M., J. L. Carrivick, and C. Williams (2011), Evidence towards a thermal lag in the response of karsaglaciaren, northern Sweden, to climate change, *Journal of Glaciology*, *57*(205), 895–903.

Röthlisberger, H. (1981), Eislawinen und Ausbrüche von Gletscherseen, *P. Kasser (Ed.), Gletscher und Klima-glaciers et climat, Jahrbuch der Schweizerischen Naturforschenden Gesellschaft, wissenschaftlicher Teil 1978*, pp. 170–212.

Ryser, C., M. Lüthi, N. Blindow, S. Suckro, M. Funk, and A. Bauder (2013), Cold ice in the ablation zone : Its relation to glacier hydrology and ice water content, *Journal of Geophysical Research : Earth Surface*, *118*, 693–705.

Salamatin, A., V. Y. Lipenkov, and K. Blinov (1994), Vostok (Antarctica) climate record timescale deduced from the analysis of a borehole-temperature profile, *Annals of Glaciology*, *20*(1), 207–214.

Shimizu, H. (1970), Air permeability of deposited snow, *Contributions from the Institute of Low Temperature Science*, *22*, 1–32.

Sicart, J. E., R. Hock, and D. Six (2008), Glacier melt, air temperature, and energy balance in different climates : The Bolivian Tropics, the French Alps, and northern Sweden, *Journal of Geophysical Research : Atmospheres (1984–2012)*, *113*(D24).

Skidmore, M. L., and M. J. Sharp (1999), Drainage system behaviour of a High-Arctic polythermal glacier, *Annals of Glaciology*, *28*(1), 209–215.

Sturm, M., J. Holmgren, M. König, and K. Morris (1997), The thermal conductivity of seasonal snow, *Journal of Glaciology*, *43*(143), 26–41.

Suter, S. (2002), Cold firn and ice in the Monte Rosa and Mont Blanc areas(spatial occurence, surface energy balance and climatic evidence), Ph.D. thesis, ETH Zurich.

Suter, S., M. Laternser, W. Haeberli, M. Hoelzle, and R. Frauenfelder (2001), Cold firn and ice of high-altitude glaciers in the Alps : Measurements and distribution modelling, *J. Glaciol.*, *47*(156), 85–96.

Suter, S., M. Hoelzle, and A. Ohmura (2004), Energy balance at a cold Alpine firn saddle, Seserjoch, Monte Rosa, *International journal of climatology*, *24*(11), 1423–1442.

Themessl, J., Matthias, A. Gobiet, and A. Leuprecht (2011), Empirical-statistical downscaling and error correction of daily precipitation from regional climate models, *International Journal of Climatology*, *31*(10), 1530–1544.

Vallon, M., J.-R. Petit, and B. Fabre (1976), Study of an ice core to the bedrock in the accumulation zone of an alpine glacier, *Journal of Glaciology*, *17*, 13–28.

Vallot, J., A. Delebecque, and L. Duparc (1892), Sur la catastrophe de Saint Gervais., *Archives des Sciences physiques et naturelles, Troisième période*, *XXVIII*.

Van de Wal, R. (1996), Mass-balance modelling of the Greenland ice sheet : a comparison of an energy-balance model and a degree-day model, *Annals of Glaciology*, *23*, 36–45.

Van der Linden, P., and J. e. Mitchell (2009), ENSEMBLES : Climate Change and its Impacts : Summary of research and results from the ENSEMBLES project, *Met Office Hadley Centre, FitzRoy Road, Exeter EX1 3PB, UK*, *160*.

Van der Veen, C. (2007), Fracture propagation as means of rapidly transferring surface meltwater to the base of glaciers, *Geophysical Research Letters*, *34*(1).

Vincent, C. (2002), Influence of climate change over the 20th Century on four French glacier mass balances, *Journal of Geophysical Research : Atmospheres (1984–2012)*, *107*(D19), 4375, doi : 10.1029/2001JD000832.

Vincent, C., M. Vallon, J. Pinglot, M. Funk, and L. Reynaud (1997), Snow accumulation and ice flow at Dôme du Goûter (4300 m), Mont Blanc, French Alps, *Journal of Glaciology*, *43*(145), 513–521.

Vincent, C., E. Le Meur, and R. Blanc (2003), Chute de séracs du glacier de Taconnaz, *Rapport destiné au SIVOM de la Haute Vallée de l'Arve (74) sur les travaux glaciologiques exécutés par le LGGE*.

Vincent, C., E. Le Meur, D. Six, M. Funk, M. Hoelzle, and S. Preunkert (2007a), Very high elevation Mont Blanc glaciated areas not affected by the 20th century climate change, *J. Geophys. Res.*, *112*(D09120), doi :10.1029/2006JD007407.

Vincent, C., E. Le Meur, D. Six, P. Possenti, E. Lefebvre, and M. Funk (2007b), Climate warming revealed by englacial temperatures at Col du Dôme (4250 m, Mont-Blanc area), *Geophys. Res. Lett.*, *34*(L16502), doi :10.1029/2007GL029933.

Vincent, C., S. Garambois, E. Le Meur, E. Thibert, and E. Lefebvre (2008), Contribution à l'étude du glacier de Tête Rousse à partir de la campagne d'observations de 2007, *Rapport effectué pour le Service du R.T.M. de Haute savoie*.

Vincent, C., S. Garambois, E. Thibert, E. Lefèbre, E. Le Meur, and D. Six (2010a), Origin of the outburst flood from Glacier de Tête Rousse in 1892 (Mont Blanc area, France), *Journal of Glaciology*, *56*(198), 688–698.

Vincent, C., M. Descloitres, S. Garambois, and A. Legchenko (2010b), Etude des cavités sous glaciaires du glacier de Tête Rousse (mai-juillet 2010), *Rapport au préfet de Haute Savoie*.

Vincent, C., O. Gagliardini, S. Garambois, A. Gilbert, D. Laigle, A. Legtchenko, and E. Thibert (2011), Rapport d'expertise scientifique sur la poche d'eau du glacier de Tête Rousse, *Rapport à la Mairie de la commune de St Gervais*.

Vincent, C., M. Descloitres, S. Garambois, A. Legchenko, H. Guyard, and A. Gilbert (2012), Detection of a subglacial lake in Glacier de Tête Rousse (Mont Blanc area, France), *Journal of Glaciology*, *58*(211), 866–878.

Vincent, C., E. Thibert, O. Gagliardini, A. Legtchenko, and A. Gilbert (2012b), Rapport de synthèse sur l'évolution du glacier de Tête Rousse en 2012., *Rapport à la préfecture de haute Savoie et à la Mairie de la commune de St Gervais*.

Vincent, C., M. Descloitres, S. Garambois, S. Legchenko, H. Guyard, E. Thibert, A. Legtchenko, and A. Gilbert (2012c), Détection d'une poche d'eau au glacier de Tête Rousse en 2010 et mesures préventives pour éviter une catastrophe, *La Houille Blanche*, *2*, 34–41.

Wagnon, P., P. Ribstein, B. Francou, and B. Pouyaud (1999), Annual cycle of energy balance of Zongo glacier, Cordillera Real, Bolivia, *Journal of Geophysical Research : Atmospheres (1984–2012)*, *104*(D4), 3907–3923.

Wagnon, P., J.-E. Sicart, E. Berthier, and J.-P. Chazarin (2003), Wintertime high-altitude surface energy balance of a Bolivian glacier, Illimani, 6340 m above sea level, *Journal of Geophysical Research*, *108*(D6), 4177.

Werder, M., I. Hewitt, C. Schoof, and G. Flowers (2013), Modeling channelized and distributed subglacial drainage in two dimensions, *J. Geophys. Res.*, accepted.

Wilson, N., and G. Flowers (2013), Environmental controls on the thermal structure of alpine glaciers, *The Cryosphere*, *7*(1), 167–182.

Wilson, N. J., G. E. Flowers, and L. Mingo (2013b), Comparison of thermal structure and evolution between neighboring subarctic glaciers, *Journal of Geophysical Research : Earth Surface*, *118*(3), 1443–1459.

Wohlleben, T., M. Sharp, and A. Bush (2009), Factors influencing the basal temperatures of a High Arctic polythermal glacier, *Annals of Glaciology*, *50*(52), 9.

Wright, A., J. Wadham, M. Siegert, A. Luckman, J. Kohler, and A. Nuttall (2007), Modeling the refreezing of meltwater as superimposed ice on a high Arctic glacier : A comparison of approaches, *Journal of Geophysical Research : Earth Surface (2003–2012)*, *112*(F4).

Zwinger, T., and J. Moore (2009), Diagnostic and prognostic simulations with a full Stokes model accounting for superimposed ice of Midtre Lovénbreen, Svalbard, *The Cryosphere*, *3*(2), 217–229.

Zwinger, T., R. Greve, O. Gagliardini, T. Shiraiwa, and M. Lyly (2007), A full Stokes-flow thermo-mechanical model for firn and ice applied to the Gorshkov crater glacier, Kamchatka, *Annals of Glaciology*, *45*(1), 29–37.

Liste des figures

Annexe A

Article : Atmospheric warming at a high elevation tropical site revealed by englacial temperatures at Illimani, Bolivia (6340 m a.s.l., 16°S,67°W)

JOURNAL OF GEOPHYSICAL RESEARCH, VOL. 115, D10109, doi:10.1029/2009JD012961, 2010

Atmospheric warming at a high-elevation tropical site revealed by englacial temperatures at Illimani, Bolivia (6340 m above sea level, 16°S, 67°W)

A. Gilbert,[1,2] P. Wagnon,[2] C. Vincent,[3] P. Ginot,[1,2] and M. Funk[4]

Received 5 August 2009; revised 28 December 2009; accepted 4 January 2010; published 25 May 2010.

[1] In June 1999, a deep (138.7 m) ice core was extracted from the summit glacier of Illimani, Bolivia (6340 m above sea level, 16°39′S, 67°47′W), and an englacial temperature profile was measured in the borehole. Using on-site and regional meteorological data as well as ice core stratigraphy, past surface temperatures were reconstructed with a heat flow model. The englacial temperature measurements exhibit a profile that is far from a steady state, reflecting an increasing atmospheric temperature over several years and nonstationary climatic conditions. Englacial temperature interpretation, using air temperature data, borehole temperature inversion, and melting rate quantification based on ice core density, shows two warming phases from 1900 to 1960 (+0.5 ± 0.3 K starting approximately in 1920–1930) and from 1985 to 1999 (+0.6 ± 0.2 K), corresponding to a mean atmospheric temperature rise of 1.1 ± 0.2 K over the 20th century. According to various climate change scenarios, the future evolution of englacial temperatures was simulated to estimate when and under what conditions this high-elevation site on the Illimani summit glacier could become temperate in the future. Results show that this glacier might remain cold for more than 90 years in the case of a +2 K rise over the 21st century but could become temperate in the first 20 m depth between 2050 and 2060 if warming reaches +5 K.

Citation: Gilbert, A., P. Wagnon, C. Vincent, P. Ginot, and M. Funk (2010), Atmospheric warming at a high-elevation tropical site revealed by englacial temperatures at Illimani, Bolivia (6340 m above sea level, 16°S, 67°W), *J. Geophys. Res.*, *115*, D10109, doi:10.1029/2009JD012961.

1. Introduction

[2] Tropical glaciers are known to be very sensitive climatic indicators [e.g., *Francou et al.*, 2003, 2004; *Favier et al.*, 2004; *Vuille et al.*, 2008]. These high-altitude sites (usually above 4800 m above sea level (asl)) are particularly vulnerable to the effects of global warming [*Vuille et al.*, 2008]; however, direct meteorological observations are very scarce and generally discontinuous. Consequently, reconstructing air temperatures over recent decades or centuries using various proxies or modeling is particularly important at these locations.

[3] The temperature distribution within cold glaciers strongly depends on surface temperature variations and provides an excellent means to investigate past climate variations in polar regions [*Ritz*, 1989; *Salamatin et al.*, 1998] and on high mountains [e.g., *Haeberli and Funk*, 1991; *Lüthi and Funk*, 2001; *Vincent et al.*, 2007] with a time scale much larger for ice sheets than for high mountain areas. In the tropical Andes, cold glaciers are encountered usually above 6000 m asl and sometimes higher, depending on the site. Temperature measurements carried out during ice core drilling at 6270 m asl on Chimborazo (Ecuador) in November 2000 and at 6090 m asl on Nevado Coropuna (Peru) in June 2003 showed that the glaciers were temperate at these altitudes. The number of very high altitude cold glacier study sites in the tropics is therefore rather limited and likely to steadily decrease in the future because of global warming [*Thompson et al.*, 2006]. Nevertheless, borehole temperatures can provide very useful information on climate change at these high elevations where direct meteorological measurements are rare or sporadic [*Hardy et al.*, 2003; *Wagnon et al.*, 2003].

[4] For the Alps, *Lüthi and Funk* [2001] and *Vincent et al.* [2007] have concluded that borehole temperature profiles reflect conditions that are far from steady state and provide clear evidence of atmospheric global warming over recent decades. The profiles also reveal that the refreezing of surface meltwater below the surface contributes to the englacial temperature increase, even at elevations as high as 4250 m asl in the Alps [*Vincent et al.*, 2007]. In this study we present the first analysis of a vertical englacial temperature profile measured in the tropical Andes. It results from an ice core drilled on Illimani, Bolivia (6340 m asl, 16°39′S, 67°47′W).

[1] IHH, IRD, La Paz, Bolivia.
[2] LGGE and LTHE, IRD, Saint-Martin-d'Hères, France.
[3] LGGE, UJF, CNRS, Saint-Martin-d'Hères, France.
[4] VAW, ETH Zurich, Zurich, Switzerland.

0148-0227/10/2009JD012961

Figure 1. Location of the Illimani drilling site in South America.

In high-latitude ice caps, deep borehole temperature profiles are complementary to isotopic proxy to investigate past temperature fluctuations using inverse problem resolution [*Kotlyakov et al.*, 2004; *Nagornov et al.*, 2001; *Ritz*, 1989]. However, the Andean ice core isotopic signal is mostly associated with precipitation variations [*Vimeux et al.*, 2005, 2009] so that no reconstitution of temperature over recent centuries is yet available from Andean ice cores. After describing the data (section 2) and the model (section 3), we interpret borehole englacial temperature using La Paz air temperature (section 4) in order to reconstruct atmospheric temperature variations over the last century at 6340 m asl on Illimani (sections 5 and 6). In section 7 we assess the future evolution of englacial temperatures according to possible climate change scenarios. The conclusions are given in section 8.

2. Data

2.1. Site Location

[5] In June 1999, a 138.7 m ice core was drilled down to bedrock on a flat pass at 6340 m asl (16°39′S, 67°47′W), just below the main summit of Illimani (Cordillera Real, Bolivia) (Figure 1) [*Knüsel et al.*, 2003]. This site is located approximately 50 km southeast of the capital La Paz. The drilling site was chosen on the flattest location where the ice flow velocities are assumed to be very small. Results concerning chemical and isotopic analysis of this ice core are given by *De Angelis et al.* [2003] and *Ramirez et al.* [2003], respectively. Using volcanic signals in ice, *Knüsel et al.* [2003] have provided an accurate dating of this ice core with reference years located at 9.9 m (1991), 17.5 m (1982), 34.2 m (1963), and 64.4 m (1883). The total ice core covers approximately 18,000 years, and the upper 60 m cover the 20th century.

2.2. Measurements of Englacial Temperature and Density

[6] The boring was performed with a Fast Electromechanical Lightweight Ice Coring System (FELICS) [*Ginot et al.*, 2002]. The borehole always remained dry, thus limiting disturbance of the thermal regime. Drilling was completed on 3 June 1999 at 1240 LT. Englacial temperatures were measured using a 150 m long thermistor chain composed of 10 thermistors (Fenwal 135-103FAG-J01) located one every 5 m over the first 45 m of the chain. Each thermistor was previously calibrated in a thermostatic bath to reach ±0.05 K minimum accuracy. The chain was first installed in the borehole on 4 June 1999 at 1510 LT with the thermistors located between 138 and 93 m depth. Measurements were carried out with a digital multimeter (Fluke 83) used for calibration 1 h and 50 min later at 1700 LT and then also at

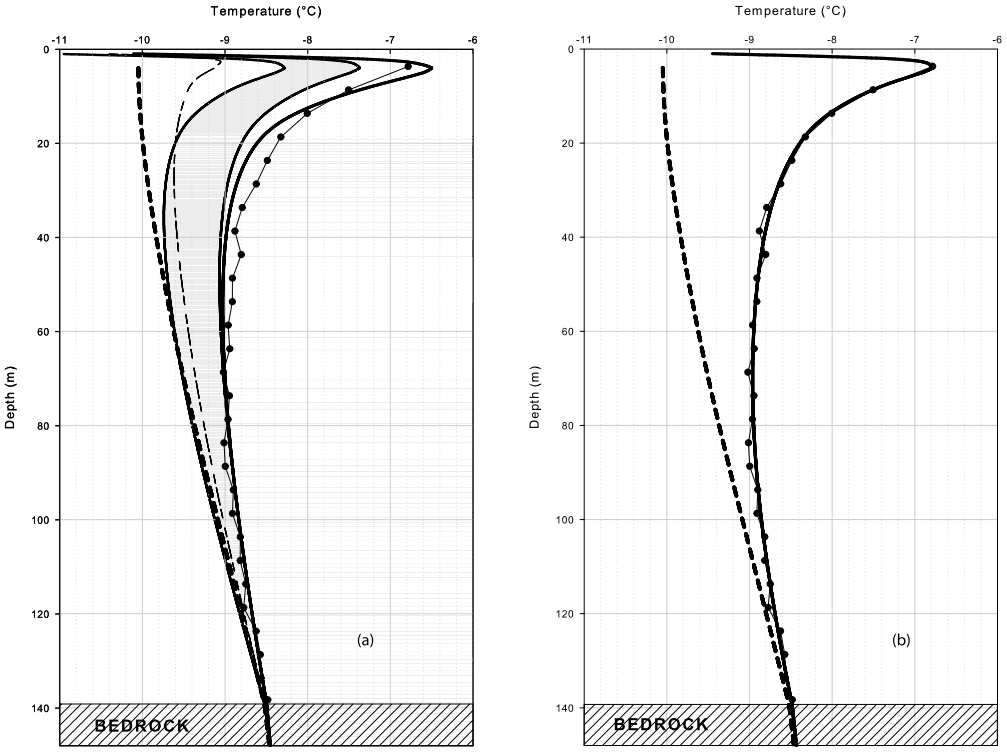

Figure 2. Vertical englacial temperature profile measured at Illimani (6340 m above sea level (asl)) in June 1999 (thin line with black dots). Modeled profile assuming a steady state climate with a constant secular temperature of 263.1 K (dashed line) and a constant geothermal flux of 22×10^{-3} W m^{-2}. (a) Modeled temperature profiles assuming a steady state before 1967 and using La Paz air temperature data after 1967 without taking into account the latent heat resulting from surface meltwater refreezing (thin dashed line) and taking into account the latent heat resulting from refreezing (melting factor a = 1.1 W m^{-2} K^{-1}) for a geothermal flux varying from 18 to 26×10^{-3} W m^{-2} (gray zone) and modeled temperature profile with a forced melting factor a = 1.7 W m^{-2} K^{-1} (thick line). (b) Modeled temperature profile assuming a steady state before 1900, assuming a 0.4 K warming between 1900 and 1962, and using La Paz air temperature after 1900 with a constant geothermal flux of 22×10^{-3} W m^{-2} and a melting factor of 1.1 W m^{-2} K^{-1} (thick line) (see section 4 for more details).

1730 and 1915 LT. Thirteen hours later, on 5 June, the chain was raised 50 m upward to perform measurements between 88 and 43 m at 0815 and 0930 LT. Finally, on 5 June, the chain was moved upward once again to measure the englacial temperatures between 38 m and the surface at 0930 and 1015 LT. The resulting englacial temperature profile with the resulting 28 points is plotted in Figure 2 (thin line with black dots).

[7] Density measurements were performed in cold rooms, measuring and weighing every section of the ice core ranging from 5 to 70 cm long, regardless of the time period covered by every section. Accuracy is assumed to be ±0.013 kg m^{-3}, taking into account the mass and size uncertainty of ice core sections. Ice layers were counted, and their thicknesses were measured along the core.

2.3. Meteorological Data Sets

[8] Since 1962, minimum and maximum daily air temperatures have been recorded in La Paz (El Alto meteorological station, 4070 m asl). Daily air temperature is approximated by the median value of the minimum and maximum values. Air temperatures were also measured (using Vaisala temperature thermistor with Gill Aspirated Radiation Shield (airflow monitoring switch)) at the drilling site by an automatic weather station (AWS) between May 1998 and March 1999, initially at 3.5 m above the surface. This data set was kindly provided by D. Hardy (University of Massachusetts).

[9] La Paz temperatures were compared with reanalyzed daily temperatures from NCEP-NCAR (15°S, 67.5°W, 500 hPa, since 1948, 2.5° grid) and with the AWS data set. La

Paz air temperatures show a difference between the mean temperature of the dry season and the mean temperature of the wet season as high as 4 K, which is similar to the seasonal thermal variability observed on Illimani by the AWS. On the other hand, reanalyzed temperatures do not agree well with AWS temperatures, particularly with a seasonal thermal variability not exceeding 2 K. Consequently, to simulate the heat flow into the glacier, La Paz temperatures seem to be more reliable than reanalyzed data.

3. Heat Flow Modeling

[10] The heat transfer equation within a cold glacier can be written as follows [*Malvern*, 1969; *Hutter*, 1983]:

$$\rho C_p \left[\frac{\partial T}{\partial t} + \mathbf{v} \cdot \mathbf{grad}(T)\right] = \mathrm{div}[k\ \mathbf{grad}(T)] + Q, \qquad (1)$$

where T (K) is the firn/ice temperature, ρ (kg m^{-3}) is the density, C_p (J kg^{-1} K^{-1}) is the thermal capacity, k (W m^{-1} K^{-1}) is the thermal conductivity, $\mathbf{v}$ (m s^{-1}) is the glacier flow velocity vector, t (s) is the time, and Q (W m^{-3}) is the latent heat released during water change of state per unit of time and volume. According to a similar study in the Alps [*Vincent et al.*, 2007], heat production by deformation and horizontal heat transfer can be neglected assuming that on this large flat pass, ice flow is slow and the horizontal englacial temperature gradient low. Consequently, equation (1) can be simplified to one dimension (z):

$$\rho C_p \left(\frac{\partial T}{\partial t} + v_z \frac{\partial T}{\partial z}\right) = \frac{\partial}{\partial z}\left(k \frac{\partial T}{\partial z}\right) + Q, \qquad (2)$$

where v_z (m s^{-1}) is the vertical glacier flow velocity.

[11] Englacial temperatures and their changes are computed at 10 day intervals using a Crank-Nicholson scheme (implicit finite difference) with a 1 m horizontal layer thickness. The geothermal flux is assumed to be constant at 10 m below the bedrock. *Noetzli et al.* [2007] showed that the three-dimensional topography has a strong influence on the heat flux variation in the summit areas of mountains, but we had no alternative other than to assume a constant geothermal flux. The temperature gradient inferred from the deepest 20 m above the bedrock allows us to assess the basal heat flux ($22 \pm 4 \times 10^{-3}$ W m^{-2}). According to the age-depth relationship, the vertical velocity is fitted by an exponential law ($v_z = v_0 \exp(-0.038z)$, $R^2 = 0.83$) with a surface vertical velocity v_0 given by the annual accumulation rate reconstructed by annual layer counting (mean value at Illimani is 0.58 m water equivalent) [*Knüsel et al.*, 2003]. The firn thermal conductivity k (W m^{-1} K^{-1}) is calculated using the Sturm density-conductivity relationship [*Sturm et al.*, 1997]

$$k = \begin{cases} 0.138 - 1.01\rho + 3.233\rho^2 & \text{if } 0.156 < \rho < 0.6 \\ 0.023 + 0.234\rho & \text{if } \rho < 0.156, \end{cases} \qquad (3)$$

where ρ is the firn/snow density. For densities higher than 0.6, we still apply equation (3) as suggested by *Sturm et al.* [1997].

[12] Surface boundary conditions depend on the surface energy balance. Modeling the surface energy budget requires meteorological data (incoming net all-wave radiation, albedo, air humidity, air and surface temperatures, and wind speed), which are usually not available on site [*Wagnon et al.*, 2003]. Consequently, the surface temperature T_{surf} (K), which is the snow temperature in the first meter of the glacier, is given by the simple parameterization [*Lüthi and Funk*, 2001]

$$T_{surf} = T_{air} - b, \qquad (4)$$

where T_{air} (K) is air temperature and b (K) is a parameter. At Illimani, air temperature is also not known. Thus, in section 4, b can be regarded as a tuning parameter rather than as a physical one because it results not only from the surface energy balance but also from the lapse rate used between La Paz and the drilling site and from the steady state temperature.

4. Results

4.1. Preliminary Results

[13] The first simulation was done assuming a steady state up to the year 1967, which means that the surface temperature is assumed to remain stable until this date. This secular temperature, which is the representative temperature of the steady state, has been tuned to fit the simulated temperature profile to measured basal temperature, resulting in a value of 263.1 K. Additionally, monthly means of La Paz air temperatures have been compared with monthly AWS air temperatures for the period May 1998 to March 1999 in order to calculate a mean lapse rate of −6.5 K km^{-1} (standard deviation of 0.4 K). Using this lapse rate, the mean annual air temperature of La Paz between 1962 and 1967 leads to a mean air temperature of 265.8 K at 6340 m asl for this period. Consequently, the parameter b of equation (4) is set to 2.7 K. The value of b clearly depends on the reference period used to represent the steady state. Nevertheless, because of the much lower warming recorded by La Paz air temperatures between 1962 and 1982, b does not vary much when longer reference periods are used. Indeed, b equals 2.70, 2.86, and 2.85 K when using 1962–1967, 1962–1977, and 1962–1982, respectively, as reference periods for the steady state.

[14] Using any b parameter mentioned in section 4.1 and La Paz temperatures, the simulation of englacial temperatures reveals strong differences with measurements carried out in 1999 (Figure 2a, thin dashed line). Indeed, the simulated englacial temperatures are too low. These differences are likely due to an additional energy contribution. We suggest that an additional energy flux could come from the latent heat due to refreezing of meltwater as previously observed on a high alpine site [*Suter et al.*, 2004].

4.2. Effect of Latent Heat Released by Refreezing Meltwater

[15] On this cold, high-altitude site (annual mean air temperature <267 K), it can be assumed that meltwater occasionally produced at the surface refreezes immediately below the surface, releasing an energy flux called $F_{refreezing}$

(W m^{-2}). This energy flux can be assessed using the degree-day parameterization [e.g., *Hock*, 2003]

$$F_{refreezing} = \begin{cases} (T_{air} - T_{ref})a & \text{if } T_{air} > T_{ref} \\ 0 & \text{if } T_{air} \leq T_{ref} \end{cases} \quad (5)$$

where a (W m^{-2} K^{-1}) is a melting factor accounting for the energy flux produced by refreezing meltwater with respect to the latent heat of melting-freezing ($L_f = 3.34 \times 10^5$ J kg^{-1}). T_{ref} is a daily temperature threshold above which the daytime surface temperature may reach 273.15 K, thereby letting melting occur. Air temperature recorded on site by the AWS in 1998–1999 showed that when daily temperature is as high as 267.1 ± 0.2 K, part of the afternoon exhibits positive air temperatures and melting may occur. T_{ref} is then assumed to be 267.1 K. If we assume that meltwater refreezes immediately below the surface, melting occurring from time to time at the surface systematically produces a latent heat release in the surface layer, that is, in the first layer of our model. Within this first layer, mass is always conserved; only heat is gained in the case of refreezing meltwater. This assumption is supported by the fact that this high-altitude site remains cold, preventing melting from being strong enough to produce running water.

[16] Ice layers were observed in the core, and a mean value of 6.8% in volume is measured in the first 37 m of the core [*Knüsel et al.*, 2003]. Taking into account the density difference between ice (920 kg m^{-3}) and firn in the upper layers (350 kg m^{-3}), the mean amount of calculated refreezing meltwater (between 1960 (37 m deep) and 1999 (surface)) is converted into a mean amount of ice layers along the core between the surface and 37 m deep. The factor a is then tuned to obtain the best agreement between the calculated and measured volume of ice within the core. We found $a = 1.1 \pm 0.1$ W m^{-2} K^{-1}, corresponding to 0.48 ± 0.03 mm K^{-1} d^{-1} in a classical degree-day formulation. This low value compared with usual snow degree-day factors [*Hock*, 2003] can be explained by the fact that this very high altitude site is cold and characterized by a continually high albedo surface and strong sublimation rates [*Wagnon et al.*, 2003].

[17] In sections 5 and 6 we use equation (5) at annual time scale. The linear regression between annual mean air temperature and annual surface melting computed with the previous degree-day approach gives a good correlation (R^2 = 0.80, n = 37 years). Thus, annual melting and annual temperature are related by (5) with $T_{ref} = 265.3 \pm 0.1$ K and $a = 0.53 \pm 0.03$ W m^{-2} K^{-1}.

[18] Using this additional flux from heat released by the refreezing of surface meltwater and assuming a steady state up to 1967 improves agreement with measurements (Figure 2a). Nevertheless, simulated englacial temperature profiles between 10 and 60 m deep still remain colder than the observed profile, no matter what melting factor or geothermal flux values are used (the gray zone in Figure 2a shows simulated profiles for a basal heat flux varying between 18 and 26 × 10^{-3} W m^{-2} and the thick line shows a melting factor forced to 1.7 W m^{-2} K^{-1}). A nonstationary climatic state before 1967 could explain this remaining lack of energy. For this reason, the assumption relative to climatic steady state before 1967 was rejected.

[19] On the other hand, we can assume a climatic steady state until 1900. Indeed, from numerical experiments, it can be shown that temperature variations before 1900 do not influence the 1999 englacial temperature profile. As a matter of fact, the continuity between the steady climatic state before 1900 and La Paz air temperature data is interrupted if the parameter b (equation (4)) remains related to the secular temperature (as in section 4.1). Consequently, as for the geothermal flux and the secular temperature, b is used to adjust the simulated profile to the observed profile. Since simulated and observed englacial temperatures mainly differ in the upper 60 m (Figure 2a), these three parameters are strongly constrained by this part of the profile. The set of parameters providing the best agreement between observations and simulations gives a geothermal flux of 21 ± 2 × 10^{-3} W m^{-2}, a secular temperature of 263.1 ± 0.1 K, and b of 2.3 ± 0.1 K. Figure 2b shows the englacial temperature profile simulated with this set of parameters using La Paz air temperatures. According to equation (4) and considering the values obtained for the secular temperature and for b, air temperature before 1900 is assumed to be 265.4 ± 0.2 K while the mean La Paz air temperature between 1962 and 1967 is 265.8 K. This implies a 0.4 ± 0.2 K atmospheric warming between the steady state (before 1900) and the mean temperature over the 1962–1967 period.

[20] In conclusion, the observed englacial temperature profile of Illimani can be explained only if we take into account both the latent heat released by the refreezing of surface meltwater and a 0.4 ± 0.2 K atmospheric warming at 6340 m asl between the beginning of the 20th century and the 1960s. An accurate parameter sensitivity test is now needed to confirm and improve the temperature reconstitution over the 20th century at this high-altitude site. This test is performed in section 5 using inverse problem analysis.

5. Borehole Temperature Profile Inversion

5.1. Bayesian Approach to Solving the Inverse Problem

[21] Bayesian inference, described by *Hopcroft et al.* [2007], was applied to assess the past surface temperature variations from englacial temperatures. This analysis was done without using La Paz temperatures for the last 37 years. In a Bayesian formulation, model parameters are described by probability distributions. The aim of Bayesian inference is to quantify the posterior probability distribution, which characterizes all of the model parameters given prior information and the data available.

[22] The past surface temperature (from 1900 to 1999) is set up as a series of linear segments with the nodes of these segments being the model parameters T_{surf}, i.e., $T_{surf} = (T_i, t_i; i = 1, 5)$, where T is temperature and t is time (t_1 and t_5 are fixed at 1900 and 1999, respectively). The other parameters are the melting factor and the geothermal flux. The secular temperature is given by the geothermal flux and the basal temperature, according to steady state conditions (see section 4.1). The latent energy flux released by the refreezing of meltwater is estimated by a linear relationship between

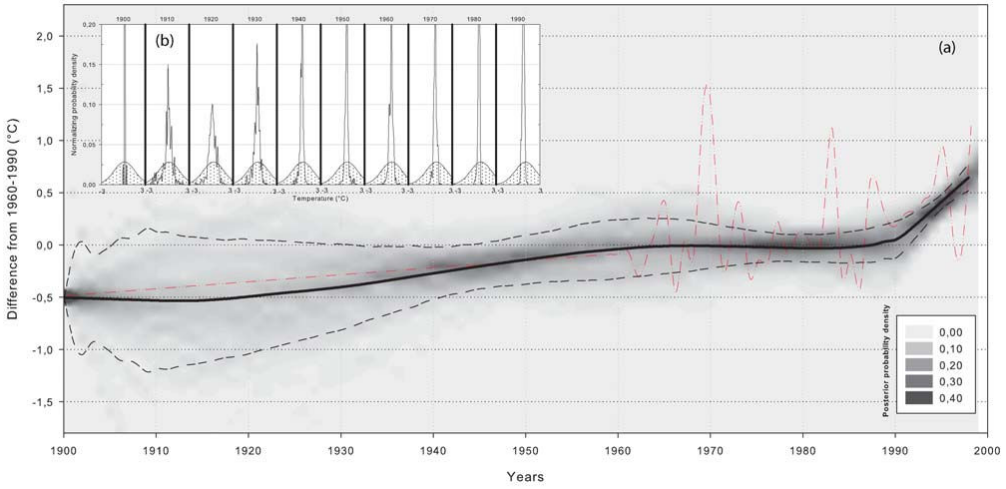

Figure 3. (a) Reconstructed air temperature at Illimani (6340 m asl) over the 20th century using borehole temperature profile inversion (thick line) compared with La Paz air temperature (red dashed line after 1962). The two black dashed lines form an envelope corresponding to model uncertainties according to posterior probability density standard deviation. The gray scale represents the past surface temperature probability distribution. (b) Posterior (thin line) and prior (dotted surface) probability density functions of surface temperature each 10 years (see section 5 for more details).

annual melting and annual temperature anomalies, according to equation (5) (see section 4.2).

[23] In order to determine posterior probability density function (pdf), the values of the parameters are generated according to the Markov Chain Monte Carlo method. The surface temperatures T_{surf}, the melting factor a, and the geothermal flux F_{geo} are updated for each iteration using a Gaussian random function.

[24] For each set of parameters, a posterior probability P is calculated using data and prior information according to

$$P = \exp\left[-0.5(\mathbf{T}_{\text{model}} - \mathbf{T}_{\text{data}})^T C^{-1}(\mathbf{T}_{\text{model}} - \mathbf{T}_{\text{data}})\right] \cdot \exp\left[-0.5(M_{\text{data}} - M_{\text{model}})^2 1/\sigma_M^2\right] \cdot P_{\text{prior}}(\boldsymbol{T}_{\text{surf}})P_{\text{prior}}(a)P_{\text{prior}}(F_{\text{geo}}), \quad (6)$$

where $\mathbf{T}_{\text{model}}$ and $\mathbf{T}_{\text{data}}$ are the vectors of modeled englacial temperatures and measured englacial temperatures, respectively. C is the covariance matrix describing measurement uncertainty. The errors on the data are assumed to be uncorrelated, which implies C to be diagonal. M_{data} is the percentage of melting feature measured within the core (6.8%), while M_{model} is the same modeled percentage (see section 4.2); σ_M is the standard deviation, which specifies the measurement uncertainty on M_{data} (1%).

[25] The prior information, P_{prior}, used to constrain parameter values to realistic values is described by Gaussian probability functions. $P_{\text{prior}}(T_{\text{surf}})$ is centered on the surface temperature variations T_{prior}, which follows a linear trend of 0.01 K yr^{-1} over the period 1900–1999. The associated standard deviation is 1.5 K. $P_{\text{prior}}(a)$ is centered on the melting factor from section 4 (a_{prior} = 0.53 W m^{-2} K^{-1}), and the standard deviation is 0.5 W m^{-2} K^{-1}. $P_{\text{prior}}(F_{\text{geo}})$ is uniform over the interval [0, 0.080] W m^{-2}. Indeed, if the absolute difference between the parameters coming from Monte Carlo algorithm and prior parameters (T_{prior}, a_{prior}) exceeds one standard deviation, the associated posterior probability P tends toward zero.

[26] The resulting value of each parameter is the average of each value of this parameter obtained by the successive iterations and weighted by its probability. The model uncertainty is determined by the standard deviation of the posterior pdf.

5.2. Results

[27] In order to assess the accuracy of the model and to confirm the choice of the parameters used in section 4, a first sensitivity test was performed on the melting factor a and on the geothermal flux. We obtain a melting factor value of 0.5 ± 0.2 W m^{-2} K^{-1} on the annual time scale (close to the previous value estimated at 0.53 W m^{-2} K^{-1}, see section 4.2). Inversion does not give a better estimate of the geothermal flux than the use of the basal englacial temperature gradient (section 3). However, a fixed melting factor (0.5 W m^{-2} K^{-1}) gives a basal heat flux value of 21 ± 2 × 10^{-3} W m^{-2}, in agreement with the value obtained in section 4.2. The subsequent inversions will be performed using the melting factor and basal heat flux as fixed parameters equal to 0.5 W m^{-2} K^{-1} and 21 × 10^{-3} W m^{-2}, respectively (Figure 3).

[28] Using these fixed parameters and T_{surf} as a free parameter, our analysis was carried out to assess past temperature variations. According to the posterior pdf (Figure 3a, in gray scale), mean values of past temperature

Table 1. Twentieth Century Temperature Trends Reconstructed at Illimani[a]

	20th Century Warming (K)	Linear Temperature Trend (K decade^{-1}) (R^2)		
		1900–1999	1950–1999	1980–1999
Inversion with surface temperature as the free parameter	1.1 ± 0.2	0.085 ± 0.01 (0.88)	0.092 ± 0.02 (0.54)	0.35 ± 0.05 (0.81)
Reconstruction from density anomaly	1.2 ± 0.2	0.087 ± 0.02 (0.68)	0.13 ± 0.05 (0.50)	0.36 ± 0.1 (0.47)
Inversion with the surface temperature and geothermal flux as the free parameters	1.1 ± 0.3	0.10 ± 0.04 (0.79)	0.087 ± 0.03 (0.41)	0.42 ± 0.1 (0.88)
Inversion with the surface temperature, melting factor, and geothermal flux as the free parameters	1.0 ± 0.6	0.13 ± 0.05 (0.79)	0.066 ± 0.05 (0.16)	0.40 ± 0.15 (0.99)
Smoothed La Paz air temperature	-	-	-	0.28 ± 0.02 (0.90)
Southern Hemisphere global temperature trend [*Trenberth et al.*, 2007]	0.7 ± 0.2	[0.056,0.077][b]	-	[0.091,0.22][c]
Regional temperature trends from *Vuille et al.* [2003]. ECHAM-4 T106 altitude >6000 m asl	-	-	[0.05,0.10]	[0.30,0.40]

[a]Illimani, Bolivia (6340 m above sea level, 16°39′S, 67°47′W) with borehole temperature profile inversions, melting quantification, and La Paz air temperature compared with Southern Hemisphere global temperature trends [*Trenberth et al.*, 2007] and regional modeled temperature trends from *Vuille et al.* [2003].
[b]For 1899–2005.
[c]For 1979–2005.

variations are plotted and compared to La Paz air temperatures. The pdf standard deviation gives the model uncertainty. Figure 3b compares the posterior and prior pdf's for every decade. It can be seen that further back in time, the posterior distribution becomes progressively more influenced by the prior pdf. Note that the secular temperature before 1900 is given by the basal heat flux using the basal temperature gradient. Without this condition, the 1900 prior and posterior pdf's would be very similar, indicating that the englacial temperature profile cannot provide any information on atmospheric temperature before this date.

[29] This borehole temperature inversion shows two atmospheric warming phases of +0.5 ± 0.3 K from 1900 to 1960 (starting approximately in 1920) and +0.6 ± 0.2 K from 1985 to 1999, corresponding to a warming of +1.1 ± 0.2 K for the 20th century. The temperature trend at Illimani agrees fairly well with the results from *Vuille et al.* [2003] (see Table 1). Inversion with the geothermal flux as a free parameter gives a 20th century warming of 1.1 ± 0.3 K. Adding the melting factor as a free parameter gives a similar result but with a larger range of uncertainty (warming of 1.0 ± 0.6 K over the 20th century). Temperature trends are summarized in Table 1 for each reconstruction in comparison with global change for the Southern Hemisphere [*Trenberth et al.*, 2007] and model results from *Vuille et al.* [2003].

6. Temperature Reconstruction Using Firn Density Anomalies

[30] Surface meltwater refreezes just under the snow surface creating a density anomaly within the firn layer. This anomaly was quantified in every section of the ice core by comparing the measured density with a computed density obtained from an empirical firn densification model (Figure 4a) [*Herron and Langway*, 1980]. In each core section, this density anomaly corresponds to an excess mass due to an amount of refreezing meltwater. Using the age-

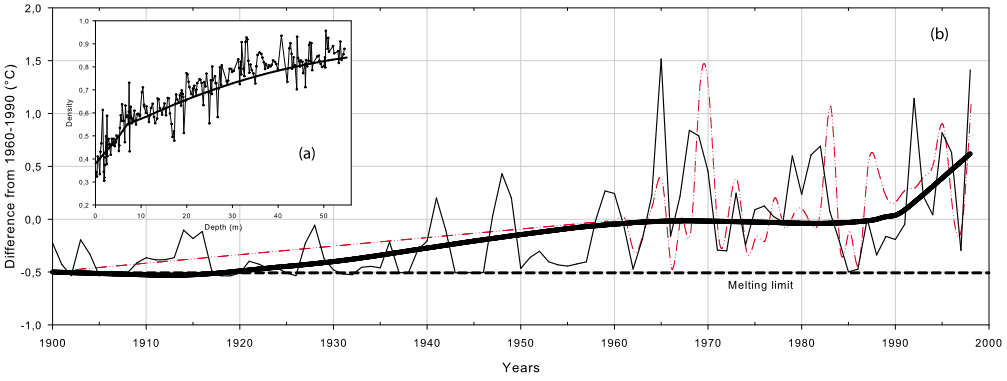

Figure 4. (a) Firn and ice density measured (thin line with black dots) and calculated according to *Herron and Langway*'s [1980] empirical firn densification model (thick line) in order to estimate density anomalies. (b) Density anomalies plotted as a function of the time in terms of temperature anomalies (thin line) (see section 6 for more details). These temperatures are compared with borehole temperature profile inversion (thick line) and La Paz air temperature (red dashed line after 1962).

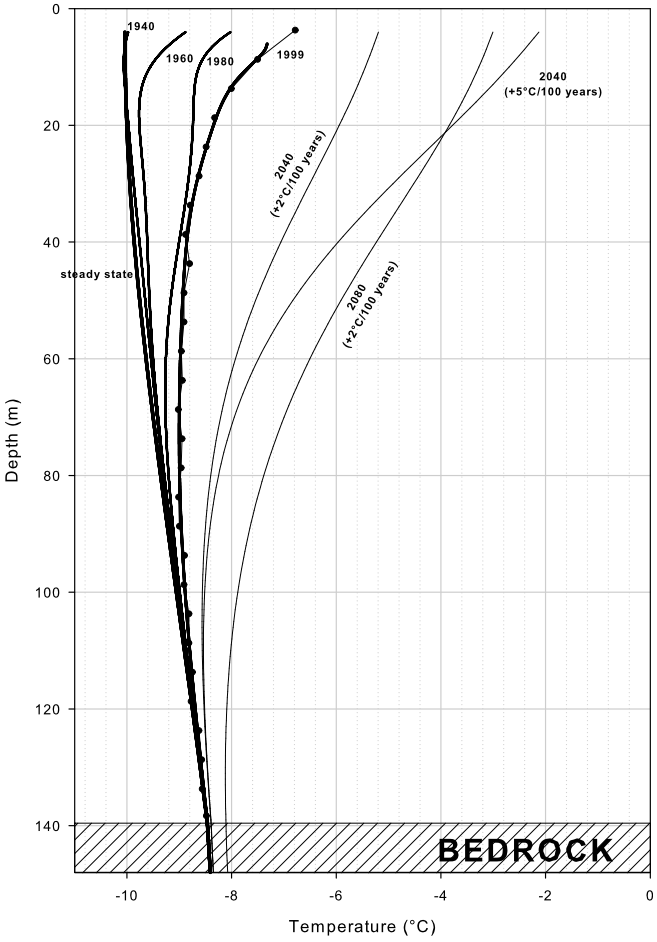

Figure 5. Simulated englacial temperature profiles in a borehole at Illimani (6340 m asl) over the 20th century (thick black lines), based on refreezing meltwater quantification with the density anomaly method compared with the observed June 1999 profile (thin line with black dots). Also shown are simulations over the 21st century (thin lines) according to two climate change scenarios (+2 K (100 years)$^{-1}$ and +5 K (100 years)$^{-1}$).

depth relationship given by *Knüsel et al.* [2003], the annual melting rate is reconstructed from 1900 to 1999. The latent heat corresponding to the annual amount of refreezing meltwater is then converted into annual air temperature according to the linear regression between air temperature and surface melting on the annual time scale used in section 4.2, a resulting from the inversion method ($a = 0.5$ W m^{-2} K^{-1}). The parameters of the densification model (surface temperature is 265.4 K, mean initial annual layer thickness is 0.58 m water equivalent yr^{-1}, and initial snow density is 380 kg m^{-3}) have been adjusted to obtain the best agreement between simulated (using the estimated annual amount of meltwater) and measured borehole englacial temperatures. These parameters are in good agreement with values reported by *Knüsel et al.* [2003], which gives confidence in the calibration. In the deepest part of the ice core (before 1940), the density measurement resolution was not accurate enough (some ice core sections covered more than a single year) to obtain a reliable annual melting quantification, making it necessary to use mean density values over several years. The resulting melting signal is therefore partly smoothed but does not influence the englacial temperature simulation.

[31] The resulting simulated 1999 profile fits the measured englacial temperature profile well (Figure 5). Temperature profile simulations for 1940, 1960, and 1980 are also plotted in Figure 5 and show that the glacier was near steady state until 1940 and then subject to strong warming

of englacial temperature, mainly due to the refreezing of surface meltwater.

[32] Reconstructing air temperature variations using melting quantification is a method which has been previously applied for alpine sites [*Henderson et al.*, 2006]. The comparison between the reconstructed temperature trends, using density anomalies or the inversion method and direct measurements from La Paz, shows good agreement (Figure 4b). For the method based on density anomalies, note that the absence of refrozen ice in an annual layer prevents us from inferring an annual temperature. It reveals that the annual temperature was lower than the reference temperature, i.e., 265.4 K. In this case, the annual temperature was set to this value.

7. Future Changes

[33] Using the same parameterization as in section 4.2, simulations for the future evolution of englacial temperature were computed according to possible future temperature change scenarios to assess when and under what conditions the high-altitude Illimani glacier could become temperate (Figure 5). Because of the strong effect of latent heat release by the melting-refreezing process, simulations show that englacial temperature may reach 273.15 K in the first 20 m depth between 2050 and 2060 with a warming of +5 K over the 21st century (estimated warming in the tropical Andes according to the SRES A2 emission scenario [*Vuille et al.*, 2008]). However, the glacier could remain cold with a reduced warming scenario of +2 K over the 21st century. These results need to be regarded with caution because simulations have been performed with the present tuned melting factor a, although because of changing energy balance factors, a is likely to change in the future.

8. Conclusion

[34] The borehole temperature profile measured in June 1999 at Illimani, Bolivia (6340 m asl, 16°39′S, 67°47′W) reflects conditions that are far from steady state. Indeed, the temperature distribution within this cold glacier provides clear evidence not only of atmospheric warming over the 20th century at this high-elevation site (1.1 ± 0.2 K over the period 1900–1999) but also of the effect of latent heat resulting from the refreezing of meltwater at the surface. Air temperature variations over the 20th century have been reconstructed using three different approaches. Two methods are based on a heat flow model: first, in a direct forward mode using a quantification of the surface melting with a degree-day approach using La Paz air temperature and, second, in an inverse mode to assess the sensitivity of each model parameter and to yield a confidence interval for air temperature trends. The third method, independent from the others, uses density anomalies along the ice core as quantification of melting-refreezing processes. The first method depends on La Paz air temperature and assumes that Illimani air temperature variations are similar to La Paz'. This assumption allows simulating borehole temperature, but there is no control on the melting factor. The second method provides a value of the melting factor and a surface temperature reconstitution independent from La Paz air temperature. The fact that both methods agree fairly well gives confidence in the results. The third approach to assessing temperature reconstitution at annual time scale yields similar temperature trends, which again strengthens the results. This high-altitude tropical site has exhibited accelerated atmospheric warming since 1985 with a 1900–1999 mean linear decadal temperature trend of 0.085 ± 0.01 K decade^{-1} and a 1980–1999 decadal trend of 0.35 ± 0.05 K decade^{-1}.

[35] At an annual time scale, Illimani and La Paz temperatures are not always in agreement as revealed by the density anomaly approach. Unfortunately, the resolution of Illimani ice core density measurements does not always allow a reliable surface melting reconstitution on an annual time scale. High-resolution density measurements would be required to improve the reconstruction and to yield reliable conclusions with this method.

[36] Temperature profile interpretation is also valuable to investigate future englacial temperature evolution according to various climate change scenarios. In the event of a +2 K rise over the 21st century, Illimani glacier at 6340 m asl is likely to remain cold, although with a +5 K warming, the glacier could reach 273.15 K in the first 20 m depth between 2050 and 2060, making ice core studies much less valuable for paleoclimatic investigations.

[37] Finally, in order to better constrain model parameters, it would be very useful to repeat englacial temperature measurements every 10 or 15 years at the same site, as in the Alps [*Vincent et al.*, 2007]. This is especially important nowadays at a time when atmospheric warming at very high elevations in the tropics appears to be accelerating.

[38] **Acknowledgments.** This study and the ice core drilling were funded by IRD (France) and PSI/University of Bern (Switzerland). We thank B. Zweifel for providing borehole temperature data and thermistor chain calibration, D. Hardy for AWS data, J.-D. Taupin and H. Bonnaveira for ice core density measurements, and the Bolivian, French, and Swiss institutions drilling teams. The thermistor chain has been kindly calibrated at ETH (Zürich, Switzerland). We thank three anonymous reviewers for their thorough reviews which efficiently helped to improve the manuscript.

References

De Angelis, M., J. Simões, H. Bonnaveira, J.-D. Taupin, and R. J. Delmas (2003), Volcanic eruptions recorded in the Illimani ice core (Bolivia): 1918–1998 and Tambora periods, *Atmos. Chem. Phys. Discuss.*, *3*, 2427–2463.

Favier, V., P. Wagnon, and P. Ribstein (2004), Glaciers of the outer and inner tropics: A different behaviour but a common response to climatic forcing, *Geophys. Res. Lett.*, *31*, L16403, doi:10.1029/2004GL020654.

Francou, B., M. Vuille, P. Wagnon, J. Mendoza, and J. Sicart (2003), Tropical climate change recorded by a glacier in the central Andes during the last decades, of the 20th century: Chacaltaya, Bolivia, 16°S, *J. Geophys. Res.*, *108*(D5), 4154, doi:10.1029/2002JD002959.

Francou, B., M. Vuille, V. Favier, and B. Cáceres (2004), New evidence for an ENSO impact on low-latitude glaciers: Antizana 15, Andes of Ecuador, 0°28′S, *J. Geophys. Res.*, *109*, D18106, doi:10.1029/2003JD004484.

Ginot, P., F. Stampi, D. Stampi, M. Schwikowski, and H. Gaggeler (2002), FELICS, a new ice core drilling system for high-altitude glaciers, *Mem. Natl. Inst. Polar Res.*, *56*, Spec. Issue, 38–48.

Haeberli, W., and M. Funk (1991), Borehole temperatures at the Colle Gnifetti core drilling site (Monte Rosa, Swiss Alps), *J. Glaciol.*, *37*, 37–46.

Hardy, D. R., M. Vuille, and R. S. Bradley (2003), Variability of snow accumulation and isotopic composition on Nevado Sajama, Bolivia, *J. Geophys. Res.*, *108*(D22), 4693, doi:10.1029/2003JD003623.

Henderson, K., A. Laube, H. W. Gäggeler, S. Olivier, T. Papina, and M. Schwikowski (2006), Temporal variations of accumulation and temperature during the past two centuries from Belukha ice core, Siberian Altai, *J. Geophys. Res.*, *111*, D03104, doi:10.1029/2005JD005819.

Herron, M., and C. Langway Jr. (1980), Firn densification: An empirical model, *J. Glaciol.*, *25*, 373–385.

Hock, R. (2003), Temperature index melt modelling in mountain areas, *J. Hydrol.*, *282*(1–4), 104–115, doi:10.1016/S0022-1694(03)00257-9.

Hopcroft, P. O., K. Gallagher, and C. C. Pain (2007), Inference of past climate from borehole temperature data using Bayesian reversible jump Markov Chain Monte Carlo, *Geophys. J. Int.*, *171*, 1430–1439, doi:10.1111/j.1365-246X.2007.03596.x.

Hutter, K. (1983), *Theoretical Glaciology: Material Science of Ice and the Mechanics of Glaciers and Ice Sheets*, D. Reidel, Dordrecht, Netherlands.

Knüsel, S., P. Ginot, U. Schotterer, M. Schwikowski, H. W. Gaggeler, B. Francou, J. R. Petit, J. C. Simoes, and J. D. Taupin (2003), Dating of two nearby ice cores from the Illimani, Bolivia, *J. Geophys. Res.*, *108*(D6), 4181, doi:10.1029/2001JD002028.

Kotlyakov, V. M., S. M. Arkhipov, K. A. Henderson, and O. V. Nagornov (2004), Deep drilling of glaciers in Eurasian Arctic as a source of paleoclimatic records, *Quat. Sci. Rev.*, *23*(11–13), 1371–1390, doi:10.1016/j.quascirev.2003.12.013.

Lüthi, M. P., and M. Funk (2001), Modelling heat flow in a cold, high-altitude glacier: Interpretation of measurements from Colle Gnifetti, Swiss Alps, *J. Glaciol.*, *47*(157), 314–323, doi:10.3189/172756501781832223.

Malvern, L. E. (1969), *Introduction to the Mechanics of Continuous Medium*, Prentice Hall, Englewood Cliffs, N. J.

Nagornov, O., Y. Konovalov, V. Zagorodnov, and L. Thompson (2001), Reconstruction of the surface temperature of Arctic glaciers from the data of temperature measurements in wells, *J. Eng. Phys. Thermophys.*, *74*(2), 253–261, doi:10.1023/A:1016661616282.

Noetzli, J., S. Gruber, T. Kohl, N. Salzmann, and W. Haeberli (2007), Three-dimensional distribution and evolution of permafrost temperatures in idealized high-mountain topography, *J. Geophys. Res.*, *112*, F02S13, doi:10.1029/2006JF000545.

Ramirez, E., et al. (2003), A new Andean deep ice core from Nevado Illimani (6350 m), Bolivia, *Earth Planet. Sci. Lett.*, *212*, 337–350, doi:10.1016/S0012-821X(03)00240-1.

Ritz, C. (1989), Interpretation of the temperature profile measured at Vostok, East Antarctica, *Ann. Glaciol.*, *12*, 138–144.

Salamatin, A. N., V. Y. Lipenkov, N. I. Barkov, J. Jouzel, J. R. Petit, and D. Raynaud (1998), Ice core age dating and paleothermometer calibration on the basis of isotope and temperature profiles from deep boreholes at Vostok Station (East Antarctica), *J. Geophys. Res.*, *103*(D8), 8963–8977, doi:10.1029/97JD02253.

Sturm, M., J. Holmgren, M. Konig, and K. Morris (1997), The thermal conductivity of snow, *J. Glaciol.*, *143*, 26–41.

Suter, S., M. Hoelzle, and A. Ohmura (2004), Energy balance at a cold, alpine firn saddle, Seserjoch, Monte Rosa, *Int. J. Climatol.*, *24*(11), 1423–1442, doi:10.1002/joc.1079.

Thompson, L. G., E. Mosley-Thompson, H. H. Brecher, M. E. Davis, B. Leon, D. Les, L. Ping-Nan, T. A. Mashiotta, and K. R. Mountain (2006), Abrupt tropical climate change: Past and present, *Proc. Natl. Acad. Sci. U. S. A.*, *103*, 10,536–10,543, doi:10.1073/pnas.0603900103.

Trenberth, K., et al. (2007), Observations: Surface and atmospheric climate change, in *Climate Change 2007: The Physical Science Basis. Contribution of Working Group I to the Fourth Assessment Report of the Intergovernmental Panel on Climate Change*, edited by S. Solomon et al., pp. 235–336, Cambridge Univ. Press, Cambridge, U. K.

Vimeux, F., R. Gallaire, S. Bony, G. Hoffmann, and J. C. H. Chiang (2005), What are the climate controls on δD in precipitation in the Zongo Valley (Bolivia)? Implications for the Illimani ice core interpretation, *Earth Planet. Sci. Lett.*, *240*, 205–220, doi:10.1016/j.epsl.2005.09.031.

Vimeux, F., P. Ginot, M. Schwikowski, M. Vuille, G. Hoffmann, L. G. Thompson, and U. Schotterer (2009), Climate variability during the last 1000 years inferred from Andean ice cores: A review of methodology and recent results, *Palaeogeogr. Palaeoclimatol. Palaeoecol.*, *281*, 229–241, doi:10.1016/j.palaeo.2008.03.054.

Vincent, C., E. Le Meur, D. Six, P. Possenti, E. Lefebvre, and M. Funk (2007), Climate warming revealed by englacial temperatures at Col du Dôme (4250 m, Mont Blanc area), *Geophys. Res. Lett.*, *34*, L16502, doi:10.1029/2007GL029933.

Vuille, M., R. S. Bradley, M. Werner, and F. Keimig (2003), 20th century climate change in tropical Andes: Observations and model results, *Clim. Change*, *59*, 75–99, doi:10.1023/A:1024406427519.

Vuille, M., B. Francou, P. Wagnon, I. Juen, G. Kaser, B. Mark, and R. Bradley (2008), Climate change and tropical Andean glaciers: Past, present and future, *Earth Sci. Rev.*, *89*, 79–96, doi:10.1016/j.earscirev.2008.04.002.

Wagnon, P., J.-E. Sicart, E. Berthier, and J.-P. Chazarin (2003), Winter-time high-altitude surface energy balance of a Bolivian glacier, Illimani, 6340 m above sea level, *J. Geophys. Res.*, *108*(D6), 4177, doi:10.1029/2002JD002088.

M. Funk, VAW, ETH Zurich, Rämistrasse 101, CH-8092 Zürich, Switzerland.

A. Gilbert, P. Ginot, and P. Wagnon, LGGE, IRD, BP 96, F-38402 Saint-Martin-d'Hères CEDEX, France. (latsfouine@hotmail.com)

C. Vincent, LGGE, UJF, CNRS, BP 96, F-38402 Saint-Martin-d'Hères CEDEX, France.

Annexe B

Rapport : Suivi du pompage de la poche d'eau intraglaciaire du glacier de Tête Rousse et expérience de traçage à la rhodamine

Suivi du pompage de la poche d'eau intraglaciaire du glacier de Tête Rousse et expérience de traçage à la rhodamine

Thomas Condom et Adrien Gilbert

Janvier 2013

Injection de la saumure dans la rimaye du glacier

Participants : Romain BIRON, Thomas CONDOM, Adrien GILBERT, Thierry LEBEL, Emmanuel THIBERT, Christian VINCENT

L G G E
Laboratoire de Glaciologie et Géophysique de l'Environnement

LTHE

1 Site d'étude

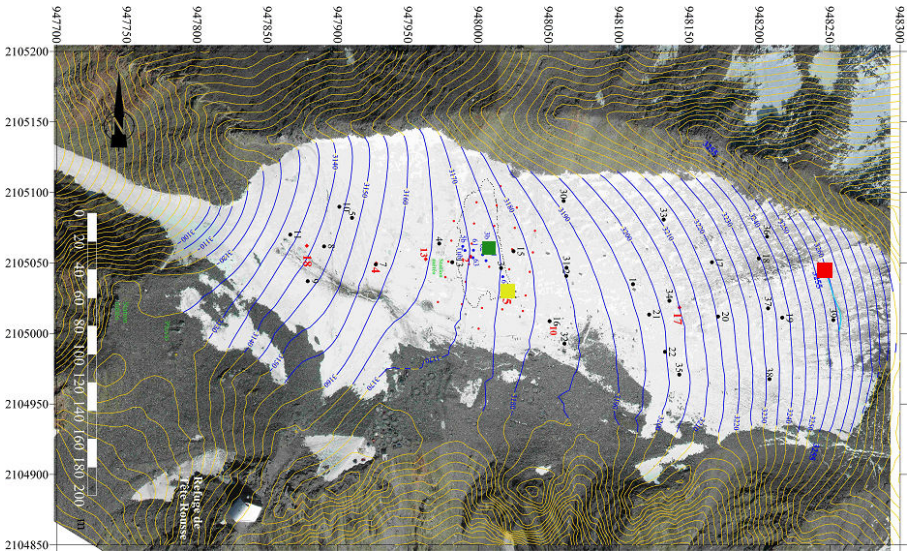

FIG. 1 – Site d'étude, point d'injection de la Rhodamine dans la rimaye (carré rouge), point de pompage (carré vert). La position approximative du forage 65 est marquée par le carré jaune (source : Rapport d'expertise scientifique sur la poche, d'eau du glacier de Tête Rousse, 30 décembre 2011)

La figure représente la position de la cavité en pointillé noir, la position des différents forages, le point d'injection de la Rhodamine pour le traçage dans la rimaye (partie amont du glacier). Le suivi du traceur avec le fluorimètre à été fait au niveau de l'exhaure (pompages au niveau des forages 1 et 61). La distance entre le point d'injection et le forage où a eu lieu le pompage est de 243 m.

X injection (Lambert 2E)	948234
Y injection (Lambert 2E)	2105059
Altitude injection (m)	3255
X pompage (Lambert 2E)	948010
Y pompage (Lambert 2E)	2105058
Altitude pompage (m)	3160
Distance plane (m)	224
Distance considérent la pente (m)	243

TAB. 1 – Points d'injection du traceur et localisation du pompage

2 Géométrie de la poche d'eau en 2010-2011-2012

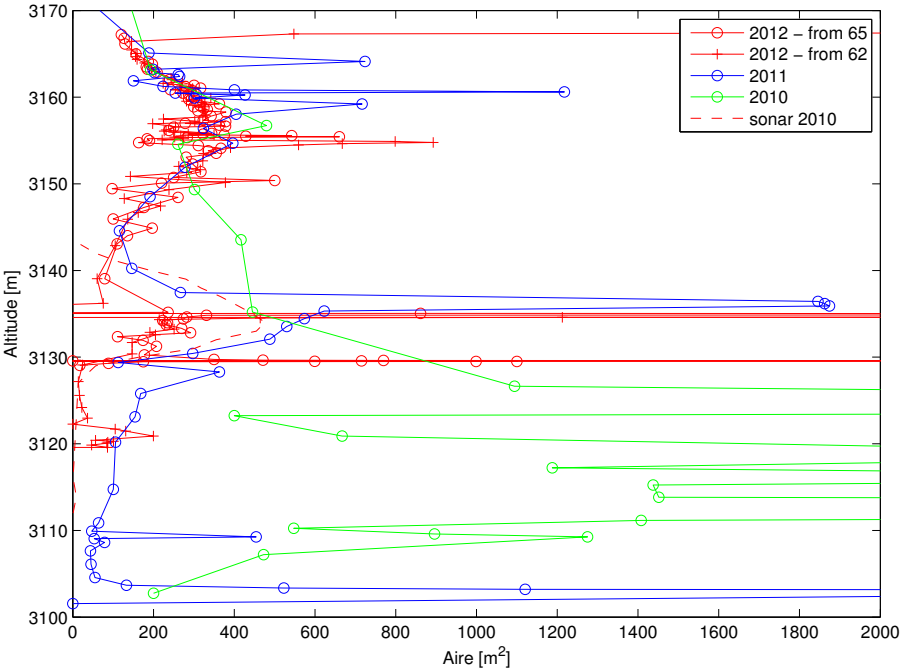

FIG. 2 – Relation entre aire et altitude dans la cavité (source : O. Gagliardini)

En 2012, 3 grands ensembles dans la cavité peuvent être distingués selon la profondeur. On note de la surface (3170 m) à 3140 un premier volume ; ensuite entre 3150 et 3130 un fort élargissement de la cavité, enfin de 3130 à 3120 m un resserrement. Cette figure indique la présence d'un seuil à 3130 m qui sera aussi mis en évidence lors du pompage (voir partie 3 suivante).

3 Description du pompage

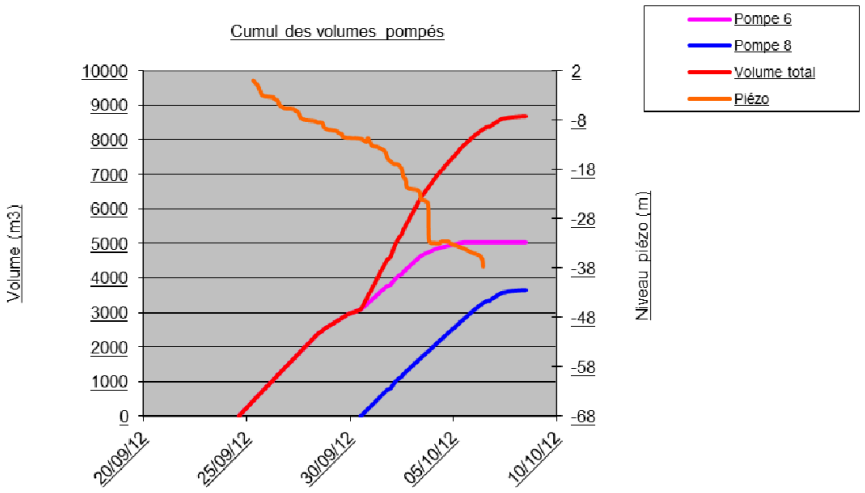

FIG. 3 – Volume pompé par les pompes 6 et 8, volume total pompé et évolution du niveau piézométrique durant le pompage (source : Compte-rendu n°3 Travaux de pompage sur glacier de Tête Rousse, Année 2012)

Deux pompes ont été installée pour le pompage de 2012, la pompe 6 (forage 1 sur la figure 1) et la pompe 8 (forage 61, cf.figure 1). Les caractéristiques générales du pompage sont les suivantes :

- Mise en route de la pompe 6 : 24/9/12 à 14 :40
- Mise en route de la pompe 8 : 30/9/12 à 15 :00
- Arrêt de la pompe 6 : 5/10/2012 à 12 :00
- Arrêt de la pompe 8 : 8/10/2012 à 12 :00
- Niveau initial dans le forage : 3168 m
- Niveau final : 3120 m
- Volume pompé : 8682 m^3

Il faut noter que la variation de niveau d'eau dans la cavité lors du pompage dépend du débit d'exhaure (débit de la pompe 6, des pompes 6+8 puis de la pompe 8), de la géométrie de la cavité et de la ré-alimentation qui est variable dans le temps.

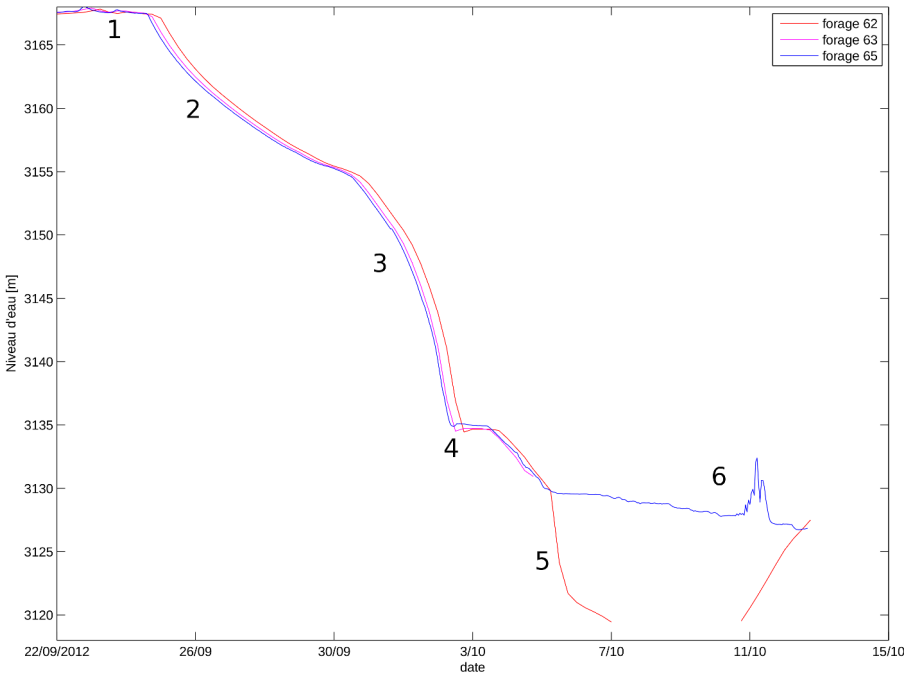

FIG. 4 – Données piezométriques dans les forages 62, 63, 65 durant la période 22/09 au 12/10 (source : O. Gagliardini)

La figure 4 présente les variations piezométriques dans les forages 62, 63 et 65 lors du pompage. Six phases se distinguent :

- Phase **1** : niveau d'eau assez stable dans la cavité avant la mise en route du pompage
- Phase **2** : rabattement du niveau d'eau dans la cavité avec le pompage de la pompe 6
- Phase **3** : accélération du rabattement lors de la mise en route de la pompe 8
- Phase **4** : à 3135 m le rabattement se stabilise ce qui peut s'expliquer par l'élargissement de la cavité à cet endroit
- Phase **5** : rabattement dans la cavité principale (forage 62) et déconnexion de la sous cavité dans laquelle se trouve le forage 65. Il y a un seuil ce qui explique cette déconnexion.
- Phase **6** : après l'arrêt des pompage, la cavité se remplit de nouveau, il y a une ré-alimentation importante le 11/10 par de l'eau de fusion et potentiellement de l'eau de pluie.

4 Description du traçage

Le fluorimètre à été installé au point de rejet des eaux de pompage et mis en marche le 28/09/2012 à 11h. Ce fluorimètre mesure en continu dans l'eau, la Température, la conductivité et la teneur en traceur (dans notre cas la Rhodamine).

Le tableau 2 présente les caractéristique du traçage. Deux traceurs ont été injecté simultanément le 28/09/2012 , 400 g de Rhodamine et 35 kg de NaCl dissout avec environ 300 litres d'eau.

L'acquisition du fluormietre s'est arrêté 73 heures après le début d'acquisition sans doute par déchargement prématuré des batterie. Heureusement le traceur à mis moins de temps pour arriver dans la cavité. Des photos de l'expérience sont visibles en annexe.

Date et heure d'injection	28/09/2012 à 12h30
Masse de traceur Rhodamine injecté (g)	400
Masse de sel injecté (kg)	35
Volume d'eau injecté durant traçage (litres)	280
Masse de traceur Rhodamine reconstitué (g)	2
Durée du parcours (h)	5
vitesse de transfert (m h^{-1})	48

TAB. 2 – Caractéristiques du traçage

La figure 5 présente 4 graphiques permettant de voir l'évolution de 6 paramètres depuis la date d'injection jusqu'à + 80 heures.

1. La première courbe présente la variation de la teneur en Rhodamine. On note tout d'abord une augmentation de + 5 heures à + 24 (maximum de teneur en Rhodamine). On considère un seuil à 1 ppb pour considérer l'arrivée du traceur. Ensuite à partir de +24 h, on observe une chute brutale du traceur en quelques heures puis un niveau stable de type bruit de fond aux alentours de 1 ppb.
2. Sur le second graphe nous observons la température de l'eau d'exhaure qui reste autour de 1°C.
3. Sur le second graphe, nous notons les variations de la température de l'air ainsi que la lame d'eau disponible en surface venant du cumul de la fonte et des précipitations liquides. L'eau disponible en surface est maximum à +14 heures suite à un épisode de pluie.
4. Le troisième graphique présente l'évolution de la conductivité de l'eau d'exhaure. Cette conductivité est initialement de l'ordre de 60 μS cm^{-1} puis augmente de manière assez constante jusqu'à une valeur de 70 μS cm^{-1}. On note un petit pic de conductivité lors de la mise en marche du second pompage (pompe 8). L'augmentation de la conductivité s'explique peut s'expliquer par un stratification naturelle existante dans le cavité et potentiellement par l'apport d'eau salée injectée durant le traçage.
5. Le 4ème graphique présente la surface du glacier, la position des pompe en profondeur et la variation piézométrique observée.

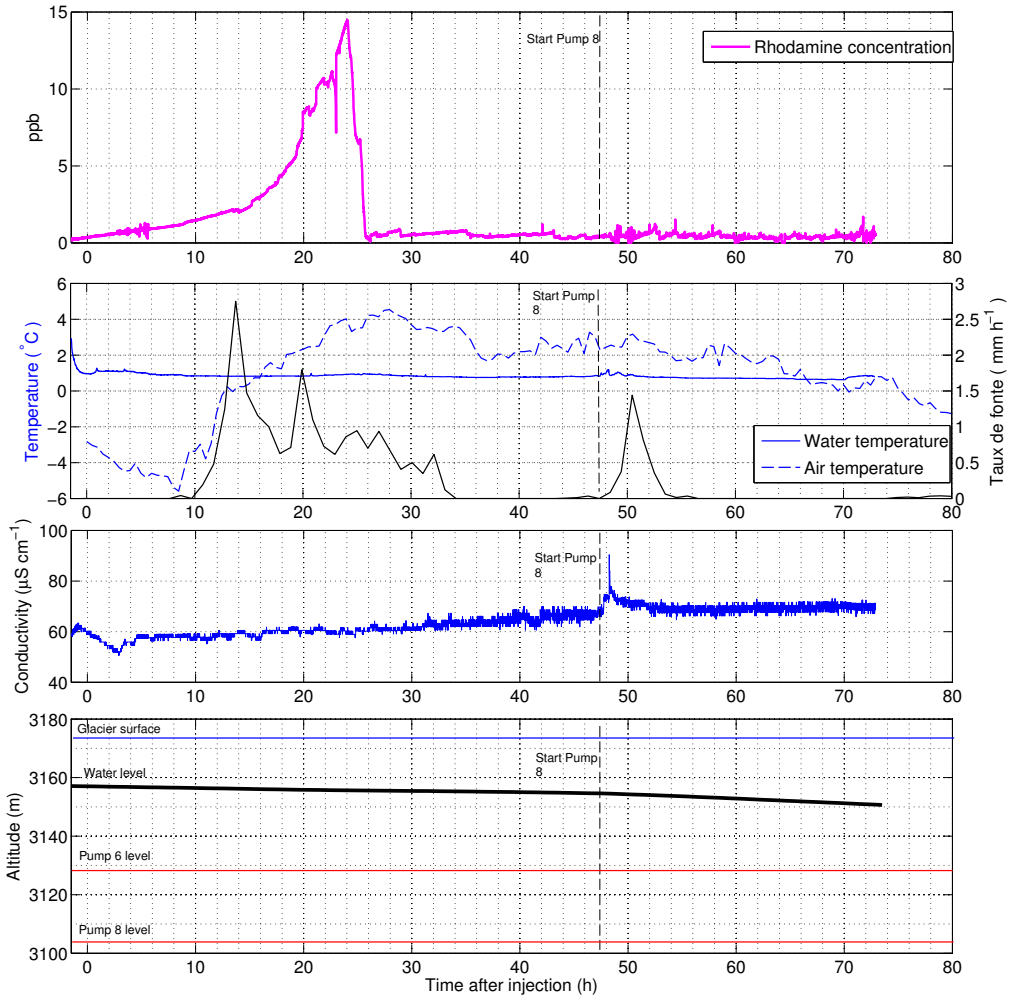

FIG. 5 – Ensemble de données horaires lors de l'expérience de traçage avec de haut en bas : (i) la concentration en Rhodamine en ppb dans l'eau d'exhaure ; (ii) la température de l'eau d'exhaure, la température de l'air (°C) ; le taux de fonte (mm.h^{-1}) ; (iii) l'évolution de la conductivité de l'eau (μS.cm^{-1}) ; (iv) l'évolution piézométrique dans la cavité et la position des pompes

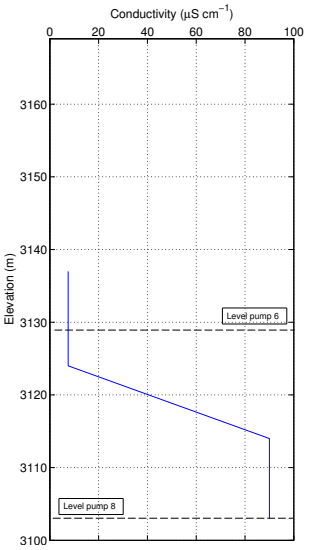

FIG. 6 – Profil de conductivité électrique de l'eau de la cavité après le pompage (source : BRGM, 2013)

Un sondage de conductivité a été réalisé dans la cavité après l'arrêt du pompage et montre une claire stratification avec de l'eau peu conductrice de l'ordre de 8 (μS cm^{-1}) entre 3137 m et 3125 m, une zone de transition entre 3125 m et 3115 m puis une zone avec de l'eau assez conductrice (90 μS cm^{-1}) au fond de la cavité. Il n'est pas exclu qu'une partie de la forte conductivité au fond de la poche d'eau soit causée par l'injection de sel lors du traçage, cependant il est aussi possible qu'une stratification naturelle existe. Dans ce cas, un échange avec les roches au niveau du substratum rocheux pourrait expliquer cette conductivité de plusieurs dizaines de μS cm^{-1} dans l'eau.

L'interprétation du traçage est la suivante :

Il existe bien une connexion hydraulique entre le point d'injection au niveau de la rimaye et la cavité principale. En considérant que le traceur circule à la même vitesse que l'eau, 5 heures ont été nécessaires pour parcourir 243 m ce qui donne une vitesse de 50 m h^{-1} (0,014 m s^{-1}). Nous expliquons la chute brutale du traceur à partir de +24h dans l'eau d'exhaure par une dilution importante causée par les apports d'eau de fonte et de pluie. Cet apport d'eau a lieu entre +10 heures et +30h. Concernant le taux de restitution de la Rhodamine, il est faible et en calculant le bilan de masse, 4 g de Rhodamine ont été extraite alors que l'injection était de 400 g. La Rhodamine non restituée est sans doute présente dans le cryokarst (conduits ou cavités).

Le traçage au sel est plus difficile à interpréter et étant donné la forte densité du mélange eau+NaCl il est probable qu'une partie de ce mélange soit présente au fond de la poche d'eau actuelle. Il faut noter le remplissage très rapide de la cavité lorsque le pompage est arrêté.

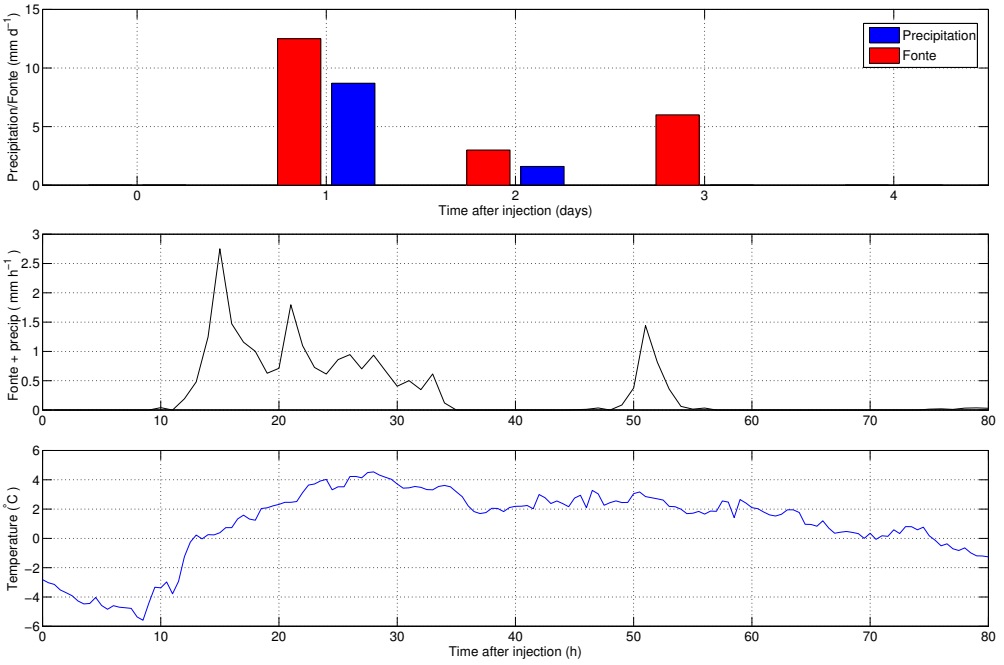

FIG. 7 – Evolution de la température de l'air, du taux de fonte et précipitation journalière durant l'expérience de traçage (0 correspond au moment de l'injection)

Le graphique 7 donne le détail de la quantité de fonte calculée et la précipitation liquide mesurée au moment du traçage. Si on intègre la quantité d'eau liquide disponible sur la surface du glacier situé au dessus de la rimaye (3950 m^2) entre +10h et +24h cela représente environ 60 m^3.

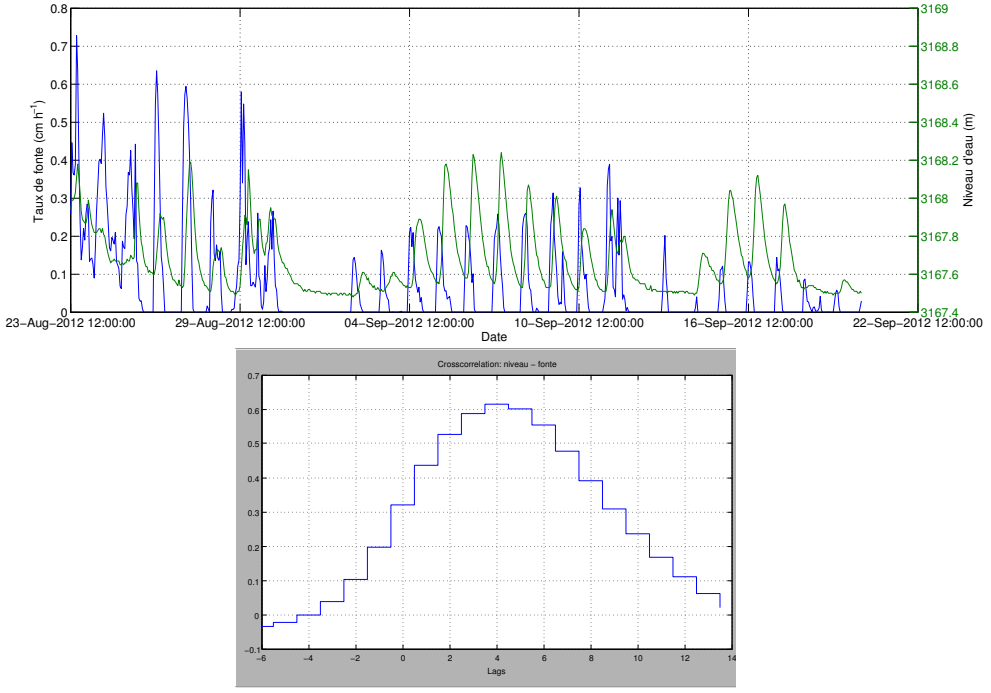

FIG. 8 – Corrélations entre le taux de fonte calculé et les variations piéométriques observées ; a) séries temporelles horaires ; b) le corrélogramme croisé entre le taux de fonte calculé et les variations piézométriques.

Les figure 8a et 8b mettent en évidence la relation entre la fusion calculé grâce à un modèle de bilan d'énergie et l'augmentation de pression observée dans la poche d'eau. En faisant un corrélogramme croisée (corrélation entre deux séries temporelles que l'ont décale successivement d'un intervalle de temps régulier donné) ont trouve une corrélation maximum lorsque le décalage est de 4 heures.

Il est finalement remarquable que 2 méthodes différentes, traçage à la Rhodamine et calcul de la fonte et observation avec observation de l'augmentation du niveau piézométrique dans la cavité donne un temps de transfert similaire de l'ordre de 4 à 5 heures.

Conclusion :

L'expérience réalisée montre que la cavité de principale de Tête Rousse est reliée à l'entrée d'eau que constitue la rimaye du glacier situé à 3250 m environ. L'eau y circule à une vitesse de l'ordre 0,014 m s^{-1} (50 m h^{-1}). Cette vitesse de drainage correspond à ce que l'on peut rencontrer dans la littérature [*Stone and Clarke*, 1996 ; *Bingham et al.*, 2005 ; *Fountain and Walder*, 1998] et correspond plutôt à drainage lent (petit conduit, écoulement dans les sédiments, présence de cavité intermédiaire [*Fountain and Walder*, 1998]). Il est cependant difficile d'interpréter la forme (notamment la dispersion) de la courbe de restitution du traçage car le traceur arrive dans un grand volume d'eau qui est pompé en un point. Ainsi l'augmentation très progressive de la concentration en traceur peut venir du drainage de type lent mais aussi de la diffusion progressive du traceur dans la poche avant d'être pompé.

Référence :

Bingham, R.G., P. W. Nienow, M. J. Sharp and S. Boon (2005), Subglacial drainage processes at a High Arctic polythermal valley glacier, *J. Glaciol.*, *51*(172), 15-24

Fountain, A.G. and J.S. Walder (1998), Water flow through temperate glaciers, *Rev.Geophys., 36*(3), 299-328.

Stone, D. B. and G. K. C. Clarke (1996), In situ measurements of basal water quality and pressure as an indicator of the character of subglacial drainage systems, *Hydrological Processes, 10*, 615-628

ANNEXES

FIG. 9 – Ouverture sur la cavité en rive droite du glacier avec en arrière plan le site de pompage

FIG. 10 – site d'installation du fluorimètre au lieu de rejet du pompage (amont du glacier du Bionassay)

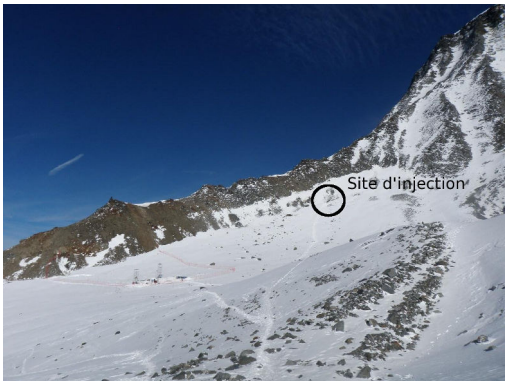

FIG. 11 – vue d'ensemble du site avec à l'amont du glacier le site d'injection

FIG. 12 – vue d'ensemble du site

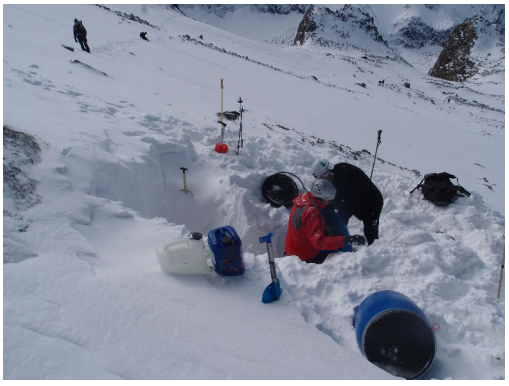

FIG. 13 – site d'injection

FIG. 14 – cavité formée après l'injection des traceurs

Annexe C

Supplementary material : Atmospheric temperature changes over the 20^{th} century at very high elevations in the European Alps from englacial temperatures

---

Supplementary Material

Atmospheric temperature changes over the 20th century at very high elevations in the European Alps from englacial temperatures

A. Gilbert and C. Vincent
2013

1 Inverse modeling: posterior Probability Density Function calculations

The inverse problem was solved using a Bayesian approach and values of the inverted parameters are given as a posterior Probability Density Function (PDF). This posterior PDF is a function of the prior PDF and data likelihood:

$$P_{post} \propto P_{prior} \times P(\mathbf{d} \mid \mathbf{m}) \tag{1}$$

where P_{post} is the posterior PDF, P_{prior} is the prior PDF and $P(\mathbf{d} \mid \mathbf{m})$ is the probability of observing the data $\mathbf{d}$ for a given parameter set $\mathbf{m}$ (data likelihood).

1.1 Free parameters in the forward model

The forward model is described in the article. Free parameters are:

- Surface temperature evolution vector $\mathbf{Ts} = (T_i,t_i \; ; \; i{=}1{,}5)$, where T_i is temperature and t_i is time.
- Melting factor a
- Surface vertical advection velocity v_0
- Steady state surface temperature T_0
- Basal flux f_b

These parameters constitute the set of parameter $\mathbf{m}$.

1.2 Proposal function

We use a Reversible Jump Markov Chain Monte Carlo (RJ-MCMC) algorithm to explore the parameter space and draw the posterior PDF (P_{post}) of each parameter. At each iteration of the RJ-MCMC algorithm, one parameter is updated. All parameters have the same probability of being changed. If the surface temperature vector is selected to be changed, only one parameter (T_i or t_i) is updated with the same probability for each. T_0, T_i, t_i and a are updated using a Gaussian random function, while the other parameters are chosen with a uniform probability within a fixed interval: $f_b \in$[0 60] mW m^{-2} and $v_0 \in$[0 10] m w.e. yr^{-1}. We therefore have:

$$\begin{aligned}
a' &= a + u \times \sigma_a && (2)\\
T_0' &= T_0 + u \times \sigma_{T_0} && (3)\\
T_i' &= T_i + u \times \sigma_{T_i} \times exp\left(\frac{i}{5}\right) && (4)\\
t_i' &= t_i + u \times (t_{i+1} - t_{i-1}) \times \sigma_{t_i} \times exp\left(\frac{i}{5}\right) && (5)\\
f_b' &= \sigma_{f_b} \times u_2 && (6)\\
v_0' &= \sigma_{v_0} \times u_2 && (7)\\
& && (8)
\end{aligned}$$

where x and x' are respectively the old and new values, u is the random Gaussian draw of mean value 0 and standard deviation 1.0, σ are scaling factors and u_2 is a random uniform draw between 0 and 1.0.

1.3 Prior probability and data likelihood

The prior information,P_{prior}, used to constrain parameter values to realistic values is described by a Gaussian probability function. $P_{prior}(\mathbf{Ts})$ is centered on a constant surface temperature with a standard deviation of 2 K. We assume that T_1 (from $\mathbf{Ts}$) must be close to T_0. Thus we add $P_{prior}(T_1)$ described by the Gaussian probability function centered on T_0 with a standard deviation of 0.2 K. P_{prior}(a) is also a Gaussian probability function centered on 0 m w.e. K^{-1} yr^{-1} if $a < 0$ and set equal to 1 if $a > 0$ (see Figure 1). The prior probability for surface vertical velocity is set to a Gaussian probability function centered on the measured values with a standard deviation of 0.5 m w.eq. yr^{-1} (see Figure 1). No prior information is given for the other parameters. Finally, we have:

$$P_{prior}(\mathbf{m}) \propto P_{prior}(\mathbf{Ts}) \times P_{prior}(T_1) \times P_{prior}(a) \times P_{prior}(v_0) \tag{9}$$

Data likelihood is calculated at each iteration using:

$$P(\mathbf{d} \mid \mathbf{m}) \propto exp\left[-\frac{1}{2}(\mathbf{d}-\mathbf{d}_{sim})C^{-1}(\mathbf{d}-\mathbf{d}_{sim})^{\perp}\right] \tag{10}$$

where $\mathbf{d}$ are the data, $\mathbf{d}_{sim}$ are the data simulated by the forward model using the parameter set $\mathbf{m}$ and C is the covariance matrix that describes measurement uncertainties. Assuming that all uncertainties are independent, C is a diagonal matrix.

1.4 Acceptance probability

The use of a reversible proposal function leads to a very simple form of acceptance probability. Thus, a parameter set $\mathbf{m}$' is accepted with a probability α given by:

$$\alpha = min\left[1; \frac{P_{prior}(\mathbf{m}') \times P(\mathbf{d} \mid \mathbf{m}')}{P_{prior}(\mathbf{m}) \times P(\mathbf{d} \mid \mathbf{m})}\right] \tag{11}$$

where $\mathbf{m}$' is the proposed parameter set and $\mathbf{m}$ the current parameter set. The frequency of acceptation of a parameter set $\mathbf{m}$ gives the posterior PDF of $\mathbf{m}$.

1.5 Simultaneous inversion

In order to deal with several sites simultaneously, the surface temperature is defined as the deviation from the steady state temperature T_0 (different at each site). The surface temperature evolution vector $\mathbf{Ts}$ is therefore the same for all sites and the surface temperature at each site is given by:

$$\mathbf{Ts}^i = \mathbf{Ts} + T_0^i \tag{12}$$

where $\mathbf{Ts}^i$ is the surface temperature at site i and T_0^i the steady state temperature at site i.
Data likelihood is calculated as the product of the data likelihood at each site:

$$P(\mathbf{d} \mid \mathbf{m}) = \prod_{i=1}^{n} P(\mathbf{d}_i \mid \mathbf{m}_i) \tag{13}$$

where n is the number of sites, $\mathbf{d}_i$ the data at site i and $\mathbf{m}_i$ the parameter set for site i. In the same way we have:

$$P_{prior}(\mathbf{m}) = \prod_{i=1}^{n} P_{prior}(\mathbf{m}_i) \tag{14}$$

1.6 Complementary result

We show here the Posterior PDF of all the free parameters after simultaneous inversion. Mean posterior PDF and standard deviation values of these parameters are given in Table 1 of the paper.

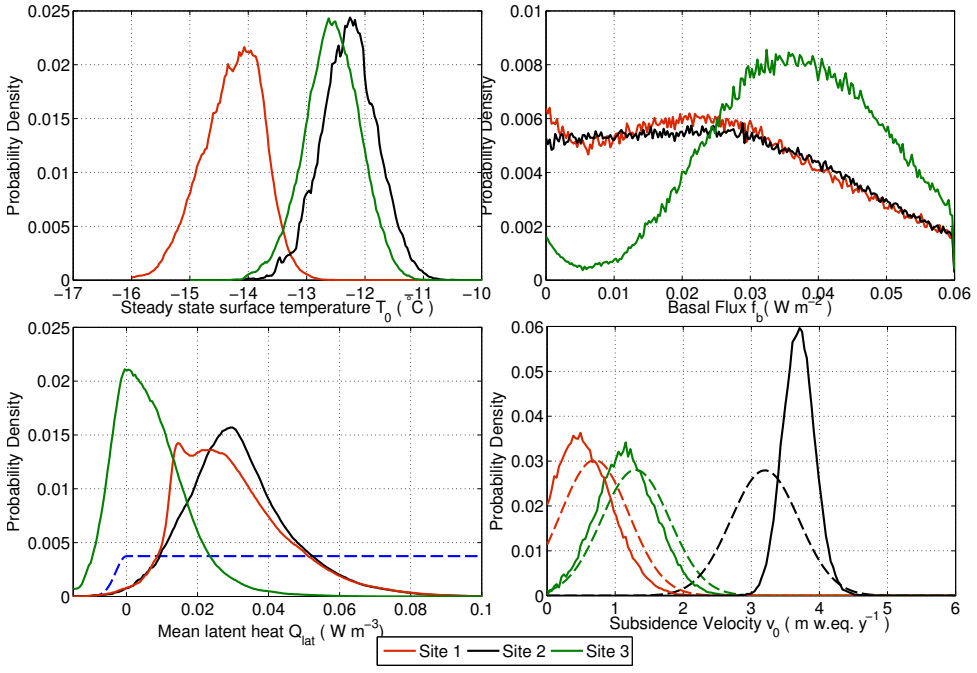

Figure 1: Posterior PDF (continuous line) and prior PDF (dashed line) of T_0, f_b, v_0 and Q_{lat} at each site from simultaneous inversion

2 Vertical velocities: validation using ice core data

In order to test the validity of the vertical advection profile which strongly influence the heat transport, dating obtained using the parameterized vertical velocity profile (equation 3 in the

manuscript) was compared with dating coming from radioactive horizons measured in the ice core (Figure 2 below). These results shows that this parameterization provides a good approximation of the vertical advection velocity.

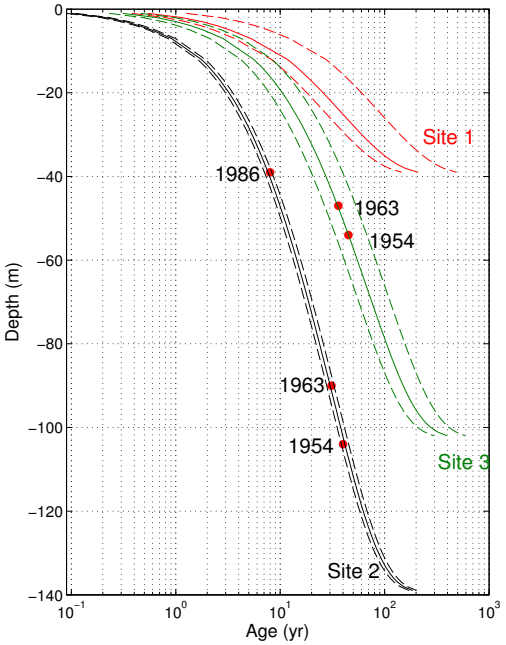

Figure 2: Depth versus age relationship calculated from the vertical velocity parameterization using surface velocity inferred by the inversion (solid line). The dashed line is the uncertainty coming from surface velocity uncertainty (standard deviation of the posterior PDF). Dots are control points coming from radioactive horizons on the ice core. Age data are not available at site 1.

3 Temperature profile initialisation using long-term temperature history from the year 800

As explained in the manuscript, a fixed temperature evolution is used to calculate an initial profile in 1900. This fixed temperature evolution was estimated from *Lüthi and Funk* [2001] and adjusted to the HISTALP [*Auer et al.*, 2007] reconstruction (see Figure 3 below).

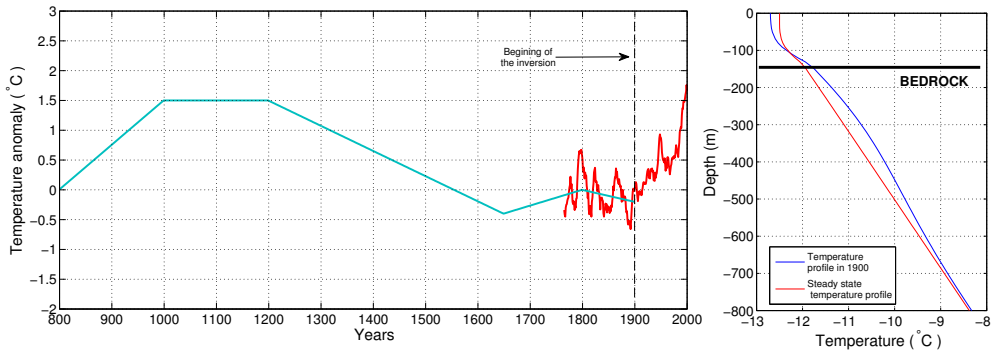

Figure 3: Past temperature history used to calculate the initial profile in 1900. The steady state profile is compared to the profile in 1900 at site 2 in the graph on the right.

The influence of the temperature history from 800 to 1900 on the final result is very low (see Figure 4) and the conclusions of the manuscript do not depend on this choice.

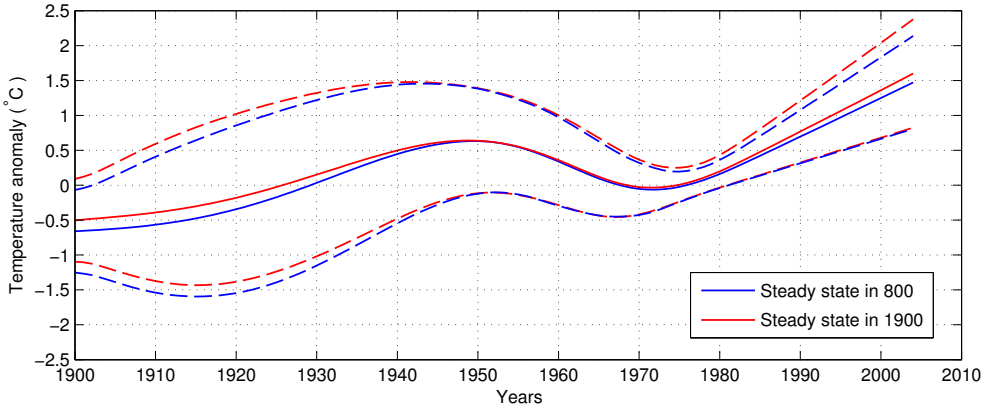

Figure 4: Comparison of different inversion results using a steady state temperature profile in 1900 (no past temperature history) and a steady state temperature profile in 800 (with past temperature history prior to 1900).

4 Three dimensional experiments

In order to validate the one dimensional analysis, three dimensional simulations have been performed using full stokes flow model Elmer/Ice including the firn compressibility as well as the density dependent variation of firn viscosity [*Zwinger et al.*, 2007]. For this purpose, velocity field was adjusted to match both measured surface velocities and firn dating coming from radioactive horizons in the ice core (Figure 2 above). This velocity field was then used to performed three

dimensional heat flow modeling at Col du Dome (Figure 5 below). Thermal properties of firn and bedrock are similar to those already presented in the manuscript.

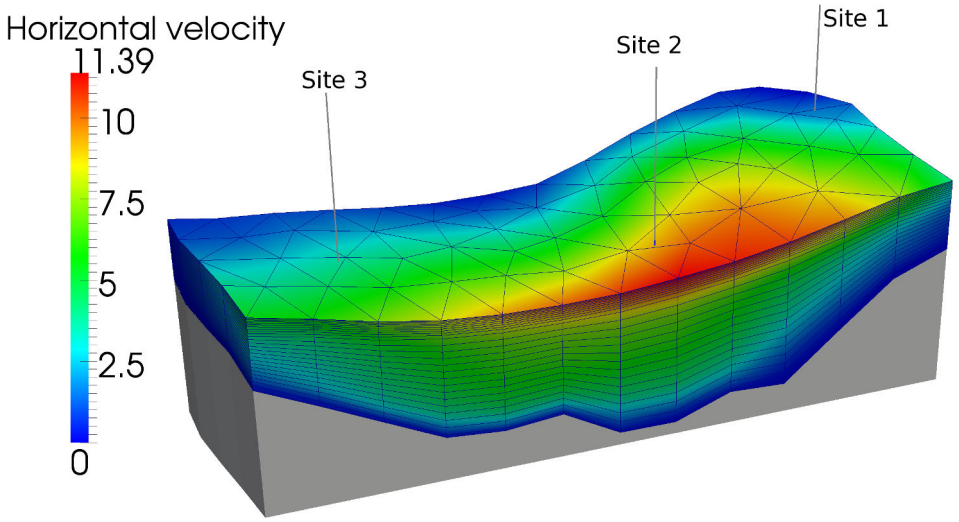

Figure 5: Three dimensional mesh used to the 3D heat flow modeling at Col du Dome. Bedrock is in grey, color scale represent horizontal velocities (m yr^{-1}) modeled using Elmer/ice model

Modeling experiment assuming 2°C surface warming during 100 years was done in 1D and 3D. Comparison between the two experiments (1D and 3D, Figure 6) shows that three dimensional effect on englacial temperatures is negligible (lower than the measurements accuracy). From these results, we can conclude that the one dimensional analysis used in the study is adequate. In addition, inversion results provide vertical velocities in agreement with the ice core dating from radioactive horizons (Figure 2). It confirms that the influence of horizontal velocities is low.

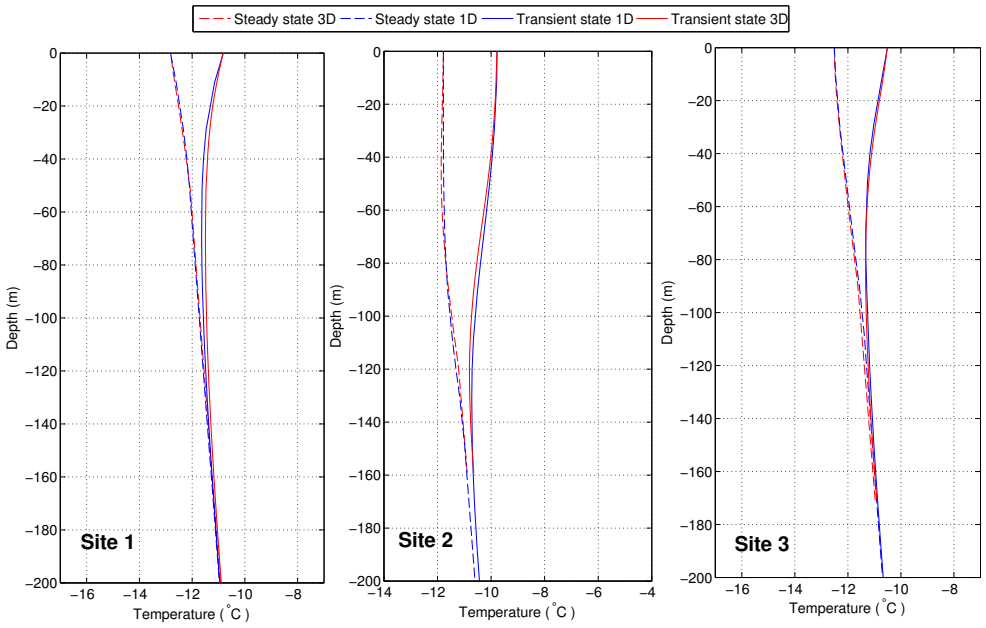

Figure 6: Modeling experiment supposing 2°C warming during 100 years using 1D model (blue lines) and 3D model (red lines)

References

Auer, I. and 31 others (2007), HISTALP - Historical instrumental climatological surface time series of the greater Alpine region 1760-2003, *Int. J. Climatol.*, *27*, 17–46.

Lüthi, M., and M. Funk (2001), Modeling heat flow in a cold, high-altitude glacier : Interpretation of measurements from Colle Gnifetti, Swiss Alps, *J. Glaciol.*, *47*(157), 314–323, doi: 10.3189/172756501781832223.

Zwinger, T. and 4 others (2007), A full Stokes-ow thermo-mechanical model for firn and ice applied to the Gorshkov crater glacier, Kamchatka, *Ann. Glaciol.*, *45*, 29–37.

Annexe D

Méthode d'intégration des éléments spectraux appliquée à l'équation d'advection/diffusion à deux dimensions

---

Formulation variationelle

La formulation variationelle du problème est équivalente à l'équation (5.2), elle est obtenue en intégrant sur tout le domaine Ω le produit de (5.2) avec une solution admissible Θ. Ω représente ici la surface formée par la coupe longitudinale du glacier. C'est cette formulation de l'équation (5.2) que l'on cherche à intégrer et qui s'écrit :

$$\iint_{\Omega} \left[\rho\, c_p \left(\frac{\partial T}{\partial t} \;+\; \vec{v}\cdot\overrightarrow{grad}\,(T)\right)\right] \Theta\, dx\, dy = \iint_{\Omega} \left[div\left(k\,\overrightarrow{grad}\,(T)\right) \;+\; Q\right] \Theta\, dx\, dy \tag{D.1}$$

où Γ est le contour de Ω. On peut monter que (D.1) est équivalente à :

$$\begin{aligned} &\iint_{\Omega} \rho\, c_p \frac{\partial T}{\partial t}\, \Theta\, dx\, dy \;+\; \iint_{\Omega} \rho\, c_p\, \vec{v}\cdot\overrightarrow{grad}\,(T)\; \Theta\, dx\, dy \\ &= \;-\iint_{\Omega} \overrightarrow{grad}\,(T)\cdot\overrightarrow{grad}\,(\Theta)\, dx\, dy \;+\; \int_{\Gamma} \Theta\, k\,\overrightarrow{grad}\,(T)\cdot\overrightarrow{d\Gamma} \;+\; \iint_{\Omega} Q\,\Theta\, dx\, dy \end{aligned} \tag{D.2}$$

Obtention du système algébrique

Discrétisation : Le domaine Ω est découpé en N_e élements Ω_e qui sont des polygônes à quatre côtés. L'équation (D.2) s'écrit ainsi :

$$\begin{aligned} &\sum_{e=1}^{N_e} \iint_{\Omega_e} \rho\, c_p \frac{\partial T}{\partial t}\, \Theta\, dx\, dy \;+\; \sum_{e=1}^{N_e} \iint_{\Omega_e} \rho\, c_p\, \vec{v}\cdot\overrightarrow{grad}\,(T)\; \Theta\, dx\, dy \\ &= \;-\sum_{e=1}^{N_e} \iint_{\Omega_e} \overrightarrow{grad}\,(T)\cdot\overrightarrow{grad}\,(\Theta)\, dx\, dy \;+\; \sum_{s=1}^{N_s} \int_{\Gamma_s} \Theta\, k\,\overrightarrow{grad}\,(T)\cdot\overrightarrow{d\Gamma_s} \;+\; \sum_{e=1}^{N_e} \iint_{\Omega_e} Q\,\Theta\, dx\, dy \end{aligned} \tag{D.3}$$

Approximation polynomiale : On utilise les polynômes de Lagrange comme base pour approcher la solution. On a :

$$T(x,y) = \sum_{e=1}^{N_e} \sum_{i=1}^{N} \sum_{j=1}^{N} T_{ij}^{e}\, h_i^e(x)\, h_j^e(y) \tag{D.4}$$

où T est la température au point de coordonnée (x, y) ; N, le degré polynomial (ici on a choisit 3) et T^e_{ij}, la valeur de T au point d'intégration (i, j) de l'élément e. h^e_i est le polynôme de Lagrange défini par :

$$h^e_i(x^{e'}_j) \;=\; \delta_{ij}\,\delta_{ee'} \;=\; \begin{cases} 1 & \text{si} \quad i = j \text{ et } e = e' \\ 0 & \text{si} \quad i \neq j \text{ ou } e \neq e' \end{cases} \tag{D.5}$$

Avec x^e_j l'abscisse du point d'intégration j en abscisse de l'élément e.

Les polynômes de Lagrange ainsi définis forment une base pour les fonctions admissibles Θ. On note $\Theta^e_{ij}(x, y) \;=\; h^e_i(x)h^e_j(y)$. L'équation (D.2) doit être vérifiée pour chaque Θ^e_{ij}.

Conditions aux limites : Pour des conditions de types Neuman (sur le flux de chaleur $\overrightarrow{F_{lim}}$) on a :

$$\int_\Gamma \Theta\, k\, \overrightarrow{grad}\,(T)\overrightarrow{d\Gamma} = \int_\Gamma \Theta\, \overrightarrow{F_{lim}} \cdot \overrightarrow{d\Gamma} \tag{D.6}$$

C'est ce qui permet par exemple d'imposer un flux basal à la base du glacier. Pour les conditions de Dirichlet (température fixée en surface), il suffit que les fonctions admissibles Θ^e_{ij} répondent à ce critère.

Intégration numérique : Les intégrales sont calculées numériquement sur chaque élément par les formules de Gauss-Lobato-Legendre. Pour cela, à chaque élément est associée une fonction de transfert de l'élément de référence (coordonnées $(\xi\,,\,\eta)$) vers l'élément réel (coordonnées $(x\,,\,y)$) (Fig D.1). On a ainsi :

$$\begin{aligned} x \;&=\; \frac{(1+\xi)(1-\eta)}{4}\,x_1 \;+\; \frac{(1-\xi)(1-\eta)}{4}\,x_2 \;+\; \frac{(1-\xi)(1+\eta)}{4}\,x_3 \;+\; \frac{(1+\xi)(1+\eta)}{4}\,x_4 \\ y \;&=\; \frac{(1+\xi)(1-\eta)}{4}\,y_1 \;+\; \frac{(1-\xi)(1-\eta)}{4}\,y_2 \;+\; \frac{(1-\xi)(1+\eta)}{4}\,y_3 \;+\; \frac{(1+\xi)(1+\eta)}{4}\,y_4 \end{aligned} \tag{D.7}$$

où $(x_i\,,\,y_i)_{i\in[1,4]}$ sont les coordonnées des quatres cotés de l'élément.

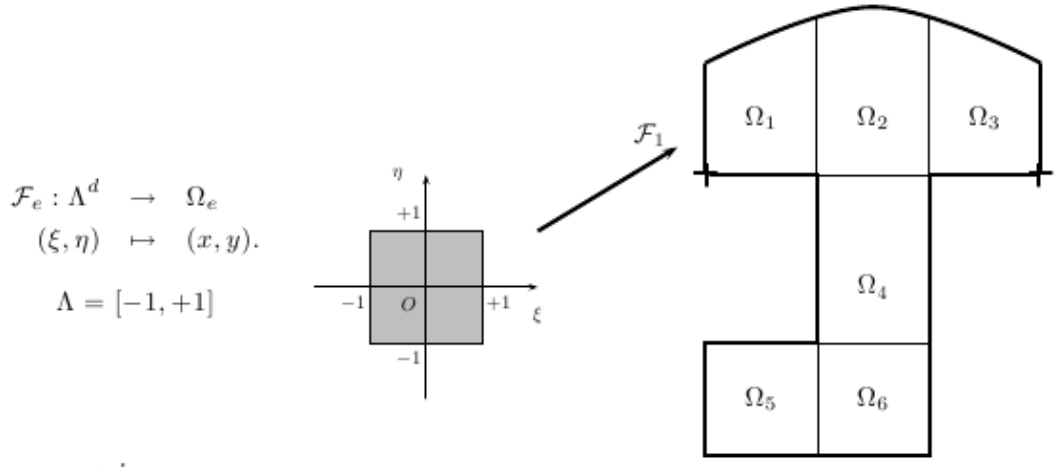

FIGURE D.1 – Illustration de la fonction de transfert de l'élément de référence vers l'élément réel

On peut ainsi écrire pour une fonction q définie sur $[-1, 1]^2$:

$$\int_{-1}^{1}\int_{-1}^{1} q(\xi,\eta)\, d\xi\, d\eta \;\simeq\; \sum_{i=0}^{N}\sum_{j=0}^{N} \omega_i\, \omega_j\, q(\xi_i, \eta_j) \tag{D.8}$$

où les ω sont les poids d'intégration et (ξ, η) les coordonnées dans l'espace de référence. Les points d'intégration (ξ_i, η_j) sont les zéros des polynômes de Legendre définis sur $[-1, 1]$ (Fig D.2).

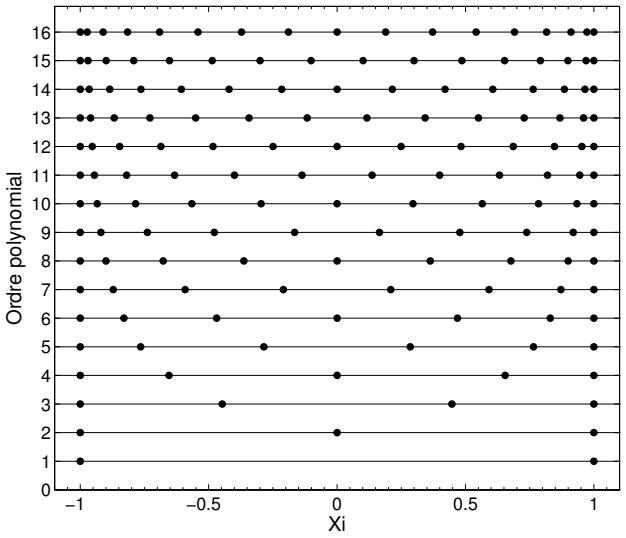

FIGURE D.2 – Points d'intégration dans l'espace de référence définis par les zéros des polynômes de Legendre

Finalement on a :

$$\begin{aligned}\iint_{\Omega_e} T(x,y)\, dx\, dy &= \int_{-1}^{1}\int_{-1}^{1} T(F^e(\xi), F^e(\eta))\, J^e(\xi,\eta)\, d\xi\, d\eta \\ &= \sum_{i=0}^{N}\sum_{j=0}^{N} \omega_i\, \omega_j\, T(F^e(\xi_i), F^e(\eta_j))\, J^e(\xi_i, \eta_j)\end{aligned} \tag{D.9}$$

ou encore par exemple pour l'intégration du gradient :

$$\begin{aligned}
\iint_{\Omega_e} \frac{\partial T}{\partial x}\, dx\, dy &= \int_{-1}^{1}\int_{-1}^{1} \left(\frac{\partial T}{\partial \xi}\frac{\partial \xi}{\partial x} + \frac{\partial T}{\partial \eta}\frac{\partial \eta}{\partial x}\right) J^e(\xi,\eta)\, d\xi\, d\eta \\
&= \sum_{i=0}^{N}\sum_{j=0}^{N} \omega_i\,\omega_j \left(\frac{\partial T}{\partial \xi}\frac{\partial \xi}{\partial x} + \frac{\partial T}{\partial \eta}\frac{\partial \eta}{\partial x}\right)(F^e(\xi_i), F^e(\eta_j))\, J^e(\xi_i,\eta_j) \\
\iint_{\Omega_e} \frac{\partial T}{\partial y}\, dx\, dy &= \sum_{i=0}^{N}\sum_{j=0}^{N} \omega_i\,\omega_j \left(\frac{\partial T}{\partial \xi}\frac{\partial \xi}{\partial y} + \frac{\partial T}{\partial \eta}\frac{\partial \eta}{\partial y}\right)(F^e(\xi_i), F^e(\eta_j))\, J^e(\xi_i,\eta_j)
\end{aligned} \tag{D.10}$$

Où J^e est le Jacobien de la fonction de transfert F^e.

Système algébrique : Avec les relations (D.3) (D.4) (D.9) et (D.10) et en utilisant l'expression des Θ^e_{ij} on obtient un système algébrique sur les T^e_{ij} qui s'écrit matriciellement :

$$\mathbf{M}\,\dot{T}(t) \;+\; \mathbf{V}\,T(t) \;=\; -\,\mathbf{K}\,T(t) \;+\; \mathbf{S}\,Q(t) \;+\; \mathbf{L}F_{lim} \tag{D.11}$$

avec $\mathbf{M}$ la matrice de masse (dépendante de ρ et c_p), $\mathbf{K}$ la matrice de rigidité (dépendante de k), $\mathbf{V}$ la matrice de vitesse (dépendante de ρ, c_p et $\vec{v}$), $\mathbf{S}$ la matrice source et $\mathbf{L}$ la matrice d'intégration des conditions aux limites en flux. T est un vecteur qui contient la température à tous les points d'intégration, Q un vecteur qui contient le terme de source à chaque point d'intégration et F_{lim}, un vecteur qui contient les flux aux limites (sur le contour Γ_s).

Evolution temporelle

On utilise un simple schéma de différences finies pour l'intégration dans le temps :

$$T(t+\Delta t) = T(t) + \Delta t\,\dot{T}(t) \tag{D.12}$$

Avec (D.11) on a :

$$T(t+\Delta t) = T(t) + \Delta t\,\mathbf{M}^{-1}\left((-\mathbf{V}-\mathbf{K})\,T(t) \;+\; \mathbf{S}\,Q(t) \;+\; \mathbf{L}F_{lim}\right) \tag{D.13}$$

La stabilité dépend ainsi du pas de temps. Plus on utilise une grille fine, plus le pas de temps doit être petit. La matrice $\mathbf{M}$ est diagonale ce qui rend son inversion immédiate.